Synthesis and application of new BODIPY-tagged NHC-metal-complexes

Development of new BODIPY-labeled transition-metal N-heterocyclic carbene complexes and their application as chemodosimeters for H_2 and CO detection, and for mechanism investigation of olefin metathesis

TECHNISCHE UNIVERSITÄT DARMSTADT

Vom Fachbereich Chemie
der Technischen Universität Darmstadt

zur Erlangung des akademischen Grades eines

Doctor rerum naturalium (Dr. rer. nat.)

genehmigte

Dissertation

vorgelegt von

Pavlo Kos
Magister der Chemie
aus Novyi Rozdil, Ukraine

Referent: Prof. Dr. Herbert Plenio
Korreferent: Prof. Dr. Boris Schmidt
Prof. Dr. Gregor Yung (Universität des Saarlandes)

Tag der Einreichung: 26 Februar 2016
Tag der mündlichen Prüfung: 11 April 2016

Darmstadt 2016
D17

Acknowledgements

Firstly, I would like to express my sincere gratitude to my supervisor, Prof. Dr. Herbert Plenio, for the opportunity to carry out my doctoral study in his research group, and for his constant support, guidance, and encouragement throughout the course of this research work. I appreciate his understanding, patience, and motivation. I am very grateful for his assistance in writing this thesis.

I would like to give special thanks Ms. Eleonore Pfeifer for her support and kindness.

I am particularly grateful to Dr. Klaus J. Wannowius for his help and assistance, and for his valuable advises.

I wish to thank my lab-mates and colleagues M. Sc. Oliver Halter, M. Sc. Meike Egert, Dipl.-Chem. Andreas Hegelein, Dipl.-Chem. Fabio Krohm, Dipl.-Ing. Natalie Peschek, Dr.rer.nat. Roman Savka, Dr.-Ing. Marc Schilz, Dr.rer.nat. Vasco Thiel, M. Sc. Roman Vasiuta, Dr.rer.nat. Jetmire Mersini, and Götz Hoffmann for the support, positive atmosphere during long working hours, and for all the fun we have had in the last four years.

I would also like to thank Dr. Tobias Meckel for his help with single molecule microscopy.

Last but not least, I would like to thank my family, friends, and especially my fiancée Nataliia Kulchytska for their constant and undwindling support throughout my Ph.D. and my life in general.

Die vorliegende Arbeit wurde am Eduard-Zintl-Institut für Anorganische und Physikalische Chemie der Technischen Universität Darmstadt unter der Leitung von Prof. Dr. H. Plenio in der Zeit von Oktober 2011 bis Juli 2015 angefertigt.

Teile dieser Arbeit sind bereits veröffentlicht oder zur Veröffentlichung eingereicht:

Papers

[1] Pavlo Kos, Roman Savka, Herbert Plenio, "*Fast Olefin Metathesis: Synthesis of 2-Aryloxy-Substituted Hoveyda-Type Complexes and Application in Ring-Closing Metathesis*", *Adv. Synth. Catal.* **2013**, *355*, 439–447.

[2] Pavlo Kos, Herbert Plenio, "*Metal Complexes of a Boron-Dipyrromethene (BODIPY)-Tagged N-Heterocyclic Carbene (NHC) as Luminescent Carbon Monoxide Chemodosimeters*" *Chem. – Eur. J.* **2015**, *21*, 1088-1095.

[3] Pavlo Kos, Herbert Plenio, "*A Fluorescent Molecular Probe for the Detection of Hydrogen Based on Oxidative Addition Reactions with Crabtree-Type Hydrogenation Catalysts*" *Angew. Chem., Int. Ed.* **2015**, *127*, 13491-13494. VIP paper.

European patent application

Kos P., Savka R., Plenio H. "Ruthenium-based metathesis catalysts, precursors for their preparation and their use". Application date: 29.10.2012. Eur. Pat. Appl. EP12190416.3. Applicant: Umicore AG & Co. KG.

TABLE OF CONTENT

1. Introduction

Over the last decades, fluorescence-based tools have found broad applications in modern science and industry. Fluorescence spectroscopy is an indispensable method in chemical and biological disciplines[1–3] and fluorescence-based methodologies[4,5] are widely used in analytical and organic chemistry, biology,[6] material science, clinical diagnosis and therapy.[7–9] Light emitting organic dyes are especially attractive for scientists as a basis for the design of different tools. Fine-tuning of the molecular structure of dyes enables the modulation of their optical and physical properties (absorbance and emission spectra, extinction coefficient, quantum yield, photostability, solubility, etc.) in a wide range. Nowadays fluorescent dyes are widely used in many areas, such as the detection of ions and molecules,[10–13] biological labeling,[14] tunable laser dyes, and solid-state solar concentrators.[15,16]

To provide a better understanding of fluorescent molecular probes, this section will cover shortly the phenomenon of fluorescence, together with a description of photophysical processes on which different applications of fluorescence dyes are based. More detailed information can be found in numerous books. Complete information about all aspects of the fluorescence phenomena, applications of fluorescent dyes and fluorescent based methodologies is provided in "*Principles of Fluorescence Spectroscopy*" by Josef Lakowicz (Springer, 3rd edition, 2006),[17] and "*Introduction to Fluorescence*" by David M. Jameson (Tailor and Francis, 2014).[18] "*Introduction to Fluorescence Chemistry*" by A. Demchenko (Springer, 2009)[19] gives excellent theoretical aspects of fluorescence, a complete overview of fluorescent detection techniques, the logic behind the design of fluorescent reporters and recognition units, mechanisms of signal transduction and many examples of applications in biochemical science. Some deeper understanding of molecular fluorescence, with a detailed description of physical and chemical processes, and particular reference to applications in physical, chemical, material, biological and medical sciences can be gained from "*Molecular Fluorescence: Principles and Applications*" by Bernard Valeur (Willey, 2001).[20] The main part of this section will be dedicated to the particular example of fluorescent dye - 4,4-difluoro-4-bora-3*a*,4*a*-diaza-*s*-indacen (BODIPY). Here will be discussed approaches to the synthesis of BODIPY core, its properties and, finally, applications of the molecular devices based on BODIPY – a variety of sensors for the detection of ions, molecules, reactive species and physical phenomena, as well as the application of BODIPY in lasers and photovoltaic devices.

1.1. Luminescence

Fluorescence as a phenomenon is a particular case of luminescence. In a broad sense, luminescence is the emission of light by any substance from an electronically excited state. Excitation can be caused by chemical reactions (chemiluminescence), electrical currents (electroluminescence), mechanical action (mechanoluminescence), radiation (radioluminescence), etc.; photoluminescence is an emission of photon upon excitation by absorbance of light quanta. Depending on the nature of the excited state, photoluminescence is divided into two types. When the emission of light takes place from the singlet state, i.e. the electron in the excited orbital has the opposite spin than the electron in the ground-state orbital, the return of this electron with the loss of energy (photon) to the ground state is allowed and proceeds very fast. This process is called fluorescence. Normally, the time a fluorophore spends in the excited state (fluorescence lifetime) for organic dyes is in a range of 10^{-8} – 10^{-11} s. On the other hand, phosphorescence takes place when the singlet state electron upon absorbance of a photon is transferred via intersystem crossing (ISC) to the triplet state with the same spin as the electron in the ground state orbital.

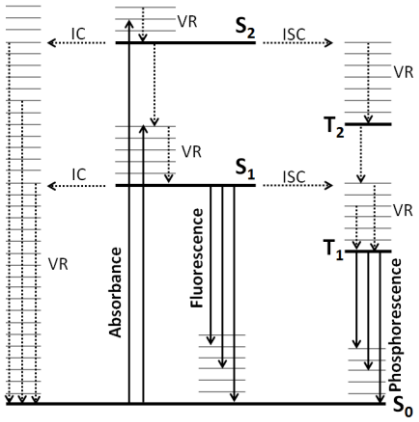

Figure 1.1: Jablonski diagram; S_0 – ground state, S_1, S_2 – singlet excited states, T_1, T_2 – triplet excited states, VR – vibrational relaxation, ISC – intersystem crossing, IC – internal conversion.

The Jablonski diagram (figure 1.1) schematically illustrates photon-induced changes in the electronic state of dye molecules. Each electronic state has a number of vibrational levels. Upon absorbance of a photon, a molecule from ground state S_0 is excited to the higher vibration states S_1 or S_2. This process is very fast and the time is too short for nuclei to change their coordinates. Next, the molecule undergoes relaxation to the lower vibration level of S_1. This process is called internal conversion. Usually, fluorescence occurs from the lowest vibrational level of S_1 to one of the vibrational levels of S_0. The relaxation and excitation processes usually proceed very fast (in total up to 10^{-12} s), that is why fluorescence lifetime is basically the time the molecule spends in the excited state.

The excited state molecule can also undergo a transition to one of the higher vibrational levels of the triplet state. This process is called intersystem crossing. Such triplet state is characterized by the same spin orientation of the electron in the excited-state orbital, as one in the ground-state orbital. Its transition to the ground state is forbidden and kinetically not favorable. However, this process still occurs, but it is much slower compared to the fluorescence. Normally, phosphorescence lifetimes are in the range of milliseconds, but substrates with phosphorescence lifetimes of minutes or even hours are also known. Heavy atoms increase the possibility of intersystem crossing and thus, for molecules with heavy atoms, phosphorescence is quite common. Some molecules can have intermediate fluorescence lifetimes and sometimes it's difficult to distinguish phosphorescence from fluorescence, for example, in some organic complexes of heavy metals.

1.1.1. Fluorescence Parameters Used in Sensing

Fluorescence as a phenomenon can be characterized by many parameters and all fluorescent sensing techniques are based on the monitoring of changes in parameters. Fluorescence intensity F is the measured intensity of emitted light by fluorophore at a given excitation and emission wavelengths. It strongly depends on many physical conditions, like temperature, concentration of dye, intensity and wavelength of light source, solvent, presence of quenching agents, etc. The dependence of fluorescence intensity F on wavelength gives *emission spectra*. The shape of the emission spectrum normally is independent of the excitation wavelength. This can be explained by the fast relaxation of the excited molecule to the lowest vibrational state S_1, so the emission takes place from the same energy level S_1 to one of the vibrational levels of S_0, regarding the excitation energy. Another important consequence of this process is that a fluorescence spectrum is usually a "mirror image" of absorbance spectrum. Excitation takes place from the ground S_0 to one of the vibrational levels of S_1, and emission – from the ground S_1 to the vibrational levels S_0. In most fluorophores vibrational energy levels S_1 and S_0 are very similar and are not significantly altered by the different electronic distributions of S_0

and S_1. This results in the symmetrical emission and absorbance spectra. However, there are many exceptions to these rules of "mirror image" and "fluorescence spectrum shape" known. Two-photon absorbance, $S_0 \rightarrow S_2$ excitation, excited state chemical reactions, excited dimer formation are a few examples of processes which alter fluorescence spectra. If the emission intensity is measured against the excitation wavelength, this gives *excitation spectra*.

Other characteristic parameters of fluorophore are *absorbance and emission maxima* (λ_{abs}, λ_{em}). Fluorescence usually occurs at lower energies and longer wavelength than excitation. The difference between λ_{abs} and λ_{em} is called *Stokes shift* after Sir G. G. Stokes who first observed this phenomenon in 1852.[21] The common reason for the Stokes shift is the loss of energy through the non-radiative vibrational relaxations, but additional energy loss can take place through the solvent stabilization of excited state, complex formation, energy transfer, etc.

Fluorescence *anisotropy I* and fluorescence *polarization P* are two related parameters which can provide information on the environment of the fluorophore and are widely used in the biochemical and biological applications of fluorescence. Upon irradiation of solution with polarized light, only molecules with the transition moment parallel to the electric vector of light can absorb this light. In low viscous media the rate of molecules rotation is much higher than the rate of fluorescence, so during fluorescence lifetime the molecule can change its orientation multiple times leading to the loss of polarization in the emitted light. Hindered rotation, for example by increasing of viscosity of environment, or when the dye is a part of the polymer, leads to a polarized emission. By recording polarization of fluorescence at two different angles, anisotropy can be calculated.

Fluorescence quantum yield Φ is perhaps the main characteristic of the efficiency of the fluorophore to emit light through the fluorescence. In common words, fluorescence quantum yield is the ratio of photons emitted through the fluorescence, to the total numbers of absorbed photons. Fluorophores with Φ value close to 1 are the best emitters, for non-fluorescent compounds Φ is approaching 0. Fluorescence quantum yield strongly depends on many conditions, like temperature, solvent polarity, type of substituents in the fluorophore, etc.

Finally, another important parameter of fluorophores is *fluorescence lifetime* τ. Basically, fluorescence lifetime is the average time that a molecule spends in the excited state prior to the return to the ground state, as detected by fluorescent spectroscopy. Fluorescence lifetime includes both relaxation pathways, radiative and radiationless (without emission of light quanta). For fluorescent compounds, the fluorescent lifetime is normally in the range of 10 ns. There are many factors that alter fluorescent lifetimes. For example, the introduction of heavy atoms increases the probability of non-radiative decay and thus, decreases fluorescence lifetime, resulting in the lower quantum yields.

1.1.2. Photophysical Mechanisms of Fluorescence Sensing

For a better understanding of the detection mechanisms of BODIPY-based molecular devices, presented in the next sections, in this paragraph the main photophysical processes and basic principles that are involved in the fluorescence sensing will be shortly discussed.

One of the most important photophysical processes responsible for the modulation of the fluorescence signal is fluorescence quenching. Fluorescence quenching is a process of decreasing fluorescence intensity of the fluorophore. A variety of factors, both intramolecular and involving the molecules of the dye and the quencher, can be responsible for fluorescence quenching. This can be collisional quenching, excited-state and ground-state complex

formations, energy transfer, molecular rearrangements, photoinduced proton or electron transfer, solvent or intramolecular relaxation, or Dexter electron transfer.

Collisional quenching requires direct contact between molecules of quencher and fluorophore and occurs when the quencher diffuses to the fluorophore during the life-time of the excited fluorophore. Upon contact, the molecule in the excited state returns to the ground state without the emission of light quanta. Collisional fluorescence quenching is described by the Stern-Volmer equation:

$$F_0/F = 1 + k \cdot \tau \cdot c(Q),$$

where F_0 and F are fluorescence intensities in the absence and the presence of quencher, respectively; k – bimolecular quenching constant; τ – fluorescence lifetime of dye in the absence of quencher; c(Q) – concentration of quencher. This mechanism is usually used to determine the diffusion coefficients of quencher in the studied environment. Many molecules can act as collisional quenchers, e.g. molecular oxygen, heavy halogens, and aromatic or aliphatic amines. This quenching mechanism is not typical for BODIPY fluorophore due to its short fluorescence life-times.

The most important mechanism in the design of BODIPY-based molecular probes is photoinduced electron transfer (PET). This process occurs in the system of electron donor *D* and acceptor *A*, where, upon excitation complex D^+A^- is formed, which returns to the ground state without photon emission. Depending on whether the fluorophore acts as a donor or acceptor, there are two types of PET – reductive and oxidative, and the direction of electron donation is determined by the redox potentials of fluorophore and quencher. The PET mechanism can be described pictorially in terms of simplified molecular orbitals scheme (figure 1.2).

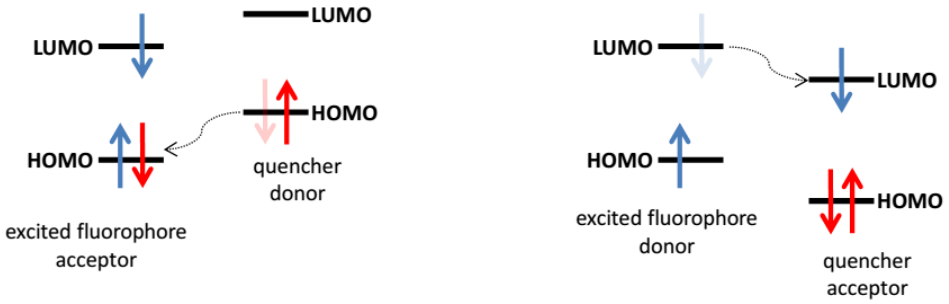

Figure 1.2: Reductive (left) and oxidative (right) photoinduced electron transfer.

Most of the PET-based molecular probes include both donor and acceptor as parts of the molecule, connected by some linker. In reductive PET, photoexcitation promotes an electron of the fluorophore from HOMO to LUMO. Subsequently, the electron from higher-energy HOMO of receptor occupies the vacant HOMO orbital of the fluorophore and prevents the relaxation through the photon emission. On the other hand, in oxidative PET, a LUMO electron of the excited fluorophore (donor) is transferred to the lower-energy LUMO of the receptor (acceptor). Manipulation of the electronic state of the receptor, for example, coordination of analyte, oxidation or reduction, changes in the energy of the receptor's HOMO and LUMO, influence the efficiency of PET. Normally, reductive PET operates in the "turn-on" probes, and oxidative PET – in "turn-off" type sensors.

Another possible mechanism of the fluorescence quenching is the *heavy atom effect*. The presence of heavy atoms in the dye molecule or collision between the excited fluorophore and quencher increases the probability of the intersystem crossing ($S_1 \rightarrow T_1$) through the spin-orbit coupling (coupling between orbital and spin magnetic moments of excited dye and quencher). The efficiency of this coupling depends on the fourth power on the atomic number of the

quencher. After a dye undergoes intersystem crossing, the relaxation $T_1 \rightarrow S_0$ through the emission is symmetry forbidden and the formed triplet state is relatively long lived. This triplet state can be quenched to the ground state by the same quencher, can undergo internal conversion, or lose energy by generating singlet oxygen. Additionally, many fluorophores in the triplet state can be involved in different photoreactions. The most well studied example is the quenching by heavy halogens, e.g. bromine or iodine. This effect has found broad applications in the photodynamic therapy, where halogenated dyes are used for the intracellular generation of singlet oxygen.

When the molecule of the fluorescent dye is constructed in the way that the EDG and EWG are separated by a conjugation chain, intramolecular (internal) charge transfer (ICT) phenomenon can be observed. Upon excitation, the electronic density distribution of the molecule is changed and changes in the dipole moment can be considered. Usually, excited molecule has a higher dipole moment, and in the non-polar solvents, fluorescence from local excited state (LE) is observed. In the polar solvent, during the lifetime of the excited state, solvent shell around the dipole is equilibrated, resulting in the fluorescence from the lower-energy state (ICT) with stabilized charge separation. These dyes are characterized by "normal" emission in non-polar solvents from LE state, but due to the solvent stabilization in the polar media, bathochromic shift and decrease in quantum yield in the emission of ICT state are observed. More rarely the ground state has the bigger dipole moment than the excited state. In this case, in polar solvents, the emission spectrum is shifted to the shorter wavelength. Interaction of an analyte with the receptor (can be both, EWG and EDG) can change the efficiency or switch on-off the ICT process by changing the polarity of ground or excited states. Many ratiometric sensors are based on this principle.

Another important process which occurs with the dye in the excited state is resonance energy transfer (RET), more often referred to as fluorescence or Förster energy transfer (FRET). FRET is a non-radiative excitation energy transfer, which occurs between excited donor and acceptor in the ground state through the dipole-dipole interaction without intermediate photon. FRET can occur if the emission spectrum of the donor overlaps with the absorption spectrum of the acceptor, so that several vibronic transitions in the donor are in resonance with the corresponding transitions in the acceptor, and they have nearly the same energy.[10] While the donor is always a fluorescent dye, the acceptor can be also a non-fluorescent compound. In this case, FRET is a quenching mechanism. If the acceptor is another fluorescent dye, a decrease in donor's quantum yield and an increase in acceptor's fluorescence are observed. FRET efficiency is strongly dependent on the distance between donor and acceptor with the optimal distances for different pairs being in a range of 1.5 – 6 nm. It is often used for the distance measurements in biological objects (for example, determination of protein conformation), for the investigation of supramolecular interactions, or mechanisms of chemical reactions. Another application of FRET is the artificial enhancement of the Stokes shift. This phenomenon has been also widely used for the design of cassettes for photovoltaic devices, which contain a cascade of FRET pairs to cover a broad range of absorbed light wavelength.

Quite similar to FRET quenching are electron-exchange interactions, commonly known as Dexter exchange of Dexter quenching. By analogy, this kind of interaction occurs through the energy transfer from the excited donor to the acceptor in the ground state, but in this case, energy is transferred through the electron exchange. The electron from the LUMO orbital of the excited fluorophore is moved to the acceptor with simultaneous or consecutive transfer of an electron from the HOMO of the acceptor to the HOMO of the donor. Dexter quenching requires much shorter distances, in comparison to those in FRET, and can be observed only at high concentrations of donor and acceptor.

1.2. BODIPY

Compounds based on the BODIPY core (4,4-difluoro-4-bora-3*a*,4*a*-diaza-*s*-indacen) are amongst the most popular fluorescent dyes and have found broad applications in chemical sensing,[10–12,22,23] and biological imaging.[24,25] Although BODIPY became popular only in the mid 1990's, it was first described in 1968 by Kreuzer and Treibs.[26] The authors attempted to conduct acylation of 2,4-dimethylpyrrole by acetyl chloride in the presence of BF_3 as a Lewis acid, but instead of the desired 2-acetyl-3,5-dimethylpyrrole they observed the formation of highly fluorescent compound 1.1 (figure 1.3).

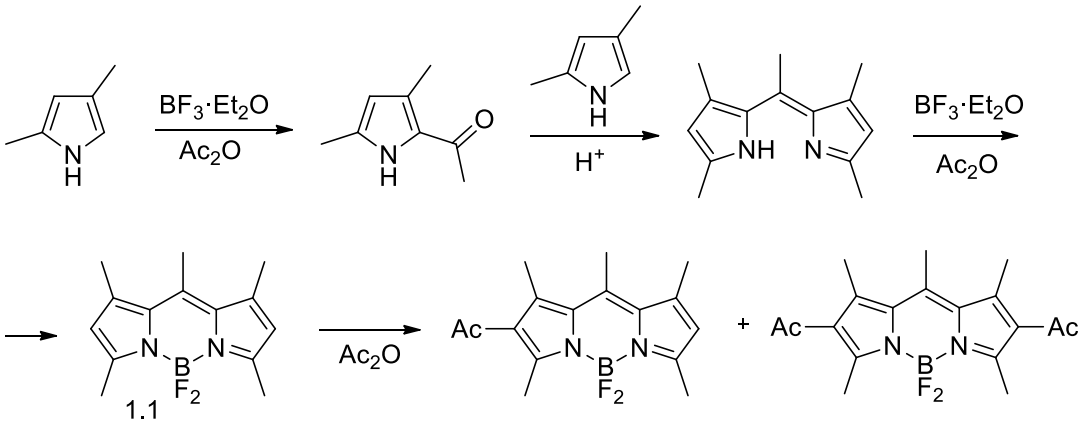

Figure 1.3: Synthesis of BODIPY by Kreuzer and Treibs.

Compared to other known dipyrrin complexes, BODIPY is characterized by very high chemical stability and decomposes only under very strong acidic or basic conditions. This allows a wide range of reactions on the BODIPY core, and renders BODIPY a very versatile substrate for tuning its properties by introducing various groups into the BODIPY core. High stability can be explained by the fact that boron, fluorine, and nitrogen are first row elements enabling efficient orbitals overlapping and efficient delocalization of π-orbitals.

1.2.1. Structure of BODIPY

BODIPY, like many other fluorescent organic dyes, is characterized by a planar structure. Coordinated BF_2 unit restricts the flexibility of dipyrrin structure leading to enhanced fluorescence. The structure of BODIPY core can be described by two equivalent resonance structures, shown on figure 1.4. In this work, for simplification, the structure with omitted positive charge on the nitrogen atom and negative charge on the boron atom will be used. The numbering of any substituents in BODIPY follows rules set for *s*-indacene, and position 8 sometimes is referred as *meso*-position by analogy to porphyrinic systems.

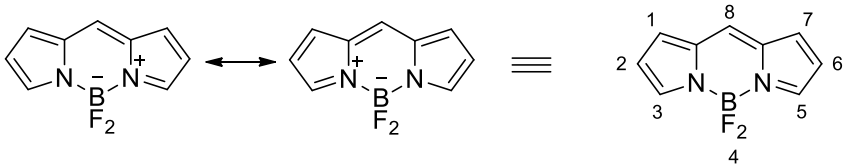

Figure 1.4: Two resonance structures of BODIPY and commonly used uncharged form with IUPAC numbering.

Such structure of BODIPY can be considered as "rigidified" monomethine cyanine dye, with the π-conjugation running along the backbone of the molecule[27] (figure 1.5).

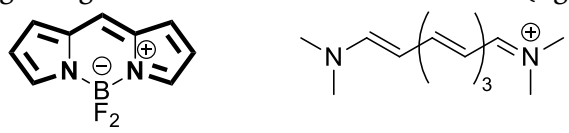

Figure 1.5: π-conjugation in BODIPY and general structure of cyanine dyes.

1.2.2. Synthesis of BODIPY Core

There are a couple of synthetic routes toward the BODIPY core and most of them are based on well-known pyrrole condensation reaction from porphyrin research.[27,28] These approaches lead to the formation of symmetrical BODIPY molecules and are based on the reaction of pyrrole with electrophile reagent. A detailed overview of modern methods of synthesis of BODIPY core, as well as the chemistry of BODIPY, are covered in numerous review articles.[27,29–31]

The synthesis of BODIPY from aromatic aldehydes is well known and widely used.[32,33] Acid-catalyzed condensation of pyrroles with aldehydes leads to the formation of dipyrrolemethanes. This reaction should normally be done in the presence of large excess of pyrrole to prevent polymerization. Dipyrrolemethanes are unstable compounds and normally are not isolated, but *in situ* oxidized to dipyrromethenes or dipyrrins with DDQ or *p*-chloranil (figure 1.6).

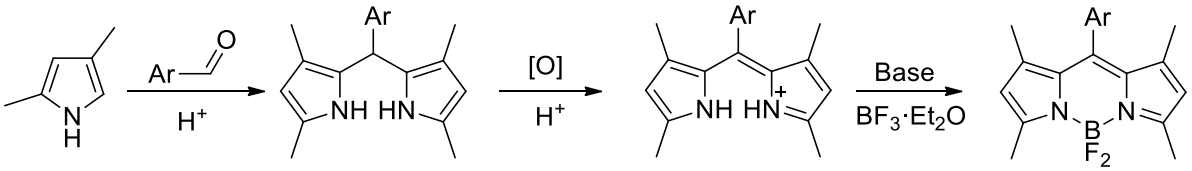

Figure 1.6: Synthesis of BODIPY by condensation of pyrroles with aromatic aldehydes.

Deprotonation of formed dipyrrins and complexation with boron trifluoride diethyl etherate affords the desired BODIPY. It should be noted that there is only one known example of BODIPY synthesis from non-aromatic aldehydes.[34] The authors were able to obtain product 1.2 (figure 1.7) in less than 2% yield from 2-methylpyrrole and 3-(phenylthio)-propenal in the presence of ytterbium (III) trifluoromethane sulfonamide as a Lewis acid. Lindsey and coworkers reported[35] that in case of substituents at *meso*-position other than aryl, oxidation of dipyrrolemethanes with DDQ or *p*-chloranil fails.

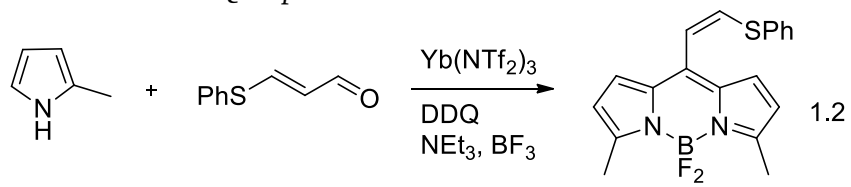

Figure 1.7: Synthesis of BODIPY by Biellmann et al..

Acylium equivalents, like anhydrides,[36] acid chlorides,[37] or orthoesters,[38] can also be used as an electrophilic agent. In this case, the reaction doesn't stop with the formation of acylated pyrrole. Under acidic conditions, 2-acylpyrrole rapidly reacts with the second molecule of pyrrole with the formation of dipyrrin. The reaction doesn't require an oxidation step and after basification and complexation with BF_3 often provides target BODIPY in higher yields,[39] compared to the aldehyde approach (figure 1.8). The reaction of pyrroles with acylium equivalents leads to the formation of symmetrical BODIPYs, but unlike with aldehydes, it allows the synthesis of alkyl-substituted dyes at *meso*-position.

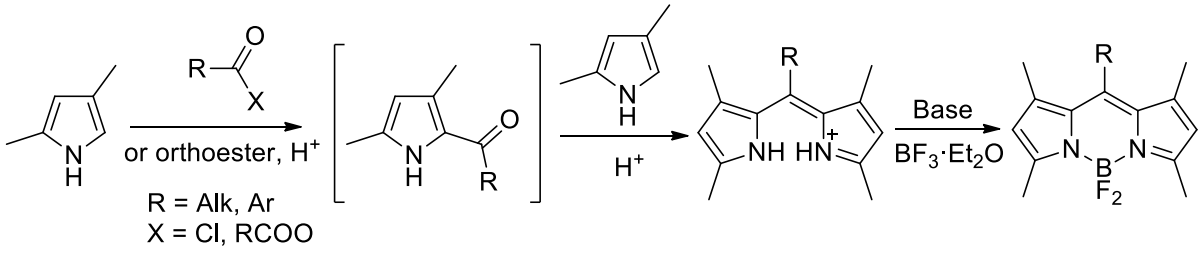

Figure 1.8: Synthesis of BODIPY by condensation of pyrroles with acylium equivalents.

Asymmetric BODIPYs can be synthesized by acid-catalyzed condensation of α-acylated 1-H-pyrrole with another pyrrole. Bringmann and coworkers reported[40] the synthesis of unsymmetric BODIPY using this approach in exceptionally high yields (figure 1.9).

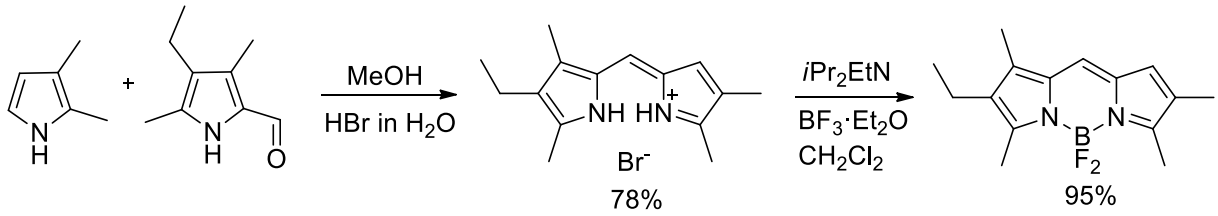

Figure 1.9: Synthesis of asymmetrical BODIPY.

In a similar approach[41] condensation of 2-formyl-pyrroles with other pyrroles is conducted in the presence of phosphoryl chloride. This method was used by Hao[42] for the synthesis of benzo-fused BODIPY dyes (figure 1.10). The authors were able to obtain unsymmetric BODIPY from 1-formyl-isoindoles and pyrroles in the presence of $POCl_3$ in moderate to good yields.

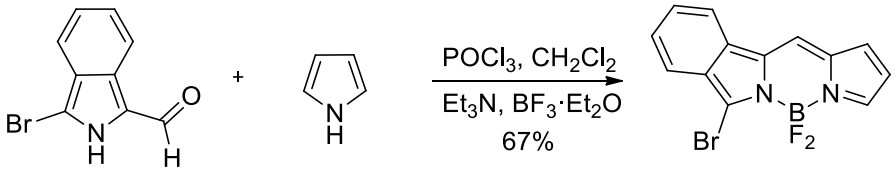

Figure 1.10: Synthesis of asymmetrical benzo-fused BODIPY by Hao et al..

Condensation of pyrrole-2-carbaldehyde with pyrrole is an especially valuable method because it is one of very few methods to access BODIPY systems without 8-substituent. Burgess and coworkers discovered[43] that pyrrole-2-carbaldehydes can form the same product in the reaction with phosphoryl chloride alone. The mechanism, proposed by the authors, deserves a closer look (figure 1.11). In this reaction, Lewis acids other than $POCl_3$ don't give desired product. This indicates that $POCl_3$ is intimately involved in the reaction. Based on the NMR and UV/Vis studies, the authors assume that $POCl_3$ reacts with pyrrole-2-carboxy-aldehyde to give a vinylogous Vilsmeyer-Hack reagent. Formation of the product relies on the electrophilic attack of this reagent (alternatively the chloride could be a phosphorus-based leaving group) on the C_2-atom of another pyrrole-2-carbaldehyde molecule. The formed intermediate then loses CO and HCl to form dipyrrin which was *in situ* complexated with boron trifluoride diethyl etherate to give BODIPY.[44]

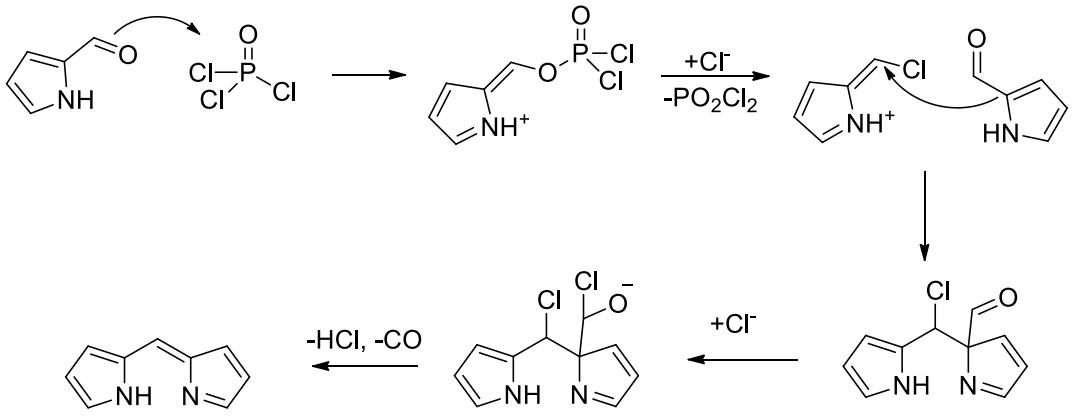

Figure 1.11: Proposed mechanism for the reaction of pyrrole-2-carboxy aldehyde with $POCl_3$.

An important method of BODIPY synthesis was described by Biellmann and coworkers,[34] who used the reaction of thiophosgene with pyrroles for the synthesis of dipyrrylthioketones (figure 1.12). Such reaction is fast and provides product in rather mild conditions in good yields without the formation of condensation products. The formed thioketones are the

important starting material for the synthesis of different 8-heteroatom and other *meso*-substituted BODIPYs. Thus, alkylation of thioketones leads to the formation of alkylthioxy dipyrrolmethenes in protonated form. Deprotonation and complexation with $BF_3{\cdot}Et_2O$ provide 8-alkylthioxy BODIPYs.

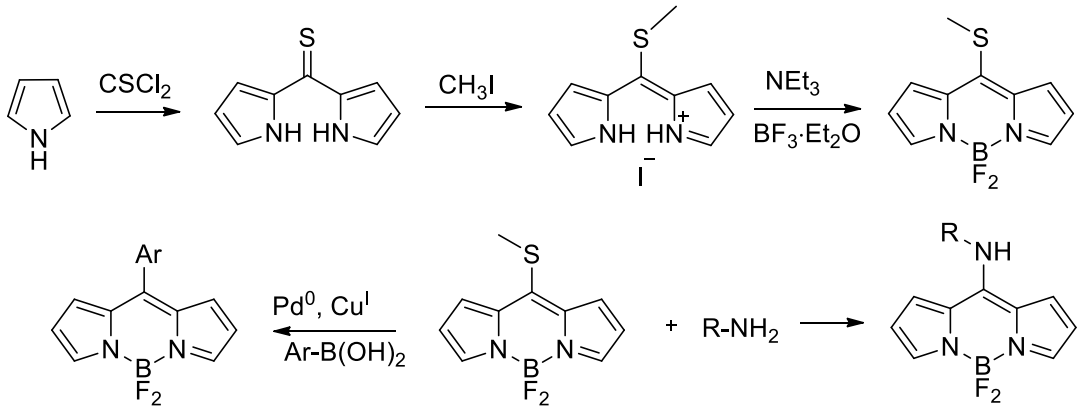

Figure 1.12: Synthesis of 8-thiomethyl-BODIPY and 8-substituted-BODIPYs from it.

In such compounds, the substituent in *meso*-position can be easily replaced by nucleophiles. For example, reaction with aliphatic amines provides corresponding 8-(amino)-BODIPYs,[45] which are characterized by blue-shifted absorbance and emission spectra, high photostability, large Stokes shifts and quantum yield close to 1, which makes them very prominent laser dyes in the visible blue spectral region. 8-thiomethylBODIPYs also react rapidly under Liebeskind-Srögl cross-coupling conditions[46] with aromatic boronic acids to provide the corresponding 8-aryl substituted BODIPYs.

Oxidation of dipyrrylthioketones by hydrogen peroxide leads to the fast and efficient formation of corresponding symmetric ketones. Dehaen[47] showed that treatment of formed dipyrrylketones with $POCl_3$ rapidly converts substrate to the bipyridinium salt. *In situ* deprotonation and complexation result in a single fluorescent compound, which was identified as the target *meso*-chlorinated BODIPY. 8-HaloBODIPYs are interesting compounds because they are very promising starting materials for the preparation of more complex *meso*-substituted BODIPY analogs (figure 1.13) via elaboration of the reactive halogen through, e.g., SN_{Ar} or transition-metal-catalyzed transformations (Suzuki, Stille, Heck, Negishi, Sonogashira, etc.).

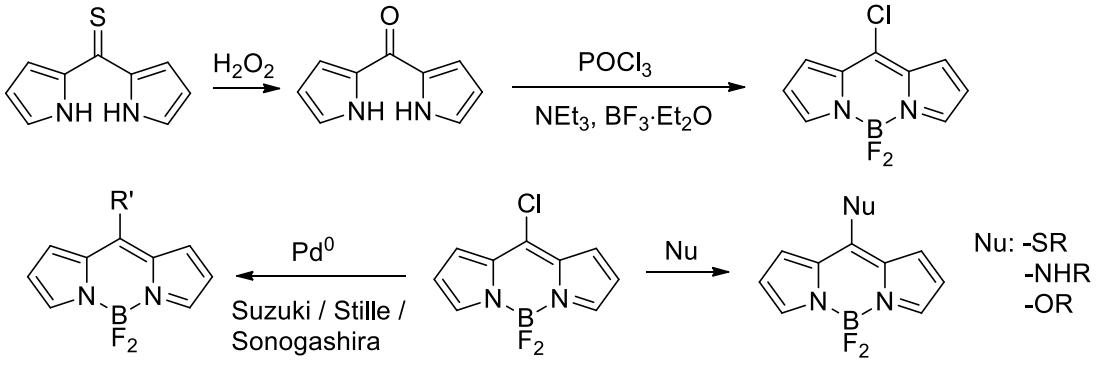

Figure 1.13: Synthesis of 8-chloro-BODIPY and other 8-substituted BODIPYs based on it.

Following the discovery of BODIPY in 1968, an impressive diversity of BODIPYs was synthesized and a variety of efficient synthetic procedures towards different BODIPY derivatives were developed. However, the parent unsubstituted BODIPY remained elusive until very recently. In 2009 three different groups simultaneously reported the independent synthesis of unsubstituted BODIPY. The problems with the synthesis of the simplest BODIPY have been related to the very low stability of the corresponding dipyrrene, which tends to

decompose at temperatures above -40 °C. Bruce et al..[48] explained the low stability of the dipyrrene by its high sensitivity towards nucleophilic addition. To overcome this problem, the authors conducted oxidation of dipyrrolemethane and subsequent complexation of formed dipyrrine at -78 °C, which allowed them to obtain the target unsubstituted BODIPY in 5-10 % yield (figure 1.14).

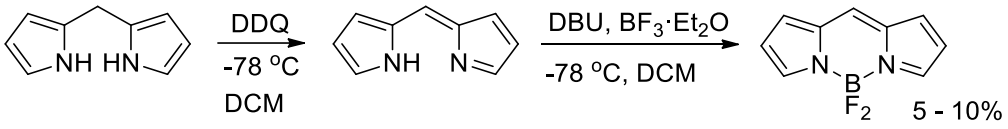

Figure 1.14: Synthesis unsubstituted BODIPY by Bruce et al..

Jung and coworkers[49] overcame the problem of low stability of dipyrrin by applying a one-pot strategy. Trifluoroacetic acid catalyzed condensation of 1-*H*-pyrrole with 2-formylpyrrole followed by deprotonation with diisopropylethylamine and subsequent complexation of the intermediate dipyrromethene with boron trifluoroetherate afforded desired product in <10 % yield (figure 1.15).

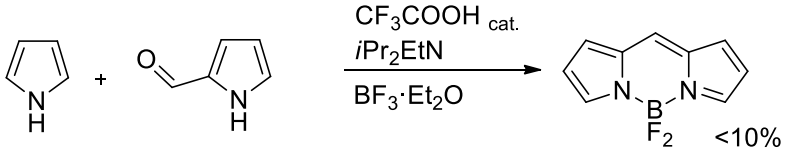

Figure 1.15: Synthesis of unsubstituted BODIPY by Jung et al..

The most successful synthesis of unsubstituted BODIPY was reported by Peña-Cabrera and coworkers,[50] who obtained the core compound using Pd^0-catalysed reduction of *meso*-thiomethyl BODIPY by the analogy to Fukuyama reaction. Applying Liebeskind-Srogl cross-coupling conditions with the boronic acid replaced by triethylsilane, authors were able to obtain target unsubstituted BODIPY in high yield (figure 1.16).

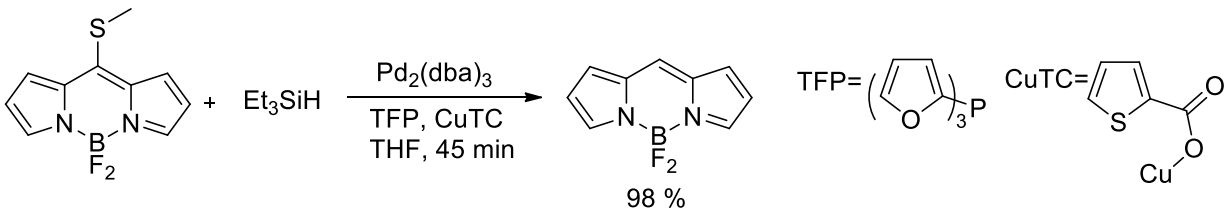

Figure 1.16: Synthesis of unsubstituted BODIPY by Peña-Cabrera et al..

Even so the majority of known methods of BODIPY synthesis are efficient one-pot reactions and provide a diversity of target dyes in moderate – to good yields, they all require inert atmosphere, dry conditions and long reaction times (hours to days). Dzuba et al.[51] have recently reported interesting improvement of BODIPY synthesis. They reasoned that the condensation step between the 2-substituted pyrroles and aldehydes (or acid chlorides) should be more facile at higher concentrations and probably most efficient under neat conditions. The condensation of 2,4-dimethylpyrrole and 4-nitrobenzaldehyde was performed with grinding by using a simple mortar and pestle, followed by the addition of a few drops of TFA and oxidation with *p*-chloranil. The reaction mixture was subsequently treated with Et_3N and $BF_3{\cdot}OEt_2$ to afford BODIPY dye. All reagents were added sequentially with grinding in ca. 5 minutes. The desired product was isolated in 29% yield, which was comparable to those reported for the same compound in literature protocols, 24–40%, but in substantially shorter reaction time.

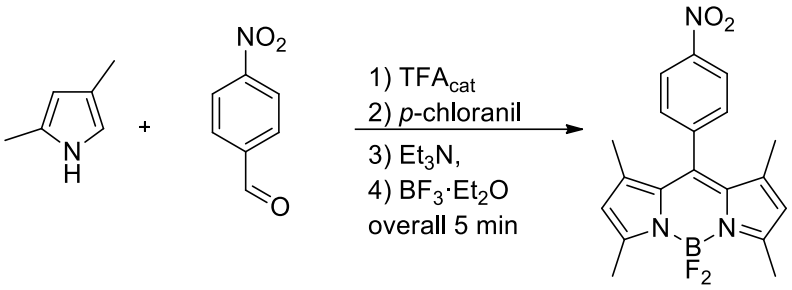

Figure 1.17: Mechanochemical synthesis of BODIPY by Dziuba.

1.3. Fluorescent Probes Based on BODIPY

A molecular probe is a molecule which is able to convert chemical or physicochemical information, such as the presence and concentration of a specific analyte, environmental viscosity, temperature, etc. into an analytically useful signal. A typical fluorescent probe combines an analyte recognition site or receptor connected to the fluorophore, which translates electronic or structural changes of the receptor into a fluorescent signal.[10]

The ideal fluorescent indicator should fulfill certain requirements. First, it should be able to produce a fluorescence response to the desired analyte without similar reaction to competing analytes (high selectivity). The fluorescence should be as bright as possible with a large fluorescence response in the presence of analyte. The extinction coefficient of dye should be high. Very important is the chemical stability of the probe, as well as high photostability, and solubility. The dissociation constant of probes which form complexes with analyte should match the analyte concentration range which will be monitored. It also is desirable to have the reversible association – dissociation of receptor and analyte as fast as possible. For many reasons indicators which can be used for measurements in visible, especially in red, or NIR light, are favored over other probes. Probes which give “turn-on” response in the presence of an analyte, or show shifts in emission or absorption spectra, are better than probes with “turn-off” response because normally they have higher signal-to-noise ratio. For biological applications the probe should have good water solubility, membrane permeability and minimal toxicity to living samples. Excitation and emission at operational wavelengths in 650-900 nm region are essential, since such light makes minimal photodamage to living systems, has good tissue permeability, and most biological samples have low fluorescence background in that region, producing a high signal-to-noise ratio.[10,17,19]

Because of its unique properties, BODIPY is an excellent choice as a fluorescent component for probe design. Good stability against chemicals and light, small molecular size, bright fluorescence with sharp excitation and emission spectra in the visible region are advantages which make BODIPY widely used as a fluorophore for indicators. Moreover, its spectroscopic and analyte binding properties can be easily customized by introducing practically any chelator and other groups at almost any position.

1.3.1. BODIPY-Based pH Sensors

Regulation of intracellular pH is essential for the normal functioning of bioprocesses in living organism. Cellular pH plays a central role in many events including cell proliferation, metastasis, apoptosis, and drug resistance.[13] Variations of intracellular pH are linked to abnormal cell growth and division, and are typical in diseases such as inflammation, Alzheimer’s disease, and cancer.[22]

Methods of nonpenetrative pH registration inside living cells are very important for clinical diagnostics of tumor and biological imaging. Hence, much effort has gone into the development of pH-sensitive fluorescent probes. In the context of bioimaging, such intracellular pH sensor should meet many requirements. It should produce a fluorescent response to the near-neutral cytosolic pH ranges (6.8-7.4) and be soluble in an aqueous environment. BODIPY with its low cytotoxicity, resistance towards aggregation, narrow emission and absorbance peaks, high extinction coefficients and excellent quantum yields became especially attractive as a reporting group for intracellular pH indicators. The fact that fluorescence of BODIPY core itself doesn't depend on the pH of the environment; its chemical robustness and good photostability make BODIPY a very desirable candidate for the design of such probes. A number of methods of conjugation chain modification and careful choice of sensing part of indicator molecule allow the efficient design of needed probe. Despite all the advantages of BODIPY, up to now, no probes which meet all mentioned criteria were reported. Most of the reported so far pH indicators as a receptor contain pyridyl,[52] imidazolyl,[53,54] aliphatic amino-,[55] imino-,[56] or phenolic OH- group,[57–59] dialkylated aromatic amino-,[52,60–64] or even aldehyde group,[65] and thus, are not enough sensitive to small changes of near neutral pH values and responsive only to moderate or strong acidic and basic pH levels.

Amongst the most popular and well-developed BODIPY-based pH indicators are systems containing amino group as a receptor. The *N*-alkylated group acts as a strong electron donor and dramatically quenches the fluorescence of BODIPY. There are two possible mechanisms of quenching and almost all these examples are "turn-on" probes. In case an amino group is connected through the spacer to the *meso*-position of BODIPY and is not conjugated to the BODIPY core, normally reductive PET is responsible for the "off"-state of dye. Protonation of the nitrogen atom prevents PET and leads to a strong fluorescence.

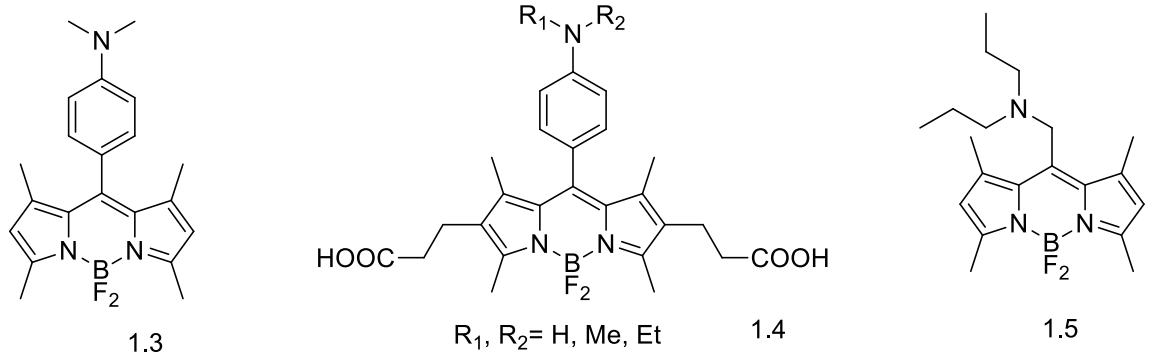

Figure 1.18: Reductive PET-based pH sensors.

Molecular probe 1.3, first reported by Wolfbeis in 1997,[61] has pK_a values in a range of 2.31 – 3.3 in different methanol – water mixtures and incorporated into a hydrogel matrix provides transparent sensor membrane which can be used to measure the pH in the range of 0.5-3.0. Molecular probes 1.4 and 1.5 are examples of fine tuning of the original structure (figure 1.18). In 2009 Kobayashi et al.[64] reported the use of sensors 1.4 for the imaging of tumor cells. These acidic pH–activatable probes were conjugated to a cancer-targeting monoclonal antibody. *Ex vivo* and *in vivo* imaging of human epidermal growth factor receptor type 2–positive lung cancer cells in mice were performed and the probe was shown to be highly specific for tumors with minimal background signal. Carboxyethyl groups in the BODIPY core were used for coupling to the proteins. Modification of the basicity of amino groups by careful selection of alkyl groups at the nitrogen atom allowed the authors to synthesize probes which were responsible for a wide range of acidic pH. Neutral forms of these probes had a quantum yield around 0.002 and upon protonation 300-fold increase in fluorescence were observed.

Both ICT and PET mechanisms are often responsible for quenching in molecular probes with amino group electronically connected to the conjugating chain of BODIPY (figure 1.19). Usually, in this type of probes, the amino group is connected through the double bond or phenyl rings to the 3- or 5- position in the BODIPY ring, but other examples are also known.[60] The mechanism of proton detection can be described on the probe, reported by Boens and coworkers[62] in 2006. In polar solvents, photo-excitation of 1.6 leads to the population of a highly polar ICT state, which is deactivated by an increase of the internal conversion rate as the energy gap between the excited and the ground state decreases (Φ decreases from 0.97 in hexane to 0.13 in MeCN). Protonation of the dimethylanilino group in 1.6 switches off any ICT interaction leading to the typical BODIPY-like narrow, structured, and solvent polarity independent absorption and emission bands.[10]

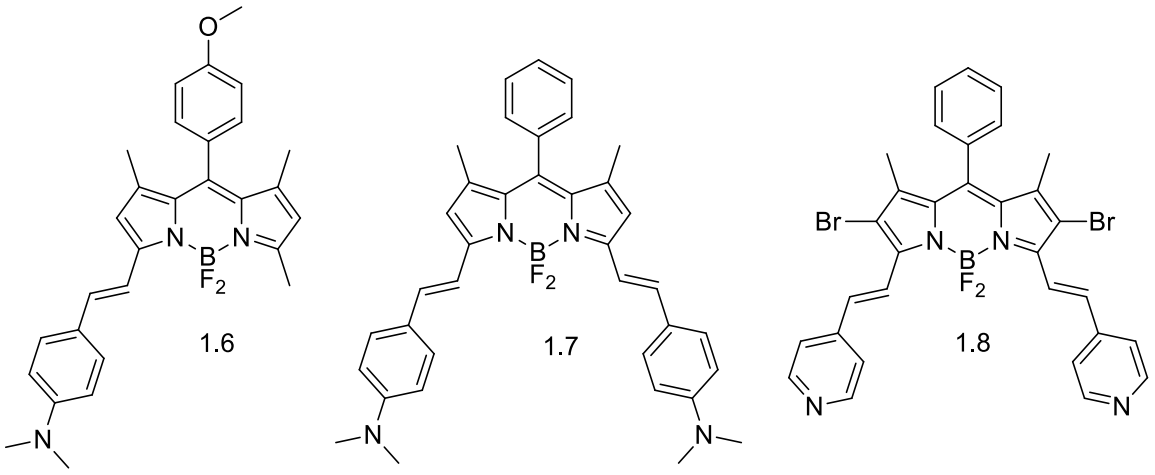

Figure 1.19: ICT based pH sensors.

Compounds 1.7 and 1.8, reported by Akkaya,[52] are based on the same principle. Because of ICT electron donating properties of substituents at 3- and 5-position in 1.7, upon protonation this compound exhibit bathochromic shift in both absorption and emission spectra. On the another hand, ICT electron accepting properties of substituents in 1.8 cause hypsochromic shift upon protonation as well as an increase in quantum yield from 0.18 to 0.68. Recently Liu[66] reported analogs of 1.7, where dimethylamino groups are substituted with polyethylene glycol functionalized piperazines with additional PEG units in the phenyl ring at *meso*-position of BODIPY. These near infra-red water-soluble probes were used for the detection of lysosomal pH.

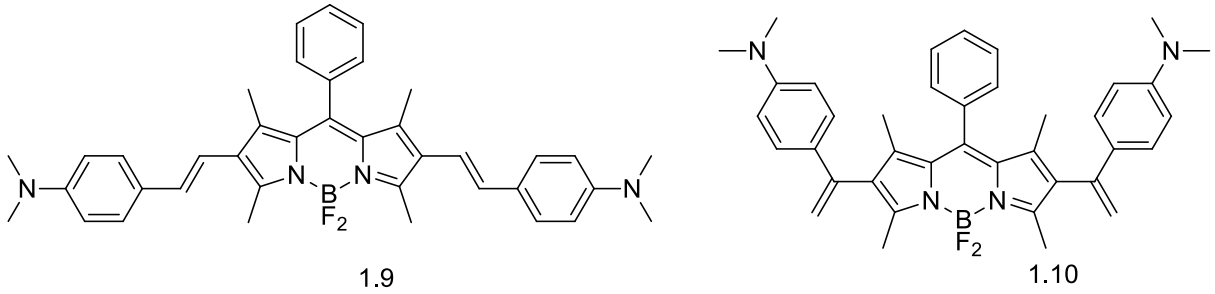

Figure 1.20: pH sensors from Shen et al..

The ICT was claimed to be responsible for the “turn-on” behavior of complexes 1.9 and 1.10 synthesized by Shen et al.[60] in 2014 (figure 1.20). Even so it is believed that substituents at 2- and 6- positions of BODIPY do not create a big impact onto conjugation within the dye, these complexes exhibit small blue shift as well as an increase in extinction coefficients in absorption spectra and increase of fluorescence without dramatic changes in the emission maxima. No fluorescence was detected for the neutral form of 1.9 in both non-polar (hexane) and polar (CH_2Cl_2) solvents. Upon protonation by TFA in CH_2Cl_2, increase of emission was

observed (Φ = 0.01) together with 38 nm blue shift of absorbance maxima. Under the same conditions compound 1.10 exhibited almost 500-fold increase in emission (quantum yield from <0.001 for neutral to 0.46 for protonated form).

Imine-based pH sensor 1.11, reported in 2013 by Chattopadhyay[56] is characterized by weak red (λ_{em} = 610 nm) fluorescence (Φ = 0.07) in methanol. During acidic titration, this molecule undergoes protonation and hydrolysis, resulting in highly fluorescent protonated aminoBODIPY 1.12 (figure 1.21). The two imine bonds are cleaved sequentially with the addition of H^+, thereby resulting in a gradual conversion of the λ_{abs} value at 570 to 525 nm, which corresponds to the monoimine dye, and ultimately to 495 nm for the chloride salt of diaminoBODIPY. The fluorescence behavior, a blue shift (93 nm) of the λ_{em} peak at 611 nm, also followed a similar trend. The change in the fluorescence color of the solution of dye 1.11 from a weak red (pH 8.2) to intense greenish-yellow (pH 0.6) was also distinctly visible.

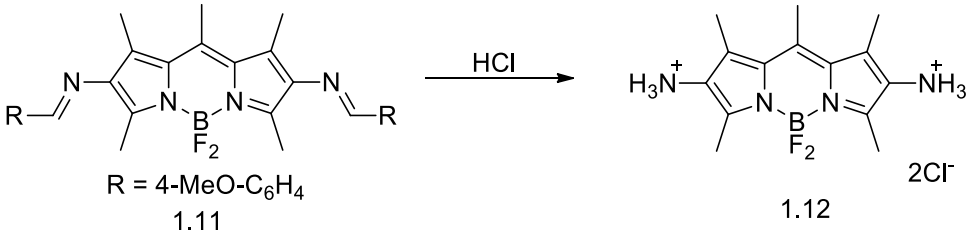

Figure 1.21: Imine based pH sensors from Chattopadhyay et al..

BODIPY-based pH sensors bearing phenolic OH group are also well documented.[57–59] All of them are “on-off”-type indicators and are based on the reductive PET principle. Upon deprotonation, formed phenolate acts as an efficient electron donor to the BODIPY core. Despite phenol itself having a pK_a value of 10.0 in water, careful tuning of its basicity by the introduction of electron-withdrawing groups into phenyl ring allows the design of sensors structure suitable for measurements of near-neutral pH values. Calix[4]aren based probe 1.13 was reported to be suitable as an indicator for the pH values 5.6 – 8.2, in which 10-fold fluorescence change was observed.[57] Recently this probe was successfully used for the intracellular pH measurements for the cell apoptosis studies.[67] Phenolic 1.14 and naphtolic 1.15 BODIPY dyes reported by Boens[58] have sensing properties similar to the calixarene-based probe (figure 1.22).

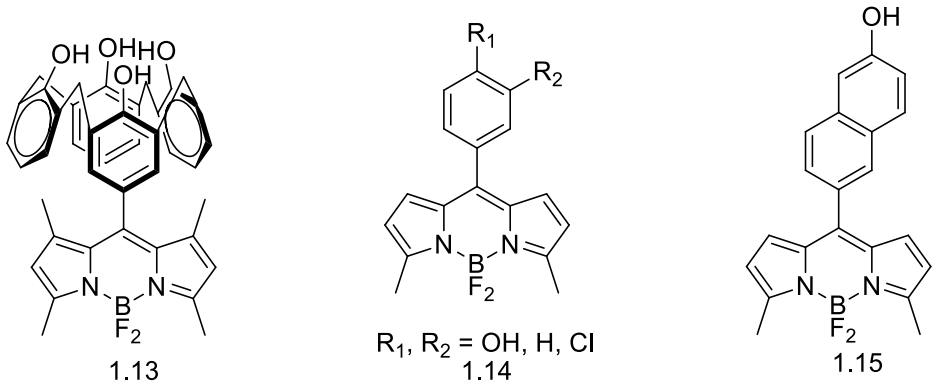

Figure 1.22: Ar-OH based pH sensors.

A somewhat different approach was chosen by Ravikanth in 2011.[65] The protons of the aldehyde group in their 3,5-diformyl BODIPY 1.16 are involved in strong hydrogen bonding with fluorine atoms and, together with electron withdrawing properties of BODIPY core, renders the carbonyl groups in such molecules extremely electrophilic. In the basic buffer, formyl groups undergo nucleophilic attack by hydroxyl anion and formed anionic product 1.17 becomes non-fluorescent because of PET quenching. This type of probes is completely reversible and in acidic conditions completely regenerates its initial fluorescence level back

while an emission maximum remains unchanged. In a pH range of 4.5 – 6.0 emission intensity was enhanced by 17 times, what makes this water-soluble probe useful for accurate measurements of acidic pH (figure 1.23).

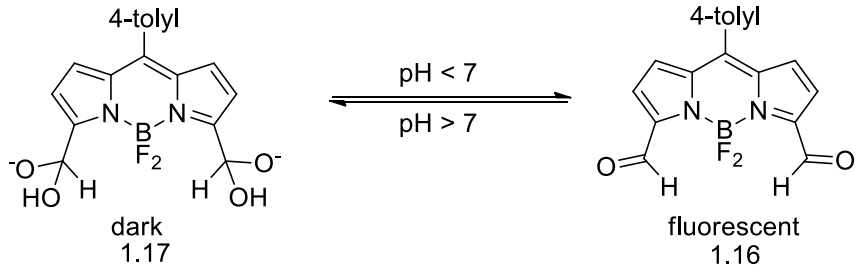

Figure 1.23: Mechanism of pH sensing for the Ravikanth probe.

Unaleroglu[68] reported in 2015 a BODIPY-based pH sensor 1.18 which doesn't bear a phenolic group for the detection in alkaline media. This red-emitting dye shows a drop in fluorescence intensity upon basification of its solution and becomes practically non-fluorescent at pH 10. This process is fully reversible and in neutral and acidic condition the dye fully regenerates its fluorescent properties. The authors showed that the quenching process is not related to the aggregation of dye molecules and the addition of the hydroxyl anion to the double bond couldn't be observed by NMR spectroscopy, so the exact mechanism remains unknown. Another alkaline pH sensor 1.19 bearing 1,3-dicarbonyl functionality was proposed by Peña-Cabrera[69] in 2015. This compound with pKa value of 6.9 in water shows a significant drop in fluorescence intensity upon basification, mainly in a pH range between 6 and 8 and at pH > 8 it becomes non-fluorescent. This behavior is related to the deprotonation of the enol form and activation of PET-based quenching (figure 1.24).

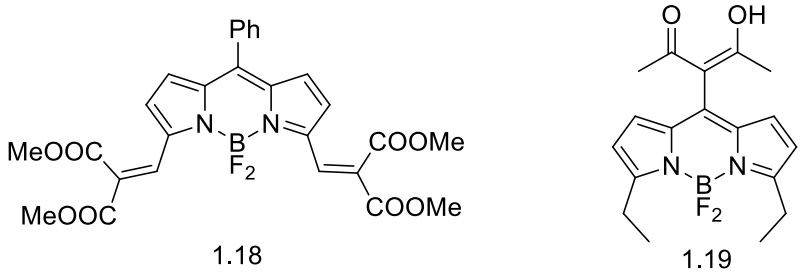

Figure 1.24: Alkaline pH sensors from Unaleroglu and Peña-Cabrera.

The biggest limitation for the use of "on-off" type pH sensors in living cell imaging is the localization of dye in the "off" state. Such problem can be solved by using FRET-based pH probes. Described by Burgess[70] probes 1.20 (figure 1.25) are fluorescent in any pH level. The authors used xanthene as a sensing group and donating part of FRET-pair. At pH values below 7, efficient FRET occurs between the phenolic form of xanthene and red-emitting BODIPY, which acts as an acceptor. Under irradiation at 488 nm, red fluorescence of BODIPY can be observed. Upon deprotonation of xanthene unit at pH > 7, the efficiency of FRET becomes minimal and only green fluorescence of xanthene unit is observed. This behavior leads to the possibility of application of such sensor as a ratiometric probe, what gives higher sensitivity in comparison to "on-off" indicators. This protein-coupled probe was shown to be membrane permeable, water soluble and was successfully used for the intracellular pH imaging.

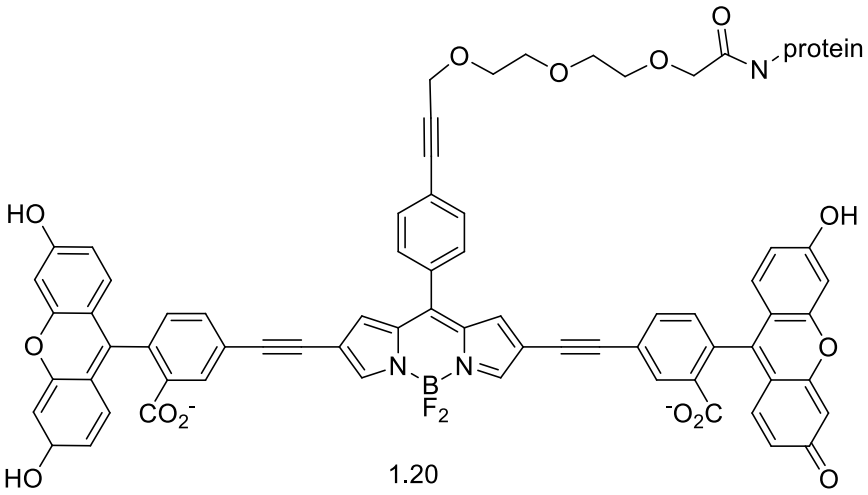

Figure 1.25: FRET-based pH sensor.

1.3.2. BODIPY-Based Metal Ion Sensors

Many metal ions play a very important role in many biological processes, while other are highly toxic and cause diseases.[10] In living organisms metal ions regulate osmotic processes, take a crucial role in catalysis, metabolism, etc. Membrane gradients of group I and II metals are the key factor in the potential energy storage and controlled release, playing the most important role in generation of action potential, osmotic regulation, cell signaling.[11] Many transition metals such as iron, zinc, copper, molybdenum, manganese, cobalt, nickel, tungsten, chromium and vanadium are essential elements in various living systems. The vast majority of the cellular transition metal concentration is bound to proteins, enzymes, metabolites, cofactors, nucleic-acids, and other small ligands like amino acids, glutathione, or citric acid. Some minor amount of metals may exist in different other forms, including hydrated ions, or loosely bound forms.[11] To study in details the metal homeostasis and dynamics in cells or organisms, metal toxicity and metal-induced diseases it is important to define the analytical methods suitable for the localization of high metal concentration within the cell or organism, and to understand the chemical form of metal ions in biological samples. Because of the high toxicity of many transition metals, it is also very attractive to develop simple and sensitive methods of metals detection it industrial waste, food, and the environment.[11]

There are very many selective and highly sensitive BODIPY-based metal probes known. Most of them, just like in the case of pH sensors, are “turn on/off” indicators. In general, these molecular devices are constructed from three parts. BODIPY plays a role of reporting part. BODIPY should be connected through the linker to the sensing part of the probe. For metal indicators as a sensing part, a variety of specific chelating ligands for certain metal are normally used. Metal binding alters the electronic and/or molecular structure of the sensing part of the molecule and induces changes that are translated into enhanced or decreased fluorescence or absorbance intensities, or changes in absorbance or emission maxima. The vast majority of metal sensors are based on PET mechanism. Normally, the chelating part contains some electron-donating atom and upon metal coordination, PET quenching takes place, leading to an increase in quantum yield. If the sensor is designed without linker part, that is the sensing moiety is connected directly to the conjugated dye, ICT mechanism of detection can be used. Although this design sacrifices some of the modularity and tunability of the classical three-component system, ITC can lead to a shift in wavelength of excitation or emission, which can result in ratiometric sensors. In the end, there are some rare examples of

probes available which are based on FRET or the unique chemical reactivity of different metal ions.

A number of reviews on the detection of metal ions were published.[10–12] With a view to the huge amount of published material, here will be highlighted only the most important examples and recent developments.

The most popular sensing systems are probes sensitive to certain metal chelating ligand attached through the phenyl group to the *meso*-position of BODIPY core. All of these probes are PET-based and work on "turn – on/off" principle. Most of them can be synthesized utilizing the same well-developed synthetic approach – condensation of a chelate-containing aromatic aldehyde or acid chloride with chosen pyrrole. Figure 1.26 shows some recently published examples of such probes.

Mn^{2+} probe 1.21 was used by Datta and coworkers[71] for the confocal intracellular detection of Mn^{2+} ions. This lipophilic cell-permeable molecule due to reductive PET is practically non-fluorescent in the absence of metal ions (Φ = 0.0038, λ_{abs} = 496 nm, λ_{em} = 507 nm). Upon coordination of Mn^{2+}, PET effect is suppressed and a 52-fold increase in the emission of the complex was observed, while no enhanced fluorescence was observed for other metal ions. The same principle was applied for the design of very similar, but selective and sensitive cryptand-based K^+ 1.22 (14-fold increase in emission in presence of potassium)[72] and Fe^{3+} 1.23 sensors (23-fold increase)[73], which share the same synthetic approach where small modifications of sensing part lead to the probes for different analytes. PEG–BODIPY–BAPTA conjugate 1.24 was reported[74] to be sensitive and selective for Ca^{2+} (80-fold increase) over most other metal ions (competing to Cd^{2+}, Pb^{2+}, and Cu^{2+}), can pass through the cell membranes without special procedures, and was used to monitor changes in the intracellular Ca^{2+} signal.

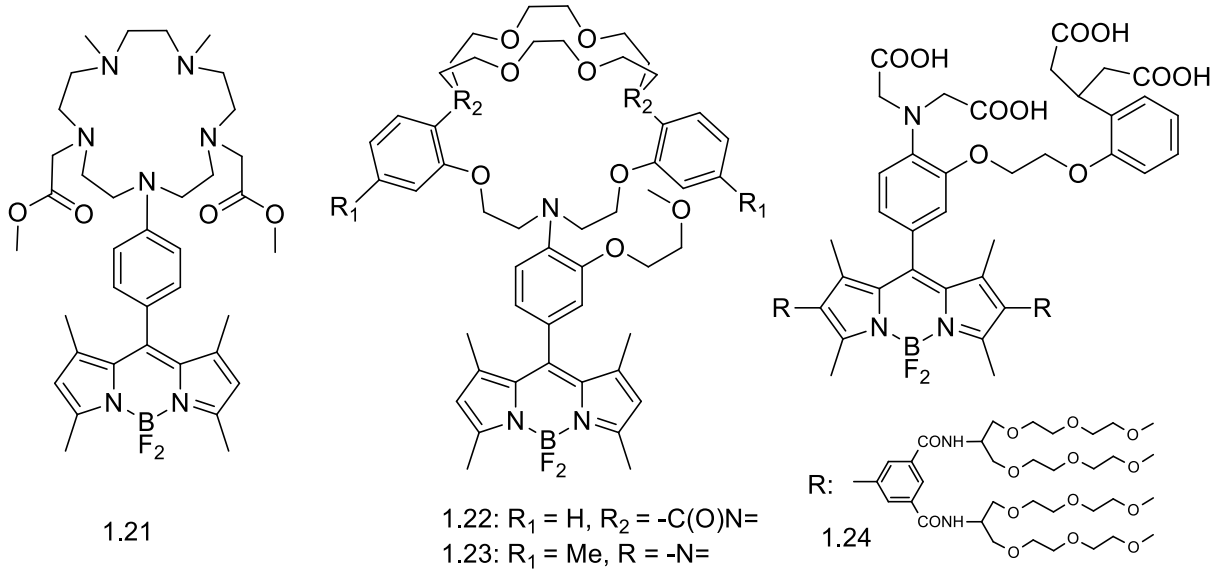

Figure 1.26: Reductive PET-based metal sensors.

Turn-on fluorescent probes can be designed based on metal-induced oxidative PET. Probe 1.25 reported by Wang et al.[75] (figure 1.27) utilize the same "turn-on" mechanism, has a strong Hg^{2+} binding affinity, shows a ~250-fold increase in fluorescence in the presence of metal ions and excellent selectivity. On the other hand, triazole-BODIPY conjugate 1.26, reported by Pandey[76] upon coordination of Hg^{2+} in water-CH_3CN mixture shows ~10-fold decrease in emission (Φ from 0.28 to 0.03) without significant changes in the emission pattern (λ_{em} = 521 nm), while appearance of additional red-shifted absorbance band was observed (λ_{abs} = 493 nm, additional band ~548 nm), what changed solution color from pile-

yellow to orange-red. This distinct color changes arouses due to the formation of Hg^{2+} complex in which the metal ion acts as an electron acceptor, activating an oxidative PET quenching mechanism.

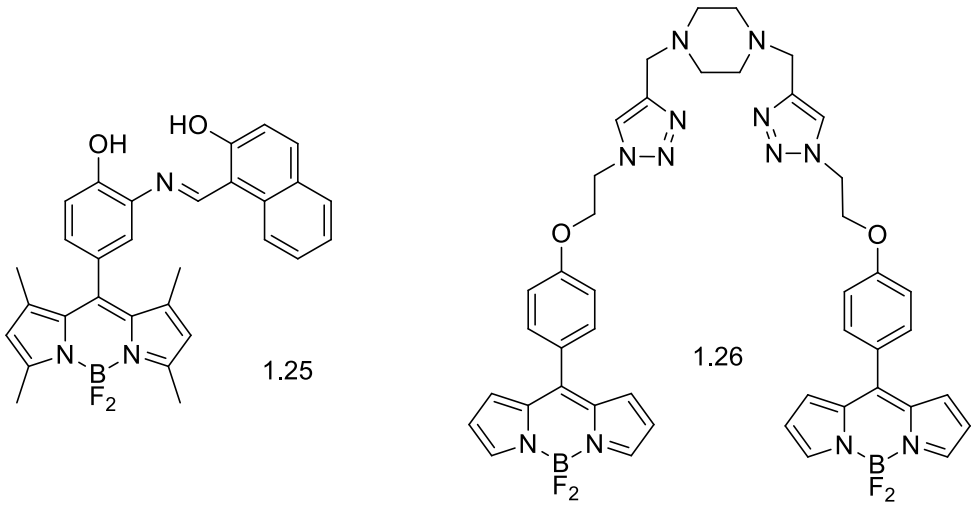

Figure 1.27: oxidative PET-based metal sensors.

PET-based sensing is also possible when metal ion recognition unit is connected without conjugation to other than *meso*-positions at BODIPY core. Some recently published examples are shown on figure 1.28. In the red emitting probe 1.27[77] obtained by attachment of the BAPTA moiety to the BODIPY scaffold at 3-position via a 3-propanamide side chain, strong fluorescence quenching due to reductive PET was observed. This PET process is switched off upon addition of aqueous Ca^{2+}, resulting in significant fluorescence enhancements (22-fold) without spectral shifts. Probe[78] 1.28 with zinc^{II} chelator bis(pyridin-2-ylmethyl)amine at 2- and 5- positions has two emission bands at 521 (quenched due to reductive PET from the tertiary amino group) and 661 nm in the buffered water solution. The binding of Zn^{2+} ions to dipicolylamine moieties disrupts the π-conjugation of distyryl groups at 1- and 7-positions with the BODIPY core, resulting in fluorescence quenching at 661 nm, and effectively stops the photoinduced electron transfer from tertiary amine groups of dipicolylamine moieties at 2- and 6-positions to the BODIPY core, leading to fluorescence enhancement at 521 nm.

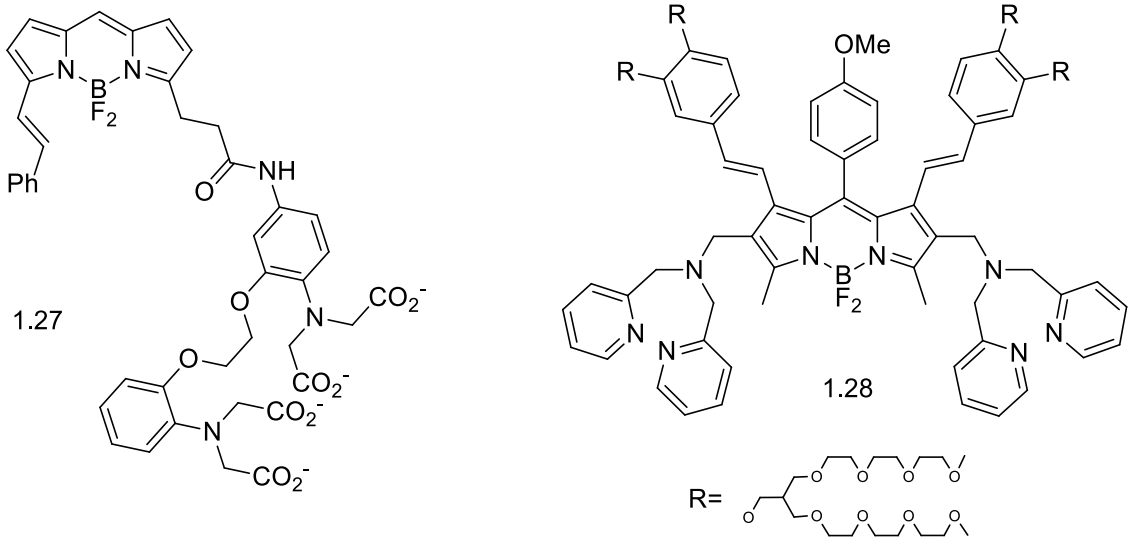

Figure 1.28: PET-based metal sensors.

Two probes which utilize other sensing principle are shown on figure 1.29. When the metal recognition unit is conjugated to 3- and/or 6- position of BODIPY core, there is an efficient ICT process from the donor nitrogen atom to the acceptor fluorophore possible, leading to a

strong fluorescence quenching. Coordinated metal reduces the electron-donating ability of the recognition unit and suppresses the ICT process, normally leading to enhanced fluorescence and shifts in the absorbance and emission spectra. Mercury^{II} probe 1.29 with dithia-dioxa-aza macrocycle conjugated to BODIPY, reported by Zhang[79] in 2015, upon addition of Hg^{2+} gives large blue shift in absorption spectra and turn-on fluorescence emission. Attached to the long polyethylene glycol chain, this probe is highly water soluble, shows excellent sensitivity and selectivity towards Hg^{2+} ions and was used for the intracellular imaging if mercury ions in HeLa cells line. The same principle is utilized in K^{+} sensor 1.30, reported by Belfield.[80] This water soluble near-IR emitting probe (644 nm) shows a 52-fold increase in fluorescence upon coordination of potassium ion and was used for two-photon fluorescence microscopy cell and tissue imaging (the two-photon absorption cross-section was determined to be 500 GM at 940 nm).

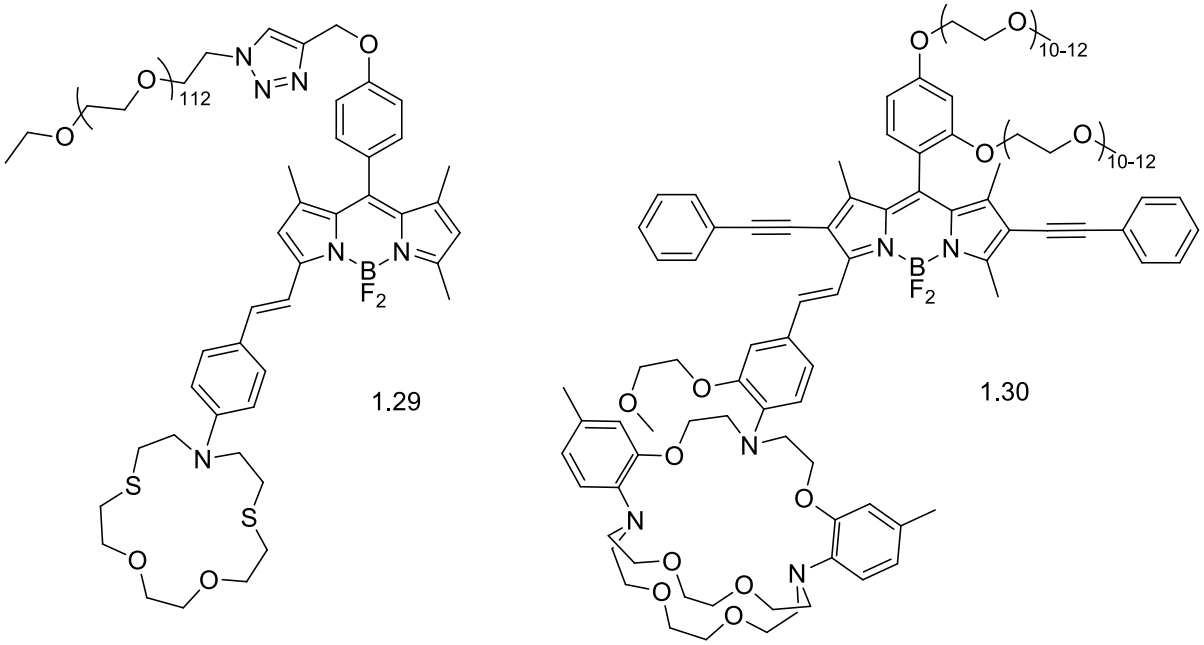

Figure 1.29: ICT-based metal sensors.

Some reported metal sensors give fluorescence response in the presence of certain metal ions due to the specific chemical reaction. For example, ratiometric probe 1.31 based on a BODIPY – rhodamine FRET system was used for detecting Hg^{2+} in the ethanol-water mixture and in live cells.[81] Hg^{2+} induced ring-opening reaction generates the long-wavelength rhodamine which can act as an energy acceptor (figure 1.30). The absorption spectrum of initial probe 1.31 shows only the absorption profile of the donor BODIPY and excitation at 488 nm resulted only in the emission BODIPY part of this system (λ_{em} = 514 nm, Φ = 0.35). The addition of Hg^{2+} promotes the formation of ring-opened product 1.32 with activated rhodamine moiety and a highly efficient FRET process is turned on. Excitation of BODIPY at 488 nm now results in the emission of rhodamine with a λ_{em} = 589 nm (Φ = 0.20). Measurement of the fluorescence intensity ratio of two wavelengths allows the ratiometric detection of Hg^{2+}.

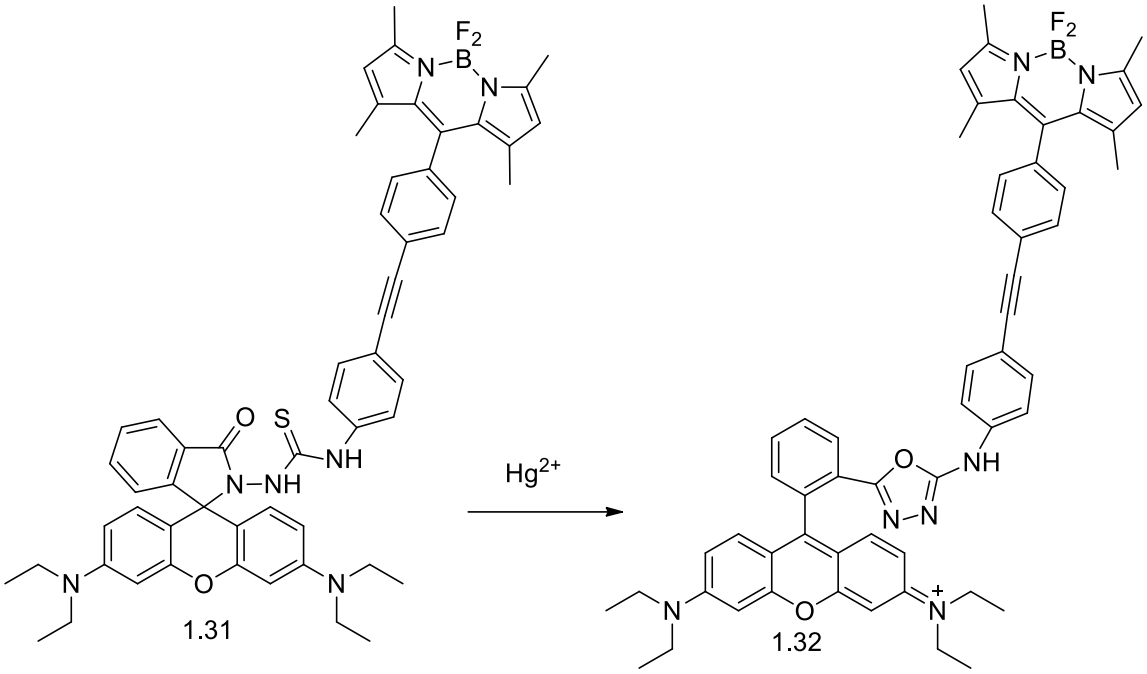

Figure 1.30: FRET-based Hg^{2+} sensor.

BODIPY probe[82] 1.33 bearing semithio-carbazone functionality at the 2nd position was reported to be useful for the detection of Au^{3+} and Hg^{2+} ions via different emission modes. Fluorescence of the initial molecule is quenched due to reductive PET effect from donating nitrogen atoms. A systematic titration of this probe with Au^{3+} revealed that emission band intensity increases linearly with the increase in the concentration of Au^{3+} in the range of 0.1–100 μM while no other metals showed similar behavior. At the maximal concentration of metal ions, 200-fold fluorescence increase was observed (figure 1.31). This response toward gold ions is due to the selective coordination of Au^{3+} to semithio-carbazone functionality which makes C=N bond extremely sensitive to hydrolysis. In the presence of water and Au^{3+} within a few minutes highly fluorescent BODIPY-carbaldehyde 1.34 is formed (λ_{em} = 512 nm, Φ = 0.83). On the other hand, in the presence of Hg^{2+}, a new emission band appeared at 542 nm and increased linearly with the increased concentration of Hg^{2+} above the range of 0.1–100 μM. In sharp contrast to the detection of Au^{3+}, detecting Hg^{2+} ions proceeded reversibly. This may be due to the 2:1 complex formation in which Hg^{2+} ions decrease the donating ability of nitrogen atoms leading to a PET shut down.

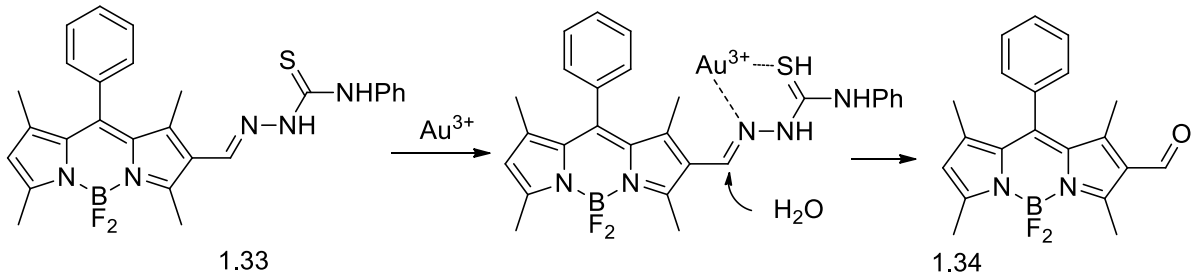

Figure 1.31: Au^{3+} and Hg^{2+} probe.

The meso-catechol subunit in probe 1.35, reported by Burdette[83] is oxidized to the corresponding *o*-quinone by an excess of $FeCl_3$, $CuCl_2$, $[Co(NH_3)_5Cl]Cl_2$, DDQ, or ceric ammonium nitrate in methanol (figure 1.32). The starting compound 1.35 is almost nonfluorescent (Φ < 0.001) in methanol due to reductive PET from catechol to BODIPY unit. Upon oxidation to *o*-quinone 1.36, significant fluorescence enhancement is observed (Φ = 0.027) because the *o*-quinone group is much weaker PET donor to BODIPY. Reactive

oxygen species such as H_2O_2, ·OH, $^1O_2$, OCl^- did not drastically change the fluorescence properties of starting compound.

Figure 1.32: RedOx based metal sensor.

1.3.3. BODIPY-Based Anion Sensors

Different anions play an important role in biological processes, they are involved in different industrial cycles, but some of them have high toxicity. Compared to pH and metal ions sensors, the development of BODIPY fluorometric probes for anions has received much less attention. This can be connected to the much more challenging task to find a specific and sufficiently sensitive recognition unit for such sensor. Most of the anion indicators known so far are based on anion-induced reactions which lead to structural changes of the probe molecule and the fluorescence response.

The most popular reported BODIPY sensors and dosimeters are those for fluoride anion. Overall those probes can be divided into two types. The first type includes indicators which are based on the ability of F^- to form strong hydrogen bonds and its high basicity in the aprotic environment. These probes normally exploit PET or ICT-mechanisms of quenching, which are switched on/off upon coordination of fluoride anion or F^- induced deprotonation. The second type of probes is based on the reactivity of fluoride anion towards silanes and organoboron compounds.

Wang and coworkers[84] reported a series of BODIPY dyes bearing phenolic OH in the *meso*-phenyl moiety for colorimetric and fluorescent detection of F^- ions by way of O–H···F hydrogen bonding interactions. It was shown that such bond formation influences the efficiency of reductive PET from oxygen to BODIPY and in most cases leads to the dramatic decrease in fluorescence. Probe 1.37 in acetonitrile has λ_{abs} = 502 nm, λ_{em} = 521 nm and Φ = 0.69. Upon addition of F^-, a gradual absorbance decrease at 502 nm was accompanied by a gradual increase at 488 nm; the fluorescence intensity of the solution decreased monotonically, and the emission peak underwent a minor blue shift. Other examined probes showed a similar response to other anions, like $H_2PO_4^-$, AcO^- or even Cl^- (probe with two phenolic OH- groups in *para*- and *ortho*- positions relative to BODIPY) probe 1.37 exhibits high selectivity to F^- anions and can be used even for naked eye sensing. However, the detection limit of F^- was estimated to be only $1.0 \cdot 10^{-5}$ M and this dye can't be used in the presence of water and other protic solvents. The phenolic OH interaction with F^- was also exploited in the probe 1.38, reported by Cao[85] (figure 1.33). In the presence of F^-, a 118 nm red shift in the absorption of probes acetonitrile solution and 'turn-off' emission response was observed. The striking pink to indigo change in ambient light was explained by the deprotonation of the phenol moiety via O–H···F hydrogen bonding interactions.

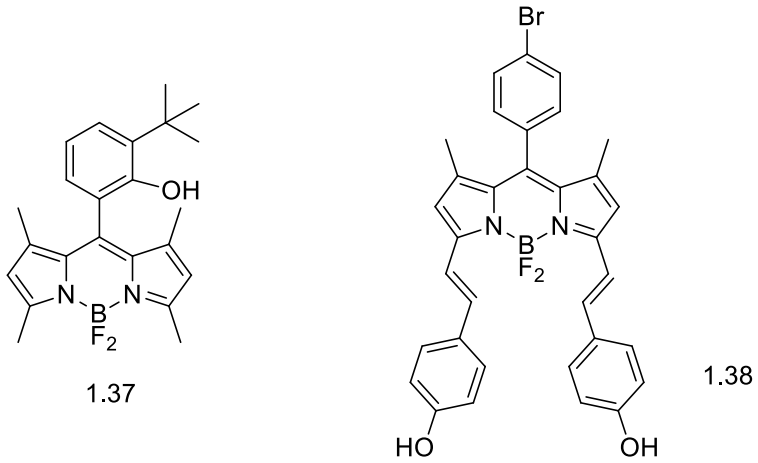

Figure 1.33: PET-based sensors for fluoride.

Systems, where *N*-heterocycle is directly connected to the BODIPY core, can also be used as selective fluoride sensors. Thus, acetonitrile – water solutions of compound 1.39[86] in the presence of F^- show striking light yellow to deep brown color change in ambient light and green to blue emission color change. The appearance of new blue-shifted absorbance bands (254, 419 nm), as well as local emission bands (402, 425 nm) with the drop in the intensity of S_1-S_0 band (512 nm), is attributed to the activation of ICT upon deprotonation of azaindole unit. For both compounds 1.40 and 1.41 significant decrease in fluorescence related to PET activation in the presence of F^- was reported[87,88] (figure 1.34).

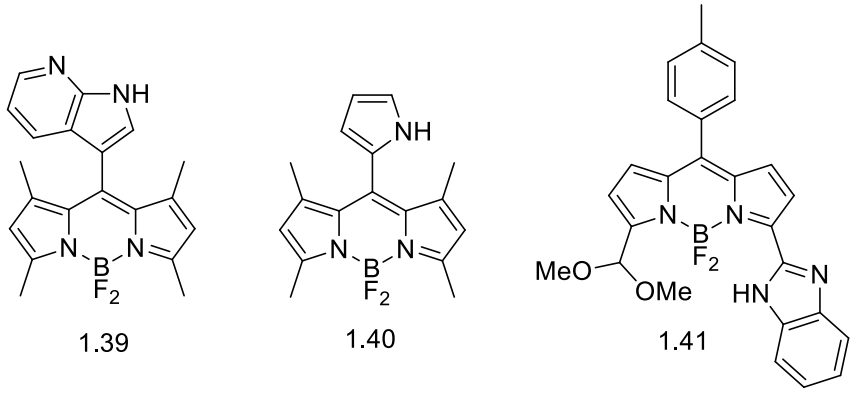

Figure 1.34: *N*-heterocycle based fluoride anion sensors.

Güler et al.[89] reported BODIPY sensor 1.42 with calix[4]pyrrol moiety as a recognition unit. In the presence of 10 eq. of F^- complete quenching of the BODIPY emission band at 532 nm, while new two bands at 450 and 480 nm were observed. A fluorescence color changes from green to blue make the reported probe to be useful for "naked eye" detection of F^- anion. The F^- anion induced deprotonation of amido thiourea moiety in the probe 1.43 reported by Rurack[90] leads to the PET-based quenching of fluorescence, which was used for the development of test-strip assay for the determination of F^- in neat aqueous solutions, such as spiked water samples and toothpaste extracts, achieving a detection limit of 0.2 ppm (figure 1.35).

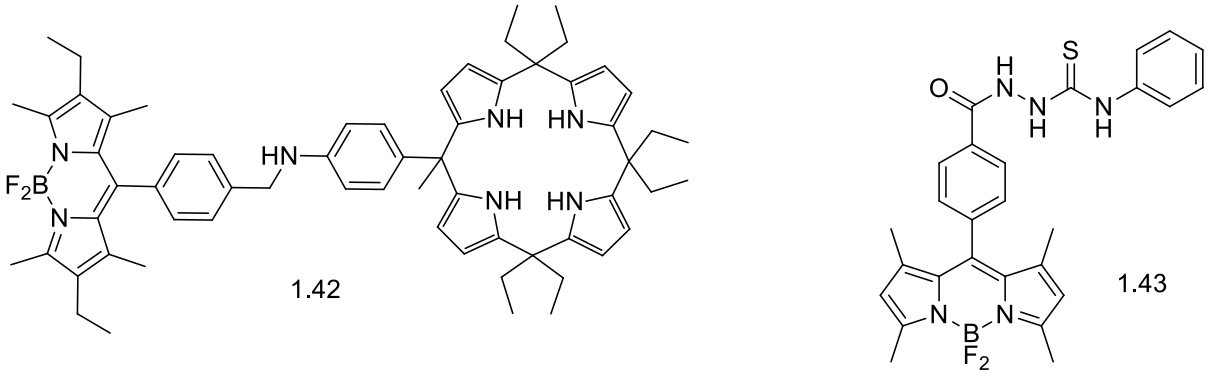

Figure 1.35: Fluoride anion sensors.

Another well-developed type of BODIPY sensors for F^- anion are probes, which exploit the extraordinary affinity of fluoride for silicon. Normally such compounds are dye molecules which contain silicon-group protected acetylenes or phenols and fluoride-induced deprotection generates some fluorescent response. Thus, for probe 1.44 (figure 1.36) reported by Zhu[91] upon titration by TBAF in CH_2Cl_2, a drop in absorbance band at 546 nm and a concomitant increase of a new band at 644 nm were observed, with a distinct isosbestic point at 567 nm, resulting in a color change from pink to indigo. Notably, the ratio of the absorbance at 644 and 546 nm increases over 3000-fold, allowing the possible colorimetric and ratiometric detection of F^- even with the naked eye. Emission maxima for protected and deprotected forms are 546 and 676 nm respectively, so this probe can be considered both "turn-on" and "turn-off" type, depending on the excitation wavelength. Fluoride-specific desilylation reaction of probe 1.45[92] leads to removal of benzyl moiety from the *meso*-pyridyl and deactivation of PET-induced quenching. Probe 1.46[93] in the presence of F^- induced a huge 107 nm blue emission shift and a 40-fold increase in intensity.

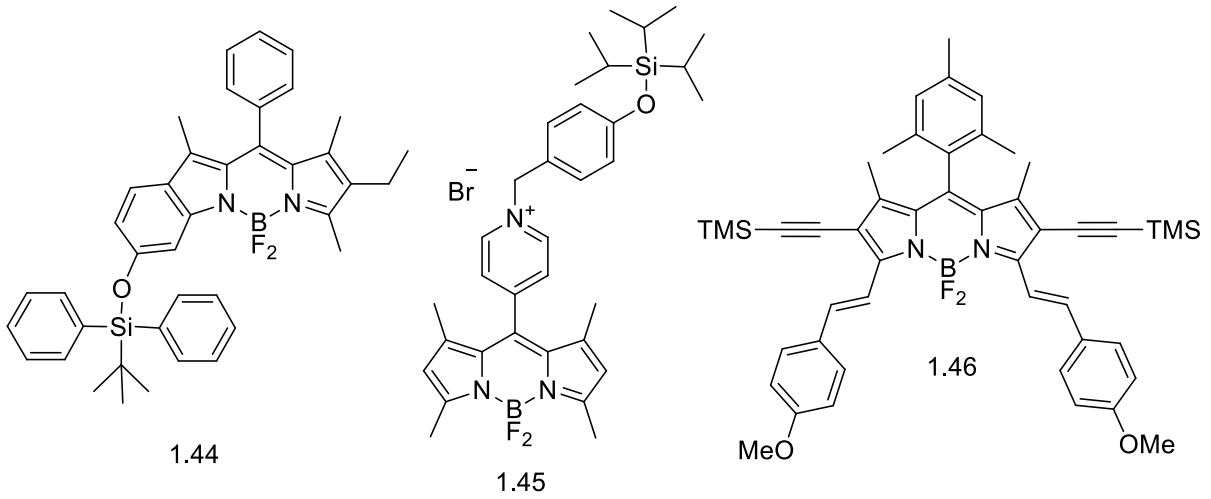

Figure 1.36: Fluoride anion probes based on the cleavage of silane protection group.

The empty p_π orbital of three arylboranes determines the strong Lewis acid nature of these compounds, which can be used for the design of effective receptors for strong Lewis bases, such as F^-. This was recently used in a number of research groups for the development of BODIPY - triarylborane dyads[94–98] (figure 1.37). Upon coordination of fluoride, the boron-containing group becomes highly electron rich and acts as an efficient PET quencher.

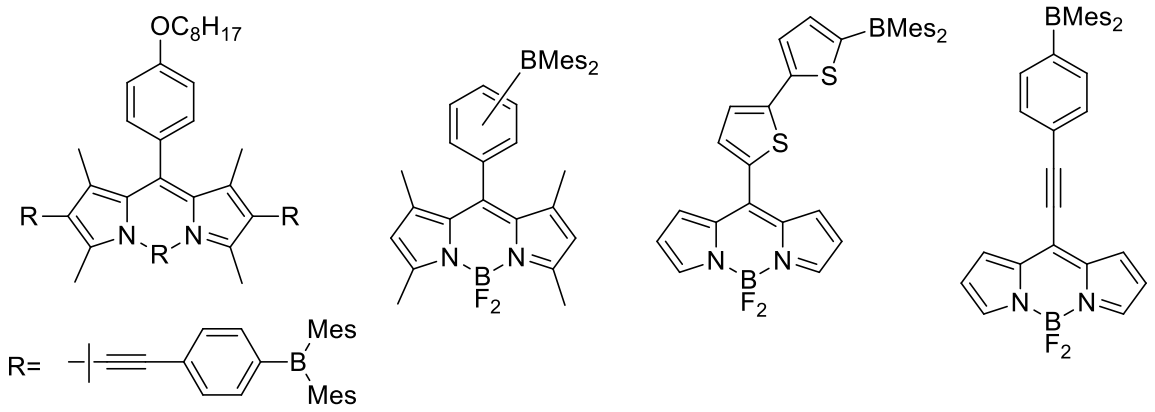

Figure 1.37: Borane-based fluoride sensors.

Most of the mentioned above arylborane containing BODIPY probes also have the ability to form complexes with the cyanide anion, which translates into similar but less efficient fluorescence quenching. A few reported selective BODIPY-based chemodosimetric probes for CN^- are based on the nucleophilic addition of cyanide anion to the carbonyl group. Thus, the reaction of CN^- with the trifluoroacetamide group of probe 1.47[99] (figure 1.38) resulted in a color change from pink to blue (33 nm bathochromic shift of λ_{abs}) and a fluorescence turn-off was attributed to cyanohydrin formation what activates ICT mechanism. The reaction is reversible and original sensor can be restored by the addition of trifluoroacetic acid. Similarly, the addition of cyanide to the salicylic aldehyde derivative in probe 1.48[100] leads to the significant quenching due to PET activation.

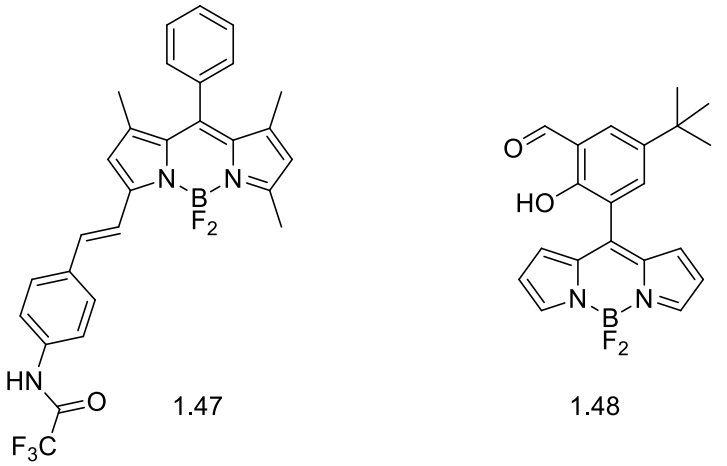

Figure 1.38: Sensors for cyanide anion.

It was shown that in some cases cyanide anion can act as competing ligand for metals in the presence of BODIPY probes for these metals. BODIPY with di(2-picolyl)amine unit at *meso*-position[101] 1.49 is quenched in the presence of Cu^{2+} due to oxidative PET effect and titration with NaCN fully restore initial emission level of the free probe due to decomplexation through the generation of tetracyanocuprate. The zinc complex of BODIPY 1.50,[102] which has bright orange fluorescence, reversibly signals anions (phosphate, acetate, and fluoride) with very large changes in both the absorption and the emission spectra due to ICT effect. The fluorescence emission intensity of the 1:1 Zn^{2+} complex of a doubly BODIPY substituted bipyridyl ligand 1.51 was shown[103,104] to be highly sensitive to anion coordination to the metal center. Oxidative PET, which is responsible for the quenching of the fluorescence in the complex, is effectively inhibited by anion coordination, leading to a 25-fold enhancement of the emission intensity.

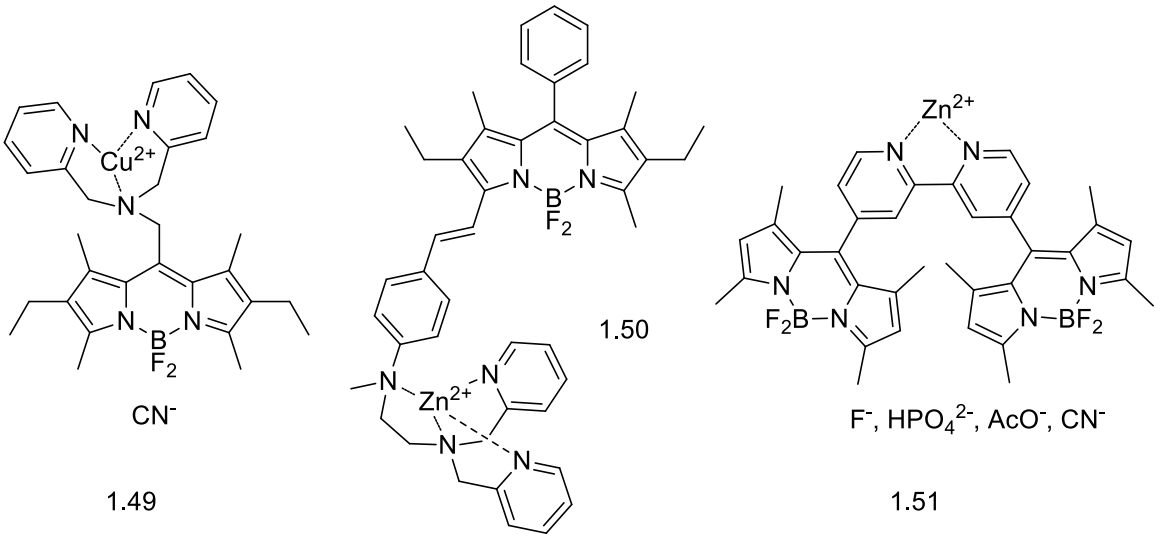

Figure 1.39: Anion probes based on competing coordination.

1.3.4. BODIPY-Based Sensors for Reactive Oxygen and Nitrogen Species

Reactive oxygen species (ROS) include the superoxide ($O_2^{\bullet-}$), hydroxyl ($HO^{\bullet}$) and peroxyl radical ($ROO^{\bullet}$), hydrogen peroxide (H_2O_2), singlet oxygen ($^1O_2$) and hypochlorous acid (HOCl).[10] ROS are produced endogenously and exogenously and are involved in a wide range of physiological and pathological processes, such as signal transduction, inflammation, carcinogenesis and neurodegenerative injury. Overproduced ROS can cause oxidative stress through the oxidation of biomolecules, and may induce cell death.[105] Reactive nitrogen species (RNS), such as nitric oxide (NO) and its higher oxides are involved in cell signaling during a variety of physiological and pathological processes. NO, peroxynitrite ($ONOO^-$), nitrogen dioxide radical ($NO_2^{\bullet}$) and nitrate (NO_3^-) are generated endogenously and play an important role in physiological events that take place in the cardiovascular, nervous and immune systems, as well as in different pathological processes.[105] Owing to their significance in human health and disease, the elucidation of the biological functions of ROS/RNS has become an important area of research.

Most of the BODIPY-based sensors for ROS and RNS are based on the specific reactivity of these species, hence, they react irreversibly and de-facto should be categorized as chemodosimeters. Among all ROS, the most developed are probes for hypochlorite. Normally such probes contain the redox-sensitive group, oxidation of which produces a fluorescent response. Probe 1.52[106] (figure 1.40) is characterized by ICT interaction between BODIPY core and pyrrole unit. In the presence of HClO, oxynitride product is generated within a few seconds and a blue shift in emission is observed (from 585 to 555 nm) with 177-fold fluorescence ratio while no changes in fluorescence were detected in the presence of other ROS. Dosimeter 1.53[107] shows “turn-on” (11-fold enhance) response in the presence of HClO due to the deactivation of reductive PET. Similarly, probe 1.54[108] in the presence of hypochlorous acid is rapidly transformed to quinone derivative, which is characterized by much higher fluorescence level. This selective and sensitive probe was used for detection of endogenous HOCl in both human and mouse macrophages.

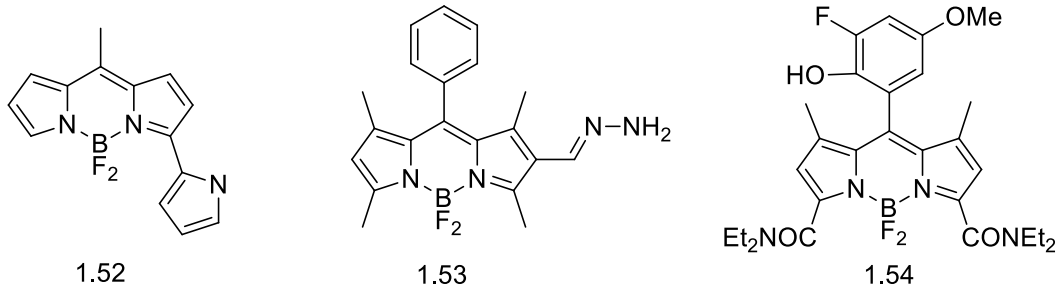

Figure 1.40: Probes for hypochloric acid.

Tellurides,[109] selenides,[110] and sulfides[111] can also be used as recognition units for HClO detection. The fluorescence turn-on mechanism, in this case, is achieved by the suppression of photoinduced electron transfer from the recognition unit to BODIPY by oxidation. These probes are characterized by very good fluorescence increase (up to 230 fold[110]) and detection limit in a nanomolar range.

An imidazopyrazinone subunit was used as a recognition group for superoxide radical anion (probe 1.55, figure 1.41). Oxidative cleavage of the antioxidant unit by $O_2^{\bullet-}$ results in the formation of acetamido pyrazine derivative with the fluorescence maxima at 542 nm.[112] BODIPY–α-tocopherol adduct 1.56 was used as a lipophilic fluorescent probe for the detection of peroxyl radicals in model membrane systems and their imaging in the lipid membranes of live cells.[113,114] Reductive PET from the chromanol moiety to the singlet- excited BODIPY renders 1.56 nonemissive. Upon peroxyl radical scavenging, oxidation of the chromanol moiety switches off PET, leading to a significant fluorescence enhancement, which is independent of the solution pH and membrane composition.[10] "Turn-on" fluorescent response of probe 1.57[115] is connected to the oxidation of boran unit by H_2O_2 with the formation of *meso*-pyridyl BODIPY. This water-soluble selective probe was used for monitoring and imaging of H_2O_2 both in vitro and in vivo.

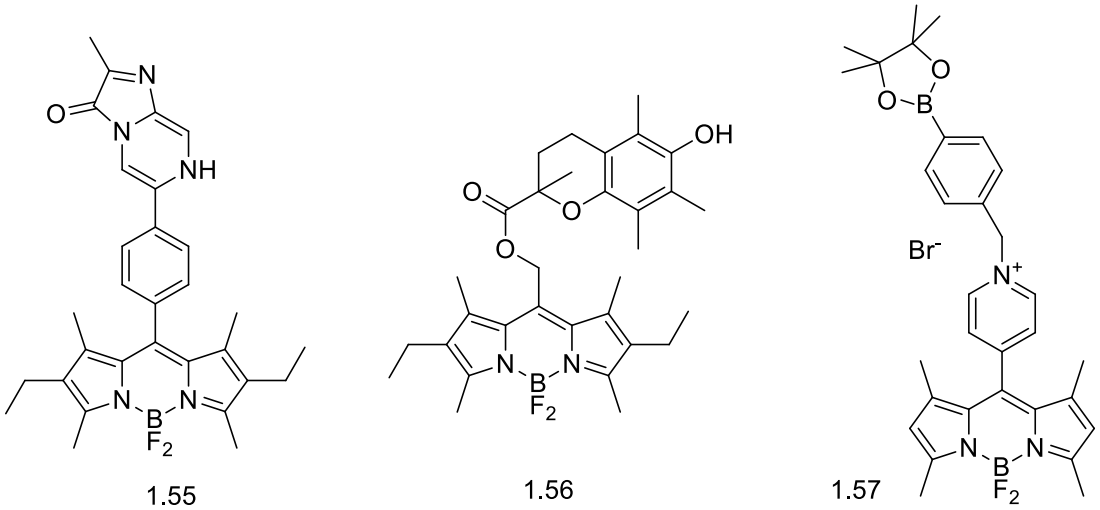

Figure 1.41: Probes for superoxide radical (left), peroxyl radical (middle) and hydrogen peroxide (right).

Many BODIPY-based dosimeters are developed for the detection of nitric oxide. Most of them are based on the reaction of phenylenediamines (PET donor) with NO under acidic conditions with the formation of benzotriazoles (PET is shut down). Some latest examples are shown on figure 1.42. Red-emitting probe 1.58[116] upon reaction with NO shows 400-fold enhancement of fluorescence and was used for the *in vivo* visualization of NO. The fluorescent probe 1.59[117] demonstrates excellent water solubility, membrane permeability, and compatibility with living cells for sensitive detection of NO.

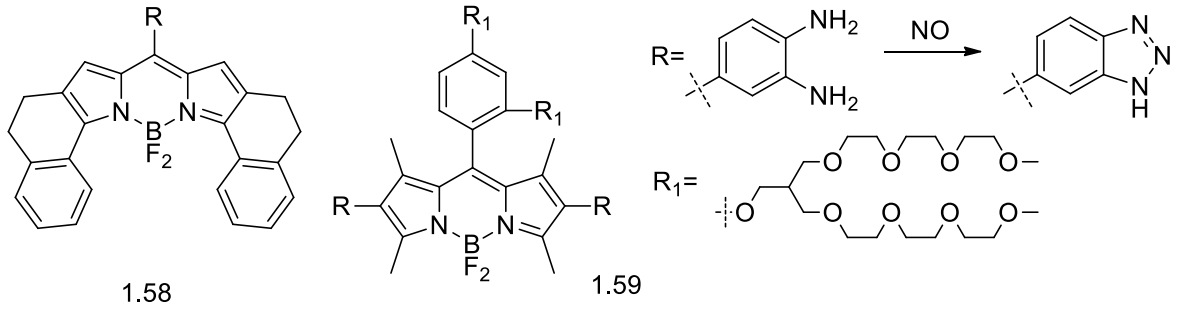

Figure 1.42: Nitric oxide sensors and fluorogenic reaction with NO.

1.3.5. BODIPY-Based Sensors for other Molecules and Phenomena

Careful selection of the receptor part allows the design of fluorescent sensors for a variety of bioactive compounds, biological macromolecules and different chemical and physical phenomena. A brief overview of the BODIPY based sensors for different peptides and proteins, monosaccharides, thiols, nitration and Diels-Alder reactions can be found in the Boens[10] review from 2012. In recent years numerous new BODIPY-containing probes were published, here only the most recent interesting examples will be covered.

The first fluorescent lipid peroxidation probe 1.60 specifically targeting lysosomes has been reported by Zhang and coworkers[118] (figure 1.43). A basic tertiary amine group enables this probe to selectively localize in acidic lysosomes. The conjugated diene moiety degrades in response to lipid peroxidation, what results in shortening of conjugation chain of the dye and fluorescence maximum shifting from 586 to 512 nm. Thus, under a confocal fluorescence microscope, the authors were able to visualize dynamic morphological changes of lysosomes and to quantify local lipid peroxidation through the ratiometric imaging.

Teoh et al.,[119] using the diversity-oriented fluorescent library (3500 BODIPY compounds) approach and high-content, imaging-based screening, developed amyloid β-peptide (Aβ) oligomer-selective probe 1.61 (figure 1.43), which shows the affinity to the target system with a K_d value of 0.48 μM. Aggregation of Aβ is implicated in the pathology of Alzheimer's disease, with the soluble Aβ oligomers thought to be the critical pathological species. Probe demonstrated dynamic oligomer monitoring during Aβ fibrillogenesis, as Aβ peptide was induced to form fibrils over time. The sensing process, in this case, is based on $\pi-\pi$-stacking interactions and hydrogen bonding between the probe and the exposed hydrophobic patches of Aβ oligomers, leading to the pronounced increase in fluorescence.

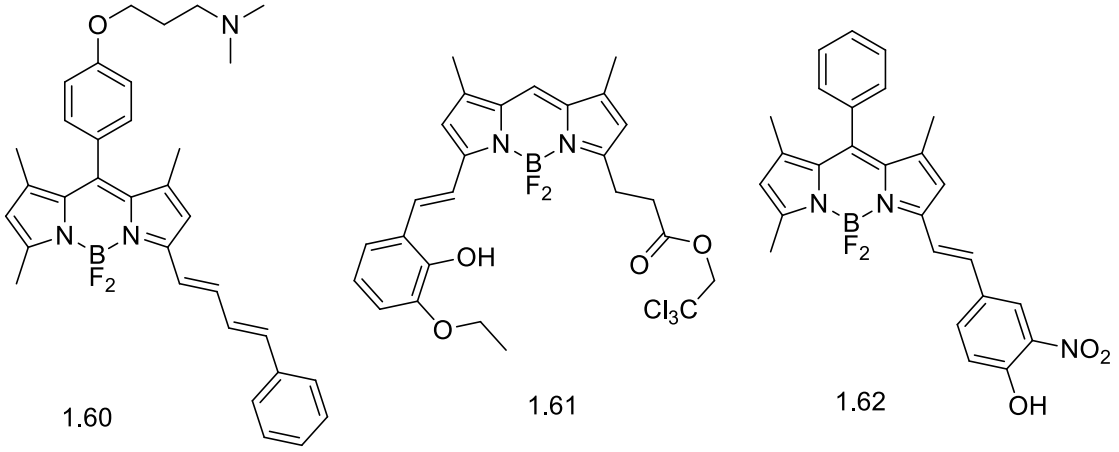

Figure 1.43: Lipid peroxidation (left), Aβ oligomers (middle) and hypoxia (right) probes.

A BODIPY dye containing a styryl substituent with a hydroxyl and nitro group 1.62 (figure 1.43) exhibits a 'turn-on' fluorescence response for hypoxic cells. The presence of the electron-withdrawing nitro group results in a highly efficient nonradiative decay of the S_1 state due to the increased ICT character. Under hypoxic conditions of tumor cells reduction of the nitro group takes place, ICT is switched off and hence a recovery of fluorescence intensity of probe 1.62 is observed (> 170 fold increase with small bathochromic shifts in absorption and emission maxima, 10 and 5 nm respectively).

Probe 1.63 was shown[120] to exhibit the remarkable 1600-fold increase in fluorescence during the reaction with *trans*-cyclooct-4-enol (figure 1.44). Fluorescence of initial tetrazine derivative 1.63 is strongly quenched due to the reductive PET from electron-rich heterocyclic moiety at *meso*-position of BODIPY. This compound rapidly reacts with strong dienophiles to produce Diels-Alder intermediate, which immediately release molecular nitrogen to form highly fluorescent product 1.64. The probe was successfully used for the visualization of both extracellular and intracellular *trans*-cyclooctadiene labeled targets with excellent signal intensity, very low background, and high temporal resolution.

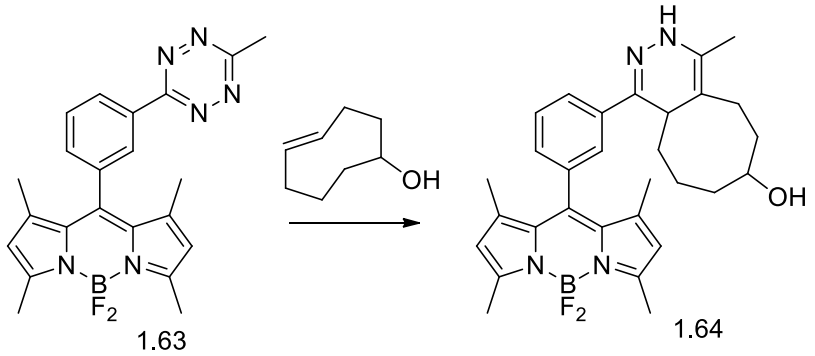

Figure 1.44: Probe for dienophiles.

The BODIPY-based fluorescent thiols indicators for intracellular detection and imaging of SH-containing targets have been studied in details recently. Most of these probes[10,121–123] are based on the oxidative PET from the excited BODIPY fluorophore to the electron-poor 2,4-dinitrobenzenesulfonate moiety, connected to the fluorophore. Reaction with thiols releases quencher and switches off PET, leading to the increase in the fluorescence (figure 1.45). This approach allowed the design of lysosome-targeting probes for intracellular thiols imaging[122] and red-shifted fluorescent indicators.[121,123] However, these probes are suffering from low selectivity and react with any aliphatic or aromatic thiols.

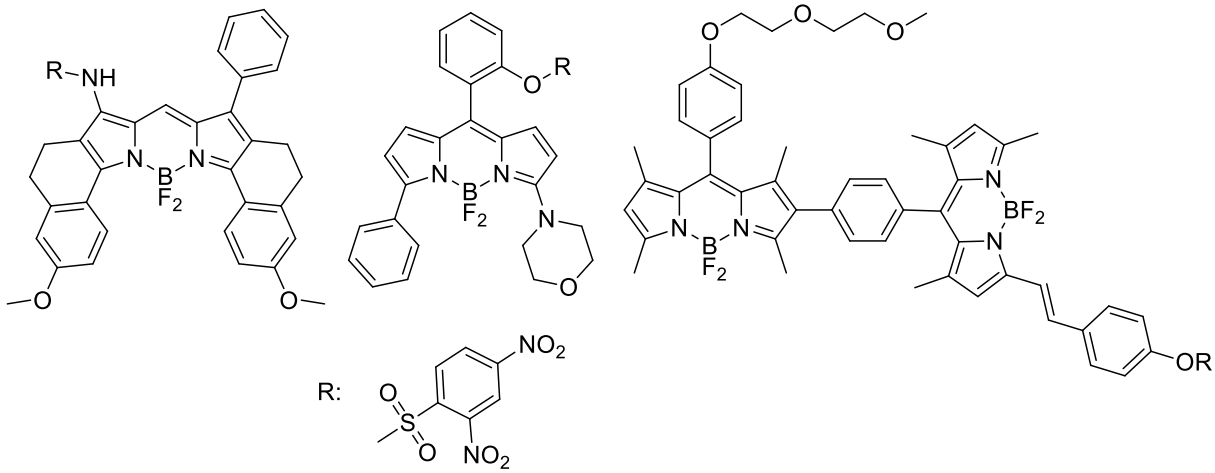

Figure 1.45: 2,4-dinitrobenzenesulfonate containing thiols probes.

Indicator 1.64 (figure 1.46), reported by Zhang and coworkers,[124] is quenched due to the reductive PET from dithiol unit (Φ = 0.03, λ_{abs} = 513 nm, λ_{em} = 545 nm, phosphate buffer). The reaction between 1.64 and H_2S triggers the disulfide bond cleavage and subsequent intramolecular cyclization, releasing 1.65 and resulting in a 7.5-fold fluorescence enhancement. In contrast, the reaction between 1.64 and other biothiols affords PET-quenched compounds with a disulfide bond 1.66 that could not undergo an intramolecular nucleophilic substitution (figure XX).

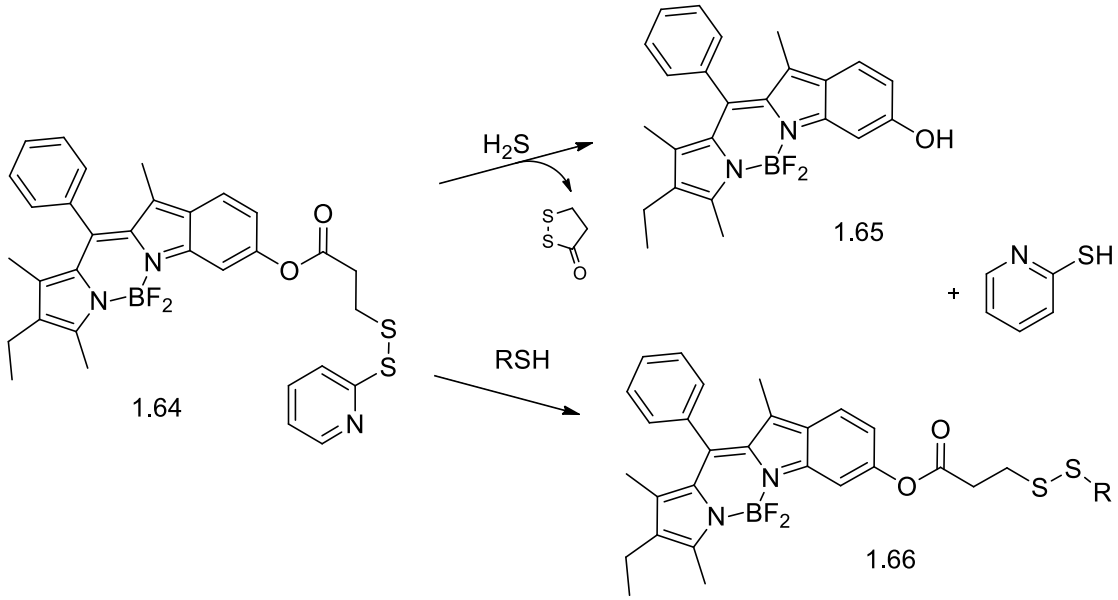

Figure 1.46: H_2S probe from Zhang and coworkers.

1.3.6. BODIPY-Based Thermometers and Viscosimeters

While fluorescent methods for the investigation of the chemical surrounding of the probe (e.g., presence/absence of analyte and its concentration) are very well developed and have found numerous applications, fluorescent sensors of physical phenomena, like viscosity and temperature, received less attention. However, the ability to measure these parameters on the local level, for example within the cell membrane, or inside the living cell, is desirable for life science research. Fluorescent probes for viscosity and temperature measurements, which can provide real-time data, are rather new and first examples of BODIPY-based sensors were published only during last decade.

In 2005, Holten and coworkers[125] showed that the fluorescence quantum yield and fluorescence lifetime for 8-phenyl BODIPY were significantly smaller than those for the sterically hindered analogs having an *o*-tolyl or mesityl group at the 8-position. It was proposed that in 8-phenyl BODIPY free rotation of phenyl unit is responsible for nonradiative relaxation of the excited state. Most of the modern fluorescent viscosimeters use such BODIPY system with the free rotating group, which is responsible for nonradiative relaxation in low-viscosity media. The increase of the fluorometric parameters Φ and τ and the rotational relaxation time with increasing solvent viscosity are consistent with the hindered rotation of the *meso*-phenyl group in the medium of high viscosity.

While the reporting part of BODIPY based viscosimeters remains unchanged, substituents at *meso*-positions can be carefully tuned for use in different regions of the cell. Molecular rotor 1.67[126] was used for investigation of viscosity in mono-, binary and ternary lipid mixtures by detection of its fluorescence lifetime. It was shown that this parameter strongly depends on the level of cholesterol, saturated *versus* unsaturated lipid ratios, and lipid phase. However,

strongly lipophilic probe 1.67 is buried within the bilayer leaflet and its lifetime reflects the viscosity of the tail region of the model lipid bilayer. As a consequence, the imaging of the plasma membrane in live cells is not possible due to the effective endocytosis of the dye 1.67 inside live cells and 1.67 is only able to report the viscosity of the lipid membranes of internal cellular organelles. The reported[127] probe 1.68 is effectively prevented from endocytosis and selectively stains the plasma membranes of live cells, because of the double positive charge located on its hydrocarbon tail. The same group reported molecular rotor 1.69[128] bearing a cholestanol moiety with the aim of targeting cholesterol-rich regions within plasma membranes of live cells. Similarly to 1.67, living cells readily endocytose the lipophilic dye 1.70, which accumulates in membranous structures inside the cytoplasm thereby allowing viscosity mapping of internal cell components.[129] This rotor was also shown[130] to be useful for viscosity determination of molecular solvents.

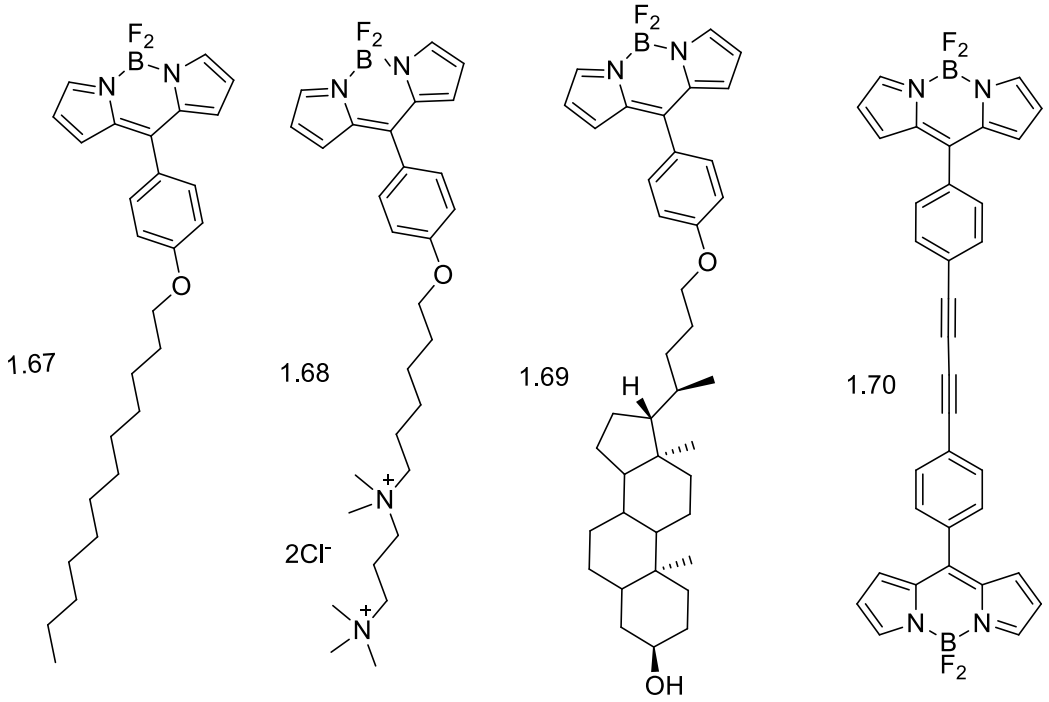

Figure 1.47: BODIPY-based molecular rotors for viscosity measurements.

Molecular rotor 1.71 bearing a triphenylphosphonium group for mitochondrial targeting and a coumarin-BODIPY dyad with a rigid phenyl spacer was reported to be an efficient self-calibrating viscosity sensor for mitochondria[33] (figure 1.48). The probe is designed in such a way, that coumarin fluorescence (427 nm) is independent on the viscosity of environment, but because of the free rotation of phenyl spacer, the fluorescence of BODIPY (516 nm) is enhanced in viscous media. Both fluorescence ratio and fluorescence lifetime (516 nm) of rotor 1.71 are in a good linear relationship with media viscosity. The rotor 1.71 was used to measure the viscosity changes upon mitochondrial apoptosis induced by treatment with monensin and nystatin.

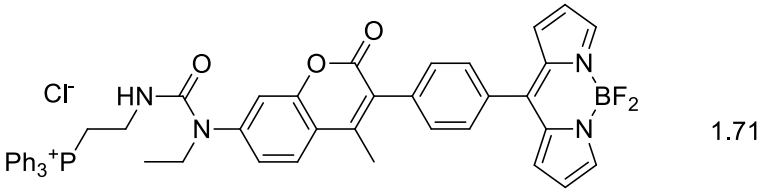

Figure 1.48: mitochondria-targeting molecular rotor.

The ability of BODIPY-based molecular rotors to sense changes in viscosity was also used for the development of fluorescent thermometers. In 2009 Hirai et al.[131] reported a supramolecular system, a copolymer, consisted of *N*-isopropyl acrylamide (NIPAM) and

BODIPY unit 1.72, which behaves as a fluorescent thermometer in water. The copolymer exhibited weak fluorescence at <23 °C but increased intensity with a rise in temperature up to 35 °C. Authors explained that the heat-induced fluorescence enhancement of system is driven by an increase in the polymer microviscosity due to a phase transition of the polymer from the coil to globule state, associated with hydration/dehydration of the polymer chain. PolyNIPAM has a polar nature at low temperature (coil), but a rise in temperature leads to a formation of a less-polar domain inside the polymer, along with globule formation. The viscous domain formed inside the globule-state polymer suppresses the rotation of the meso-pyridinium group of the BODIPY units, resulting in heat-induced fluorescence enhancement (more than 8-fold increase). Polymer 1.72 showed reversible fluorescence enhancement or quenching regardless of heating or cooling process.

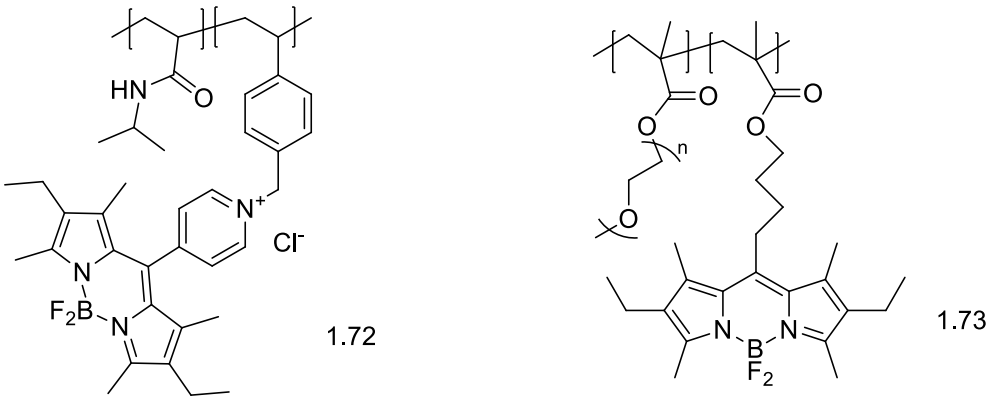

Figure 1.49: BODIPY-containing polymers for temperature detection.

Fluorescent thermo-sensitive polymers, based on 2-(2-methoxyethoxy)ethyl methacrylate 1.73 (figure 1.49), reported by Liras and coworkers[132] have important advantages. These polymers show similar lower critical solution temperature at 26 °C, but this temperature can be easily modulated by copolymerization with longer oligo(ethylene glycol) methacrylates. BODIPY is connected to the methacrylic polymer by a short methylene chain, allowing better coupling to the dynamics of the thermo-sensitive polymer and this system shows increased thermal fluorescent response.

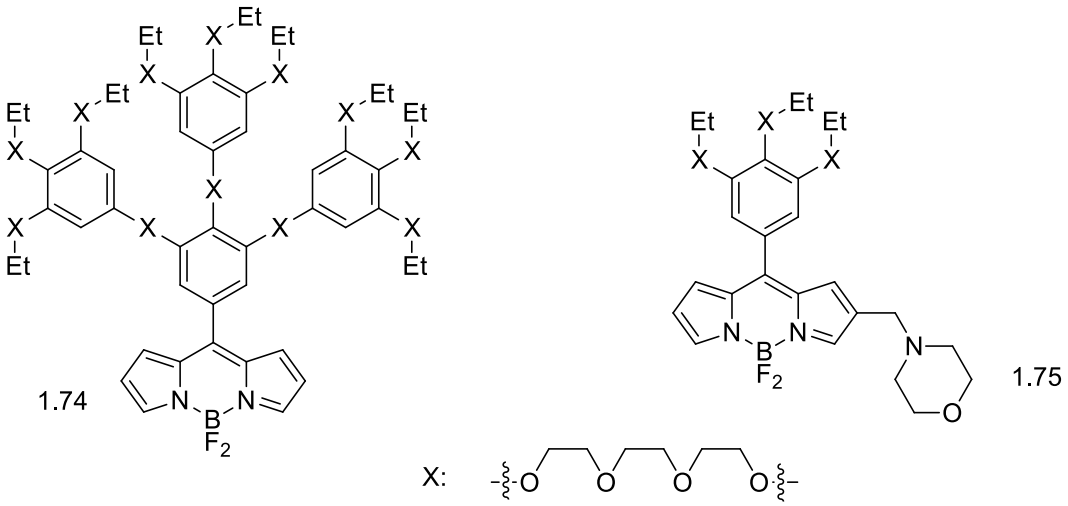

Figure 1.50: BODIPY-based oligo(ethylene glycol) dendrons for temperature detection.

The increased microviscosity at elevated temperatures is also responsible for the fluorescence enhancement in BODIPY-based oligo(ethylene glycol) dendron 1.47[133] (figure 1.50). The fluorescence of the hydrophobic BODIPY is quenched at low temperatures when dendrimeric triethylene glycol is hydrated and rotation of fluorophore is not hindered. Increased temperature destroys hydrogen bonds and BODIPY unit becomes wrapped by the dehydrated triethylene glycol groups. The emission intensity of 1.47 showed a 61-fold increase upon

heating, together with the bathochromic shift of 7 nm, which is attributed to the donor–acceptor interaction between the benzene moieties and the BODIPY during the heating process. Incorporation of pH-sensitive morpholino group into similar dendron, allowed Kuang and coworkers[134] to develop lysosome-targetable fluorescent thermometer. Probe 1.75 showed linear dependency of fluorescence intensity on the temperature in the range of 298 – 328 K.

1.4. BODIPY in Therapy

The biggest challenge in anticancer drugs development is to find cancer cell selective drug. One of the most prominent approaches is the photodynamic therapy (PDT). Compared to traditional tumor therapy such as surgery, chemotherapy, and radiotherapy, PDT has unique advantages: a) it can be applied to the site which surgery cannot touch; and to people who are not suitable for surgery, chemotherapy, and radiotherapy; b) it doesn't require expensive equipment and can be reused safely and effectively; c) it does not produce immunosuppression; d) it can be used after surgery, chemotherapy, and radio- therapy or used at the same time, with a synergistic effect.[135] PDT requires three key elements: oxygen, a photosensitizer, and light. The mechanism of action of PDT is the following: absorption of light causes photosensitizer molecule to undergo excitation to the singlet excited state ($S_0 \rightarrow S_1$ transition) and through the ISC to the triplet state ($S_1 \rightarrow T_1$). Instead of emissive relaxation, the dye in the presence of oxygen generates reactive oxygen species, mainly $^1O_2$, which causes damage to the cancer cell. Because the singlet oxygen half-life is extremely short, PDT has a very localized effect which takes place only where three key components are present. The main attribute of PDT is its potential for dual selectivity, i.e. preferential accumulation of the photosensitizer in diseased tissues, and focusing light to confine the damage to the targeted region.[9]

Currently, the most important photosensitizers in the photodynamic therapy of cancer are porphyrin derivatives.[135] However, carefully designed photosensitizers based on BODIPY have numerous advantages. They have high extinction coefficients, excellent chemical and photostability, low "dark" toxicity, facile availability and can be easily structurally modified to modulate their properties. With proper modifications of dye structure, appropriate lipophilic/hydrophilic balance for selective accumulation in tumor tissue and high singlet-to-triplet ISC efficiencies can be reached. Most efforts in latest research are dedicated to the design of photosensitizers with absorption and emission near 800 nm, improved specificity to targets, and dual-modality for imaging and therapy.[9]

A number of excellent reviews were published on this topic recently. In 2012 Burgess[9] and You[136] simultaneously published very similar reviews, later in 2013, some short review article was published by Dan.[135] In 2015 Zhong[137] and coworkers published an overview of BODIPY dyes with high triplet excited state quantum yields, their synthesis, and applications. Here only latest results in this area will be covered.

Fluorescence occurs from the singlet excited state of BODIPY, so the high quantum yields for PDT potential agents are not desired. Consequently, BODIPY has to be modified to suppress the fluorescence and increase singlet-to-triplet ISC.[9] Most widely used approach to enhance the photosensitizing properties is to utilize fluorescence quenching by heavy atom effect. 1,3,5,7-tetramethyl BODIPY does not significantly populate triplet states on excitation and has a poor quantum yield for singlet oxygen generation. The Nagano[138] group first reported 2,6-diodo analog to be efficient $^1O_2$ generating BODIPY dye, 23.9 times more active than methylene blue (non-iodinated BODIPY is almost two times less efficient compared to methylene blue). Since presence of another functional group in other position does not have a significant effect on the triplet Φ, this strategy of introduction of heavy halogen atoms into 2nd

and 6th positions of BODIPY core was widely used for development of highly active photosensitizers with increased membrane permeability, selectivity, absorbance in red region of spectra and increased “dark-light” toxicity ratio.

In 2013 Burgess et al.[139] reported double-targeting candidate 1.76 for PDT (figure 1.51). This diiodo-BODIPY based molecule was designed to contain a fragment that targets the TrkC receptor. Molecule 1.76 had submicromolar photocytotoxicities to cells that were engineered to stably express TrkC or cancer neuroblastoma lines with high levels of TrkC. Control experiments showed that 1.76 is not cytotoxic in the dark and has significantly less photocytotoxicity toward cells that do not express TrkC. Authors showed that 1.76 permeates into TrkC-containing cells and is localized in the lysosomes. This observation indirectly indicates that agent 1.76 enters the cells via the TrkC receptor.

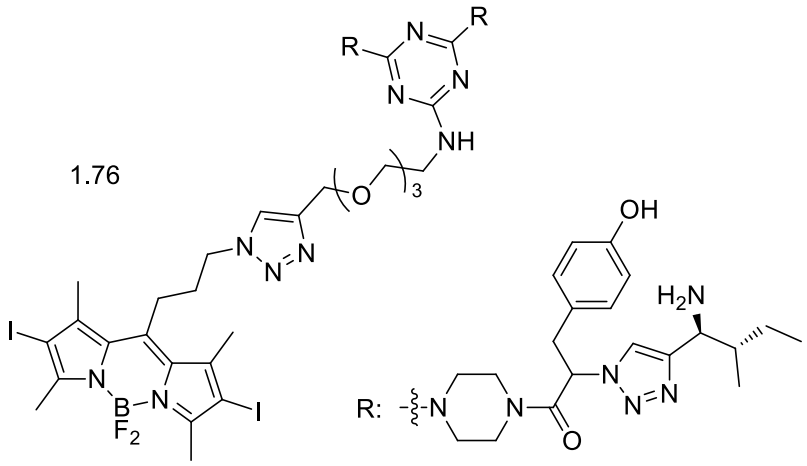

Figure 1.51: photosensitizer for PDT by Burgess et al..

BODIPY was also efficiently used to overcome the poor selectivity and the severe toxicity of the widely used anticancer drug cisplatin. The antitumor activity of cisplatin results from its hydrolysis inside the cell with the loss of one or both of the chloride ligands, and subsequent covalent binding of the formed Pt species toward DNA. Wang et al.[140] reported cisplatin analog 1.77 as a potential chemotherapy drug with one of the ligands in metal complex being replaced by BODIPY moiety enabling activation by irradiation. Later the authors improved the structure of proposed molecule by the introduction of two iodine atoms into BODIPY core[141] (1.78, figure 1.52). Released after dissociation BODIPY can act as an efficient photosensitizer. This, together with chemotherapeutic properties of Ru moiety, resulted in cytotoxicity more than one order of magnitude higher than that of cisplatin while selectivity was greatly improved.

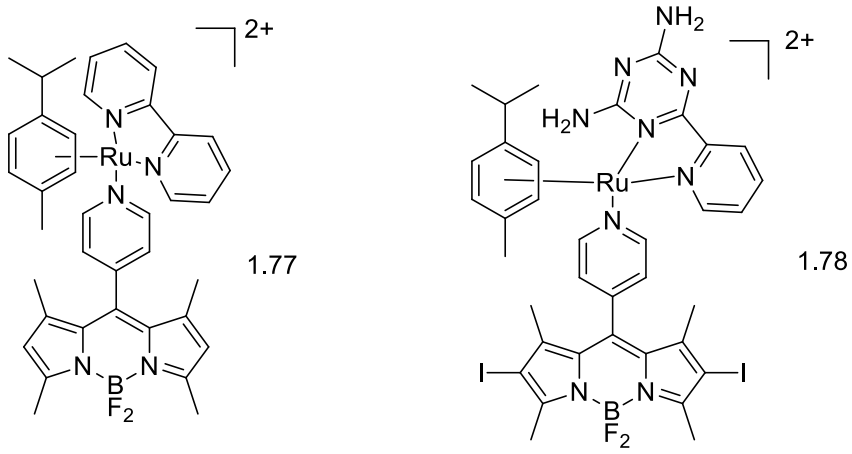

Figure 1.52: BODIPY-based cisplatin analogs from Wang et al..

The intracellular concentration of glutathione can be up to 1000 times higher in cancer cells compared to normal. This was used by Akkaya[142] to increase the spatiotemporal selectivity of their reported photosensitizer 1.79 (figure 1.53). This molecule contains the 2,4-dinitrobenzenesulfonate group, which act as a quencher and dye 1.79 can generate cytotoxic singlet oxygen only after glutathione-mediated cleavage of the electron-withdrawing module. Reported PDT agent can be excited in the therapeutic window (at 655 nm), has good water solubility and membrane permeability, and shows very low toxicity towards cells other than cancer cells.

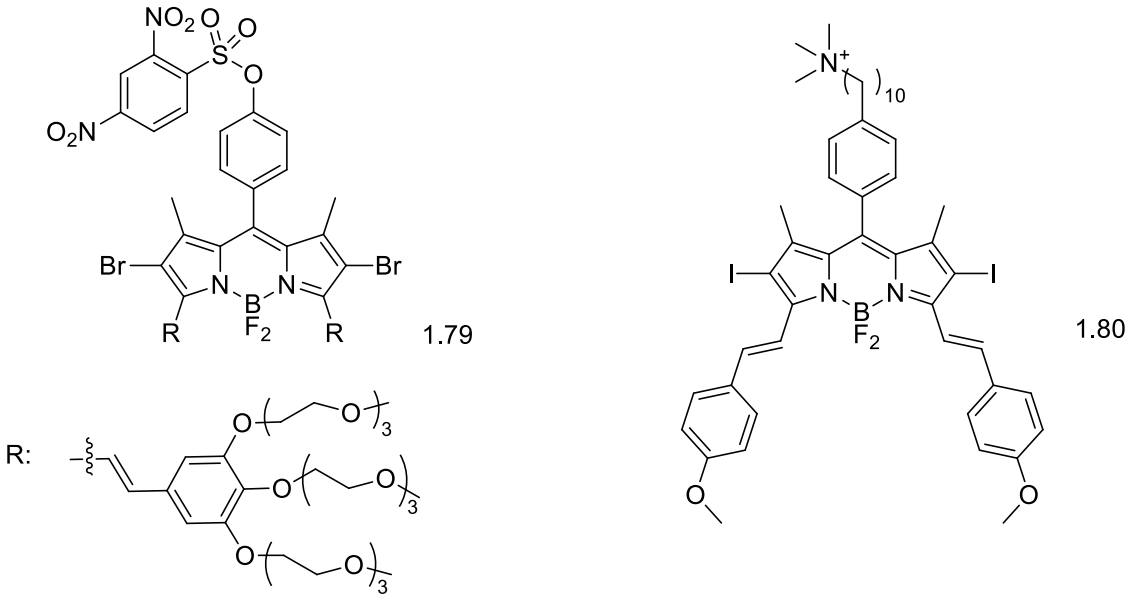

Figure 1.53: Selective PET agents from Akkaya (left) and Li (right).

Li et al.[143] proposed supramolecular vesicles based on diiodo-BODIPY 1.80 as a drug candidate, which combine chemo- and photodynamic activity. This supramolecular assembly was constructed from photosensitizer 1.80 based on its host–guest interaction with water-soluble pillar[5]arene. Such combination has good DOX (doxorubicin, anticancer chemotherapy agent) encapsulation efficiency and the formed DOX-loaded vesicles showed rapid DOX release in cancer cells low-pH environment. Such DOX-loaded vesicles are selectively delivered into tumor cells, could well localize in lysosomes and exhibit a remarkable combination of chemo- and photodynamic activities against A549 cancer cells.

1.5. BODIPY in Photovoltaic Devices

Increasing consumption of fossil fuels and continuously growing demand for new renewable energy sources have stimulated research aimed at the development of new and improvement of existing types of solar cells. Organic dyes based photovoltaic (OPV) devices are nowadays under intense investigation as a cheap and relatively simple alternative for efficient, but expensive and energy-intensive in their production crystalline Si-based and GaAs thin film based solar cells.[16,144]

BODIPY can be employed for photocurrent generation in solar cells in two types of devices. It can act as a sensitizer for titanium dioxide in dye-sensitized solar cells (DSSC) or it can be employed as an electron donor in planar- or bulk-heterojunction solid solar cells, extremely thin absorber cells, and soft junction cells.

A couple of reviews on this topic was published recently. Bessette and Hanan[15] wrote a comprehensive review of applications of BODIPY in solid heterojunction solar cells. The authors presented the variety of synthetic methodologies, photophysical studies, and design of

the most promising small BODIPY molecules or polymeric materials for efficient solar cells. Also, a brief introduction to OPV concepts can be found in this excellent review. The development and evolution of BODIPY dyes for DSSCs were covered in the review from Gayathri.[16] Here will be shortly discussed only the recent most important results in this field, not mentioned in these review articles.

Despite the attractive photophysical properties of BODIPYs, the main drawback in the application of its derivatives in narrow absorbance band in 470 – 500 nm region, typical for this dye. The main challenge in the improvement of DSSCs and junction cells is the enhancement of light-harvesting efficiency in the broad spectral region, especially in the red / NIR region. There are different strategies to generate dyes with the desired characteristics, mainly by extension of conjugation chain by fusing rings on the pyrrole units, fusing an aromatic units on the zigzag edge of the BODIPY core, generating a push–pull motif by derivatization at the α-, β- and/or *meso*-positions,[15] or construction of energy transfer cassettes.

The latter approach was used by Galateia and coworkers[145] in their "scorpion"-shaped porphyrin-BODIPY cassette. Solar cells sensitized by triad 1.81 (figure 1.54) exhibited a power conversion efficiency (PCE) value of 5.17% under illumination (AM1.5, 100 mW cm^2) and with a TiO_2 film of 12 mm thickness, with a sensitization time of 3 h without any coadsorbent. The PCE value of DSSC was enhanced to 6.20% when a thin layer of reduced graphene oxide was incorporated between TiO_2 and compound 1.81.

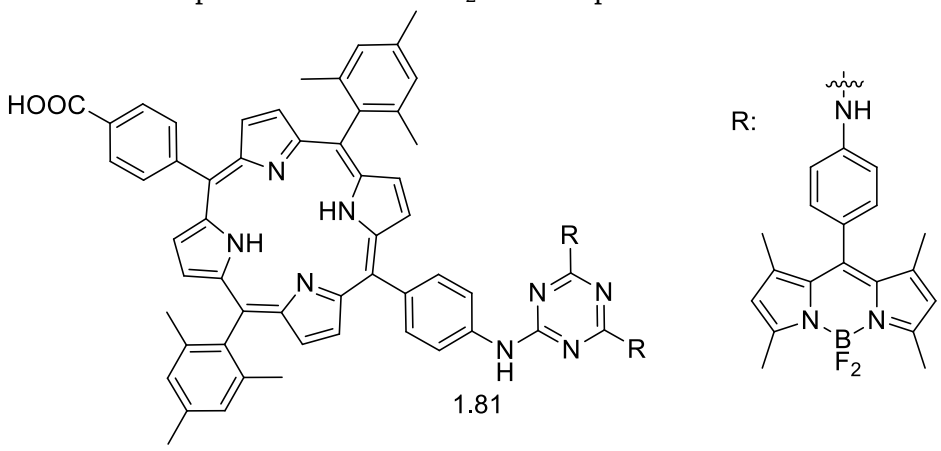

Figure 1.54: Porphyrin-BODIPY cassette for DSSC and bulk heterojunction OPV by Galateia et al..

The same dye was utilized by authors for the bulk heterojunction solution-processed organic solar cells using 1.81 as donor and fullerene derivative [6,6]-phenyl C_{71} butyric acid methyl ester as an electron acceptor.[146] With THF as a solvent, cells showed an overall PCE of 3.48%, and when the active layer of the solar cell was processed using a mixture of 4% v/v of pyridine in THF solvent, it achieved a PCE value of 5.29%.

Porphyrins are the most popular dyes for DSSCs.[15] Derivatisation of porphyrin core with BODIPYs is the promising way to improve dye's photophysical properties and this approach is used in multiple studies. However, reported BODIPY-porphyrin systems still show relatively low PCE values. The highest electronic conversion efficiency of DSSC at about 12.3%[147] was reported for BODIPY-free porphyrin system. A complete review of the synthesis, properties, and applications of BODIPY-porphyrin conjugates can be found in work published by Khan et al..[148]

2,6-conjugated BODIPYs 1.82 which contain a rigid alkyl-functionalized phenothiazine core as the donor part and one or double cyanoacetic acid units as acceptor and anchoring part were reported by Wu[144] (figure 1.55). Nanocrystalline TiO_2-based dye DSSCs were fabricated

using these dye molecules as light-harvesting sensitizers and exhibited photovoltaic performance with an overall conversion efficiency of 4.52% under AM 1.5 irradiation (100 mW cm^2). The structure-property relationship shows that both conjugated bridge and acceptor play key roles in increasing the efficiency of DSSCs. Electron-rich furan and two cyanoacetic acid-based BODIPY dye appear to enhance light harvesting capacity and help convey the charge transfer from the excited dye molecules to the conduction band of TiO_2.

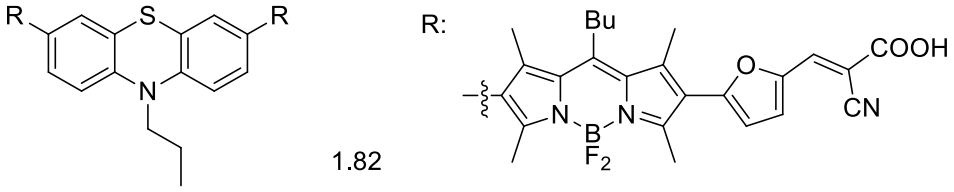

Figure 1.55: Sensitizer for DSSC from Wu et al..

BODIPY can be successfully used for the design of small molecule junction cells when combined with such traditional building blocks for OPV like thiophene and carbazole. Zhang et al.[149] recently reported a series of tunable absorbing star-shaped BODIPY derivatives containing a different number of carbazole units. The most promising compound 1.83 (figure 1.56) with four carbazole units exhibited a strong near-infrared absorption up to 850 nm with a high extinction coefficient and considerable intrinsic hole mobility in junction devices. The near-infrared organic solar cells based on 1.83 exhibited a potential power conversion efficiency of 2.70% and a high open-circuit voltage of 0.85 V.

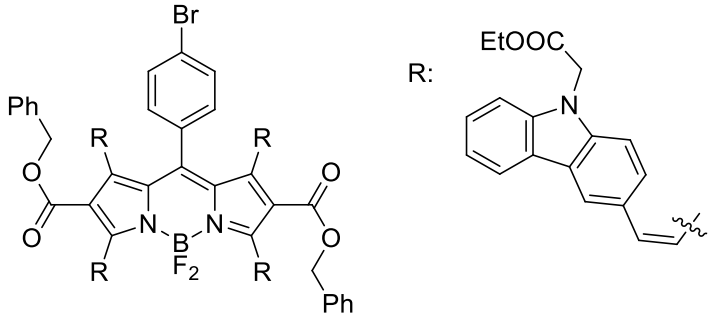

Figure 1.56: Dye for OPV by Zhang et al..

Zhan et al.[150] used diketopyrrolopyrrole - thiophene π-bridge between two BODIPY units to makes a BODIPY dimer 1.83 capable of capturing and exploiting visible solar photons via intramolecular energy transfer (figure 1.57). Crystalline blend film of 1.83 with a fullerene (C_{71}) derivative [6,6]-phenyl C_{71} butyric acid methyl ester resulted with the OPV with increased absorbance and PCE compared to analogs. The cells based on 1.83 exhibits the best PCE of 3.62% (average 3.40%) with an open-circuit voltage of 0.73 V.

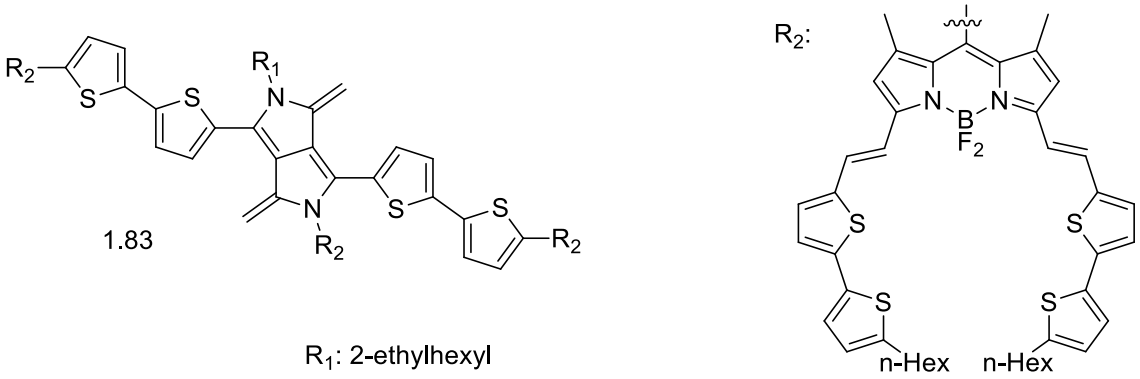

Figure 1.57: Dye for OPV by Zhang et al..

1.6. BODIPY as a Laser Dye

Dye lasers are amongst the most versatile and efficient laser sources of today. Compared to other types of lasers, dye lasers have greater tunability and can cover the entire visible and near-IR region. Intense absorption and emission spectra with a small overlap, high quantum yield, excellent photostability, short fluorescence lifetime, negligible triplet state formation rate, and low absorption of excited state at pumping and lasing wavelength are the requirements for efficient laser dye. Unique fluorescent properties of BODIPY render this molecule a perfect candidate for development of efficient laser dyes. Several BODIPY derivatives have been shown to exhibit laser activity and lasers based on BODIPY solutions, BODIPY-doped polymeric matrices, and BODIPY-doped liquid crystals were reported.

The first BODIPY as a potential laser dye was examined in the early 1990s by Boyer and coworkers.[151–153] The authors examined for a laser activity a broad collection of simplest BODIPY structures bearing different substituents with the aim to determine the influence of functional groups on lasing properties. It should be noted that the authors didn't find any relations between absorption and emission maximums, extinction coefficients, quantum yields of BODIPYs and laser efficiencies of examined structures. However, it was shown that dyes bearing heavy halogens at 2- and 6- position exhibit no laser properties and distortion of the planarity caused by strong steric interactions between alkyl units also caused a total loss of laser activity. These works gave a start for intense development and examination of new BODIPY structures for applications in lasers, many of developed molecules have since become commercially available. Overview of BODIPYs as laser dyes can be found in the Ph.D. thesis from Benstead,[154] here only most interesting results will be discussed.

In order to produce laser dyes with red-shifted emission, a regular approach of extension of BODIPY's conjugation system by introduction of one styryl / phenyl unit in 3- or two groups in both 3- and 5- positions have been applied.[155,156] In one of the latest works from Zhang et al.[157] a set of BODIPYs with extended conjugation and ITC effect were synthesized and tested for laser activity (figure 1.58). New dyes under transversal pumping at 532 nm exhibit highly efficient (up to 57%) and stable laser emission tunable from the green to NIR spectral region (570–725 nm).

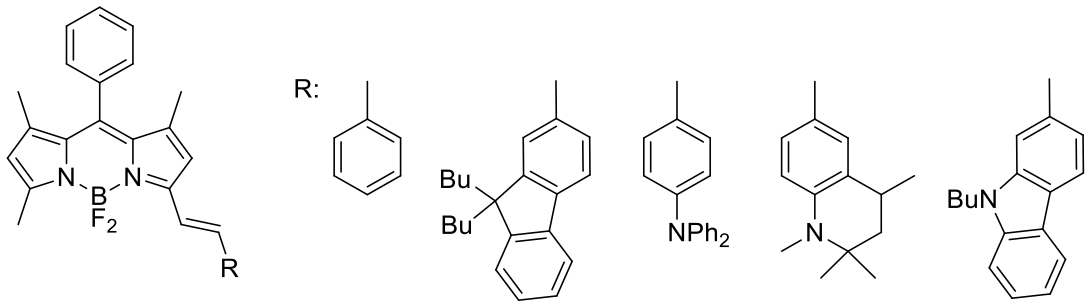

Figure 1.58: A set of potential laser dyes from Zhang et al..

The development of highly efficient and stable blue-emitting dyes to overcome some of the most important shortcomings of available chromophores is more challenging. In 2011, a new class of 8-amino substituted blue-shifted BODIPY dyes was reported[45]. The emission of theses dyes can be modulated in a wide spectral range (430 – 500 nm) by modulation of the electron-donor strength of the substituent at the nitrogen atom. BODIPY 1.84 (R = H, figure 1.59) showed 63% lasing efficiency under 400 nm pumping wavelength (0.7 mM solution in ethyl acetate).

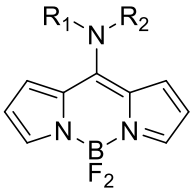

R_1: H, CH_3,
R_2: H, CH_3, CH_2CHCH_2, CH_2CCH

1.84

Figure 1.59: BODIPY dyes for blue lasers.

The development of laser dyes which can absorb UV light and show efficient and stable emission in the Vis or NIR region (500 – 700 nm) is of great importance, since it constitutes the only way to generate, efficiently and without undesired re-absorption/re-emission processes, the required tunable UV laser radiation by frequency doubling. Recently Esnal and coworkers[158] reported FRET-utilizing coumarin–BODIPY hybrids involving push-pull amino or hydroxycoumarins covalently linked to the BODIPY chromophore through to the amino or hydroxyl coumarin heteroatom. The developed fluorescent dyads undergo lasing under UV irradiation (250 – 350 nm) with good efficiency and high stability, allowing wavelength finely tunable over a wide range (520–700 nm). The highest lasing efficiencies (up to 51% at 355 nm) were recorded from hybrids based on two hydroxycoumarins and 3,5-disubstituted BODIPY (1.85, figure 1.60). These hybrids also proved to be the most photostable, with laser emission remaining up to 55% of its initial level after $5 \cdot 10^4$ pump pulses at a 10 Hz repetition rate.

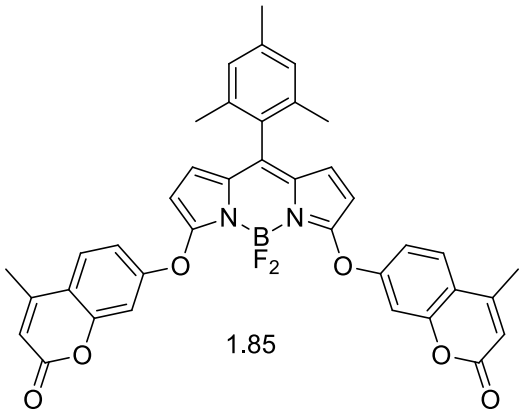

1.85

Figure 1.60: FRET-based coumarin-BODIPY hybrid from Esnal et al..

A similar rational design of an asymmetric cassette triad based entirely on BODIPY chromophores was reported by Duran-Sampedro.[159] Their FRET-system showed efficient light harvesting over the entire UV-Vis spectral region, leading to a bright and stable red-edge laser emission at 665 nm with a quantum yield of 72% regardless of the excitation wavelength.

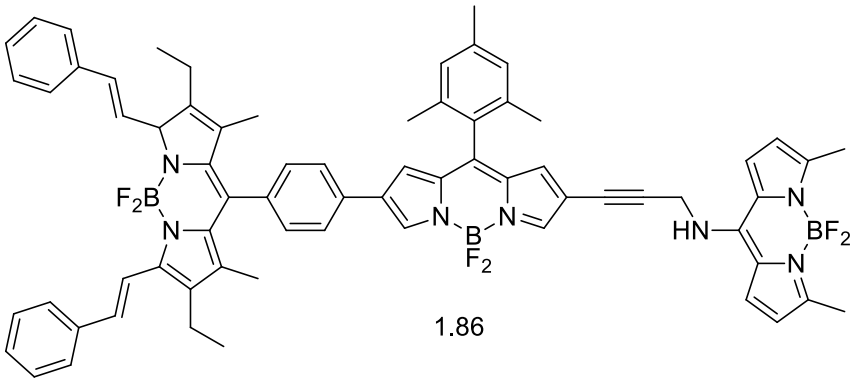

1.86

Figure 1.60: FRET-based BODIPY triad from Duran-Sampedro et al..

Under transversal pump conditions at 355 nm, broad-line-width laser emission was obtained from a triad solution. In agreement with the photophysical behavior, the cascade of FRET processes inside triad 1.86 leads to a highly efficient (up to 49%) and monochromatic laser emission centered at 665 nm. Moreover, 1.86 also exhibits excellent photostability, maintaining 100% of the initial emission intensity after 10^5 pump pulses.

2. Scope of the Dissertation

Fluorescence-based techniques are amongst the most sensitive analysis methods with unique temporal and spatial resolution. Fluorescence tools have found broad applications in chemical and biological disciplines, clinical research, industry, pollution control, etc., and the development of more advanced probes is thus essential.

The goal of this dissertation is to develop synthetic routes towards different BODIPY-labeled NHC-transition metal complexes and to study the changes of the fluorescence signal in the course of the reactions involving the metal center. Such transformations should alter the electron density at a metal, and potentially modulate the efficiency of fluorescence quenching, leading to detectable changes in the emission spectra of the fluorophore. A detailed understanding of the nature of organometallic compound – fluorescent properties relationships may result in the development of new classes of fluorescent molecular probes with unique properties. Moreover, BODIPY labeling of homogeneous catalysts can be a useful tool for mechanistic investigations of catalytic transformations.

The scope of the dissertation is outlined in the following scheme:

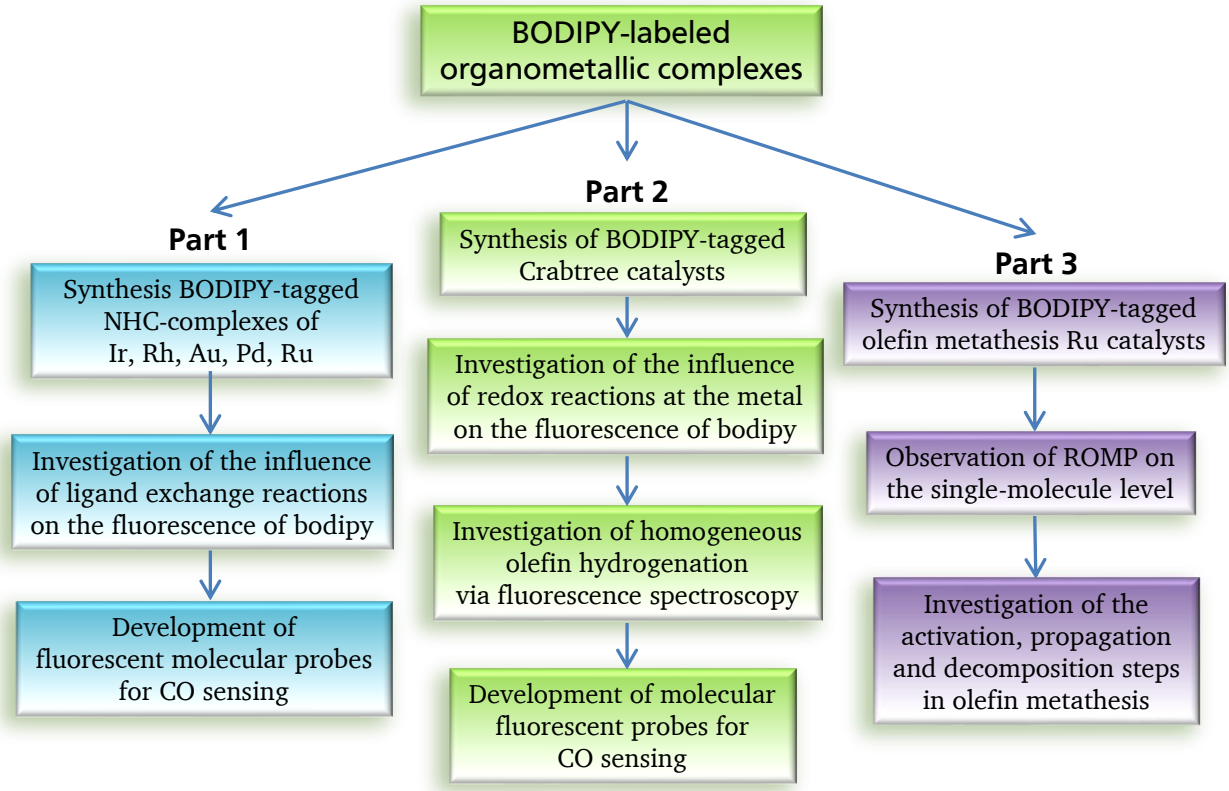

In order to achieve the assigned goals, the thesis will be divided into three parts, and the following tasks will be performed:

Part 1:

- Synthesis of different fluorescent NHC precursors tagged with the BODIPY fluorophore.
- Determination of the photophysical properties and chemical behavior of the obtained NHC ligands in the synthesis of various transition metal complexes.

- The ligand with optimal chemical stability and fluorescent properties will be used in the synthesis of NHC-transition metal (Au, Ir, Rh, Pd, Ru) complexes. Photophysical data of these new complexes will be measured with an emphasis on whether the metals quench, enhance or do not affect the emission profile of the original BODIPY-tagged NHC ligand.

- The changes in the fluorescence of complexes in the course of ligand-exchange reaction will be explored, aimed towards understanding the influence of the electronic properties of the metal center on the emission spectra.

Part 2:

- With the aim to explore the potential application of BODIPY-labeling in mechanistic studies of homogeneous hydrogenation and molecular hydrogen detection, fluorescent analogs of Crabtree complex will be synthesized and their photochemical properties will be determined.

- The catalytic activity of the fluorophore-tagged Crabtree catalyst will be studied and the fluorescence of BODIPY during this reaction will be monitored with an emphasis on whether the oxidative addition of hydrogen and consecutive steps lead to changes in the emission profile of the fluorophore.

- The applications of the studied complexes in molecular sensing will be explored. The reaction of (NHC-BODIPY)MCl(cod) complexes (M=Ir, Rh) with CO will be used for the development of carbon monoxide probes. The effect of the oxidative addition of H_2 to Ir^I in a fluorophore-tagged Crabtree catalyst on the fluorescence intensity will be used for hydrogen sensing.

Part 3:

- Synthetic routes towards different BODIPY-tagged Grubbs-Hoveyda complexes will be investigated with the aim to explore the possibility of using such catalysts for mechanistic studies of metathesis reaction.

- Fluorophore-tagged Grubbs-Hoveyda complex with a trialkoxysilyl group for surface immobilization will be synthesized. Glass coverslips with covalently bonded catalyst will be exposed to the ROMP monomers and reaction will be monitored with single molecule fluorescent spectroscopy with the aim to study the initiation of pre-catalyst, chain propagation and termination on the single-molecule level.

- The reaction of synthesized BODIPY-tagged metathesis complexes with olefins will be conducted and the course of reactions will be monitored with UV-Vis and fluorescence spectroscopy. Obtained data will be analyzed with the aim to study the initiation step of olefin metathesis, as well as catalytic cycle and decomposition, at low concentrations of the pre-catalyst.

3. Results and discussion

3.1. BODIPY-Tagged *N*-Heterocyclic Carbene complexes as Luminescent Carbon Monoxide Chemodosimeters

3.1.1. Sensors for Carbon Monoxide

Carbon monoxide is a colorless and odorless gas. It is highly toxic in concentrations higher than 30 ppm.[160] On the other hand, CO plays an important role as the secondary messenger in human normal biological functions.[161] CO has received a great deal of attention since it is a biological regulator of anti-inflammatories, modulating vasorelaxation, vascular smooth muscle, and tissue injury.[162,163] Although CO plays a significant role in physiological processes, many aspects of its functions still need to be explored. Therefore, the development of fluorescent sensors suitable for real-time, spatial, and temporal tracking and monitoring of CO at the cellular level is an important challenge for chemists. Even so the sensitive and selective fluorescent sensors are desirable for biological studies, no probe which can fulfill all of above mentioned requirements has been reported and only a few other CO probes are known. Yoon et al.[164] published a review of chemosensors for gases, where most of the sensors for CO are covered. Recently Schiller and coworkers[161] made an excellent overview of physiology, controlled release, and methods of detection of CO. Attention is also given to fluorescent and colorimetric sensors. Earlier in 2013, a small highlight of known fluorescent probes for CO was released.[165]

Established methods for CO detection include gas chromatography,[166] laser infrared absorption,[167] electrochemical assays,[168,169] and colorimetric CO sensing.[170,171] The first fluorescent CO probe was reported by Chang[172] in 2012 and is based on palladium-mediated carbonylation reactivity (figure 1). The initial cyclopalladated dimer is characterized by very weak fluorescence (λ_{em} = 503 nm and Φ = 0.001) due to quenching by palladium via heavy-atom electronic effect. Upon binding of CO, a carbonylation reaction concomitantly releases reduced Pd(0) and a more fluorescent BODIPY dye (λ_{em} = 507 nm and Φ = 0.44). Within 60 min of reaction under close to physiological conditions (pH 7.4 buffer, 37 °C, 50 μM [$Ru(CO)_3Cl$(glycinate)] as a CO source), the probe produced a 10-fold increase in fluorescence. The authors observed dose-dependent fluorescence response at 1 μM [$Ru(CO)_3Cl$(glycinate)] concentrations. The fluorescence turn-on response of reported chemosensor was found to have good selectivity over other biologically relevant reactive oxygen, nitrogen, and sulfur species. Moreover, this probe was used to visualize changes in CO levels in living cells using confocal microscopy. However, low fluorescence response and long reaction time are required for the probe to reach its maximum fluorescence level. This strongly limits the application of this molecule as an efficient *in vivo* fluorescence sensor for CO.

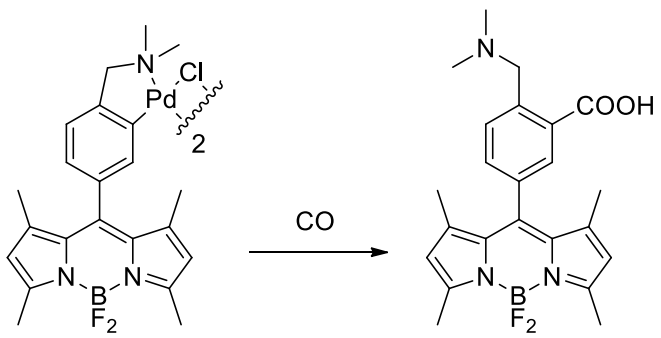

Figure 1: Fluorescent CO probe based on a carbonylation reaction from Chan et al..

Another reaction-based CO sensor was reported by Liu.[173] 4-Iodonaphthalene-1-sulfonate was shown to be practically non-fluorescent in aqueous media (Φ = 0.0063 at λ_{ex} = 320 nm). The reported sensing system was constructed by dissolving probe, sodium azide, and palladium acetate/xantphos (2%) in the water-DMSO mixture (figure 2). Such solution displays a dramatic increase in fluorescence (>100-fold) within several minutes after exposure to CO gas due to the Pd-mediated conversion of the initial naphthalene derivative to highly fluorescent 4-aminonaphthalene-1-sulfonate (Φ = 0.767). The proposed mechanism of the reaction involves the oxidative addition of Pd to C-I bond, iodide to azide ligand exchange, followed by insertion of CO, resulting in the formation of azidocarbonyl derivative. This intermediate undergoes Curtius rearrangement with the formation of isocyanate, which is quickly hydrolyzed with the formation of final amine. It was shown that such system can be successfully used for the detection of 50 ppm concentrations of CO in air. Despite its good fluorescent response and moderate reaction time, this probe requires multiple components to produce an analytical signal in the presence CO. This and the high toxicity of azide limit use of this probe in potential applications.

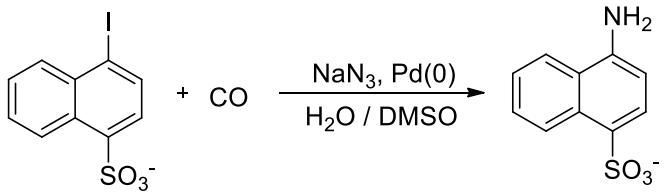

Figure 2: CO chemodosimeter from Liu et al..

Except for the reactivity of CO in palladium-mediated reactions, its ability to form strong complexes with transition metals has also led to applications in the development of CO probes. Thus, the standard *in vitro* test for CO is the carboxy-myoglobin assay, which utilizes the affinity of CO to the iron center in heme. It this test, CO is added to a solution of reduced desoxy-myoglobin and the formation of carboxy-myoglobin is followed via absorbance spectroscopy.[174] In 2004, Guilard and coworkers[175] described the ability of cobalt^{III} corroles to selectively absorb CO and later this group reported[171] hybrid materials or mesostructured silica incorporating cobalt^{III} corrole complexes which exhibited excellent absorption of CO with high selectivity towards other gases.

Sancenón et al.[176,177] recently showed that CO can be detected selectively with high sensitivity by the binuclear rhodium complex (figure 3), which contains two cyclometalated phosphine ligands. Its chloroform solution undergoes a color change from violet to yellow via replacement of acetic acid ligands by CO when air samples containing CO were bubbled through it. The binuclear rhodium complexes were also adsorbed on silica and used as colorimetric probes for “naked eye” CO detection in the gas phase. When the gray-purple colored silica solids containing the rhodium probes were exposed to air containing increasing concentrations of CO, two colors were observed, in agreement with the formation of two different products. The results are consistent with an axial coordination of the CO molecule in one axial position (pink-orange) or in both (yellow). A collection of binuclear rhodium complexes displayed high CO selectivity with remarkable detection limits. Such silica gel samples were capable of CO detection by the “naked eye” at concentrations as low as 0.2 ppm in air. Furthermore, the binding of CO in all rhodium complexes was fully reversible.

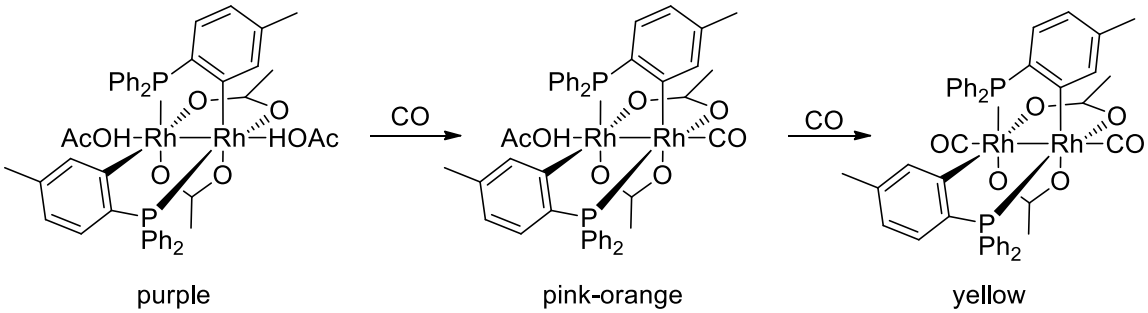

Figure 3: Fluorometric CO probe from Sancenón.

In 2012 He et al.[178] presented the design of a genetically encoded fluorescent probe that is capable of selectively imaging CO in living cells. In this probe, the unique CO-binding selectivity of CooA, a dimeric CO-sensing heme protein from *Rhodospirillum rubrum* was utilized. CooA is a homodimer that contains one *b*-type heme per 25 kDa monomer and is capable of selectively binding to CO. The authors decided to insert a yellow fluorescent protein into CooA with the intention of using the natural selectivity of CooA toward CO to construct an effective reporter. It was shown that upon CO binding to the heme of CooA, the electronic and structural properties undergo changes what results in fluorescent response. The fluorescence emission (at 528 nm) of the purified probe increased by a factor of two after incubation with CO (final concentration= 10 μM) for 10 minutes when excited at 516 nm. In addition, the probe shows a good selectivity for CO over other relevant heme ligands and is capable of imaging CO fluctuations inside living HeLa cells.

3.1.2. Synthesis of BODIPY-tagged NHC-ligands

Taking into account that among the few known ones there is no known fluorescent carbon monoxide probe which has a short response time and high selectivity and sensitivity at the same time, it is very attractive to explore the possibility of application of BODIPY-tagged (NHC)MCl(cod) (M=Ir, Rh) complexes as a potential CO chemodosimeters. The reaction of such complexes is well known[179] and substitution of electron donating cod ligand with EWG carbon monoxide ligands should strongly alter the electron density at metal center. This may lead to changes in the quenching ability and, respectively may translate to the changes in the emission intensities.

N-heterocyclic carbenes (NHC) are amongst the most prominent ligands in transition metal chemistry. During the last years, many efficient transition metals catalyzed reactions have been established, in which the excellent performance of NHC-metal complexes in catalytic transformations is rivaling that of the traditional phosphine-metal complexes.[180–182] Most prominent are applications of (NHC)Ru complexes in olefin metathesis and of (NHC)Pd complexes in Pd-catalyzed cross-coupling reactions;[183–189] furthermore NHC complexes with Au and other transition metals enable efficient chemical transformations.[190,191]

NHC metal complexes show higher stability in comparison to other types of complexes used in homogeneous catalysis and the dissociation of the NHC – metal bond normally requires high activation energy and is unlikely under typical reaction conditions. The fact that the NHC remains attached to the metal center during the chemical transformation make the NHC an ideal site for the BODIPY attachment with the aim to monitor characteristic changes in the fluorescence emission of the (NHC-BODIPY) transition metal complexes as a consequence of these transformations. This approach could also open the door to single-molecule experiments of such reactions,[192–194] enable the monitoring of metal catalyzed transformations,[195,196] or changes in metal oxidation state.

Earlier Leen et al.[47] reported the synthesis of *meso*-halogenated BODIPYs and showed that halogen atom in these compounds can be easily replaced by nucleophilic agents, such as alcohols, amines, or C-nucleophiles. It was decided to use this reactivity of 8-chloro BODIPY for the synthesis of an NHC precursor, in which fluorophores can be connected to the azolium group directly (figure 4). For this, the reaction of *meso*-chloro BODIPY, synthesized according to Lee's procedure,[47] with 1*H*-imidazole was conducted. In the presence of K_2CO_3 in CH_2Cl_2, the reaction proceeds at room temperature to provide imidazole **1** in excellent yield (95%). However, all attempts to synthesize imidazolium salts using alkyl halides for quaternization resulted in complete decomposition of the starting imidazole **1**. Using ethyl triflate at low temperatures, the target BODIPY-tagged NHC precursor **2** was obtained in 86% yield.

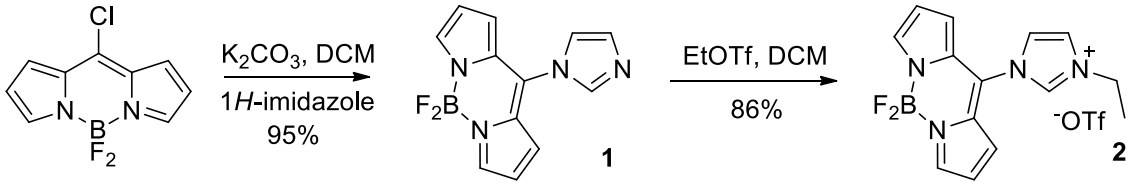

Figure 4: Synthesis of imidazolium salt **2**.

The direct connection of BODIPY to the carbene renders compound **2** very attractive for the synthesis of different transition metal complexes with the aim to monitor chemical transformations at the metal center. Normally Ag-NHC complexes are easily prepared and are convenient precursors for the synthesis of many other transition metal complexes via transmetalation reaction.[197,198] However, all attempts to prepare Ag complex from **2** and Ag_2O resulted in complete decomposition of the starting imidazolium salt. Decomposition was also observed when **2** was treated with base, either Na-*tert*-amylate in the synthesis of Au, Rh, and Ir complexes or K_2CO_3 at elevated temperatures in the synthesis of Au complex. This can be due to the high lability of C-N bond between BODIPY and imidazole moiety, which, being a good leaving group, can be replaced even with weak nucleophiles. Additionally, protons at 3- and 5- positions of BODIPY are known to be relatively acidic. This might explain the decomposition in the presence of Na-*tert*-amylate.

To overcome these problems, it was decided to use a short linker between imidazole and BODIPY. As the most convenient basis for the new NHC-precursor, *N*-alkyl-*N*'-aryl-imidazolium halide was chosen. Such type of carbenes form sufficiently stable complexes with Ir and Rh, and at the same time, the synthetic route is simpler compared to other strategies. For this approach, 4-(1*H*-imidazol-1-yl)-3,5-dimethylphenol **3** was used, which can be obtained following a modified procedure[199] from 4-amino-3,5-dimethylphenol, glyoxal, NH_4Cl, and formaldehyde in 68% yield. Nucleophilic substitution of chlorine in *meso*-Cl-BODIPY provided target the imidazole **4** in 62% yield (figure 5). Compound **4** can be easily quaternized with ethyl triflate. However, the obtained imidazolium salt contained 5-10% of impurities and any attempt to purify this material led to decomposition and even less pure sample. Thus, purification by column chromatography (eluent: $CHCl_3$/MeOH) resulted in complete decomposition of imidazolium salt with the formation of 8-methoxy BODIPY and corresponding quaternized derivative of phenol **3**.

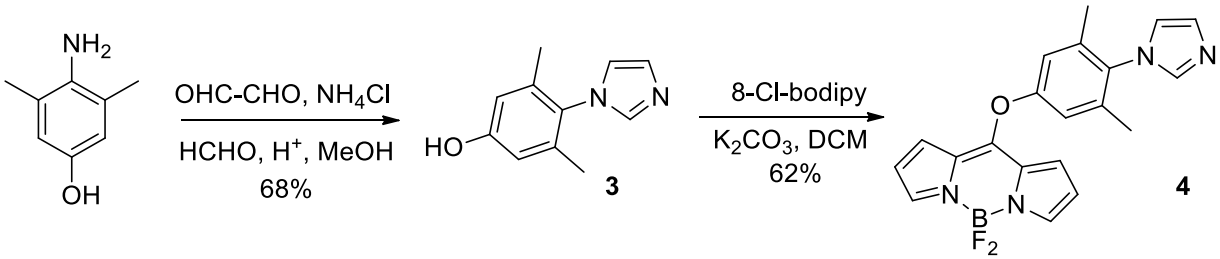

Figure 5: Synthesis of imidazole **4**.

Compared to oxygen in **4**, the acetylene linker in similar NHC precursor was expected to provide a more stable connection. Moreover, better conjugation between BODIPY and carbene through the triple bond can improve sensing properties of desired complexes. It was thus decided to introduce BODIPY core via Sonogashira cross-coupling using 2-iodoBODIPY and acetylene **7** (figure 6). The chemistry of Pd-catalyzed transformations of halogenated BODIPYs is well known[30] and 2-iodopodipy is easily accessible via two-step synthesis.[200] Synthesis of BODIPY-labeled imidazolium salt **9** was done in five steps with an overall yield of 30% starting from 4-bromo-2,6-dimethylaniline. Imidazole **5** was constructed following a procedure, similar to the one used for the synthesis of imidazole **3**. The consecutive introduction of TMS-acetylene via Sonogashira coupling and deprotection, followed by a second cross-coupling of the formed acetylene with 2-iodo BODIPY provided imidazole **8**. The formed imidazole can be easily converted to the respective azolium salt **9** with ethyl triflate. Like expected, NHC-precursor **9** is more stable compared to **4**, however, all attempts to synthesize Au and Ir complexes of respective carbene again led to the formation of complicated mixture and separation of target complexes was not possible. This may be explained by activation of the triple bond towards nucleophilic addition as a consequence of coordination of transition-metal species to it.

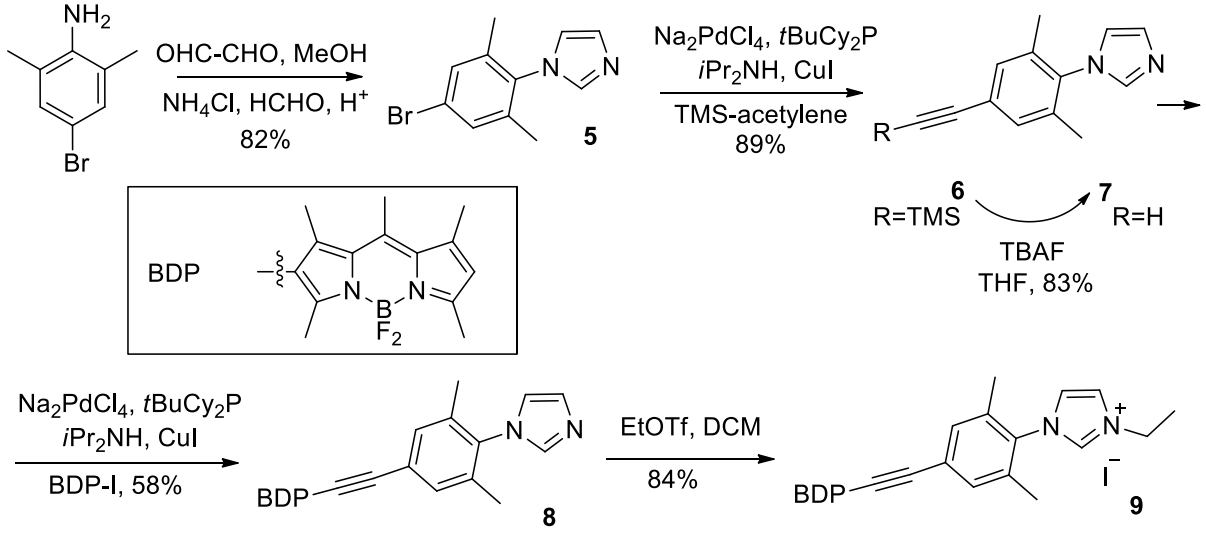

Figure 6: Synthesis of azolium salt **9**.

The synthesis of the BODIPY-substituted azolium salt **12**·HI was achieved in three steps with an overall yield of 64%. Lithiation of **5** with BuLi at -90 °C followed by the reaction with triisopropoxyborane provided a crude diisopropyl derivative of **10**, which was hydrolyzed in concentrated HCl under reflux (figure 7). Similar boronic esters can be easily hydrolyzed with NH_4Cl at room temperature, however, all attempts to conduct such hydrolysis under milder conditions provided **10** in very small yields or no reaction was observed at all.

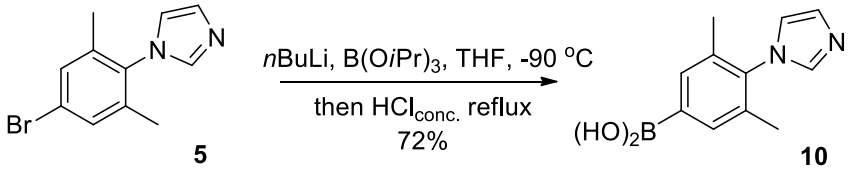

Figure 7: Synthesis of boronic acid **10**.

The best yield in the Suzuki coupling between **10** and 2-iodoBODIPY was obtained with $Pd(PPh_3)_4$ in THF-toluene-water mixture. The formed imidazole **11** was converted to imidazolium salt **12**·HI by heating in a sealed flask under neat conditions with 10 equivalents of *i*PrI. With the aim to increase the solubility of target complexes in water, imidazolim salt **13**·HI containing triethylene glycol unit was synthesized from **11** and 1-iodo-3,6,9-

trioxadecane in toluene under reflux. In both cases, pure product was separated by precipitation from the reaction mixture with diethyl ether (figure 8).

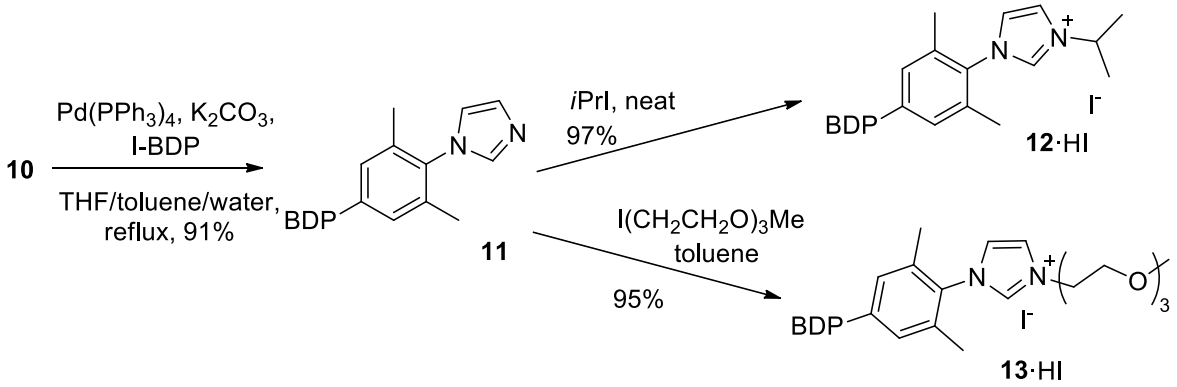

Figure 8: Synthesis of imidazolium salts **12**·HI and **13**·HI.

3.1.3. Synthesis of (NHC-BODIPY) Metal Complexes

The BODIPY-substituted azolium salts **12**·HI and **13**·HI can be used for the synthesis of NHC-metal complexes. The various complex-forming reactions proceed in good yields, despite the fact that bases are needed to deprotonate the azolium salt and with the BODIPY unit itself being slightly sensitive to strong bases. First, Na-*tert*-amylate was used to *in situ* generate the free carbene, whose reaction with $[MCl(cod)]_2$ (M= Rh, Ir) gave the respective [(**12**)MI(cod)] in modest yields. Best yields were obtained when the base was first added to $[MCl(cod)]_2$ prior to the addition of **12**·HI. This improvement can be explained by the *in situ* generation of *tert*-pentoxy complexes $[M(OtPent)cod]_2$, which act as milder deprotonation agents. Based on mass spectrometry, only formation of iodo complexes was observed (figure 9).

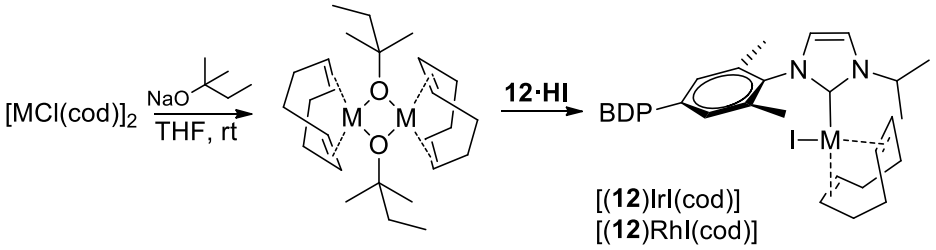

Figure 9: Synthesis of Ir and Rh complexes.

Even better yields of the respective Rh and Ir complexes were obtained, using the in-situ generated Ag complexes of carbenes **12** or **13** as a mild NHC transfer reagent.[201] The reaction of **12**·HI or **13**·HI with Ag_2O proceeds in CH_2Cl_2 in the absence of light at room temperature in 30 min (figure 10). However, separation of the expected pure Ag complex is not possible. Analysis of the NMR data of separated substance showed a complex mixture of products. This can be due to the low stability of the corresponding [(**12**)AgI] or [(**13**)AgI] complexes. The addition of $[MCl(cod)]_2$ to the reaction mixture results in the formation of target complexes, which can be purified by simple filtration through a short plug of silica. According to mass spectrometry, only chloro complexes are formed in this reaction, and they can be converted into the closely related iodo complexes by treatment of [(**12**)MCl(cod)] with an excess of KI. [(**13**)MCl(cod)] were not separated and converted to the respective [(**13**)MI(cod)] *in situ*.

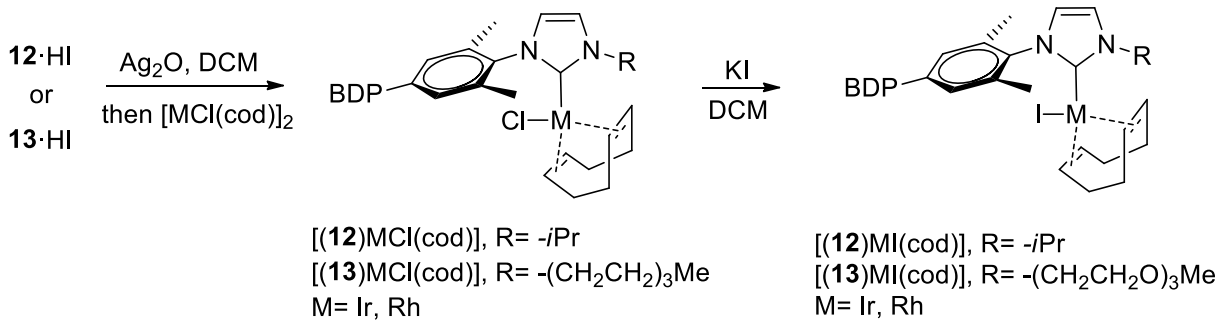

[(**12**)MCl(cod)], R= -*i*Pr
[(**13**)MCl(cod)], R= -$(CH_2CH_2)_3Me$
M= Ir, Rh

[(**12**)MI(cod)], R= -*i*Pr
[(**13**)MI(cod)], R= -$(CH_2CH_2O)_3Me$
M= Ir, Rh

Figure 10: Synthesis of Ir and Rh complexes.

Complexes [(**12**)MX(cod)] (X= Cl, I) and [(**13**)MI(cod)] can be easily converted to the respective CO-complexes by bubbling CO gas through their CH_2Cl_2 solutions. This ligand exchange reaction is complete within 30 min and simple precipitation from pentane provides pure target compounds in nearly quantitative yields (figure 11).

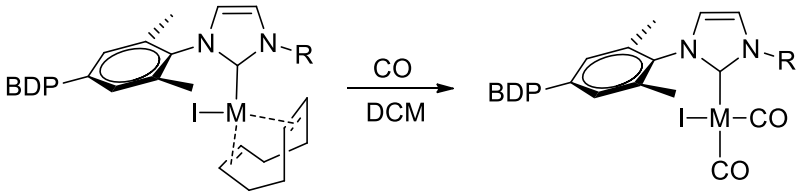

[(**12**)MX(cod)], R= -*i*Pr
[(**13**)MI(cod)], R= -$(CH_2CH_2)_3Me$
M= Ir, Rh; X= Cl, I

[(**12**)$MX(CO)_2$], R= -*i*Pr
[(**13**)$MI(CO)_2$], R= -$(CH_2CH_2O)_3Me$
M= Ir, Rh; X= Cl, I

Figure 11: Reaction of cod complexes with CO.

The *in situ* generated NHC-Ag complex [(**12**)AgI] was used for the synthesis of [(**12**)(SIMes)$RuCl_2$(ind)] according to a synthetic protocol previously reported by our group.[202] NHC-transfer reactions required higher temperatures to efficiently remove pyridine ligand in starting [(SIMes)$RuCl_2$(ind)py], causing the formation of target complex in lower yield compared to previously described reactions. After purification by column chromatography, complex [(**12**)(SIMes)$RuCl_2$(ind)] was obtained in 52% yield (figure 12).

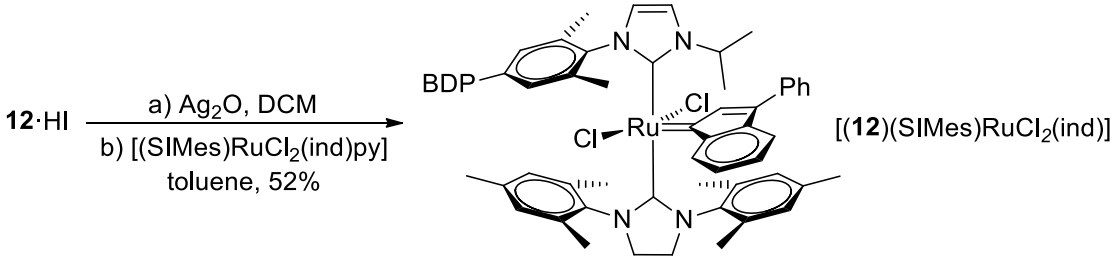

Figure 12: Synthesis of BODIPY tagged bis-NHC Ru complex.

Complex [(**12**)PdI_2(Clpy)] was conveniently synthesized directly from the respective azolium salt and $Pd(OAc)_2$ employing 3-chloropyridine as the solvent and K_2CO_3 as a base[203] (figure 13). Complex [(**12**)AuI] was obtained from carbene **12**, generated *in situ* by deprotonation of **12**·HI with Na-*tert*-amylate, and [$AuCl(SMe_2)$]. Sufficient yields (89%) were obtained only when the reaction was conducted in the dark at -78 °C. According to mass spectrometry, the iodo complex is the only product in this reaction.

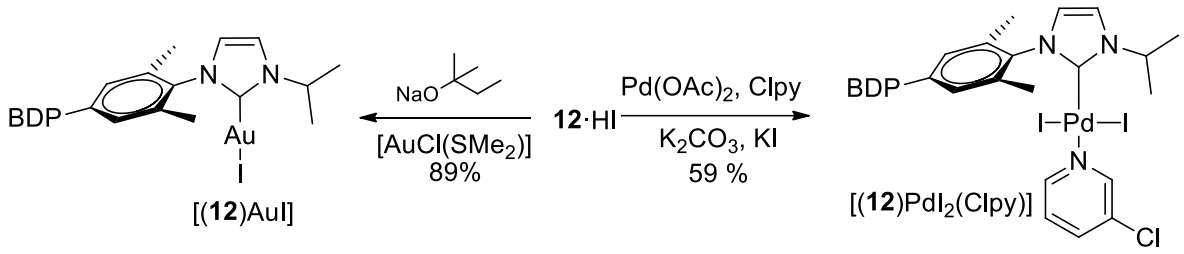

Figure 13: Synthesis of Au and Pd complexes.

3.1.4. Spectroscopic Properties of Synthesized Compounds

The absorption spectra of the new compounds are dominated by the BODIPY chromophore, displaying an intense low energy band in the 510 nm region attributed to the S_0-S_1 excitation[204] (figure 14). Absorption and emission wavelengths of the BODIPY unit in ligand **12** do not change significantly upon formation of the various metal complexes (table 1). The fluorescence properties of azolium salt **12**·HI and of the various metal complexes are summarized in table 1.[17] The fluorescence quantum yields (Φ) of complexes [(**12**)RhCl(cod)], [(**12**)RhI(cod)], [(**12**)IrCl(cod)], [(**12**)IrI(cod)] and of [(**12**)(SIMes)$RuCl_2$(ind)] were shown to be very small (table 1). The palladium complex [(**12**)PdI_2(Clpy)] is weakly fluorescent while the respective gold complex [(**12**)AuI] is characterized by an excellent fluorescence quantum yield, close to that of the azolium salt **12**·HI. Compared to a Pd^{2+} complex with a BODIPY-functionalized thiourea ligand, which displays excellent fluorescence quantum yields,[205] the modest Φ of [(**12**)PdI_2(Clpy)] was unexpected.

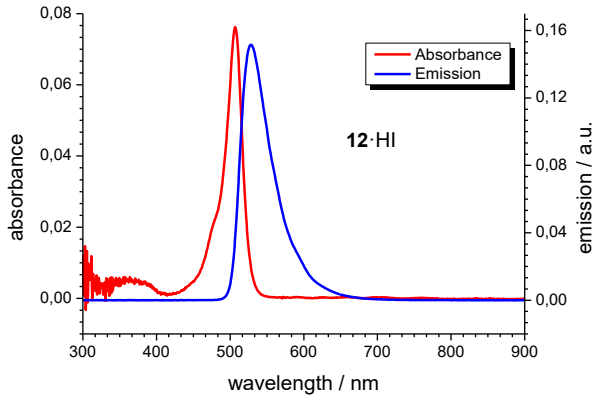

Figure 14: Absorbance (red line) and emission (blue line, λ_{exc} = 512 nm) spectra of 1 µM 1,2-dichloroethane solution of **12**·HI.

It is not clear, which quenching mechanism is primarily responsible for the low brightness of those metal complexes. Two possible mechanisms may be considered: reductive PET from electron donating transition metal to BODIPY (electron acceptor), and the heavy atom effect of the transition metal. TD-DFT calculations provide evidence that only in certain bonding situations the typical fluorescence quenching via intersystem crossing of Pd may be less important.[206] Taking in account that the quantum yields of the complexes containing heavy iodine atom are comparable to the Φ values of corresponding Cl-analogues, the mechanism of reductive PET quenching in such complexes is more likely. Based on this, a change in the electron density at the transition metal center should lead to different brightness.[207] It thus appears reasonable, that reactions leading to significant changes in the electron density at the metal center, also lead to modulated fluorescence intensity.

Compound	Φ	λ_{abs}, nm	λ_{em}, nm
12·HI	0.75	507	529
[(**12**)RhCl(cod)]	0.016	506	531
[(**12**)RhI(cod)]	0.016	506	530
[(**12**)IrCl(cod)]	0.008	506	530
[(**12**)IrI(cod)]	0.009	506	530
[(**12**)RhCl$(CO)_2$]	0.65	506	531
[(**12**)RhI$(CO)_2$]	0.53	506	531
[(**12**)IrCl$(CO)_2$]	0.63	506	531
[(**12**)IrI$(CO)_2$]	0.58	506	532
[(**12**)AuI]	0.70	506	529
[(**12**)PdI_2(Clpy)]	0.033	506	530
[(**12**)(SIMes)$RuCl_2$(ind)]	0.003	506	529

Table 1: Fluorescence quantum yields Φ, absorption maxima λ_{abs} and emission wavelength λ_{em} for azolium salt **12**·HI and the respective NHC metal complexes, determined in ethyl acetate (**12**·HI in CH_2Cl_2) vs. rhodamine 6G (Φ_{st} = 0.95 in EtOH).

3.1.5. Reaction of cod-Complexes with Carbon Monoxide

The well-known ligand exchange involving 1,5-cyclooctadiene (cod) in [(**12**)MX(cod)] (M= Rh, Ir; X= Cl, I) with carbon monoxide generates [(**12**)MX$(CO)_2$] (M= Rh, Ir; X= Cl, I) in virtually quantitative yield.[179] In the present context, this reaction converts weakly fluorescent [(**12**)MX(cod)] complexes into strongly fluorescent [(**12**)MX$(CO)_2$] (table 1) – despite the presence of 4d (Rh) or 5d (Ir) transition metals and halogeno ligands.[208–212] Replacing an electron-rich ligand (cod) by an electron-deficient ligand (CO) converts the fluorescence quenched complexes into complexes with excellent brightness. Such ligand exchange reactions have the potential to lead to fluorescent CO probes. For the synthesized complexes, the exchange of cod by CO is essentially irreversible and even in the presence of a massive excess of cod (10^5 fold), no decrease in the fluorescence was observed. Consequently, the Ir and Rh complexes appear to be efficient molecular probes for CO[213]. The ratio of the fluorescence quantum yields of the respective cod and carbonyl complexes show excellent turn-on-ratios, which also depend on the nature of the solvents employed (table 2). Ethyl acetate was found to be a convenient solvent for such studies with excellent fluorescence attenuation Φ([(**12**)IrCl$(CO)_2$])/Φ([(**12**)IrCl(cod)]) = 80.

Solvent	Dipole moment	[(**12**)RhI(cod)]			[(**12**)RhI$(CO)_2$]		
		Φ	λ_{abs}, nm	λ_{em}, nm	Φ	λ_{abs}, nm	λ_{em}, nm
Acetonitrile	3.92	0.017	504	529	0.13	504	530
1,2-Dichloroethane	1.8	0.011	509	532	0.57	509	534
1,4-Dioxane	0.45	0.033	508	533	0.50	508	533
Tetrahydrofuran	1.63	0.011	508	532	0.53	508	534
Toluene	0.36	0.11	512	535	0.55	512	535
Ethyl acetate	1.78	0.016	506	530	0.53	506	531

Table 2: Fluorescence quantum yields Φ, absorption maxima λ_{abs} and emission wavelength λ_{em} for the [(**12**)RhI(cod)] and [(**12**)RhI$(CO)_2$] in different solvents.

Evidence for the relationship between the electron density at the transition metal and Φ comes from the respective metal-centered redox potential of the [(**12**)MX$(CO)_2$] complexes, which were determined by cyclic voltammetry. The Rh^I/Rh^{II} redox potential in [(**12**)RhI(cod)] ($E_{1/2}$= 0.84 V) and that of the BODIPY unit in [(**12**)RhI(cod)] ($E_{1/2}$= 1.19 V) were found to be in the normal range.[214] Oxidation of the carbonyl complexes was found to be irreversible in the CV experiment; only an oxidation wave was observed. However, even in the absence of a reduction wave (probably, due to the dissociation of CO from Rh^{II} complex), the oxidation

half-wave is still a good indicator of the Rh or Ir electron density in the respective carbonyl complexes. The half wave oxidation potential of [(**12**)RhI(CO)$_2$] ($E_{ox}(Rh^{I}/Rh^{II})$ = 1.39 V) is ca. 500 mV more anodic than the corresponding half wave potential in [(**12**)RhI(cod)]. This firmly establishes the electron-deficient nature of the metals in the carbonyl complexes.

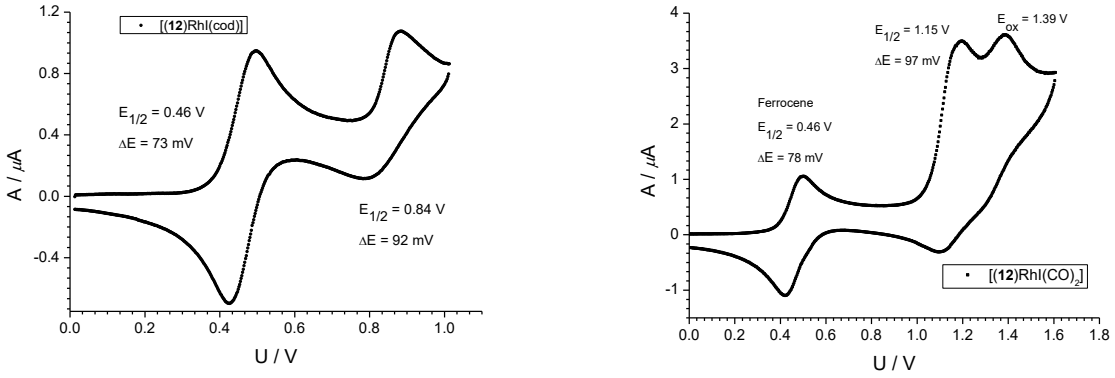

Figure 15: Cyclic voltammogram of [(**12**)RhI(cod)] (left) and [(**12**)RhI(CO)$_2$] (right).

The apparent dependence of Φ on the electron density at the transition metal provides evidence for a significant contribution of the PET quenching mechanism. Somewhat unexpectedly, both the chloro and the iodo complexes with Rh and Ir show approx. the same Φ (table 1). This again provides evidence, that intersystem crossing involving the iodo ligand or the metal, does not seem to play a prominent role for fluorescence quenching in the Rh and Ir complexes reported here. The relationship between the electron density (rather the energy of the HOMO) of a quencher and the fluorescence quantum yield was established by Nagano et al. for organic fluorophores with appended quenchers,[215] but this has not been demonstrated before for transition metal centers.

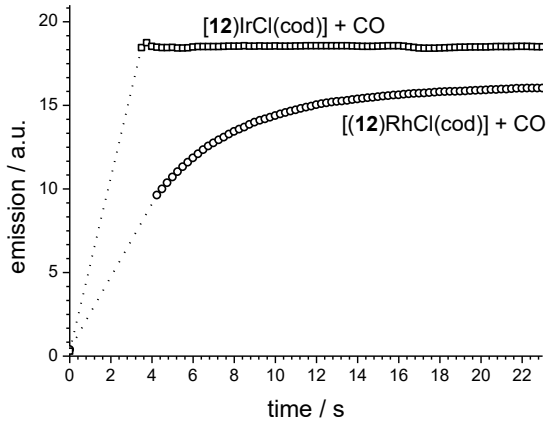

Figure 16: Fluorescence – time traces for the reaction of [(**12**)MCl(cod)] (M= Rh, Ir) (c= 2.0·10^{-6} mol·L^{-1} in ethyl acetate, 298K) with 10 equiv. of CO (c= 2.0·10^{-5} mol·L^{-1}, 9.0·10^{-8} mol).

The reaction rate of [(**12**)MX(cod)] with carbon monoxide is an important parameter concerning the potential use of such complexes for CO detection. Solutions of complexes [(**12**)RhCl(cod)] and [(**12**)IrCl(cod)] (c= 2.0·10^{-6} mol·L^{-1}) in ethyl acetate were exposed to ten equivalents of carbon monoxide (figure 16). Even at such low concentrations, the ligand exchange reaction is complete within a few seconds. In conducted experiments the first reliable fluorescence intensity was measured after ca. 4 s. Already at this point, the conversion of [(**12**)IrCl(cod)] to [(**12**)IrCl(CO)$_2$] is virtually finished (> 98% of the final fluorescence intensity), while it takes the related Rh complex approx. 20 s to reach the same level of fluorescence. The nature of the halogeno ligand (chloro, iodo) does not have a significant influence on the rate of CO incorporation. With respect to two very important parameters for

CO detection, i. e. fluorescence enhancement and the rate of the fluorogenic reaction, the iridium complexes are superior to the previously reported CO probes.[165]

The fast response of the Ir complexes to small volumes of CO is demonstrated on figure 17. In standard cuvettes, the addition of less than 1 nanomole of CO leads to a detectable change in the fluorescence intensity. Upon addition of six portions of 0.6(±0.2) µl each to a solution of [(**12**)IrCl(cod)] (c= 1.0 ·10^{-5} mol·L^{-1}), an instant increase in the fluorescence intensity to a higher plateau is observed. It should be noted, that all experiments were carried out in standard solvents under ambient atmosphere.

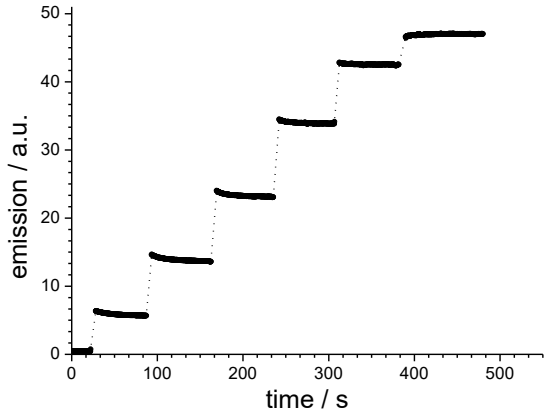

Figure 17: Fluorescence – time trace for the addition of six times 0.6(±0.2) µl of CO to a solution of [(**12**)IrCl(cod)] (c=1.0·10^{-5} mol·L^{-1} in ethyl acetate); final addition leads to full fluorescence intensity.

The reactions of solutions of [(**12**)IrCl(cod)] with atmospheric air to which defined amounts of CO had been added, were also studied, to learn more about the tolerance of the chemodosimeter to impurities contained in air. It can be seen (figure 18), that the final level of fluorescence is proportional to the amount of CO in the sample and that the response is the same as in the clean samples, even though the reaction time is significantly extended due to the slow phase transfer of CO from gas to the solution.

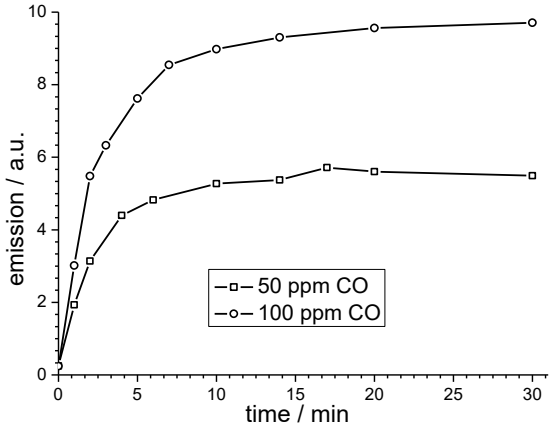

Figure 18: Emission-time plots for [(**12**)IrCl(cod)] (c= 1.0·10^{-5} mol·L^{-1}) in ethyl acetate exposed to atmospheric air containing 50 or 100 ppm of CO.

The newly developed complexes thus fulfill the basic requirements for use as a carbon monoxide sensor.

Based on this, the development of a water-soluble version of the Ir complex for *in vivo* studies appears to be an attractive target.[31] With the aim to study the possibility of application of triethylene glycol complexes [(**13**)MI(cod)] as a water-soluble intracellular CO probes, first, quantum yields of [(**13**)MI(cod)] and [(**13**)MI($CO)_2$] (M=Ir, Rh) in ethyl acetate were

determined. As expected, these complexes have similar fluorescence properties to the respective *i*Pr-analogues. However, all attempts to record fluorescence spectra of good quality during quantum yield measurements in water failed because of high intensity of scattered light overlapping the emission spectra of complexes. This can be due to the insufficient water solubility of the complexes, leading to the formation of colloidal solutions. To overcome the solubility problem, similar measurements in the water-DMSO mixture were conducted. To our surprise, higher emission levels of carbonyl complexes were not observed.

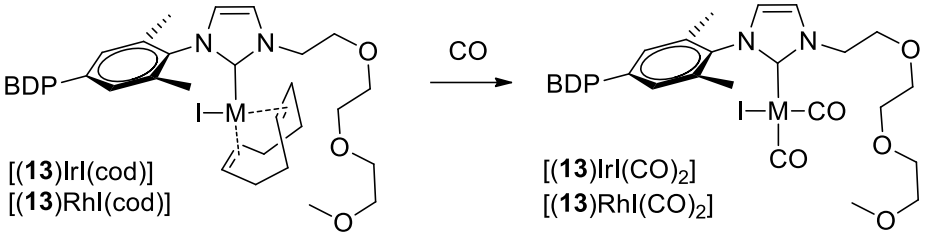

Figure 19: Potential CO molecular probes with increased water solubility.

The newly developed complexes were investigated for potential application as intracellular fluorescent CO probes. *In vivo* studies, carried out in cooperation with Prof. Dr. Stefan H. Heinemann (Friedrich Schiller University Jena), showed that these complexes have a low fluorescence response and relatively high cytotoxicity when used in the biological environment. One possible reason for the low increase in emission upon the reaction with CO is solvent effect. Thus, complex [(**12**)RhI(CO)$_2$] showed significantly lower quantum yield in acetonitrile, compared to other tested organic solvents. This can be explained by highly efficient non-radiative relaxation of S_1 in the polar solvent. Water, being more polar, can suppress the emission of carbonyl complex even better. Additionally, the ability to form hydrogen bonds with CO ligands can reduce its dissociation energy, and might lead to the efficient dissociation of CO molecules with the formation of quenched decomposition products.

3.1.6. Reaction of BODIPY-tagged Gold Complex with Thiols

In order to strengthen the hypothesis that increasing/decreasing electron density at the transition metal leads to quenching/unquenching of the BODIPY fluorescence, the fluorescence intensity during the reaction of complex [(**12**)AuI] with dodecanethiol (RSH) to [(**12**)AuSR] was studied. [(**12**)AuI] is characterized by an excellent fluorescence quantum yield of Φ=0.70. However, the coordination of a highly electron-rich thiolato ligand instead of the halogeno ligand should lead to a significant increase in the electron density at gold. The addition of 1-dodecanthiol to [(**12**)AuI] leads to a small drop in the brightness (figure 19), which (in the absence of added base) is probably due to the partial formation a gold-thiolate complex. After addition of the base Et_3N, a more pronounced drop in the fluorescence intensity is observed, which is due to the complete formation of the gold-thiolate complex. This translates into a decreased brightness of the fluorophore.

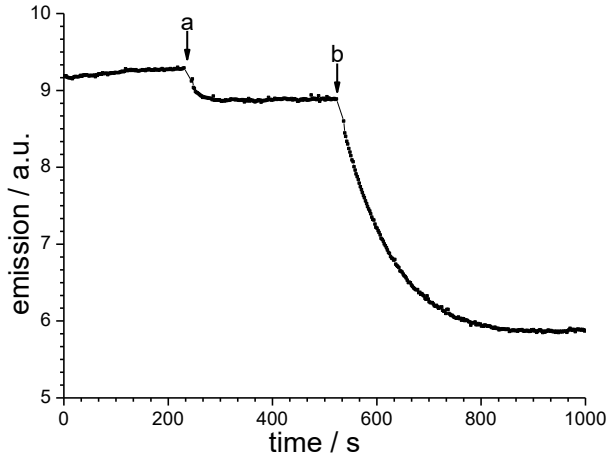

Figure 19: Fluorescence – time trace for the reaction of [(**12**)AuI] ($1.0 \cdot 10^{-6}$ mol·L^{-1}) with 1-dodecanethiol ($2.5 \cdot 10^{-4}$ mol·L^{-1}) and triethylamine ($2.5 \cdot 10^{-4}$ mol·L^{-1}) in 1,2-dichloroethane at 303K. Addition of 1-dodecanethiol (arrow a) and addition of triethylamine (arrow b).

To demonstrate, that this decrease is not due to the presence of Et_3N, the order of addition of the reagents was inverted. Indeed, when Et_3N was added first only a negligible change in the fluorescence intensity is observed (figure 20) confirming that the formation of the Au-thiolato complex is responsible for the drop in the fluorescence level. The observed relationship between fluorescence brightness and electron density at the transition metal is in accord with a major quenching pathway via the established PET mechanism.

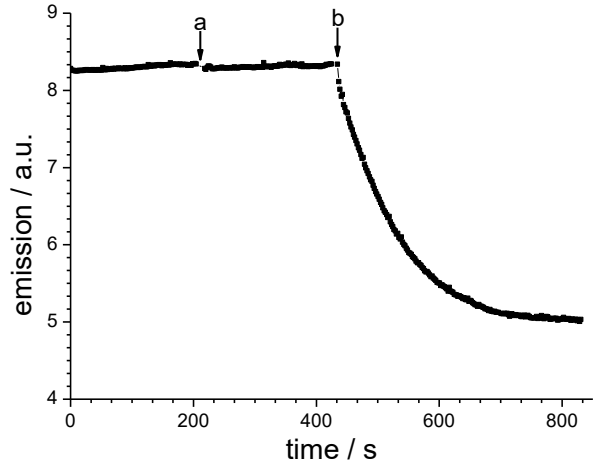

Figure 20: Emission-time plot for the reaction of [(**12**)AuI] (1.0·10-6 mol·L-1) with 1-dodecanethiol ($2.5 \cdot 10^{-4}$ mol·L^{-1}) and triethylamine ($2.5 \cdot 10^{-4}$ mol·L^{-1}) in 1,2-dichloroethane at 303K (excitation wavelength 506 nm). Addition of triethylamine (arrow a) and addition of 1-dodecanethiol (arrow b).

3.1.7. Trace Determination of Catalytic Metal Complexes

Another potentially attractive feature of BODIPY-tagged transition metal catalysts is the detection of minute amounts of the residual complex in the "purified" products of the catalytic transformation. The contamination of products from a homogeneously catalyzed reaction with transition metals is undesirable and strict limits for acceptable metal residues apply.[216] The quantification of trace metal residues is often based on expensive techniques such as ICP-OES. In the case of non-quenched NHC-BODIPY tagged metal complexes, like [(**12**)AuI], the simple evaluation of the fluorescence intensity enables the quantification of trace metal impurities. This is of course only valid under the reasonable assumption of stable NHC-metal bonds during and after the catalytic transformation, which may not apply to all catalytically active complexes. However, NHC ligands are well known for the formation of stable NHC-metal

complexes. The detection limit for this gold complex (in the absence of 531 nm fluorescent impurities) was determined. Concentrations of the NHC-Au complex of down to at least $1 \cdot 10^{-9}$ mol·L^{-1} can be quantified, which is well below the tolerable limits for heavy metal residues in various applications.

3.2. BODIPY-tagged *N*-Heterocyclic Carbene Complexes as Fluorescent Hydrogen Chemodosimeters

3.2.1. Sensors for Molecular Hydrogen

Hydrogen is a colorless, odorless and tasteless gas. The reaction of hydrogen with oxygen is highly exothermic with low ignition energy and wide explosion concentrations range. This poses risks when handling hydrogen, but also offers chances in energy production under controlled reaction conditions. With a view to the dwindling resources of fossil fuels and excessive CO_2 emissions, hydrogen gas utilization is an ideal way to solve the energy shortage in the near days.

In addition, hydrogen has been widely applied in various areas, e.g., industrial fabrication process, medical procedures, laboratories, and energy carrier on vehicles. Increased use of hydrogen in energy production will inevitably create demand for hydrogen sensing, to properly address safety issues. Other applications for hydrogen sensing concern the food industry,[217] the detection of certain bacteria,[218] diagnostics for lactose intolerance[219] or hydrogen-metabolizing organisms.[220]

Numerous types of hydrogen sensors are currently utilized in hydrogen-powered transport, fire alarms, process and flue gas analyzers and leakage detectors. These methods are based on several mechanisms, including traditional GC, MS, laser gas analysis and thermal conductivity. Modern hydrogen sensors include hydrogen-specific palladium-based, metal oxide and catalytic bead, electrochemical-based, surface acoustic wave and micro resonance-based sensors.

Thermal conductivity is the most widely applied measuring method for the determination of hydrogen. Normally thermal conductivity devices require high operating temperatures and the presence of oxygen, resulting in lower hydrogen detection limit around 50 ppm. Gas chromatography has long response times, is expensive, and requires well trained personal. An advantage, however, is the ability to measure other gases in the presence of hydrogen. Mass spectrometers show higher selectivity and sensitivity but are even more expensive. A laser gas analyzer is based on the absorption of laser light by molecular hydrogen, which re-emits light at a different frequency. The intensity of light observed at various shifted frequencies is directly proportional to the concentration of hydrogen in the measured gas mixture.[221]

There are different types of palladium-based hydrogen sensors. The most popular class of sensors is based on palladium resistors. A thin film of palladium deposited between two metal contacts shows a change in conductivity on exposure to hydrogen due to the phase transition in palladium. Such sensors can detect as low concentrations of hydrogen as 0.5% and are cheap to produce, but often require high operating temperatures and high power. The palladium field-effect transistors or capacitors contain a thin film of palladium on the semiconductor surface. Absorption and further dissociation of molecules of hydrogen cause a change in the electronic properties of the device, which causes a voltage shift in the capacitance versus voltage curve. These sensors have fast response time, but are cross-sensitive to oxygen, and to gases such as acetylene, that can dissociatively adsorb and form atomic hydrogen at the surface.[221]

Another type of palladium sensors includes optical sensors[222,223] consisting of a layer of palladium coated on an optically active material that transforms the hydrogen concentration to an optical signal. The absorption of hydrogen changes the refractive index of the palladium coating. Another approach is a palladium micromirror on the cleaved end of the optic fiber. Hydrogen changes the reflection properties of such mirror and the H_2 concentration is calculated from the detected changes in the back reflected light.[221]

Well-developed are sensors utilizing the changes in the resistance of palladium nanoparticles (nanocubes, mesowires etc.) deposited on the surface.[224,225] Cheap alternative to the palladium-based resistance is metal oxide sensors. At elevated temperatures hydrogen reacts with the surface of oxide or with absorbed oxygen. Such oxidation reaction produces an electron in the body of semiconductor (metal oxide), leading to detectable changes in conductivity.[226,227] These devices have very fast response times and a broad gas detection capability, but they have high power consumption, work at high temperatures and are not selective to hydrogen.[221]

Electrochemical hydrogen sensors detect changes in current generated by the electrochemical reaction of H_2. Their advantages are low power, high sensitivity, and good selectivity, but have a limited temperature range of operation and can be easy contaminated by some other gases.[221]

Electrical sensors offer the potential of spark-induced explosions, often have high energy consumption and require sophisticated equipment, furthermore, miniaturization is limited. While the small electrical devices for hydrogen sensing are well developed, there is no progress in the development of simple chemical hydrogen detection assays. Simple probes which give fluorescence or colorimetric response on hydrogen what can be detected by “naked eye” are desired, but fluorescent molecular probes for hydrogen have so far not been reported. The US-based company “Element One, inc.”[228] produces hydrogen-sensing products, in which a Pd-catalyzed reaction of tungsten trioxide with hydrogen is exploited. Their visual hydrogen gas indicators use thin films or nanoparticles of the tungsten oxide. A typical thin film indicator consists of a transparent polymer substrate, a 500 nm thick layer of nanoporous tungsten oxide, a 3 nm layer of a palladium catalyst, and a 100 nm thick protective coating. In the presence of H_2 such film reversibly changes its color from light gray to black due to the reduction of WO_3 to a mixture of compounds with tungsten in lower oxidation states. Using this technology the company produces indicating paints and specialty coatings, inks, marking pens, indicating tapes, etc.[229]

Despite the increased demand for new sensing technologies for hydrogen detection, no fluorescent probes for molecular hydrogen were reported for today. Applications of known small electric devices for H_2 sensing have numerous drawbacks, like high operational temperatures and low energy efficiency, relatively high detection limits, and often long response times. Efficient and easily available fluorescent probe would be a great alternative. The most complicated problem in the development of H_2 sensor is to design its receptor part. The most prominent approach is to exploit the ability of molecular hydrogen to form hydride complexes with various transition metals through the oxidative addition reaction. Such reaction changes the oxidation state of metal, leading to the changes in electron density. Similarly to the described CO-probes, these changes should alter the ability of a metal to quench the fluorescence of reporting part of the molecule.

Iridium-based Crabtree type complexes are amongst the most popular catalysts[230] for asymmetric hydrogenation reactions.[231–233] The oxidative addition of H_2 to a transition metal often is the first step in such reactions and formally converts an electron-rich Ir^{I} to an electron-deficient Ir^{III}. It is very attractive to exploit this transformation for the design of

fluorescent molecular probe for hydrogen detection, where the oxidation of Ir would trigger the increase in fluorescence of BODIPY. A very important property of Crabtree type complexes is the lack of reactivity towards oxygen or water. It was decided to design BODIPY-labeled complex which would combine excellent stability and catalytic activity of SIMes-based Crabtree complexes with the ability to produce fluorescence response in the presence of hydrogen. For this, the ideal choice would be to develop a synthetic route towards BODIPY-tagged SIMes ligand, in which fluorophore moiety is separated from the carbene by an alkyl chain to minimize its influence on the electronic and steric properties of carbene.

3.2.2. Synthesis of Ligand

The synthesis of the SIMes ligand analog with an appended BODIPY fluorophore is outlined in figure 21. Diamine **14** was synthesized in three steps from oxalyl chloride, mesityl aniline, and 4-bromo-2,6-dimethylaniline according to the procedure, described by Xu and Gilbertson.[234] Trimethylsilylacetylene is Sonogashira coupled to monobromo *N*,*N*'-diaryldiamine **14**,[235] followed by the removal of the trimethylsilyl-protective group with TBAF, which provides acetylene **15**. The acetylene is formed in excellent yield and high purity, and was used in the next step without further purification. Another Sonogashira reaction with iodo-BODIPY provides the fluorophore-tagged dark-purple diamine **16** in moderate yield. All attempts to improve the yield by application of another Pd catalyst ($Pd(PPh_3)_4$), phosphine ligands, loading of catalyst, other solvent or mixture of solvents, reaction time, and temperature, resulted in the same or even lower yields.

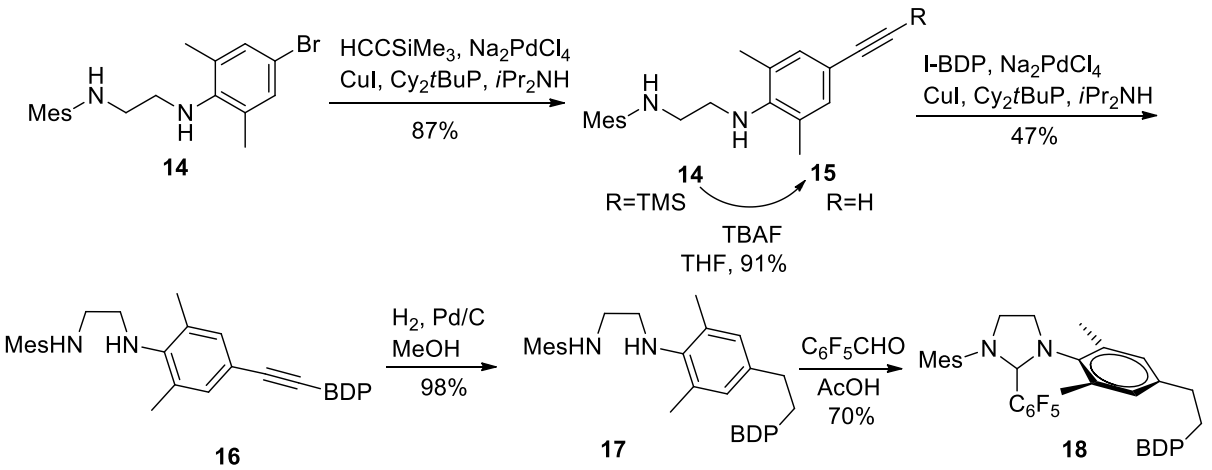

Figure 21: Synthesis NHC precursor 18.

Hydrogenation of the alkyne group gives bright orange diamine **17**, in which the fluorophore is electronically decoupled from the potential metal coordinating site. The cyclization of the diamine with C_6F_5CHO provides imidazolidine **18**. This compound is a useful NHC transfer reagent, which generates carbene at elevated temperatures and is widely used for the synthesis of NHC-transition metal complexes.[236]

3.2.3. Synthesis of Complexes

The main advantage in the application of 2-(Pentafluorophenyl)imidazolidine **18** over the corresponding imidazolinium salt is its ability to generate the carbene thermally in the absence of a base. This is crucial for the synthesis of complexes containing base-sensitive groups like BODIPY. Heating of toluene solution of **18** and $[IrCl(cod)]_2$ in a sealed flask at 343 K for 2 h provides complex **19** in 89% yield (figure 22). Exchange of the chloride by triflate anion using AgOTf in CH_2Cl_2 in the presence of pyridine provides "cationic" complex **20b** in nearly quantitative yield. Earlier it was shown that catalytic activity and stability of Crabtree complexes are strongly related to the coordination ability of counter anion.[231] With

the aim to study the activity of synthesized BODIPY-tagged complexes in hydrogenation, a complex with the BArF counter anion was obtained. Both TfO^- and $BArF^-$ readily replace chloride at room temperature and simple filtration through the thin pad of celite provides the target cationic complexes in excellent yields.

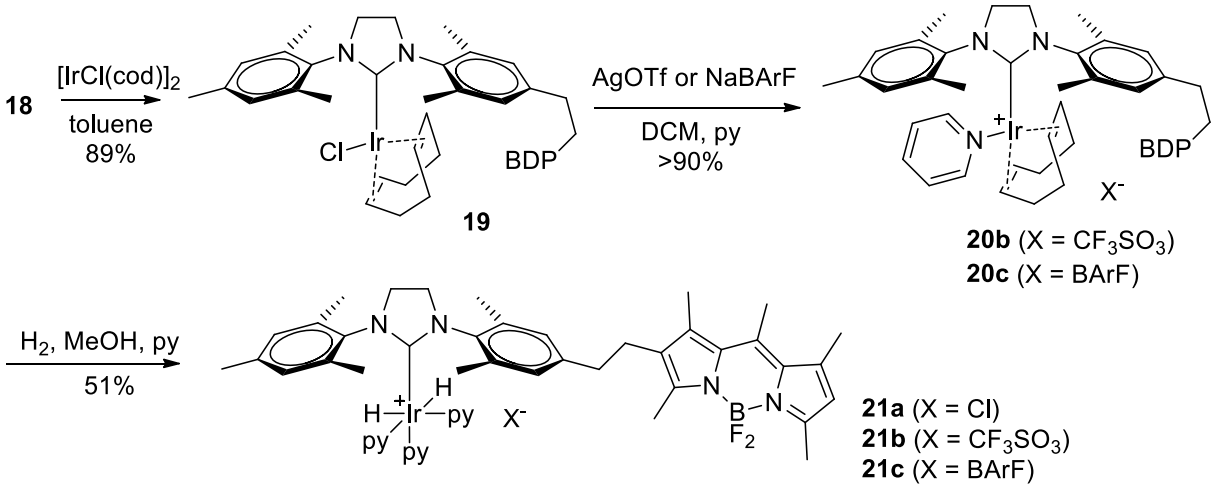

Figure 22: Synthesis of BODIPY-tagged Crabtree-type complexes.

A methanol solution containing complexes **20** and 100 equiv. of pyridine reacts with hydrogen, to form the respective cationic dihydride complexes **21** within a few minutes. The triflate complex **20b** was isolated and characterized, but is somewhat prone to decomposition in solution. Complex **20b** displays the characteristic hydride signal at δ -22.4 ppm. The same highly characteristic hydride shift was observed for closely related complex $[(IMes)Ir(H)_2(py)_3]^+Cl^-$ (δ -22.5 ppm), which was synthesized by Duckett et al. and used in NMR hyperpolarization experiments.[237]

3.2.4. Spectroscopic Properties

The fluorescence properties of the BODIPY containing compounds **16** – **21** were studied and all found to absorb and emit in a narrow range close to λ_{max}(exc)= 510 nm and λ_{max}(em)= 524 nm, except for diamine **16**, absorbance of which is shifted to longer wavelengths and emission is strongly quenched (table 3). The Ir(I) complexes **20** and **19** are weakly fluorescent (fluorescence quantum yields Φ(**19**) = 0.022, Φ(**20b**) = 0.038) and hydride complex **21b** is strongly fluorescent (Φ(**21b**) = 0.51). To compare the fluorescence of **21b** to **20b**, absorbance and emission spectra were recorded in pyridine due to the low stability of former in noncoordinating solvents.

Compound	Φ	λ_{abs}, nm	λ_{em}, nm
17	0.11	510	522
18	0.59	510	523
19	0.022	509	523
20b	0.049	511	525
20c	0.038	509	523
21b	0.51	511	523

Table 3: Fluorescence quantum yields Φ, absorption maxima λ_{abs} and emission wavelength λ_{em} for imidazolidine **17** and the respective NHC Ir complexes, determined in 1,2-dichloroethane (**17**, **18**, **19**, **20c**) and pyridine (**20b**, **21b**) vs. rhodamine 6G (Φ_{st} = 0.95 in EtOH).

In the course of the reactions of methanol solutions of **19**, **20b** or **20c** with hydrogen, a very pronounced increase in the fluorescence intensity was observed (figure 23). This increase in brightness denotes the formation of the respective Ir^{III} complex **21** following the oxidative addition of H_2. This reaction is independent of the nature of the anion and appears to be

complete within a few minutes. However, this is true only for weakly coordinating anions such as TfO^- and $BArF^-$, and the final intensity of fluorescence in the reaction of **19** with hydrogen is strongly dependent on the nature of the solvent, the amount of pyridine, temperature, ect.. The electron-deficient cationic Ir complex is also able to coordinate CO, and at 1000 ppm a CO complex is observed with fluorescence comparable to that of the hydride complex.

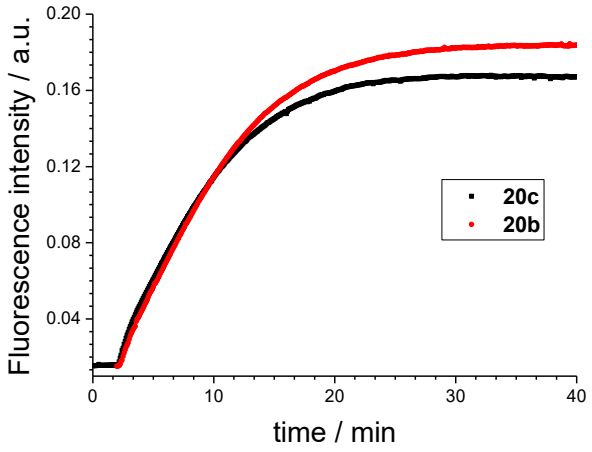

Figure 23: Emission–time plots for the reaction of **20b** (red) and **20c** (black; $1.0 \cdot 10^{-6}$ mol·L^{-1}) in methanol containing pyridine ($1.0 \cdot 10^{-4}$ mol·L^{-1}) with hydrogen.

3.2.5. Paper Strip Detection of Hydrogen

In order to demonstrate the hydrogen sensing properties of the iridium complexes, a simple paper strip method was employed. A filter paper was impregnated with a solution of **20b** in propylene carbonate (b.p. 242 °C) (c= 10^{-3} mol/L). Due to the high polarity of this solvent and its high boiling point, a solution of complex **20b** in propylene carbonate is highly stable under ambient atmosphere and the fluorescence of the paper strip does not change in the presence of ambient air. One of the paper strips was exposed to an atmosphere of pure hydrogen. Within a few minutes the highly fluorescent Ir^{III} complex is generated (figure 24). Using this simple filter paper assay, it is possible to detect hydrogen at a concentration corresponding to the lower explosion limit (4% vol) and to distinguish this from a lower hydrogen concentration (1% vol). In this experiment, all four paper strips were exposed to the atmosphere of H_2 mixture for 10 min. The time of exposure plays a crucial role here since at longer exposure time the difference in fluorescence of different paper strips is not so pronounced.

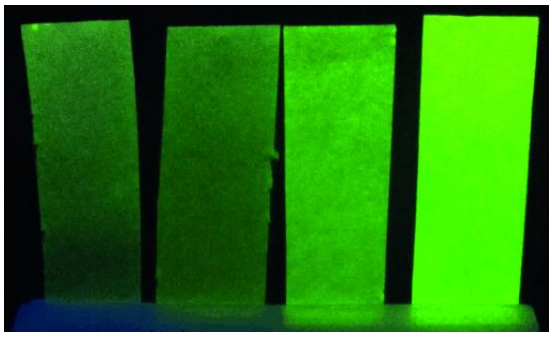

Figure 24: Four filter paper strips (left to right: a–d) impregnated with a solution of **20b** in propylene carbonate and irradiated with broadband UV light. Strip (a) exposed to ambient air; strip (b) exposed to 1 % (vol) H_2; strip (c) exposed to 4 % (vol) H_2 (lower explosion limit), and strip (d) exposed to pure H_2.

3.2.6. Catalytic Activity

Next the catalytic properties of the new iridium complexes were studied. Catalytic studies were limited to **20b** and **20c** containing weakly coordinating anions, because coordinating anions are detrimental for substrate conversion.[238] The reactions with hydrogen were carried out in 1,2-dichloroethane solvent, since the donor solvents used for the hydrogen sensing experiments are known to inhibit olefin hydrogenation, probably by impeding coordination of the olefin. The room temperature reaction of the test substrates allylbenzene with hydrogen employing **20c** provides the fully hydrogenated product within 10 min in nearly quantitative yield at 0.5 mol% catalyst loading (figure 25).

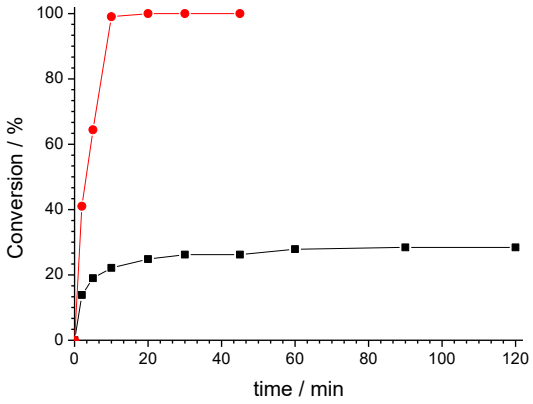

Figure 25: Conversion-time plot for the catalytic hydrogenation of 0.1 mol·L^{-1} allylbenzene by **20c** (1.0·10^{-3} mol·L^{-1}, 1 mol %) (red) and 0.002 mol·L^{-1} allylbenzene by **20c** (1.0·10^{-5} mol·L^{-1}, 0.5 mol %) (black) in 1,2-dichloroethane with H_2.

Next, the time-dependent fluorescence intensity of **20b** and **20c** during the catalytic hydrogenation reaction with H_2 and allylbenzene in 1,2-dichloroethane solvent was monitored. For this reaction a lower catalyst loading (0.1 mol %) and a much lower concentration of **20b** (1.0 · 10^{-6} mol·L^{-1}) was chosen, to ensure that the catalyst is fully consumed during the catalytic reaction. Consequently, only a ca. 30% conversion of allylbenzene into the hydrogenation product propylbenzene was observed (figure 25). The catalytic reaction with hydrogen and olefin is characterized by a pronounced increase in the fluorescence intensity (figure 26). However, the final level of fluorescence in 1,2-dichloroethane is lower than that observed in MeOH/pyridine (figure 23), indicating the formation of an Ir^{III} species different from complex **21**. This is not surprising as it is known, that in nonpolar solvents in the absence of the stabilizing cod ligand and after consuming the olefins in the hydrogenation reaction, trimeric[239,240] as well as higher nuclearity iridium-hydride clusters are formed.[241] A hydrogenation experiment carried out in the NMR tube using **20c** and allylbenzene shows the formation of numerous iridium-hydride species as evidenced by a large number of ^{1}H NMR resonances in the range 0 to -30 ppm, thus confirming findings by Brown et al. for related complexes.

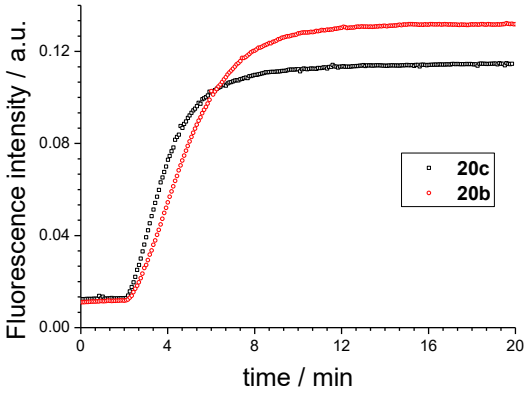

Figure 26: Emission–time plots for the reaction of **20b** (red) and **20c** (black; $1.0 \cdot 10^{-6}$ mol·L^{-1}) in 1,2-dichloroethane with H_2 (fluorescence gain 11.7 and 9). Excitation wavelength – 510 nm.

The time-dependent fluorescence intensity of the BODIPY was monitored during the catalytic conversion of different substrates (allylbenzene, styrene, cyclohexene, α-terpinene). The increase of the fluorescence intensity during these reactions is virtually the same as observed for the iridium dihydride complex in 1,2-dichloroethane in the absence of olefinic substrate (figure 27). One interpretation is that the steps in the catalytic cycle following the oxidative addition of hydrogen do not lead to significant changes in the fluorescence intensity of the iridium complex. With a view to the high sensitivity of the fluorescence intensity to modulated electron density, we consider this to be unlikely. The similar fluorescence intensities are more easily explained by assuming, that the iridium dihydride species is the dominant ones in the catalytic reaction. Accordingly, a dihydride complex appears to be the resting state of the catalytic reaction, as was suggested before.[242,243] Notably, the formation of the iridium-dihydride species occurs faster than substrate conversion. In a separate experiment at 0.1 mol % catalyst loading, the full conversion of the substrate requires about 10 min (figure 25), while the final level of fluorescence is reached within approximately 4 min. It is, therefore, unlikely, that the fluorescent product observed, is the decomposition product of the catalyst following substrate conversion.

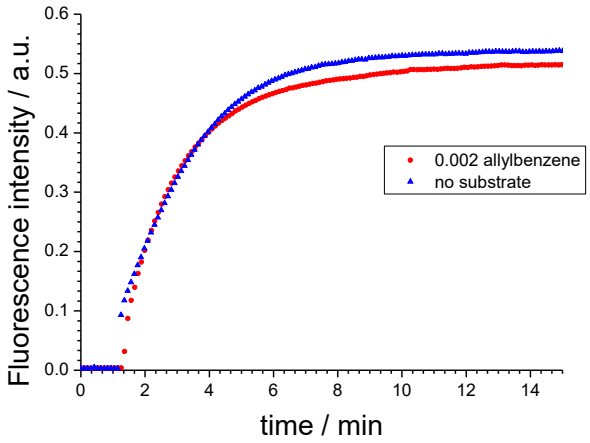

Figure 27: Emission–time plot for the catalytic hydrogenation of 0.1 mol·L^{-1} allylbenzene with **20b** (red; $1.0 \cdot 10^{-5}$ mol·L^{-1}) in 1,2-dichloroethane; same reaction conditions, but without olefin (blue).

3.3. Synthesis and Applications of BODIPY-Labeled Metathesis Catalysts

3.3.1. Olefin Metathesis

Olefin metathesis has become a powerful tool for the formation of carbon-carbon double bonds. The reaction started as an industrial heterogeneous high-temperature processes and is now an efficient laboratory and industrial method for the synthesis of pharmaceuticals,[244,245] polymers,[246] and natural products.[247] First developed[248] Mo and W-based carbene complexes are characterized by high activity, but their extreme sensitivity towards oxygen, water, and different functional groups strongly limited their applications. The development of ruthenium-based carbene complexes by Grubbs[249] further popularized this reaction. An important improvement was reported by Hoveyda,[250] who replaced benzylidene and phosphine ligands in Grubbs catalyst by bidentate benzylidene ether ligand (figure 28). These complexes are amongst the most popular metathesis catalysts due to their thermal stability, as well as moisture, and oxygen tolerance.

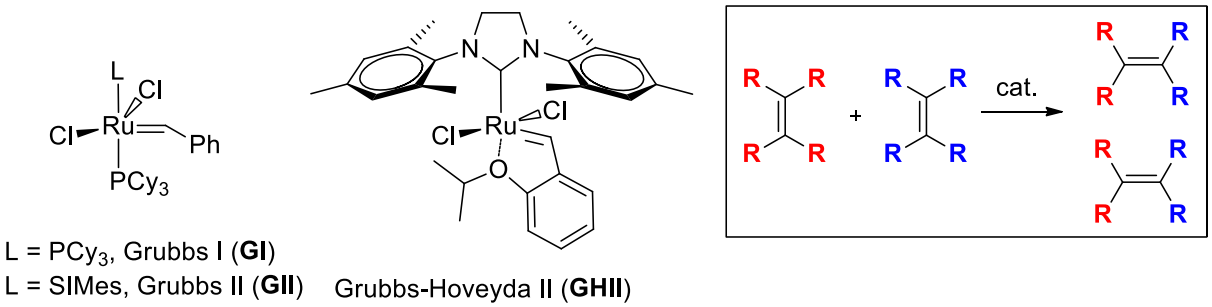

L = PCy_3, Grubbs I (**GI**)
L = SIMes, Grubbs II (**GII**) Grubbs-Hoveyda II (**GHII**)

Figure 28: Left: examples of Ru-based metathesis catalysts; right: general reaction scheme.

Metathesis reactions involve an apparent interchange of groups around two double bonds which results in the new olefin constructed from two halves of reacted alkenes. Depending on the nature of the olefins, and the type of the product formed, there are six main classes of metathesis reaction (figure 29). Cross metathesis (CM) is the simplest example, where two olefins exchange substituents. Substrates containing two linked double bonds can form new cyclic olefin (Ring-Closing Metathesis, RCM) or polymer (Acyclic Diene Metathesis, ADMET), depending on the nature of the linker, the size of the formed cycle, catalyst or reaction conditions. An example of the opposite reaction to the ADMET is an ethenolysis – a reaction of polymers with ethylene with the formation of lower molecular weight products. Strained cyclic olefins (norbornene, cyclopentadiene, cyclooctadiene etc.) readily form polymeric olefins in the presence of metathesis catalyst (Ring Opening Metathesis Polymerization, ROMP). Variation of RCM where one of the double bonds is replaced by a triple bond called Enyne metathesis (EYM).

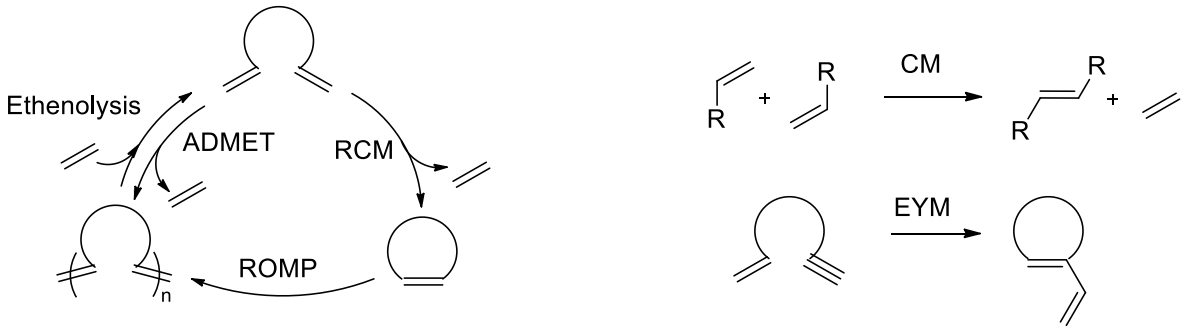

Figure 29: Types of olefin metathesis.

According to the accepted mechanism, proposed by Chauvin and Herrissón,[251] the reaction proceeds through a coordination of olefin to the alkylidene (M=C) species resulting in a π-complex, which undergoes rearrangement into metallacyclobutane. Latter can then undergo cycloreversion to produce a new olefin product through the formation of another π-complex (figure 30).

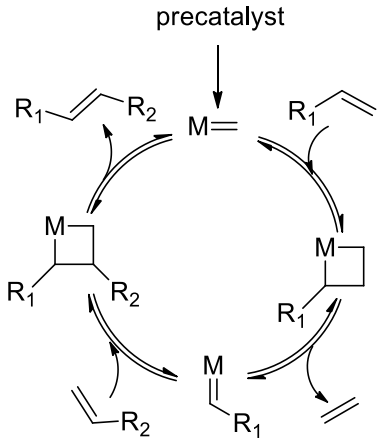

Figure 30: Mechanism of olefin metathesis proposed by Chauvin.

A detailed understanding of each step of this mechanism and of how the catalyst's structure influences the rate of each step and the stability of species involved in the catalytic cycle, can lead to the development of new more efficient complexes.

3.3.2. Single-Molecule Observation of ROMP

Single molecule fluorescent microscopy (SMFM) has become a powerful tool for investigating biophysical and chemical processes in molecular biology over the last two decades. Only recently this powerful imaging technique, with unique high spatial (submicrometers) and temporal (milliseconds) resolution, was used to reveal mechanisms of "classical" organic reactions, heterogeneous catalysis and supramolecular interactions.[252] In 2007, Kiel and coworkers[192] used SMFM to localize individual probes and to study the kinetics of association and dissociation of Cu^{2+} ion with the surface-immobilized dye-ligand conjugate. Similarly, the Blum research group reported[205,253–255] the application of SMFM for imaging the coordination of BODIPY-tagged Pt and Pd complex to the glass surface. Monitoring of titanosilicate zeolites catalyzed epoxidation of the BODIPY-tagged substrate with SMFM was used for catalytic sites mapping and to study the substrate diffusion at heterogeneous catalyst – solution surface.[256] Rybina et al.[193] studied the kinetics and the mechanism of *m*CPBA-mediated epoxidation of BODIPY-tagged olefin on the single-molecule level. In 2014 Jung and coworkers used SMFM to visualize Cu^{I}-catalyzed azide–alkyne "click" cyclization of acetylene-bearing BODIPY dye.[257] The current status and problems in the application of SMFM techniques for studying chemical processes was covered in two excellent mini-reviews,[252,258] and book chapters.[259,260]

Despite the huge potential of this method for the investigation of catalytic reactions, this field of application of SMFM still remains virtually untouched. In the area of transition-metal catalyzed reaction, ensemble averaging complicates the determination of mechanistic aspects of such transformations. Application of SMFM method to study homogeneous catalysis would help in the rational design of new more efficient catalyst. With our experience in the design of BODIPY-tagged complexes and in the olefin metathesis, it became especially attractive to study the ROMP on the single-molecule level using rationally-designed fluorophore-labeled Grubbs-Hoveyda derivative. A detailed understanding of the processes behind chain-termination, catalyst deactivation and back-biting, which can be investigated on the single-molecule level, could finally provide more control over the course of polymerization. There

are only a few examples of the application of SMFM in the olefin metathesis in the literature. Thus, in 2011 Esfandiari and Blum[261] used SMFM to distinguish homogeneous vs. heterogeneous metathesis polymerization by imaging the location of the early stages of the reaction. Scheinhardt et al. used fluorophore-tagged metathesis catalyst for the labeling of polyethylene nanocrystals with following monitoring of these nanoparticles orientation.[262] A similar approach was used by Wirtz and coworkers[263] for the tagging of terminal double bonds of surface-bound styrene units, and to monitor the reaction using SMFM technique.

Design of the Complex for Single-Molecule Observation of ROMP

Earlier Vorfalt[264] et al. reported GHII complex bearing dansyl moiety at benzylidene group (figure 31), which he used for the investigation of the contribution of the release-return mechanism in the olefin metathesis. In the initial complex, ruthenium quenches the fluorescence of the fluorophore. Upon initiation of precatalyst, the dissociation of the tagged ligand from a metal complex takes place, and the fluorescence is restored due to the spatial separation between fluorophore and quencher.

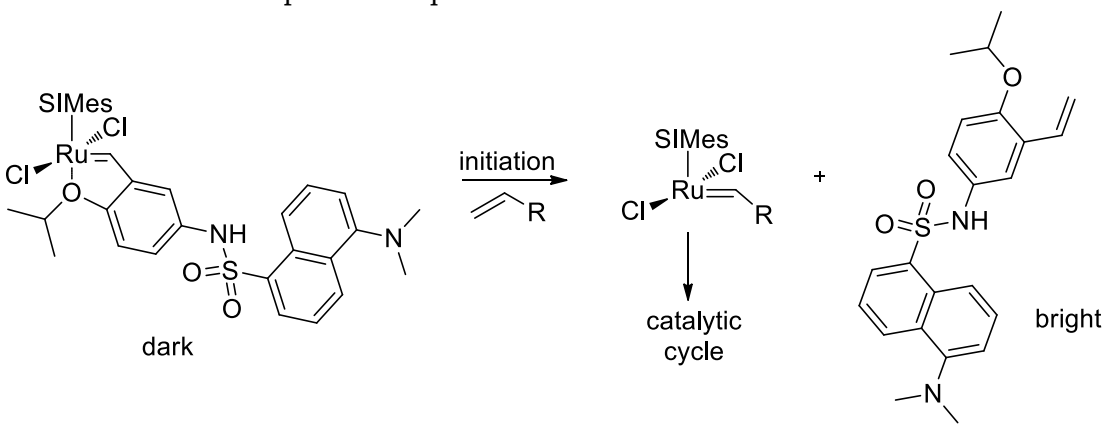

Figure 31: Initiation of fluorophore-tagged Grubbs-Hoveyda complex from Vorfalt et al..

It was decided to use a similar strategy for the fluorescent labeling of ROMP-catalyst for our SMFM studies. To achieve the efficient excitation at the wavelength window of the available laser source, and for the sake of better photostability, higher brightness, and thus, higher signal-to-noise ratio, it was decided to use BODIPY as a fluorophore. Additionally, the target complex should have reactive trialkoxysilyl groups for surface immobilization. To study ROMP under conditions, close to those in the solution, this group should be separated from the reaction center with sufficiently long spacer. The outline for the rational design of the chosen catalyst molecule is provided in figure 32.

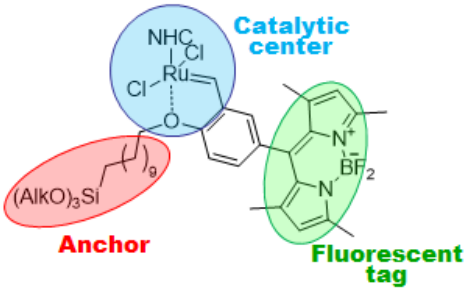

Figure 32: Design of the BODIPY-tagged metathesis catalyst for the SMFM studies of ROMP.

When such a complex is covalently bound to the surface, it would be possible to track the course of the individual chain growth reaction using SMFM (figure 33). Each event of monomer insertion between BODIPY and Ru should lead to spatial separation of quencher and fluorophore, and thus, to the pronounced increase in the BODIPY's emission. This would

give the opportunity to study the kinetic of the polymerization reaction on the single molecule level, investigate the chemical reactivity of catalyst on the surface, and, potentially, reveal the mechanistic aspects of such reactions, not available using ensemble analysis techniques.

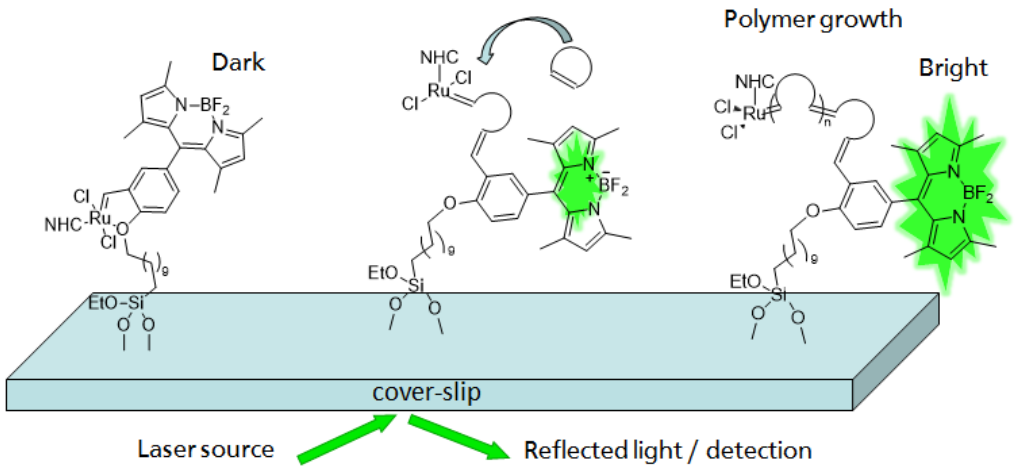

Figure 33: TIRF imaging of ROMP at the solution / surface interface.

Synthesis of the BODIPY-tagged Complex for Surface Immobilization

As a starting material for the synthesis of target complex, commercially available 3-bromo-4-hydroxybenzaldehyde **22** was used. This benzaldehyde readily reacts with 2,4-dimethylpyrrole in the presence of catalytic amount of trifluoroacetic acid to provide the corresponding dipyrrolemethane. One-pot oxidation with chloranil, deprotonation, and complexation with $BF_3{\cdot}Et_2O$ resulted in the formation of BODIPY **23** in 32% yields (figure 34). Stille coupling of **23** with tributyl(vinyl)tin in the presence of $Pd(PPh_3)_4$ provided respective styrene **24** in high yields.

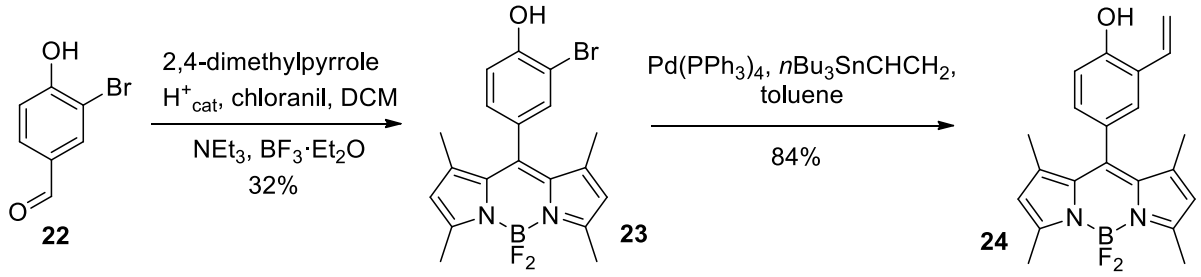

Figure 34: Synthesis of BODIPY-tagged styrene **24**.

For the synthesis of Grubbs-Hoveyda-type complex bearing trialkoxysilyl group, styrene **24** was alkylated with (11-bromoundecyl)triisopropoxysilane (figure 35). The triisopropoxysilane group was chosen for its higher thermal and chemical stability, compared to the triethoxysilane group. At the same time, this group is sufficiently reactive towards the activated glass surface and provides the proper density of covalently-bound complex on the coverslips. However, even traces of water in the reaction mixture result in the partial formation of dimerized **25**, which can't be separated from the respective monomer. (11-Bromoundecyl)triisopropoxysilane was prepared by basic solvolysis of commercially available (11-bromoundecyl)trichlorosilane with *i*PrOH in the presence of NEt_3.

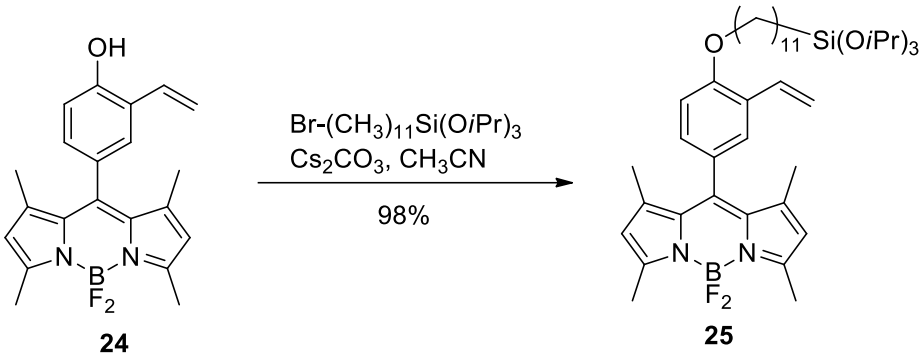

Figure 35: Synthesis of styrene **25**.

Complex **26** was synthesized from styrene **25** and Ru precursor [$RuCl_2$(SIPr)ind(py)] in toluene at 70 °C. Because of the triisopropoxysilyl group, the purification of the final complex is limited, and target compound **26** was obtained in the acceptable purity by evaporation of the reaction mixture and washing solid residue with dry pentane and methanol in a good yield (figure 36).

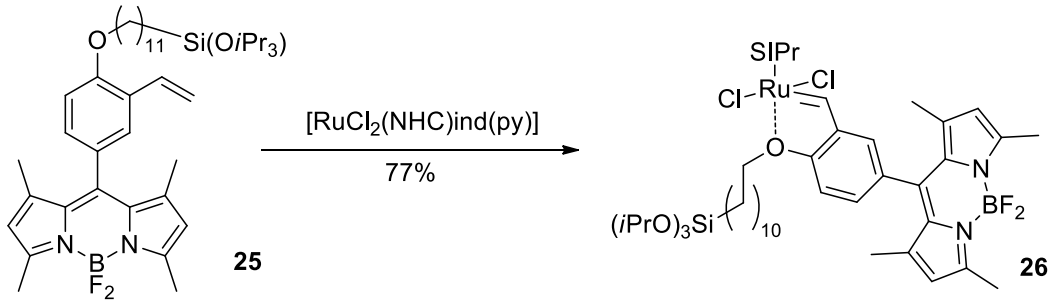

Figure 36: Synthesis of BODIPY-labeled Grubbs-Hoveyda-type complex **26**.

Spectroscopic Properties and Single-Molecule Observation of ROMP

Absorbance and emission spectra of the synthesized compounds **23** – **26** are characterized by the domination of $S_0 \rightarrow S_1$ and $S_1 \rightarrow S_0$ transition bends of BODIPY respectively. Manipulations with substituents of the *meso*-phenyl group of BODIPY do not alter absorbance and emission maxima of the fluorophore (λ_{abs} = 504 nm, λ_{em} = 518 nm, figure 37). However, ruthenium quenches dramatically the fluorescence of BODIPY in complex **26**, probably due to the heavy atom effect, or reductive PET from Ru to BODIPY. Additionally, the absorbance spectrum of **26** is characterized by the LMCT band of lower intensity around 370 nm.

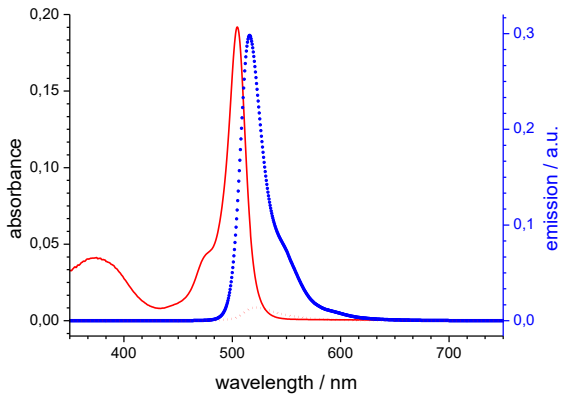

Figure 37: UV-Vis (solid line) and fluorescence (dotted line) spectra of $2.0 \cdot 10^{-6}$ mol·L^{-1} solutions in toluene of **25** (blue) and **26** (red). Excitation wavelength – 504 nm.

To test the newly synthesized complex **26** in ROMP, first, an ensemble monitoring of the emission of BODIPY in the reaction of **26** with norbornene was conducted. Just as expected, a pronounced increase in the emission of the fluorophore can be observed due to the spatial separation of quencher and fluorophore. The respective emission at 518 nm – time trace for the ROMP of norbornene (0.1 mol·L^{-1}), catalyzed by **26** (2.0·10^{-5} mol·L^{-1} in toluene), is shown in figure 38. As can be seen from the plot, even after 6 hours of reaction time, the initial complex is still not completely initiated. Moreover, this trace can't be described with pseudo-first or second order reaction kinetics. This can be explained by the fact that in ROMP, initiation of precatalyst is a rate-limiting step, and shortly after some small part of the complex had been initiated, the active species rapidly polymerize the substrate, leading to the dramatic decrease in the concentration of monomer. The continuous slow increase in the emission even after 4 hours can be caused by initiation of the remaining traces of norbornene, initiation by internal double bonds of polymer chains, or some decomposition processes.

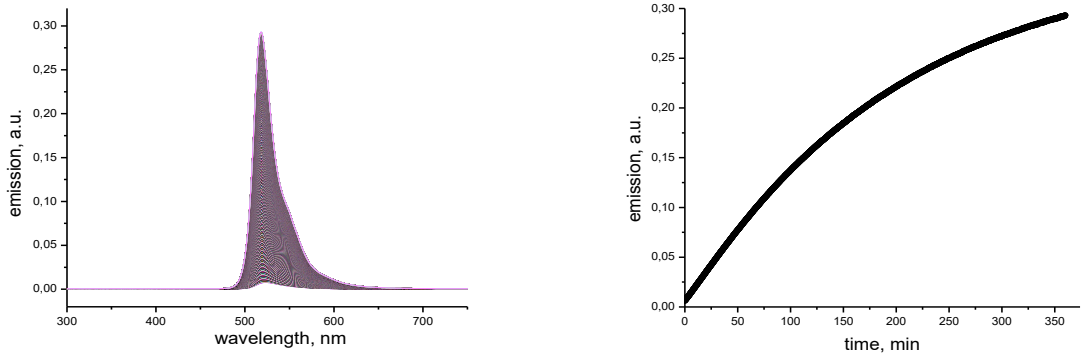

Figure 38: Emission traces for the ROMP of norbornene (0.1 mol·L^{-1} in toluene) catalyzed by **26** (2.0·10^{-5} mol·L^{-1}), excitation wavelength 504 nm (left). Emission-time trace at 518 nm (right).

This experiment clearly shows that ensemble averaging complicates the interpretation of experimental data, and, in this case, it is not possible to perform a detailed analysis of such results.

In order to study ROMP on a single molecule level, a set of glass cover-slips with covalently bound fluorophore-tagged Grubbs-Hoveyda complex was prepared. First, coverglasses (25 mm diameter, 0.17 mm thickness) were treated with plasma on both sides with the aim to clean the surface from possible fluorescent contaminants, and to generate chemically active Si-OH bonds on the surface. The plasma-etched cover-slips were introduced into the diluted solution of **26** and triethoxyethylsilane (100 eq) in heptane (1.0·10^{-10} mol·L^{-1}) and remained in the solution for 30 s, then the cover-slips were removed and the liquid was immediately drained from the surface with pressurized air. Triethoxyethylsilane was used as a competition reagent to reduce the surface density of complex. This solution was prepared using dilution method. It was found, that application of more concentrated solutions results in a too high density of dye on the surface, and, in this case, the observation of separate molecules is not possible. The dry coverslips were intensively extracted in Soxhlet apparatus with dry diethyl ether under inert atmosphere in order to remove physisorbed material.

A series of SMFM experiments were done in collaboration with Dr. Tobias Meckel (TU Darmstadt, Biological department, Membrane dynamic). The prepared cover-glasses were investigated in the absence of a substrate in order to find optimal acquisition parameters and to study the photophysical properties of immobilized complex under intense laser irradiation (figure 39).

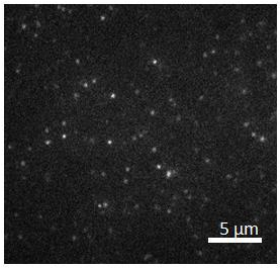

Figure 39. TIRF-image of **26** immobilized on the glass surface. Excitation at 488 nm for 10 ms, intensity of 2 kW·cm^{-2}. Diffraction limited signals were recorded with an EMCCD camera running at a frame rate of 20 Hz through a bandpass emission filter (500 – 550 nm).

Single-molecule experiments were carried out on a custom built total-internal-reflection-fluorescence (TIRF) microscope. It was found, that irradiation of the sample with the laser light of 2 kW·cm^{-2} power and 488 nm wavelength results in the high-frequency blinking of the dye. Since no even partial regeneration of fluorescent spots population on the region of cover-slips with mechanically removed immobilized dye was observed, this effect can't be connected with rapid interchange of fluorescent molecules between the glass surface and solution. However, the lowering of laser power results in the decrease in the blinking frequency. This shows that observed blinking is probably due to the photobleaching of BODIPY and is related to the continuous "on-off" states switching, even so the emission of the fluorophore in this complex is quenched by Ru atom. Detailed analysis of recorded videos showed, that more than 95% of the surface-bound dye remains in the "off"-state even under 0.1 kW·cm^{-2} laser irradiation (figure 40). Similar photoinduced bleaching of BODIPY was observed also by Rybina et al..[193] This photobleaching occurs very fast and the system equilibrates within a few seconds. However, it is not permanent and BODIPY restores its fluorescence in the absence of a laser light irradiation.

Figure 40. Photobleaching of **26** immobilized on the glass surface, 1 (left) and 500 (right) frames of the video, recorded with EMCCD camera running at a frame rate of 20 Hz. Excitation at 488 nm for 10 ms, intensity of 0.1 kW·cm^{-2}.

Figure 41 depicts the changes in the average intensity of the separate frames of the recorded video. To observe a ROMP of norbornene derivative, dimethyl cis-5-norbornene-*endo*-2,3-dicarboxylate was added at frame 250. This addition caused a small increase in the average intensity, probably due to the formation of the unquenched BODIPY groups which are also bleached rapidly.

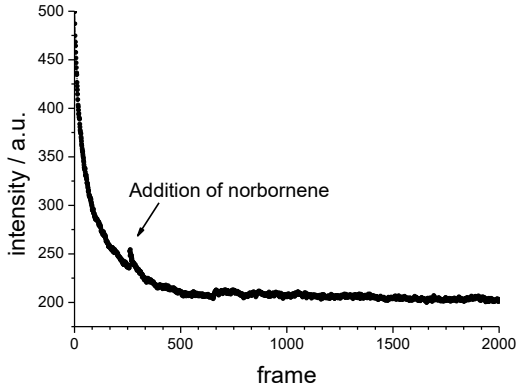

Figure 41. Average intensity vs frame plot, TIRF video of the reaction of **26** with ROMP substrate, recorded with EMCCD camera running at a frame rate of 20 Hz. Excitation at 488 nm for 10 ms, intensity of 0.1 kW·cm^{-2}.

Low photostability of our probe under used acquisition conditions, which cause rapid "on-off" transitions of BODIPY and photoinduced bleaching, result in insufficient life-time of dye in the active state for the extended observation of ROMP on the single-molecule level. A possible solution to this problem would be to use a laser source of even lower power, what would require more sensitive detection system. Additionally, the lowering of the frame rate may also minimize photoinduced bleaching and at the same time it would optimize signal-to-noise ratio. Another problem which needs to be improved is the relatively high surface density of dye molecules. Further dilutions of solution for dip-coating, as well as the increase in the amount of competition reagent, do not lead to the desired improvement of the amount of immobilized complex. In order to decrease the surface population of dye, the application of another method for the surface immobilization, for example, spin-coating, should be considered.

3.3.3. Bodipy-tagged Grubbs-Hoveyda complexes for Initiation of Olefin Metathesis Investigation

Pre-catalyst activation has a significant impact on the overall course of the metathesis reaction. Most of the Ru-based complexes are 16-electron species, which first have to undergo initiation by losing a ligand, during which the active 14-electron species are formed. It is considered that activation of the pre-catalyst involves a sequence of steps and can occur via different mechanisms (dissociative, associative, or an interchange[265,266]). In the dissociative mechanism, pre-catalyst first lose one ligand to form 14-electron intermediate with the consecutive binding of alkene; associative mechanism involves the preliminary formation of 18-electron species through the coordination of olefin, followed by dissociation of ligand; interchange mechanism presumes simultaneous binding of alkene and loss of ligand.[266,267]

The mechanism of initiation of Grubbs-Hoveyda complexes was studied extensively over the last decade,[265,266,268–270] by using a variety of experimental techniques and computational tools.[271,272] A detailed study of the activation of a set of Grubbs-Hoveyda-type complexes was carried out in our group earlier by using UV/Vis techniques.[265,266] The symmetry of the ligand field around ruthenium and the donor strength of the ligands modulate the LMCT and d–d bands of ruthenium. Kinetic analysis of the changes in the intensity of these bands and the dependence of the observed rate constants on the concentration of the substrate showed that the initiation rate and the activation pathway are strongly dependent on the identity of the substrate, its concentration, and type of catalyst. Later, Vasco Thiel in our group investigated the mechanism of RCM using NMR techniques.[270] Analysis of the conversion-

time data provided information on activation, catalysis and decomposition rate constants for a large set of benzylidene-substituted Grubbs-Hoveyda complexes.

Interpretation of UV/Vis data,[265,266] or conversion-time curves from NMR experiments[270] requires complicated mathematical models and often accurate analysis is impossible without simplifications. Additionally, such experiments often require much higher concentration of precatalyst, compared to the concentrations, which are needed for the efficient catalytic transformation.

It was very attractive for us to investigate the initiation of BODIPY-tagged Grubbs-Hoveyda complexes using fluorescent spectroscopy. The high sensitivity of this method gives a chance to monitor the activation step at complex concentrations which are not available for most of the other methods and close to those, used in preparative synthesis. Additionally, the initiation step of BODIPY-tagged complexes can be followed with both, UV/Vis and fluorescent spectroscopy, what would lead to the more accurate interpretation of the results and potentially would give us a better understanding of the initiation mechanism.

By analogy to the complex, used for the boomerang mechanism investigation by Vorfalt,[264] and to the complex, reported here for the single-molecule experiments, in was decided to study the initiation of the GH complexes bearing BODIPY at the benzylidene moiety. Initiation of such complex leads to the release of the fluorophore-tagged styrene, resulting in the deactivation of the fluorescence quenching and pronounced increase in the emission. Parallel detection of the changes in the $S_1 \rightarrow S_2$ BODIPY emission band and LMCT and following analysis of data can reveal the important information about the operating pathway and the elementary steps of the pre-catalyst activation.

Synthesis of BODIPY-tagged Complexes

Synthesis of target pre-catalysts with the BODIPY label at the chelating benzylidene moiety was done by applying a similar strategy to the one, used for the synthesis of the complex for single-molecule observation of ROMP. Alkylation of 3-bromo-4-hydroxybenzaldehyde **22** with *iso*-propyl iodide provided corresponding 3-bromo-4-*iso*-propyloxibenzaldehyde **27** in 98% yields. Similarly to benzaldehyde **22**, the acid-catalyzed reaction of **27** with 2,4-dimethylpyrrole in CH_2Cl_2 provides corresponding dipyrrolemethanes. Followed one-pot oxidation with chloranil, deprotonation, and complexation with $BF_3{\cdot}Et_2O$ results in the formation of BODIPYs **28**. Pd^0-catalysed Stille coupling of **28** tributyl(vinyl)stannane in toluene at elevated temperature provided the respective styrene **29** excellent yields (figure 42).

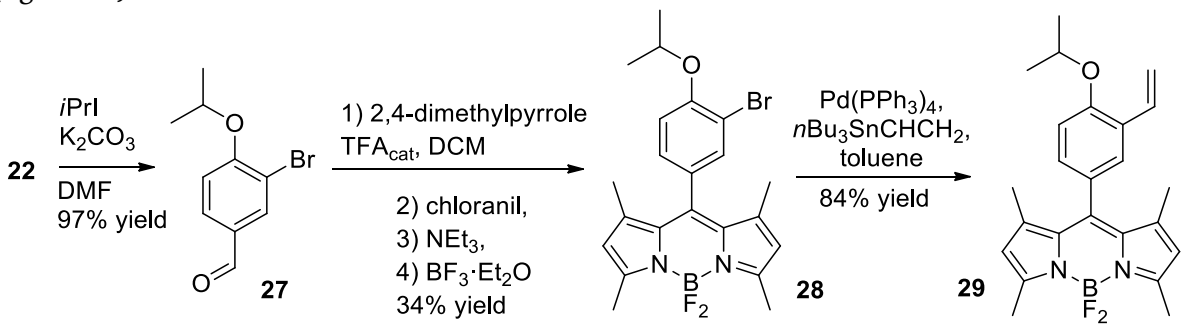

Figure 42: Synthesis of BODIPY-tagged styrene **29**.

For the synthesis of target BODIPY-labeled complexes, styrene **29** was reacted with Ru precursors [$RuCl_2$(NHC)ind(py)] (NHC=SIMes, SIPr) in the presence of acidic resin Amberlyst A15. This method was earlier used in our group for the synthesis of fast-initiating Grubbs-Hoveyda complexes[273,274] and has a big advantage over most other methods of

synthesis of this type of complexes, since it require much milder reaction conditions, provides products in excellent yields, and normally column purification of the crude product is not required (figure 43).

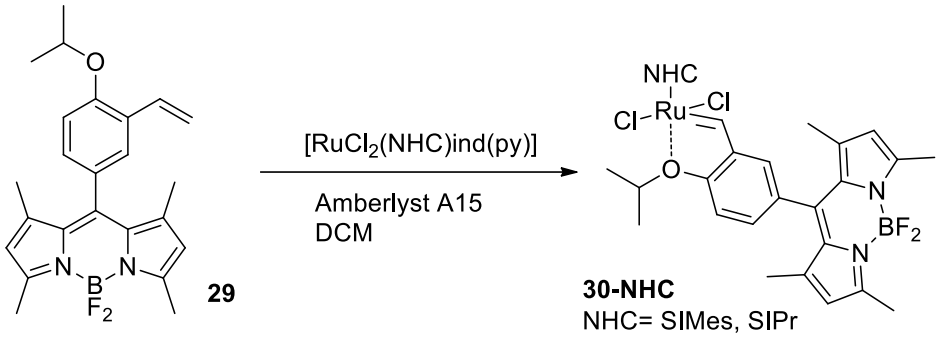

Figure 43: Synthesis of BODIPY-labeled Grubbs-Hoveyda-type complexes **30**.

Spectroscopic Properties and Initiation of BODIPY-tagged Grubbs-Hoveyda Complexes

The absorption spectra of compounds **28** – **30** are dominated by the BODIPY chromophore, displaying an intense band in the 502 nm region. Additionally, the UV−Vis spectra of complexes **30** are characterized by LMCT absorbance bands in the 370 nm region. BODIPY derivatives **28** and **29** are green fluorescent (Φ=0.27 for **29** in toluene) while the emission of BODIPY fluorophore in ruthenium complexes **30** is quenched (Φ = 0.004 for **30**-SiMes in toluene), probably due to heavy atom effect or photoinduced electron transfer from ruthenium. Emission maxima of fluorophore are relatively independent of the nature of substituents at the similar BODIPYs and can be observed at 516 nm in the compounds **28 – 30** (figure 44).

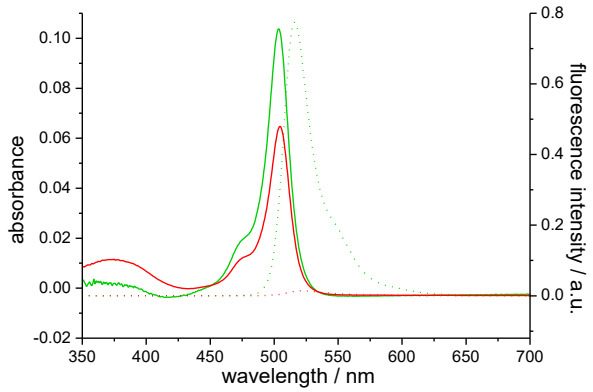

Figure 44: UV-Vis (solid line) and fluorescence (dotted line) spectra of $5.0 \cdot 10^{-6}$ mol·L^{-1} solutions in toluene of **29** (green) and **30**-SIMes (red).

Similar to described previously BODIPY-tagged complexes, changes in the electron density at the ruthenium should modulate the efficiency of quenching. Observation of these changes in the presence of different olefins can provide us with information about the mechanism of initiation and the catalytic cycle of metathesis reaction.

The established mechanism of initiation for Grubbs-Hoveyda complexes involves a sequence of steps. First, activation of precatalyst **A** with substrate results in the cleavage of Ru-O bond, coordination of olefin and formation of π-complex **B**. Depending on the nature of pre-catalyst, substrate, and concentrations, **A→B** transformation can proceed through dissociative, interchange, or associative pathway. Next, **B** undergoes rearrangement with the formation of

ruthenacyclobutane **C** and following cleavage of it yields π-complex **D**. Dissociation of styrene is the last initiation step and the formed active species enter the catalytic cycle (figure 45).

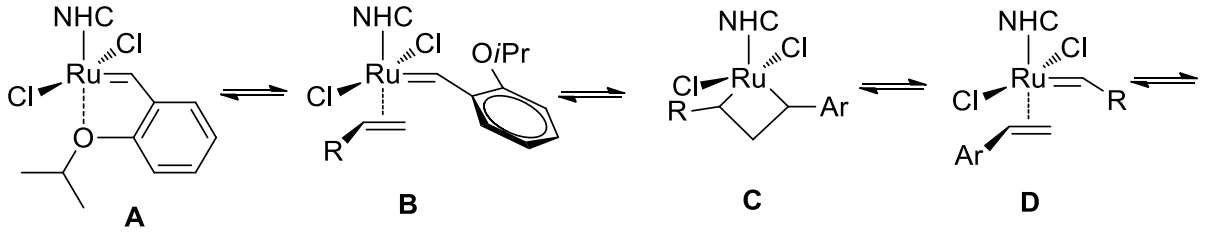

Figure 45: Mechanism of the GHII initiation.

Earlier in our group Vasco Thiel[266] and Tim Vorfalt[265] investigated the mechanism of the pre-catalyst initiation by monitoring time-dependent changes in the LMCT band absorption of different Grubbs-Hoveyda complexes with a variety of substrates. In this research, the absorbance vs time data for the olefin initiation was fitted to a single exponential or a hyperbolic function to obtain the respective k_{obs}. Based on the detailed analysis of the k_{obs} vs. c(olefin) curves, it was shown that the initiation in these complexes follows two parallel pathways, a dissociative and an interchange mechanism, and the influence of these pathways strongly depends on the steric and electronic properties of catalyst and substrate. Later, detailed analysis of recorded absorbance-time traces at different wavelengths, including maximum at 380 nm, showed that there is more than one process that can be monitored by UV-Vis. Often the best fit of the traces could be achieved only when the sum of two or three exponential functions was applied. However, it is complicated to make the certain decision about the nature of each observed rate constant based only on the analysis of the UV-Vis data.

In order to study the mechanism of pre-catalyst activation, the reactions of complex **30**-SIMes with the olefinic substrates DEDAM and BuVE were studied under pseudo first-order conditions (c(olefin) ≫ c(**30**-SIMes)) as a function of the substrate concentration (0.01 – 1.0 mol·L^{-1}) at constant concentration of complex ($1.0 \cdot 10^{-6}$ mol·L^{-1}) in toluene solvent at 303 K. The kinetic evaluation of pre-catalyst activation is based on time-dependent UV−Vis spectra at the maximum of the peak at 376 nm, and fluorescence intensity at the maximum peak at 515 nm.

First, the reaction of **30**-SIMes with BuVE was carried out (figure 46). This reaction leads to catalytically inactive Fischer-type carbenes following a single olefin metathesis event.[265] In the UV-Vis spectrum, a decrease of the respective 378 nm absorbance band can be observed while the intensity of the absorbance band of BODIPY remains at the same level. The best fit was obtained when the absorbance vs time data for the BuVE initiation was fitted to a sum of two exponential functions, $A = A_1 \cdot \exp(k^1_{obs} \cdot t) + A_2 \cdot \exp(k^2_{obs} \cdot t) + A^{\infty}$, where $A_{1,2} = (A^0_{1,2} - A^{\infty}_{1,2})$ and $k^{1,2}_{obs}$ – respecting pseudo-first order constants (figure 46). This fit can represent a kinetic model, where two parallel processes are taking place under pseudo-first order conditions. The dependencies of the rate constants k_{obs} on the BuVE concentrations are shown in figure 46.

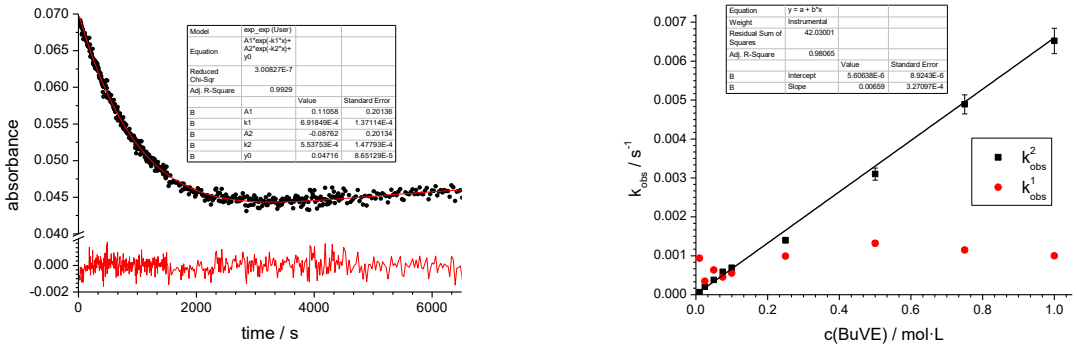

Figure 46: Absorbance (at 378 nm) – time curve for the initiation of **30**-SiMes ($1.0 \cdot 10^{-6}$ mol·L^{-1}) with BuVE (0.1 mol·L^{-1}, left) in toluene at 303K fitted with a sum of two exponential functions. The plot of k_{obs} vs. c(BUVE) (right) A linear fit of k_1 data yields k_1 = 0.00659 mol·L^{-1}·s^{-1} .

By analogy to the initiation with BuVE, the reaction of **30**-SIMes with DEDAM was also monitored and obtained absorbance-time curves were fitted with double exponential function (figure 47).

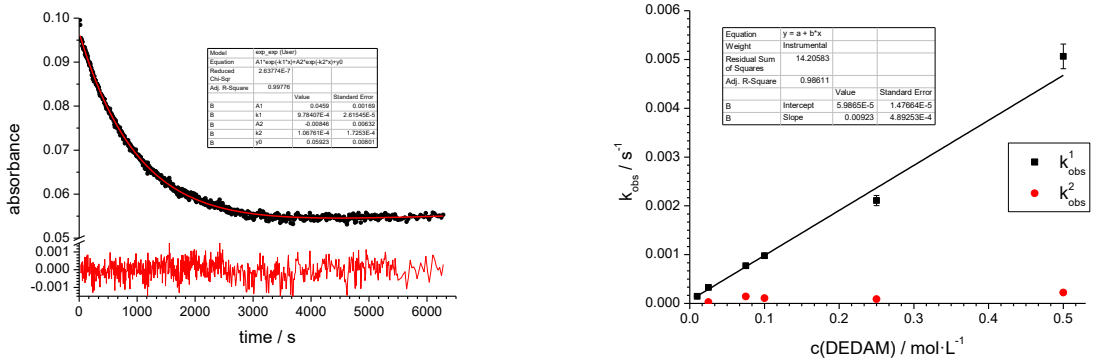

Figure 47: Absorbance (at 378 nm) – time curve for the initiation of **30**-SiMes ($1.0 \cdot 10^{-6}$ mol·L^{-1}) with DEDAM (0.1 mol·L^{-1}, left) in toluene at 303K fitted with a sum of two exponential functions. The plot of k_{obs} vs. c(DEDAM) (right). A linear fit of k_1 data yields k_1 = 0.00923 mol·L^{-1}·s^{-1}.

Rate constants k_{1obs} show linear dependency on c(olefin) and the linear fit of this data provides the second-order initiation constant, k_{1abs}(BuVE) = 0.00659 mol·L^{-1}·s^{-1} and k_{1abs}(DEDAM) = 0.00923 mol·L^{-1}·s^{-1} with intercept close to zero. This behavior is in agreement to the data from Tim Vorfalt and it's linear dependency on the concentration of olefin without "saturation" at high olefin concentrations shows that interchange pathway in predominant for the initiation of **30**-SiMes with BuVE or DEDAM. On the other hand, rate constants k_{2obs} seem to be independent of the concentration of substrate, and it is unclear to which process does this constant belong. Interestingly, in this experiment the initiation constant for DEDAM is a little higher than those for BuVE, while BuVE is known to be a more active substrate for the initiation of different Grubbs-Hoveyda complexes.[265,266]

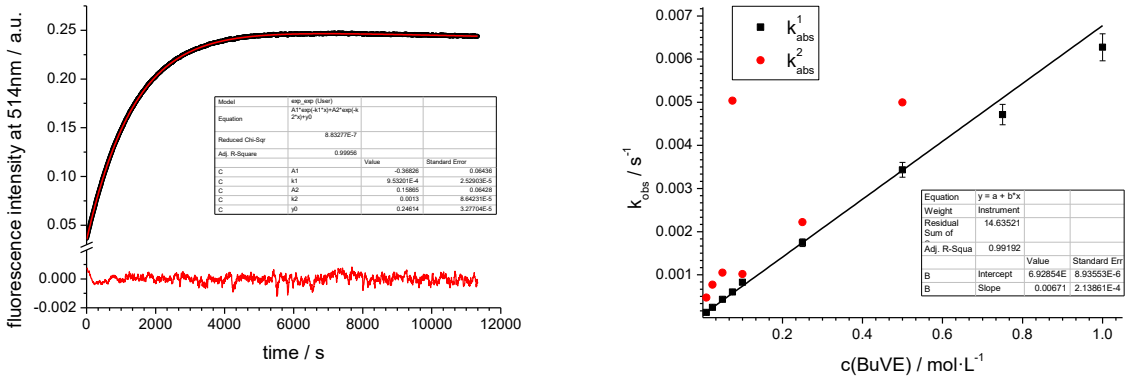

Figure 48: Fluorescence intensity (at 514 nm) – time curve for the initiation of **30**-SIMes ($1.0 \cdot 10^{-6}$ mol·L^{-1}) with BuVE (0.1 mol·L^{-1}, left) in toluene at 303K fitted with a sum of two exponential functions. The plot of k_{obs} vs. c(BuVE) (right). A linear fit of k_1 data yields k_1 = 0.00671 mol·L^{-1}·s^{-1}.

The same reactions of **30**-SiMes with BuVE (figure 48) and DEDAM (figure 49) under identical conditions were monitored by fluorescence spectroscopy. Initiation of precatalyst leads to the pronounced increase in the fluorescence intensity due to the release of BODIPY-tagged styrene and deactivation of ruthenium-mediated quenching. The obtained fluorescence intensities at 514 nm vs time data were fitted to double exponential function. Rate constant k^1_{obs} shows identical (to the k^1_{obs} obtained from UV-Vis measurement linear dependency) on the concentration of the substrate. Linear fit of such plots yields k_{1em} (BuVE) = 0.00671 mol·L^{-1}·s^{-1} and k_{1em} (BuVE) = 0.00709 mol·L^{-1}·s^{-1} which are practically equal to the k_{1abs} from the absorption spectroscopy experiments.

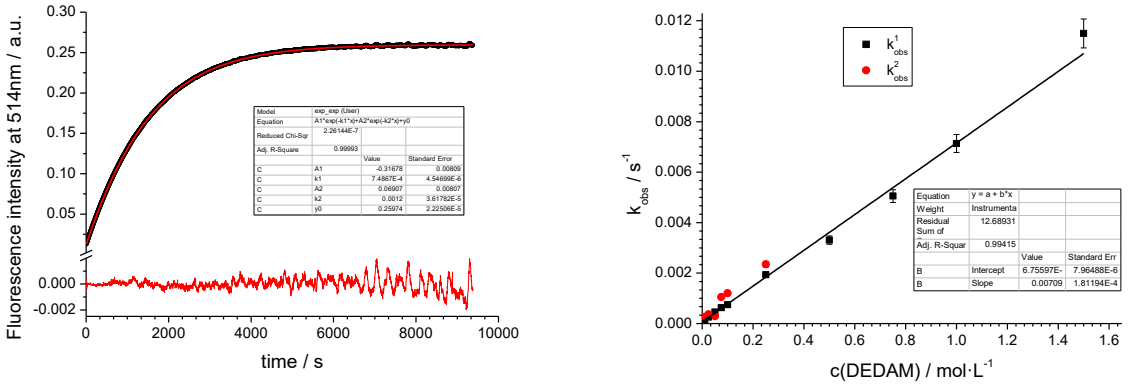

Figure 49: Fluorescence intensity (at 514 nm) – time curve for the initiation of **30**-SIMes ($1.0 \cdot 10^{-6}$ mol·L^{-1}) with DEDAM (0.1 mol·L^{-1}, left) in toluene at 303K fitted with a sum of two exponential functions. The plot of k_{obs} vs. c(DEDAM) (right). A linear fit of k_1 data yields k_1 = 0.00709 mol·L^{-1}·s^{-1} .

The absorbance band at 378 nm is commonly attributed to LMCT from chelating oxygen to the ruthenium. The major influence on the decrease of the absorbance is due to the first step of the initiation pathway, cleavage of the Ru-O bond. On the other hand, the fluorescence of the BODIPY can be restored only after the fluorophore is dissociated and ruthenium and BODIPY are spatially separated. The fact that both UV-Vis and fluorescence experiments result in the same rate constants shows that the **A→B** (figure 45) transformation is a rate limiting step and determines the rate of the initiation of Grubbs-Hoveyda complexes.

3.3.4. Investigation of Catalytic Cycle and Decomposition of BODIPY-tagged Olefin Metathesis Catalysts.

BODIPY-tagged Grubbs-Hoveyda complexes **26** and **30** are of a great interest for the investigation of the initial steps of olefin metathesis, e.g. activation of pre-catalyst and first events in the ROMP. But these complexes are not suitable for mechanistic studies of the catalytic cycle and catalyst decomposition. However, the understanding of the nature of the intermediates and kinetics of these processes can guide the development of more efficient catalysts and reactions. Detection of the intermediates throughout the catalytic cycle, which are present in minute amounts, is a challenging task. These active species were previously studied using various techniques, including NMR,[275,276] mass-spectroscopy,[277] or DFT calculations.[278] In these studies the detection of intermediates required the application of low temperatures, high concentrations of complexes, or was possible only in the gaseous phase using custom-synthesized catalyst.

In order to learn more about the metathesis propagation and catalyst deactivation under conditions, maximally close to those, used in the preparative synthesis, we have developed Grubbs-Hoveyda complex with BODIPY tag at SIMes ligand. Previously described NHC precursor **18** is a perfect candidate for the synthesis of such complex. Being separated in such complex with the aliphatic C2 linker, BODIPY make a negligible electronic and steric influence on the catalytic center, at the same time it should give a detectable fluorescent response on the small changes in the electron density of Ru.

Synthesis of Metathesis Catalysts Bearing BODIPY Tag at NHC Ligand

Imidazolidine **18** was used as a convenient NHC-precursor for the synthesis of BODIPY-tagged Grubbs-Hoveyda complexes **31** and **32**, where the fluorophore is connected to the SIMes ligand. In 2007 Grubbs and coworkers[279] reported the synthesis of Grubbs-Hoveyda II with SIPr ligand from 2-(Pentafluorophenyl)imidazolidine and Grubbs-Hoveyda I precursor. The authors obtained target complex in 80% yield when components were heated in toluene at 60 °C for 5 h. Similarly, 1,3-Bis(2,4,6-trimethylphenyl)-2-(pentafluorophenyl)imidazolidine readily generate free SIMes carbene at 60 °C and provide GII from GI complex in 4 h in 91 % yield. However, no reaction of **18** with GHI was observed at 60 °C. To facilitate the generation of carbene from **18**, the higher reaction temperature was required. Complex **31** was formed in 11% yield only when reagents were heated at 100 °C for 2 h (figure 50) followed by addition of CuCl for the efficient dissociation of PCy_3 from the formed intermediate. The reaction of **18** with Grubbs I at different conditions resulted in lower yields or complete decomposition of starting reagents.

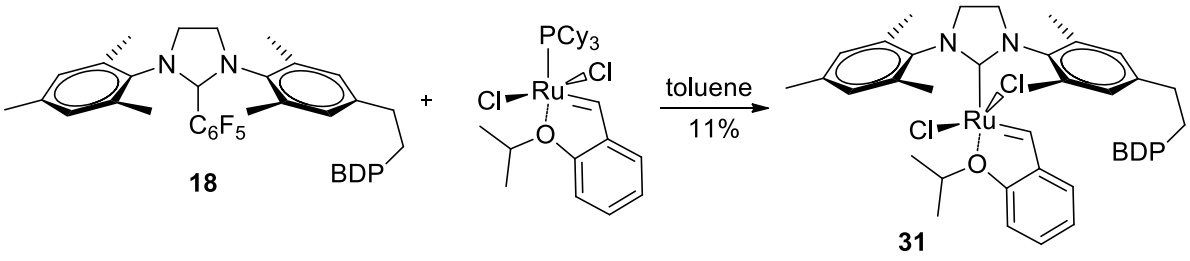

Figure 50: Synthesis of BODIPY-labelled Grubbs-Hoveyda-type complex **31**.

Higher yields were obtained in the reaction of **18** with [$(PCy_3)_2RuCl_2$(ind)], what can be explained by the higher stability of Ru precursor at higher temperatures. Heating the components in toluene at 100 °C for 2 h provided complex **32** in 66% yield (figure 51).

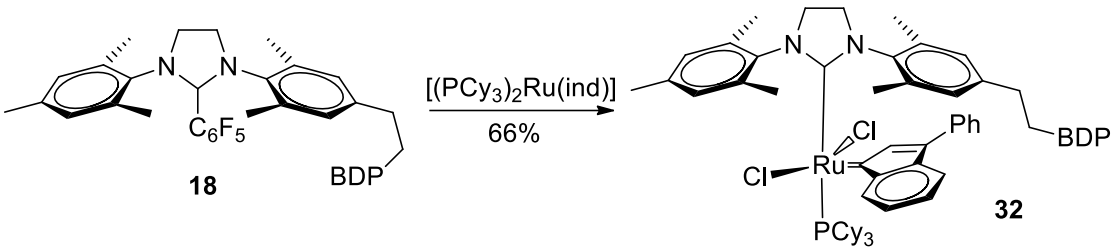

Figure 51: Synthesis of BODIPY-labelled Grubbs-Hoveyda-type complex **32**.

Reaction of Complexes 31 and 32 with Olefin Substrates

Similarly to the previously described BODIPY-tagged complexes, the absorption spectra of the complexes **31** – **32** are dominated by the BODIPY chromophore, displaying an intense band in the 512 nm region attributed to the S_0-S_1 excitation. The UV−Vis spectra are characterized by LMCT absorbance bands in the 370 nm region. Emission of the fluorophore in compounds **31** – **32** is quenched (Φ = 0.01 for **30**-SiMes in toluene, reference compound – rhodamine 6G). Emission maxima of BODIPY for both **31** and **32** are in the region of 525 nm.

Earlier Nolan[280] reported that the reaction of $[(PCy_3)_2Ru(ind)]$ with SIPr carbene is reversible and dissociation of free SIPr ligand from the Ru is not as difficult as believed, and can take a part in the deactivation of the catalyst. If this mechanism takes place for NHC ligand in complexes **31** and **32**, or electron density at the metal center is strongly changed, even a small amount of dissociated ligand should lead to a strong increase in fluorescence of BODIPY. These two scenarios are unlikely under normal reaction conditions for SIMes-based Grubbs-Hoveyda complexes; however, even small changes in electronic configuration at Ru should result in a detectable fluorescence response.

First, the reaction of **31** ($1.0\cdot10^{-6}$ mol·L^{-1}) with BuVE (0.25 mol·L^{-1}) was carried out in toluene solvent at 303 K and monitored with absorption and fluorescence spectroscopy. Under excitation at 512 nm, a small two-fold increase in emission can be observed (figure 52). According to pseudo-first order reaction conditions, obtained fluorescence intensity at 525 nm – time trace was fitted with a double exponential function to give two rate constants: k^1_{em} = 0.00918 s^{-1} and k^2_{em} = 0.00155 s^{-1}.

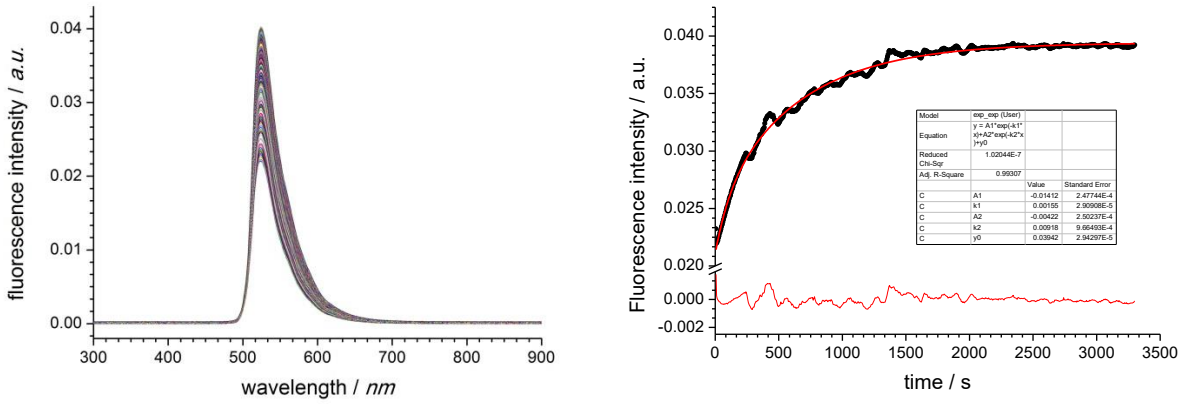

Figure 52: Emission traces for the initiation of **31** ($1.0\cdot10^{-6}$ mol·L^{-1}) with BuVE (0.25 mol·L^{-1}) in toluene at 303K, excitation at 512 nm (left). Fluorescence intensity (at 525 nm) – time curve fitted with sum of two exponential functions, k^1_{em} = 0.00918 s^{-1} and k^2_{em} = 0.00155 s^{-1} (right)

In the UV-Vis spectra, a pronounced decrease in the LMCT band can be observed (figure 53). Respective absorbance at 376 nm – time trace can be fitted with a double exponential

function to provide two pseudo-first order rate constants, k^1_{abs} = 0.00845 s^{-1} and k^2_{abs} = 0.00056 s^{-1}. Both k^1_{abs} and k^1_{em} are practically equal and probably report on the same event, i.e. the initiation of Grubbs-Hoveyda complex **31**. However, the role of the second rate constants from fluorescent and absorbance experiments is unclear.

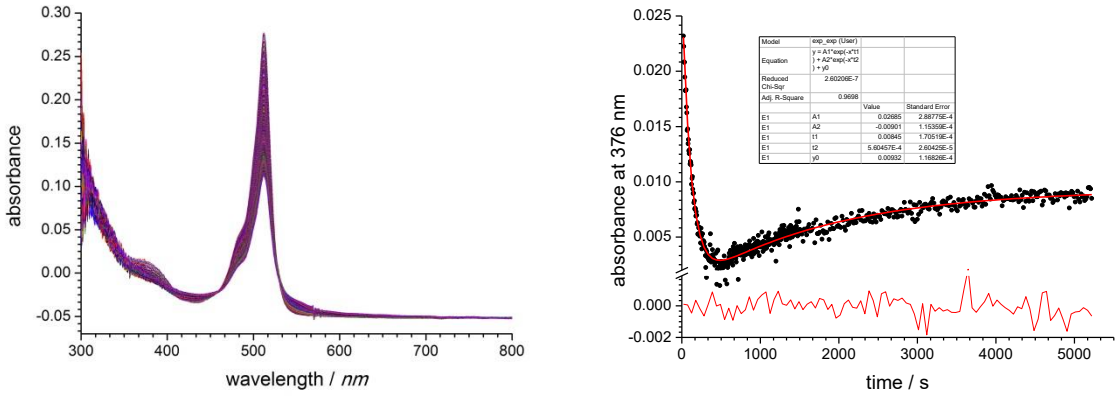

Figure 53: Absorbance traces for the initiation of **31** ($1.0 \cdot 10^{-6}$ mol·L^{-1}) with BuVE (0.25 mol·L^{-1}) in toluene at 303K (left). Absorbance (at 376 nm) – time curve fitted with sum of two exponential functions, k^1_{em} = 0.00845 s^{-1} and k^2_{em} = 0.00056 s^{-1} (right)

To our surprise, a dramatic decrease in the absorbance band of BODIPY (512 nm, $S_0 \rightarrow S_1$ transition) was also observed (figure 53), together with a small increase in the absorbance at longer wavelengths around 555 nm. The respective absorbance at 512 nm – time trace couldn't be successfully described with the double exponential function and required a more complicated kinetic model. The preliminary fit of absorbance traces at 512 nm was done using the sum of three exponential functions (figure 54); double exponential function was used to fit absorbance at 555 nm – time traces.

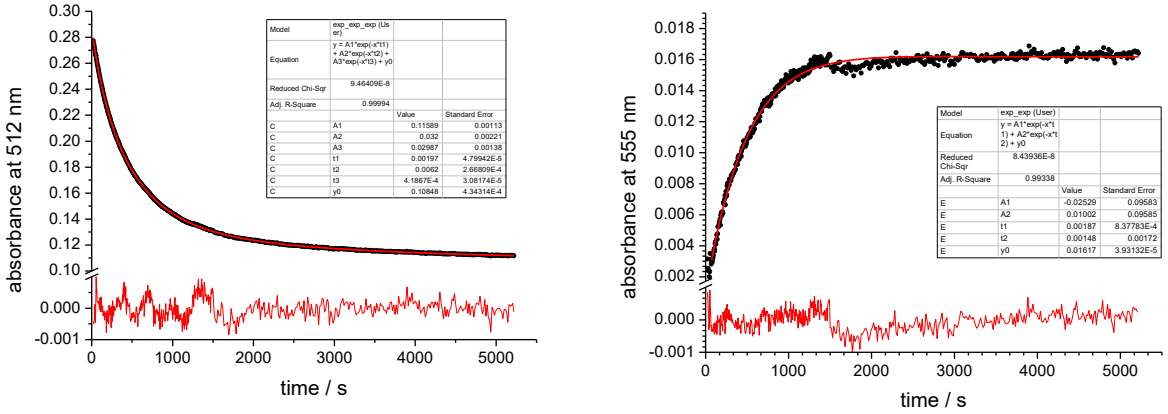

Figure 54: Absorbance – time curves for the initiation of **31** ($1.0 \cdot 10^{-6}$ mol·L^{-1}) with BuVE (0.25 mol·L^{-1}) in toluene at 303 K. Left: trace at 512 nm, fitted with sum of three exponential functions; k_{obs} values: 0.00197, 0.0062 and 0.00042 s^{-1}. Right: trace at 555 nm, fitted with double exponential function; k_{obs} values: 0.00187, 0.00148 s^{-1}.

Changes in the absorbance at 555 nm may be not related to the BODIPY unit and can be explained by the formation of ruthenium intermediate species. Earlier, similar appearance of the broad absorption band in 550 nm region was observed by Tim Vorfalt[265] for the initiation of regular Grubbs-Hoveyda complex with ethylvinyl ether experiment. Also, an increase in the absorbance in this region is very characteristic for the fast initiating phenoxy analogues of Grubbs-Hoveyda complexes.[273] On the other hand, there are no literature references for the chemical process which could lead to the decrease of BODIPY absorbance without notable

absorbance maximum shifts. Chemical reaction and decomposition of BODIPY unit are very unlikely under applied reaction conditions. Different photophysical processes, which are responsible for some changes in the fluorescence of BODIPY, normally lead to very small changes or have no influence on the absorption of the fluorophore at all. Only ICT, depending on the structure of dye, can result in a decrease of absorbance band. However, together with changes in the extinction coefficient of this band, ICT normally lead to the appearance of new blue- or red-shifted band. The absence of additional bands, electronic isolation of BODIPY and reaction site of the molecule, small changes in the dipole moment of the complex during the reaction with BuVE, and application of non-polar solvent, render this scenario implausible. Another possible explanation would be the formation of BODIPY dimers. For different fluorescent dyes the formation of excited- and ground-state complexes is well documented; however, for BODIPY, it is rather an exception. Depending on their types, BODIPY dimers can be fluorescent or quenched, and their absorbance and emission maxima can be shifted to longer or shorter wavelength.[281,282] Aggregation for BODIPY is not typical even at relatively high concentrations, and often noticeable changes in absorbance spectra can be observed only in hours or even days. However, the formation of BODIPY dimers can be facilitated in confined media.[283] Changes in the conformation of BODIPY-labeled proteins can lead to the shortening of the distance between two adjacent fluorophores and such a formation of BODIPY dimers has been successfully utilized for the analysis of protein activities and protein structure determination.[284,285] Earlier Grubbs and coworkers[286] proposed a mechanism of phosphine-containing Ru complexes deactivation, where binuclear Ru species were proposed to be the major decomposition product. Formation of similar binuclear Ru product during the reaction of **31** with olefins would facilitate the aggregation of BODIPYs and can explain the observed drop in absorbance at 512 nm even at low concentration of complex.

To better understand observed changes in absorbance spectra, a set of measurements with fixed concentration of olefin (0.25 mol·L^{-1}) and different concentrations of complex **31** (1.0 – 3.0·10^{-5} mol·L^{-1}) was conducted and changes in absorbance spectra were monitored. If aggregation of BODIPY is responsible for the drop in absorbance, this phenomenon should be faster and more pronounced at higher complex concentration.

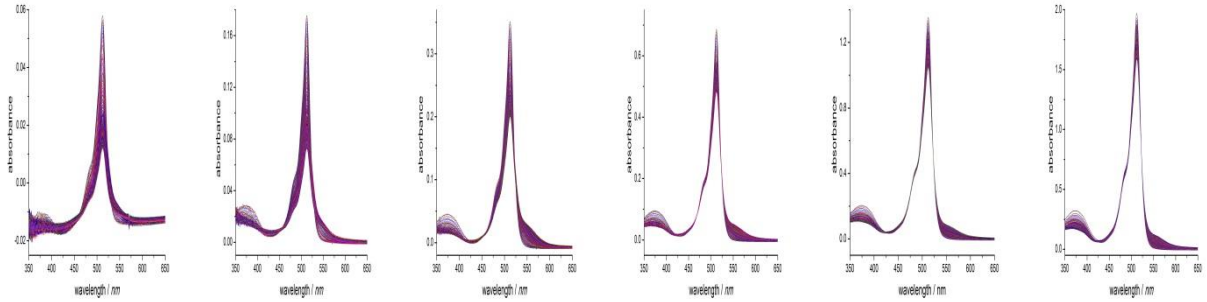

Figure 55: Absorbance spectra for the reaction of **31** with 1-hexene (0.2 mol·L^{-1}) in toluene at 303 K. Concentrations of **31**, from left to right: 1.0·10^{-6}; 2.5·10^{-6}; 5·10^{-6}; 1.0·10^{-5}; 2.0·10^{-5}; 3.0·10^{-5} mol·L^{-1}.

The obtained absorbance spectra can be seen in figure 55. Unexpectedly, the relative decrease in absorbance at 512 nm is bigger at lower concentrations. For 2.0·10^{-5} mol·L^{-1} complex concentration, the extinction coefficient at the end of the reaction is equal to 41% of that at the beginning of the reaction, and for 2.5·10^{-6} mol·L^{-1} complex concentration, the same value is equal to 82%. This shows that this process is probably not related to the dimers formation.

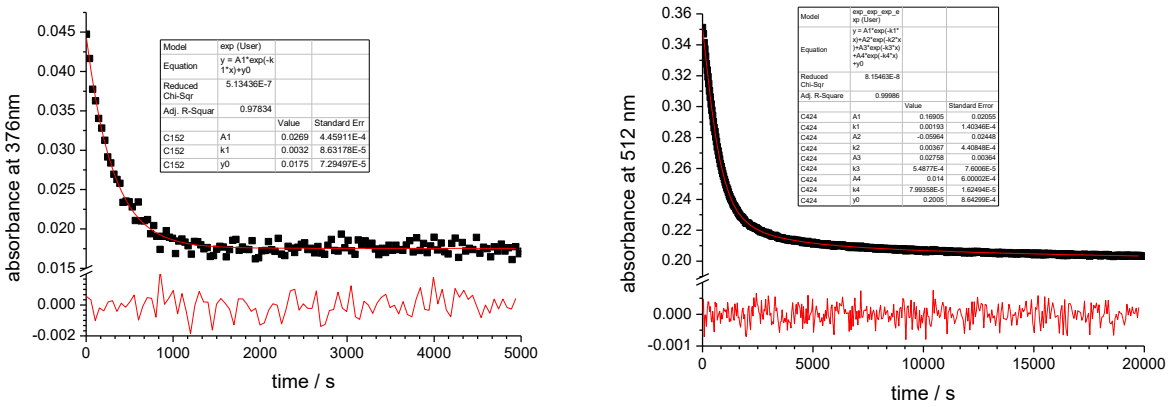

Figure 56: Absorbance – time traces at 376 nm (left) and 512 nm (right) for the reaction of **31** with 1-hexene (0.25 mol·L^{-1}) in toluene at 303 K.

The corresponding absorbance– time traces at 512 nm have a complicated pattern and can't be successfully described with the simple kinetic model. They can't be fitted to single or double exponential functions and satisfactory fit can be achieved only when the sum of four exponential functions was applied. Constants derived this way show no correlation to the k_{obs} obtained from the fit of absorbance – time traces at 376 nm (figure 56). Since absorbance-time traces at 376 nm reach plateau much faster, the drop in absorbance at 512 nm seems to be not related to the initiation reaction and is most likely due to some consecutive steps.

Reaction of [(12)(SIMes)RuCl$_2$(ind)] with DEDAM

Bis-NHC ruthenium benzylidene[195,287,288] and indenylidene[202] complexes, in which one of the NHC ligands is characterized by reduced donor properties, have been shown to be useful catalysts for metathesis transformations of sterically hindered olefins, especially for RCM reaction leading to tetrasubstituted olefins. This activity of bis-NHC complexes can be explained by their slower initiation and higher stability at elevated temperatures required for metathesis transformation. The mechanism of initiation was proposed to be similar to the corresponding PCy_3 analogs, where at elevated temperatures the dissociation of ligand takes place, leading to the formation of catalytically active ruthenium species. Despite the unique properties of this class of complexes, the detailed catalytic studies were done only with benzylidene complexes earlier in our group.[195] To figure out which NHC is liberated during the initiation step, two complexes were synthesized, in which either SIMes or NHC with reduced donating properties were tagged with the dansyl fluorophore. The fluorescence of the fluorophore in both initial complexes was quenched; upon the dissociation of tagged NHC, an increase in the emission intensity should be detected. It was shown that in the course of metathesis reaction the NHC with better electron donating properties remains attached to the Ru center, whereas the dissociation of NHC with reduced electron density is responsible for pre-catalyst activation.

To study the activation pathway in synthesized complex [(**12**)(SIMes)RuCl$_2$(ind)], the similar initiation experiment was conducted and changes in the fluorescence were monitored. Experiments were carried out at 353 K in toluene solution with a complex concentration of $1.0 \cdot 10^{-6}$ mol·L^{-1} and 0.5 mol·L^{-1} concentration of DEDAM. To study the thermal activation, the same experiment was conducted in the absence of olefin. The obtained fluorescence intensity at a maximum of emission – time traces are shown in figure 57.

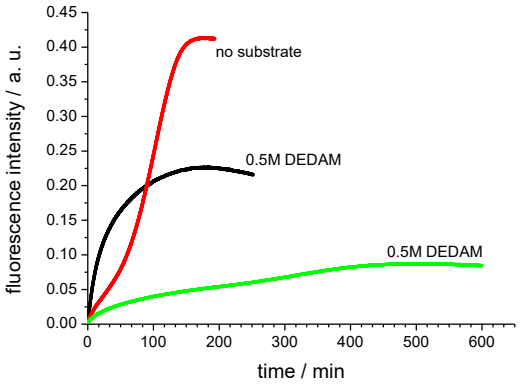

Figure 57: Fluorescence intensity at 540 nm – time traces for the reaction of [(**12**)(SIMes)$RuCl_2$(ind)] ($1.0 \cdot 10^{-6}$ mol·L^{-1}) with DEDAM (0.5 mol·L^{-1}) (green and black) in toluene at 353 K. Excitation wavelength – 518 nm. The same reaction, but without olefin (red).

A dramatic increase in the fluorescence level was observed in all experiments, indicating that the dissociation of carbene **12** is at least partially responsible for complex activation. However, conducted experiments are not well reproducible and different final fluorescence intensity and rates of the emission increase were observed. The highest final fluorescence was observed in the absence of olefin, indicating that at these conditions the dissociation of ligand **12** is dominated. Lower final emission value in the presence of DEDAM can be explained by competing dissociation of both NHCs. This competing dissociation of ligands shows that mechanism of initiation in this case in more complicated than the simple liberation of less electron-donating ligand and substrate plays an important role in the initiation of complex [(**12**)(SIMes)$RuCl_2$(ind)].

4. Summary and Conclusions

The primary goal of this thesis was to develop synthetic routes towards different BODIPY-tagged *N*-heterocyclic carbene-transition metal complexes and to explore their potential as fluorescent sensors and for the investigation of catalytic transformations. It was shown that the modification of the electron density at the metal center alters the efficiency of fluorescence quenching processes. Based on this, a highly sensitive fluorescent chemodosimeters for CO detection and the first known fluorescent hydrogen sensor were developed.

In the following paragraphs, the most important aspects of my work will be presented as a short summary.

1. A new BODIPY-tagged NHC **12** and BODIPY-tagged NHC complexes with Ir, Rh, Au, Ru, and Pd were prepared (figure 58).

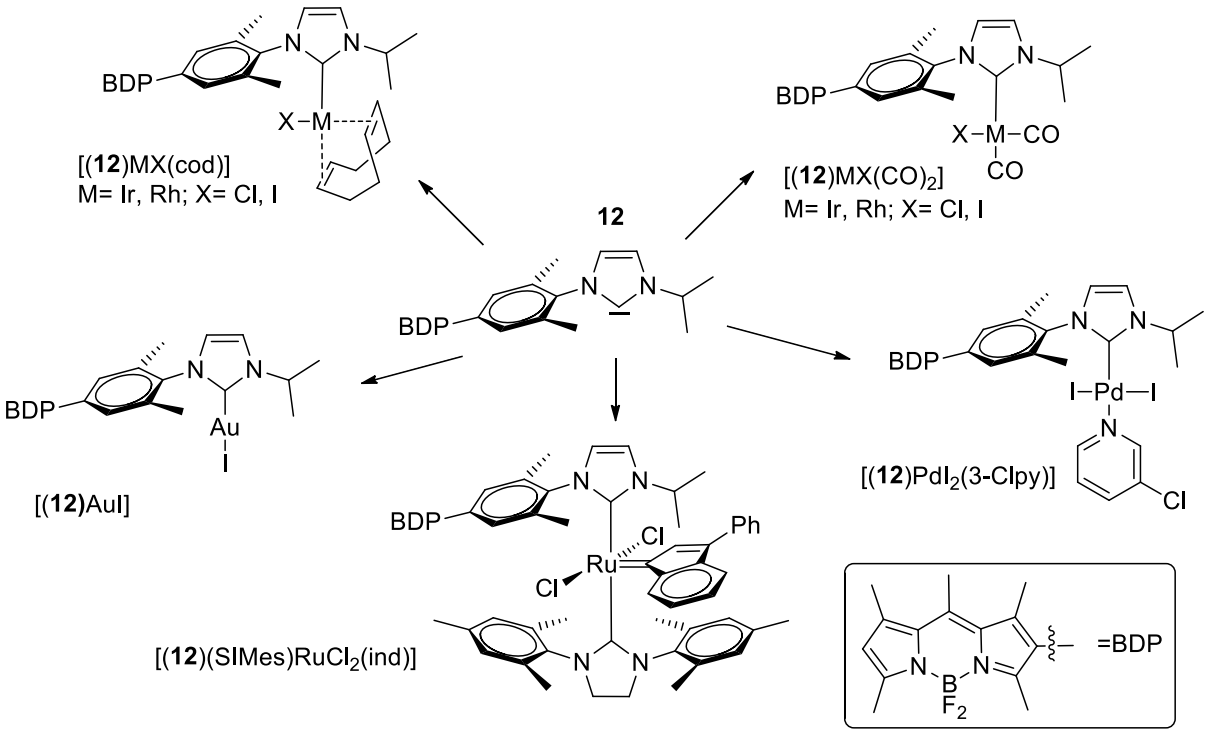

Figure 58: Transition metal complexes containing BODIPY-tagged NHC ligand.

2. The spectroscopic properties of the new complexes were determined. The synthesized compounds are characterized by very different fluorescence properties: strongly quenched complexes ($\Phi<0.01$) with Ru or electron-rich Ir and Rh, a partially quenched Pd complex ($\Phi=0.033$) and a strongly fluorescent Au complex ($\Phi=0.70$). Ligand-exchange reactions were shown to lead to pronounced changes in the brightness of the BODIPY unit in an organometallic complex of a given metal. The manipulation of the electron density at the transition metals modulates the efficiency of PET quenching, because electron-rich transition metals lead to decreased fluorescence, whereas electron-deficient metal centers lead to enhanced fluorescence emission.

3. Complexes [(**12**)MX(cod)] (M=Rh, Ir; X=Cl, I; $\Phi=0.008–0.016$) were converted into strongly fluorescent complexes [(**12**)MX(CO)$_2$]($\Phi=0.53–0.70$) upon reaction with carbon monoxide. The unquenching of the Rh and Ir complexes appears to be a consequence of the decreased electron density at Rh or Ir in the respective carbonyl complexes (figure 59).

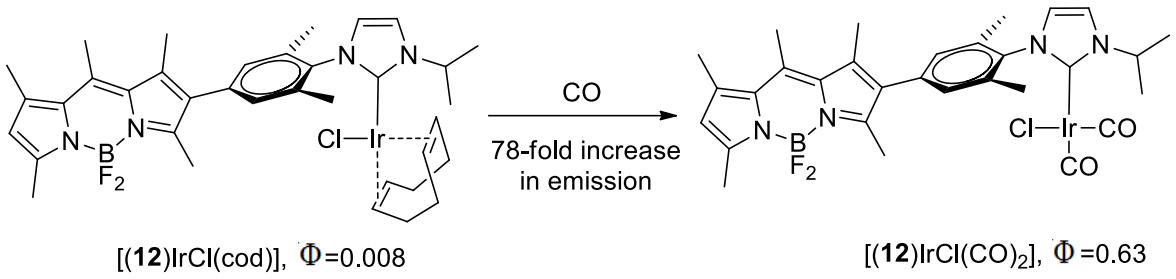

Figure 59: Reaction of [(**12**)IrCl(cod)] with CO.

The newly developed cod-complexes can be used as efficient chemodosimeters for CO with excellent turn-on ratios and fast response time. The signal generating cod→CO ligand exchange reaction is finished in less than 4 s for the Ir complex and 20 s for the Rh complex, resulting in a more than 50-fold increase in the emission intensity. Moreover, these complexes have excellent sensitivity towards CO. Thus, the addition of less than one nanomol of CO to the solution of [(**12**)IrCl(cod)] leads to a detectable change in the fluorescent intensity (figure 60).

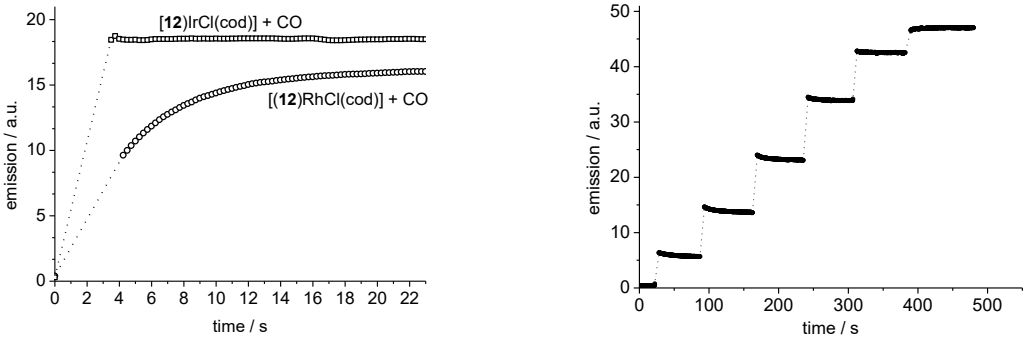

Figure 60: Left: emission-time traces for the reaction of [(**12**)MCl(cod)] (M=Rh, Ir) (c = $2.0 \cdot 10^{-6}$ mol·L^{-1} in ethyl acetate, 25°C) with CO (10 equiv; c = $2.0 \cdot 10^{-5}$ mol·L^{-1}, $9.0 \cdot 10^{-9}$ mol). Right: emission-time trace for the addition of six times 0.6(±0.2) μL of CO to a solution of [(**12**)IrCl(cod)] (c = $1.0 \cdot 10^{-5}$ mol·L^{-1} in ethyl acetate, 25°C); final addition leads to full fluorescence intensity.

The newly developed complexes are moisture and air stable and can be used for the detection of the CO level in atmospheric air. However, *in vivo* studies of closely related triethylene glycol-substituted complexes [(**13**)MI(cod)] (M=Rh, Ir), conducted in cooperation with Prof. Dr. Stefan H. Heinemann (Friedrich Schiller University Jena), showed that these complexes are not suitable for the CO detection in living cell due to the low fluorescence response in aqueous media and relatively high cytotoxicity.

4. A Crabtree-type Ir^{I} complex tagged with BODIPY was synthesized. The oxidative addition of H_2 converts the weakly fluorescent Ir^{I} complex (Φ = 0.038) into a highly fluorescent Ir^{III} species (Φ = 0.51).

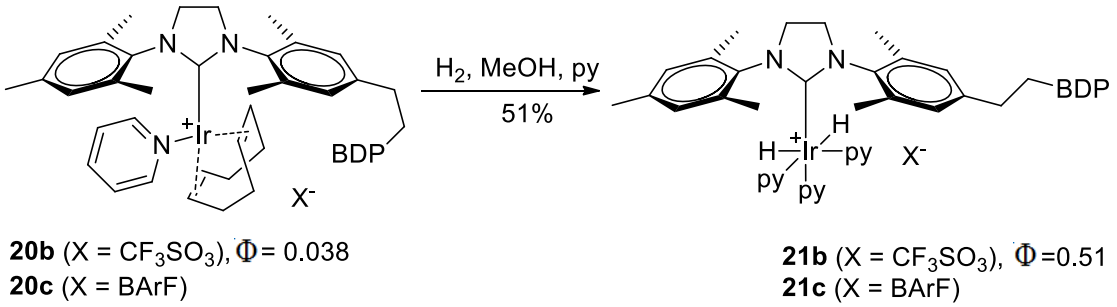

Figure 61: Reaction of BODIPY-tagged Crabtree complexes **20** with H_2.

5. The catalytic properties of the new iridium complexes were studied. The room-temperature reaction of the test substrate allylbenzene with hydrogen in the presence of **20c** provides

the fully hydrogenated product within 10 min in nearly quantitative yield at 0.5 mol % catalyst loading in 1,2-dichloroethane. The time-dependent fluorescent intensity of complexes **20** ($c=1.0\cdot10^{-6}$ mol·L^{-1} in 1,2-dichloroethane, 0.1 mol% catalyst loading) during the catalytic reaction with different olefin substrate was monitored. The increase in the fluorescence intensity is virtually the same as observed for the experiment conducted under the same conditions in the absence of substrate. Based on this, it is likely that an iridium dihydride species is the resting state of the catalytic reaction.

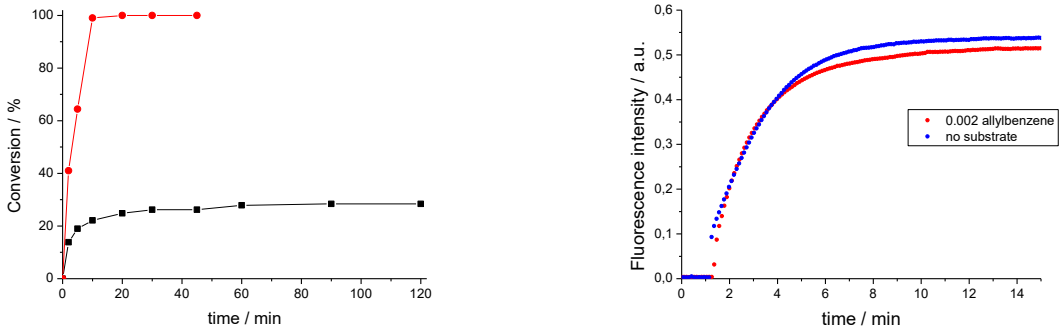

Figure 62: Left: conversion-time plot for the catalytic hydrogenation of 0.1 M allylbenzene by **20c** ($1.0\cdot10^{-3}$ mol·L^{-1}, 1 mol %) (red) and 0.002 M allylbenzene by **20c** ($1.0\cdot10^{-5}$ mol·L^{-1}, 0.5 mol %) (black) in 1,2-dichloroethane with hydrogen. Right: fluorescence – time plots for the catalytic hydrogenation of 0.002 mol·L^{-1} allylbenzene with **20c** ($1.0\cdot10^{-3}$ mol·L^{-1}, 0.5 mol %) (red); same reaction conditions, but without olefin (blue).

6. A simple paper strip method for H_2 detection was developed. By exposing filter paper impregnated with a solution of **20b** in propylene carbonate to a H_2-containing atmosphere, it is possible to detect hydrogen at a concentration corresponding to the lower explosion limit (4% vol) and to distinguish this from a lower hydrogen concentration (1% vol).

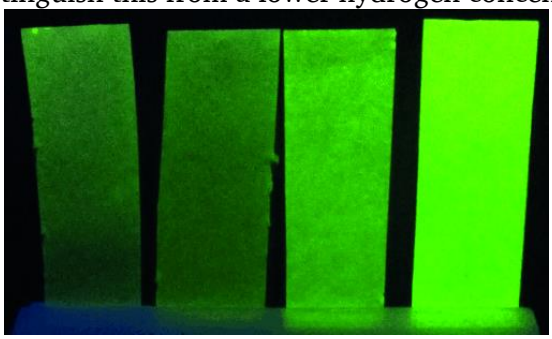

Figure 63: Four filter paper strips (left to right: a–d) impregnated with a solution of **20b** in propylene carbonate and irradiated with broadband UV light. Strip (a) exposed to ambient air; strip (b) exposed to 1 % (vol) H_2; strip (c) exposed to 4 % (vol) H_2 (lower explosion limit), and strip (d) exposed to pure H_2.

In the absence of H_2, the solution of **20b** in this solvent is highly stable and doesn't change its fluorescence properties in the presence of ambient air over long periods of time. Being relatively cheap, easy to use, and sufficiently sensitive to detect hydrogen at its lower explosion limit concentration, this paper strip assay can develop into popular method to detect industrial H_2 leaks. Complexes **20** are the first reported fluorescent molecular probes for H_2.

7. Five BODIPY-tagged metathesis complexes were synthesized, with the fluorophore connected to either the NHC or the benzylidene group (figure 64). The fluorescence of BODIPY in all complexes is strongly quenched by ruthenium.

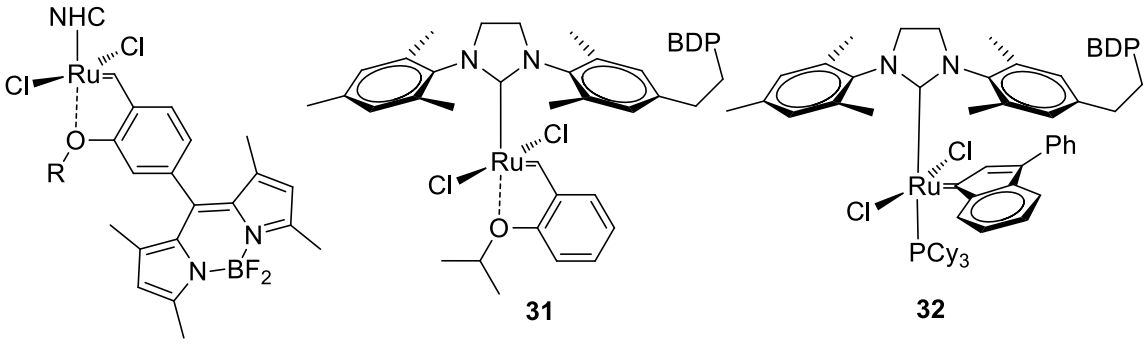

26: NHC= SIPr, R= $(CH_2)_{11}Si(OiPr)_3$
30-NHC: NHC= SIMes, SIPr; R= *i*Pr

Figure 64: Newly developed BODIPY-tagged olefin metathesis complexes.

8. Complex **26** was used for the observation of the ROMP of a norbornene on the single-molecule level. For this, **26** was immobilized on a glass surface and the modified coverslips were investigated using a TIRF microscope. Fluorescence properties of surface-bound single molecules were investigated. Irradiation of the sample with laser light results in the high-frequency blinking of the dye. The observed blinking is considered to be related to the continuous "on-off" states switching due to the photobleaching of BODIPY. Under the used acquisition parameters, our probe has an insufficient active state life-time for the extended observation of ROMP on the single-molecule level. Further improvement of the catalyst structure and acquisition parameters is required.

9. Reactions of synthesized compounds **30** – **32** with different olefins were conducted and changes in the emission and absorption spectra were monitored by fluorescence and UV/Vis spectroscopy. Upon initiation of complex **30**-SiMes, a pronounced increase (up to 30-fold) in the fluorescence intensity of BODIPY unit is observed. A detailed kinetic analysis of the corresponding emission-time traces at 512 nm showed identical rate constant values to those, derived from the analysis of the drop in absorbance intensity of the LMCT band. This indicates that the dissociation of Ru-O bond is a limiting step of the initiation reaction.

In this thesis it was shown that fluorescence spectroscopy is a very useful tool in organometallic chemistry. Changes in the electron density at the metal center of the fluorophore-tagged complex translate into changes in the emission intensity of fluorescent labels. This phenomenon can be used for the development of unique molecular sensors. Additionally, such complexes could become valuable for the detailed investigation of catalytic transformations at metal centers. Detectable changes in the fluorescence can be used for the detection and the quantification of the individual species in complex reaction mixtures, which are present in small concentrations not amenable to most other spectroscopic techniques.

5. Experimental Part

General experimental. All reactions involving transition metal complexes were conducted in oven-dried glassware. Reactions were performed in Schlenk flasks under a positive pressure of argon or nitrogen. The flasks were fitted with rubber septa and gas-tight syringes with stainless steel needles or double-cannula were used to transfer air- and moisture-sensitive liquids.

Materials. All chemicals were purchased as reagent grade from commercial suppliers and used without further purification unless otherwise noted. CH_2Cl_2 (99.5) and pentane (99) were obtained from Grüssing GmbH, Toluene from Sigma-Aldrich (Lab. Reagent grade, 99.3%). These solvents were dried and degassed by using a column purification system from Innovative Technology Inc. Tetrahydrofuran was dried under sodium and distilled under argon atmosphere. All solvents were stored over molecular sieves (4 Å). Preparative chromatography was performed using Merck silica 60 (0.063 – 0.2 mm). 2-iodo-1,3,5,7,8-pentamethyl-4,4-difluoro-4-bora-3a,4a-diaza-*s*-indacene[289] and 1-iodo-2-[2-(2-methoxyethoxy)ethoxy]ethane[290] were synthesized following known procedures.

Instrumentation. ^{1}H, ^{19}F, and ^{13}C-NMR spectra were recorded on a Bruker DRX 500 or Bruker ARX 300 spectrometer. The chemical shifts are given in parts per million (ppm) on the delta scale (δ) and are referenced to tetramethylsilane (^{1}H, ^{13}C-NMR = 0.0 ppm), the residual peak of $CHCl_3$ (^{1}H-NMR = 7.26 ppm, ^{13}C-NMR = 77.16 ppm), the residual peak of DMSO (^{1}H-NMR = 2.50 ppm, ^{13}C-NMR = 39.52 ppm) or hexafluorobenzene (^{19}F-NMR = -164.90 ppm). Abbreviations for NMR data: s = singlet; d = doublet; t = triplet; q = quartet; sep = septet; m = multiplet; bs = broad signal. Mass spectra were recorded on the Finnigan MAT95 spectrometer using electron ionization (EI). UV-Vis spectra were recorded on Analytik Jena Specord 600 UV-Vis spectrometer, fluorescence spectra were recorded on J&M TIDAS S700/CCD UV/NIR 2098 spectrometer combined with J&M TIDAS LSM monochromator with 75 W Xenon light source and temperature-controlled cuvette holder. Cyclic voltammetry was performed using a standard electrochemical instrumentation consisted of an EG&G 273A-2 potentiostat-galvanostat. A three-electrode configuration was employed. The working electrode was a Pt disk (diameter 1 mm) sealed in the soft glass with a Pt wire as a counter electrode. The pseudo reference electrode was an Ag wire. Potentials were calibrated internally against the formal potential of ferrocene (+0.46 V vs. Ag/AgCl). All cyclic voltammograms were recorded in dry CH_2Cl_2 under an atmosphere of argon, supporting electrolyte N*n*Bu$_4$PF$_6$ (c = 0.1 mol/L). Samples for emission and absorption measurements were contained in 1 cm × 1 cm quartz cuvette (Hellma Analytics), kinetic measurements with gases were conducted in 1 cm × 1 cm quartz cuvette equipped with septa (Hellma Analytics) using Hamilton 1700 series gas tight syringes.

5.1. Experimental Procedures and Compounds Characterization

Synthesis of 8-(1*H*-imidazol-1-yl)-BODIPY 1

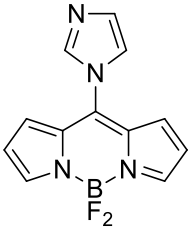

1

To a flame-dried Schlenk flask equipped with stirring bar and containing *meso*-chloro BODIPY (500 mg, 2.2 mmol, 1 eq), 1*H*-imidazole (226 mg, 3.3 mmol, 1.5 eq) and potassium carbonate (762 mg, 5.5 mmol, 2.5 eq), dichloromethane (20 mL) was added. Flask was sealed and stirred overnight at room temperature. To the reaction mixture water (100 mL) was added and the product was extracted with dichloromethane (3 × 25 mL). Combined organic layers were washed with brine (100 mL), dried over magnesium sulfate and volatiles were removed under reduced pressure to afford the product as a dark red microcrystalline solid (542 mg, 95% yield).

^{1}H NMR (500 MHz, $CDCl_3$) δ 7.97 (s, 2H, H_{BODIPY}), 7.96 (s, 1H, $H_{imidazole}$), 7.43 (t, J = 1.2 Hz, 1H, $H_{imidazole}$), 7.33 (s, 1H, $H_{imidazole}$), 7.14 (d, J = 4.3 Hz, 2H, H_{BODIPY}), 6.64 (d, J = 4.3 Hz, 2H, H_{BODIPY}).
^{13}C NMR (126 MHz, $CDCl_3$) δ 145.94, 138.98, 137.75, 131.44, 130.46, 129.46, 122.55, 119.76.

Synthesis of imidazolium salt 2

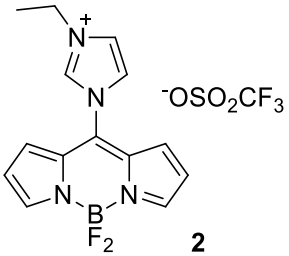

2

To a flame-dried Schlenk flask equipped with stirring bar and containing imidazole **1** (726 mg, 2.8 mmol, 1 eq), dichloromethane (25 mL) and ethyl trifluoromethyl sulfonate (401 μL, 3.1 mmol, 1.1 eq) were added. Flask was sealed and stirred overnight at room temperature. To the resulting suspension diethyl ether (100 mL) was added, the precipitate was filtered and washed two times with another batch of diethyl ether (2 × 20 mL). The filter cake was dried under vacuum to give the product (1.07 g, 86% yield) as a red microcrystalline solid.

^{1}H NMR (500 MHz, DMSO-d_6) δ 9.92 (s, 1H, $H_{imidazole}$), 8.40 (t, J = 1.8 Hz, 1H, $H_{imidazole}$), 8.38 (s, 2H, H_{BODIPY}), 8.22 – 8.17 (m, 1H, $H_{imidazole}$), 7.45 (d, J = 4.3 Hz, 2H, H_{BODIPY}), 6.85 (d, J = 4.2 Hz, 2H, H_{BODIPY}), 4.34 (q, J = 7.3 Hz, 2H, CH_2CH_3), 1.55 (t, J = 7.3 Hz, 3H, CH_2CH_3).

Synthesis of imidazoles 3 and 5

General procedure. To the solution of corresponding aniline (1 eq) in methanol was added glyoxal (40% in water, 1 eq) and the mixture stirred at rt for 2 h. The resulting yellow suspension was transferred to a bigger flask and diluted with additional methanol. NH_4Cl (2 eq) and formaldehyde (37% in water, 2.1 eq) were added and the reaction mixture was heated under reflux for 1 h. To the hot solution, phosphoric acid (85%) was slowly added through the top of the condenser and the resulting mixture was refluxed for another 4 h. The reaction mixture was cooled to rt. 80% of solvent were evaporated under reduced pressure. The residue were poured into ice water (300 mL) and the solution was basified. The resulting precipitate was filtered, dried under reduced pressure and washed with 100 mL of hot pentane.

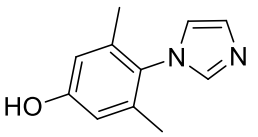

3

4-(1*H*-imidazol-1-yl)-3,5-dimethylphenol **3** was obtained as a white solid (5.3 g, 78% yield) from 4-amino-3,5-dimethylphenol (5 g, 36.4 mmol), methanol (18 mL, 150 mL for dilution), glyoxal (4.16 mL, 40% in water, 36.4 mmol), NH_4Cl (3.9 g, 72.8 mmol), formaldehyde (5.83 mL, 37% in water, 76.4 mmol), phosphoric acid (5.1 mL, 85%). The final solution was basified with 40% NaOH to pH ~6-7 and later carefully with saturated $NaHCO_3$ to pH ~4.
^{1}H NMR (300 MHz, CD_3OD) δ 7.59 (s, 1H, NC*H*N), 7.16 (s, 1H, NC*N*CHN), 7.05 (s, 1H, NCHC*H*N), 6.60 (s, 2H, H_{Ar}), 1.93 (s, 6H, CH_3).

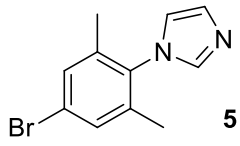

5

1-(4-bromo-2,6-dimethylphenyl)-1*H*-imidazole **5** was obtained as off-white microcrystalline solid (20.6 g, 82% yield) from 4-bromo-2,6-dimethylaniline (20.0 g, 0.1 mol), methanol (50 mL, 400 for 86arbine86), glyoxal (11.4 mL, 40% in water, 0.1 mol), NH_4Cl (10.7 g, 0.2 mol), formaldehyde (16 mL, 37% in water, 0.21 mol), phosphoric acid (14 mL, 85%). Final solution was basified to pH 9 with 40% NaOH.
^{1}H-NMR (300 MHz, $CDCl_3$): δ 7.40 (s, 1H, NCHN), 7.28 (s, 2H, H_{Ar}), 7.22 (s, 1H, NC*H*CHN), 6.86 (s, 1H, NCHC*H*N), 1.97 (s, 6H, CH_{3Ar}).
^{13}C-NMR (75 MHz, $CDCl_3$): δ 137.89, 137.16, 135.02, 131.23, 130.03, 122.69, 119.74, 17.34.

Synthesis of imidazole 4

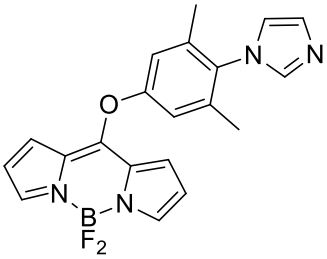

To a flame-dried Schlenk-flask, equipped with a stirring bar and containing potassium carbonate (244 mg, 1.8 mmol, 2 eq), *meso*-chloroBODIPY (200 mg, 0.9 mmol, 1 eq) and imidazole **3** (167 mg, 0.9 mmol, 1 eq), dichloromethane (20 mL) was added. The flask was sealed and the reaction mixture was stirred overnight at room temperature. The resulted suspension was filtered and the filtrate was evaporated under reduced pressure. The product was purified by filtration through the pad of silica (Cyclohexane/ethyl acetate, 1:3), the filtrate was evaporated and residue were dried under vacuum to give the product as a red solid (210 mg, 62% yield).

^{1}H NMR (300 MHz, $CDCl_3$) δ 7.78 (s, 2H, H_{BODIPY}), 7.52 (s, 1H, NCHN), 7.30 (s, 1H, NC*H*CHN), 7.06 (s, 2H, H_{Ar}), 6.96 (s, 1H, NCHC*H*N), 6.86 (d, J = 4.2 Hz, 2H, H_{BODIPY}), 6.47 (d, J = 3.8 Hz, 2H, H_{BODIPY}), 2.07 (s, 6H, CH_3).

Synthesis of 1-(2,6-dimethyl-4-((trimethylsilyl)ethynyl)phenyl)-1H-imidazole 6

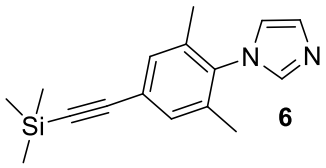

6

To a flame-dried Schlenk-flask equipped with stirring bar, septa and containing **5** (5 g, 19.9 mmol, 1 eq), Na_2PdCl_4 (56.6 mg, 0.119 mmol, 0.01 eq), tert-butyldicyclohexylphosphonium tetrafluoroborate (136.3 mg, 0.238 mmol, 0.02 eq) and CuI (37.9 mg, 0.119 mmol, 0.01 eq), diisopropylamine (100 mL) was transferred via cannula and the mixture was carefully degassed via "freeze and thaw" technique. After being warmed to r.t., TMS-acetylene (2.98 mL, 20.9 mmol, 1.05 eq) was added via syringe, the flask was sealed, the reaction mixture was warmed up to 80 °C and remained stirred at this temperature for 4 h. After the mixture was cooled down to r.t., the precipitate was separated by filtration and washed twice with diethyl ether (2 × 25 mL). The volatiles were evaporated in vacuo to give the product as a brownish oil (4.76 g, 89 % yield) which was used in the next step without further purification.

^{1}H NMR (300 MHz, $CDCl_3$) δ 7.47 (bs, 1H, NCHN), 7.26 (bs, 3H, NC*H*CHN, H_{Ar}, overlapped with solvent residual peak), 6.94 (bs, 1H, NCHC*H*N), 1.98 (s, 6H, CH_{3Ar}), 0.25 (s, 9H, $CH_{3\ TMS}$).

^{13}C NMR (75 MHz, $CDCl_3$) δ 136.16, 135.90, 131.86, 124.09, 104.00, 95.60, 17.35, 0.01.

Synthesis of 1-(4-ethynyl-2,6-dimethylphenyl)-1H-imidazole 7

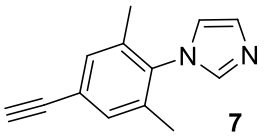

7

To a round-bottom flask equipped with stirring bar and containing a solution of **6** (1.53 g, 5.7 mmol, 1 eq) in THF (20 mL), tetrabutylammonium fluoride (1.89 g, 6.0 mmol, 1.05 eq) was added and the mixture was stirred at rt for 1 h. Resulted solution was diluted with water (150 mL) and extracted with diethyl ether (3 × 30 mL). Combined organic layers were washed with brine and dried over anhydrous $MgSO_4$. The solution was collected by filtration and evaporated under reduced pressure to provide brownish oil as a product (0.93 g, 83% yield), which was used in the next step without further purification.

^{1}H NMR (500 MHz, $CDCl_3$) δ 7.43 (s, 1H, H, NCHN), 7.29 – 7.20 (m, 3H, NC*H*CHN, H_{Ar}), 6.88 (s, 1H, NCHC*H*N), 3.08 (s, 1H, CCH), 1.99 (s, 6H, CH_3).

^{13}C NMR (126 MHz, $CDCl_3$) δ 137.23, 136.48, 136.10, 132.02, 130.04, 122.98, 119.79, 82.71, 78.21, 17.36.

Synthesis of imidazole 8

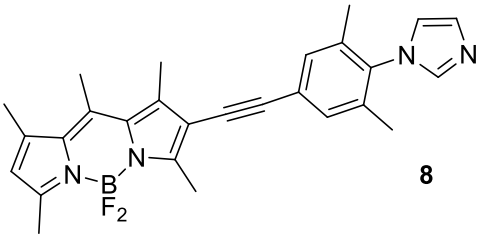

8

2-iodo-1,3,5,7,8-pentamethyl-4,4-difluoro-4-bora-3a,4a-diaza-*s*-indacene (300 mg, 0.77 mmol, 1 eq) and **7** (167 mg, 0.85 mmol, 1.1 eq) were loaded into flame-dried Schleck flask equipped with the stirring bar and septa. Diisopropylamine (10 mL) was added via cannula and the mixture was additionally degassed (1 cycle of freeze-pump-thaw). Na_2PdCl_4 (4.5 mg, 15.4 μmol, 2 mol %), CuI (2.9 mg, 15.4 μmol, 2 mol %) and $Cy_2tBuP{\cdot}HBF_4$ (10.6 mg, 30.8 μmol, 4 mol %) were added and the mixture was heated up to 80 °C in the sealed flask and remained stirred at this temperature overnight. Formed white precipitate was filtered off and washed with diisopropylamine (3 × 10 mL). The filtrate was evaporated under reduced pressure and the remaining dark viscous oil was purified by column chromatography (cyclohexane / ethyl acetate, 1:4). The product was obtained as a dark purple microcrystalline solid (206 mg, 58% yield).

^{1}H NMR (500 MHz, $CDCl_3$) δ 7.55 (s, 1H, $H_{Imidazole}$), 7.31 (s, 3H, H_{Ar}, $H_{Imidazole}$), 6.94 (s, 1H, $H_{Imidazole}$), 6.12 (s, 1H, H_{BODIPY}), 2.67 (s, 3H, $CH_{3\ BODIPY}$), 2.62 (s, 3H, $CH_{3\ BODIPY}$), 2.56 – 2.52 (m, 6H, $CH_{3\ BODIPY}$), 2.43 (s, 3H, $CH_{3\ BODIPY}$), 2.03 (s, 6H, $CH_{3\ Ar}$).

^{13}C NMR (126 MHz, $CDCl_3$) δ 156.47, 154.73, 143.14, 142.07, 140.35, 137.14, 136.02, 135.38, 133.45, 131.16, 131.05, 129.28, 124.84, 122.58, 120.18, 114.53, 94.83, 83.66, 17.64, 17.45, 16.81, 15.99, 14.74, 13.57.

^{19}F NMR (282 MHz, $CDCl_3$) δ -149.59 (1:1:1:1 pattern, $J(^{19}F - ^{11}B)$ = 31.7 Hz).

Synthesis of BODIPY-imidazolium salt 9

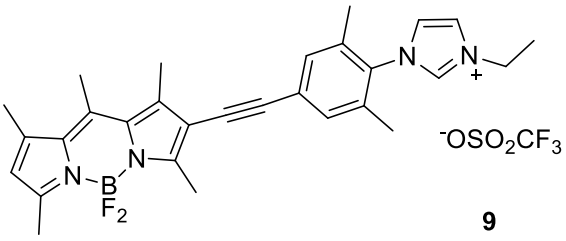

9

To a flame-dried Schleck flask equipped with stirring bar and containing **8** (298 mg, 0.65 mmol, 1 eq) and dichloromethane (4 mL), ethyl trifluoromethylsulfonate (84.7 μL, 0.72 mmol, 1.1 eq) was added. The flask was sealed and stirred overnight at room temperature. To the resulting solution diethyl ether (100 mL) was added, the precipitate was filtered and washed two times with another batch of diethyl ether (2 × 20 mL). The filter cake was dried under vacuum to give the product (177 mg, 84% yield) as a red microcrystalline solid.

^{1}H NMR (300 MHz, DMSO-d_6) δ 9.45 (s, 1H, NCHN), 8.13 (s, 1H, NC*H*CHN), 7.98 (s, 1H, NCHC*H*N), 7.54 (s, 2H, H_{Ar}), 6.37 (s, 1H, H_{BODIPY}), 4.32 (q, J = 7.2 Hz, 2H, CH_2CH_3), 2.67 (s, 3H, $CH_{3\ BODIPY}$), 2.56 (s, 6H, $CH_{3\ BODIPY}$), 2.48 – 2.43 (m, 6H, $CH_{3\ BODIPY}$), 2.09 (s, 6H, $CH_{3\ Ar}$), 1.53 (t, J = 7.3 Hz, 3H, CH_2CH_3).

^{13}C NMR (75 MHz, DMSO-d_6) δ 156.62, 152.41, 144.58, 143.56, 140.03, 136.95, 135.54, 133.31, 133.02, 130.90, 130.12, 124.97, 123.67, 123.02, 122.91, 94.27, 83.92, 44.90, 17.09, 16.80, 16.49, 15.38, 14.84, 14.32, 13.10.

^{19}F NMR (282 MHz, DMSO-d_6) δ -80.76 (s, 3F, CF_3), -147.06 (1:1:1:1 pattern, $J(^{19}F-^{11}B)$ = 26.8 Hz, 2F, BF_2).

Synthesis of boronic acid 10

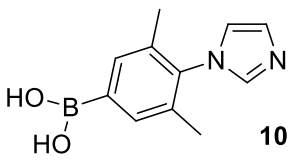

10

To a solution of 1-(4-bromo-2,6-dimethylphenyl)-1*H*-imidazole **5** (10.0 g, 39.8 mmol, 1 eq) and $B(OiPr)_3$ (11.78 mL, 59.7 mmol, 1.5 eq) in thf (100 mL) cooled to -78 °C was dropwise added *n*-BuLi (35 mL, 2.5 M in hexane, 87.6 mmol, 2.2 eq). Next, the mixture was stirred at -78°C for 1 h, then allowed to warm to rt and stirred overnight. The reaction was quenched by addition of concentrated aq. NH_4Cl (5 mL) and the volatiles were evaporated in vacuum. HCl (50 mL, 37% aq.) was added and the solution was

heated to reflux for 1 h, then cooled down to rt and carefully adjusted with NaOH (1 M solution) to pH 5 and then with a saturated $NaHCO_3$ solution to pH 8. A white precipitate formed, was collected by filtration and dried under vacuum to provide a white solid (6.3 g, 72% yield). The product was used in the next reaction without additional purification.
^{1}H-NMR (300 MHz, $CDCl_3$): δ 7.77 (s, 2H, H_{Ar}), 7.66 (s, 1H, NCHN), 7.37 (s, 1H, NC*H*CHN), 6.98 (s, 1H, NCHC*H*N), 2.09 (s, 6H, CH_{3Ar}). ^{1}H-NMR (300 MHz, D_2O), Na-salt of **2**: δ 7.68 (s, 1H, NCHN), 7.41 (s, 2H, H_{Ar}), 7.25 (s, 1H, NC*H*CHN), 7.17 (s, 1H, NCHC*H*N), 2.02 (s, 6H, CH_{3Ar}).
^{13}C-NMR (75 MHz, $CDCl_3$): δ 140.7 (br, $CB(OH)_2$), 136.51, 136.36, 133.87, 133.74, 127.66, 120.73, 17.62.
^{13}C NMR (75 MHz, D_2O), Na-salt of **2**: δ 138.41, 133.61, 133.07, 131.02, 127.77, 121.58, 121.04, 16.51.
HR-MS (EI), m/z: 594.28871 $[3M - 3H_2O]^{+\bullet}$, calcd. 594.2894 (Δ = -0.7 mmu).

Synthesis of imidazole 11

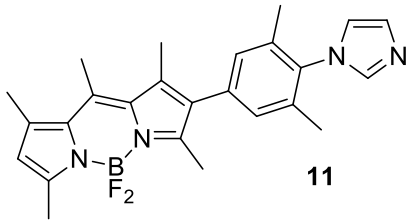

11

Boronic acid **10** (1.0 g, 4.63 mmol, 1.5 eq), 2-iodo-1,3,5,7,8-pentamethyl-4,4-difluoro-4-bora-3a,4a-diaza-*s*-indacene (1.2 g, 3.09 mmol, 1 eq) and K_2CO_3 (6.4g, 46.3 mmol, 10 eq) were loaded into 250 mL flame-dried Schlenk flask equipped with a stirring bar. Toluene (50 mL), thf (50 mL) and water (10 mL) were added and the mixture degassed (2 cycles of freeze-pump-thaw). $[Pd(PPh_3)_4]$ (107 mg, 0.093 mmol, 2 mol %) was added and the mixture heated in a sealed flask at 70°C overnight. After evaporation of the volatiles under reduced pressure, water (150 mL) was added and the mixture was extracted with CH_2Cl_2 (3 x 50 mL). The combined organic layers were washed with brine (100 mL), dried over anhydrous $MgSO_4$, filtered and evaporated. The product was purified by column chromatography (cyclohexane / ethyl acetate, 1:1) to afford the product as an orange microcrystalline solid (1.82 g, 91% yield).
^{1}H-NMR (300 MHz, $CDCl_3$): δ 7.69 (s, 1H, NCHN), 7.34 (s, 1H, NC*H*CHN), 7.01 (s, 3H, H_{Ar}, NCHC*H*N), 6.10 (s, 1H, H_{BODIPY}), 2.65 (s, 3H, $CH_{3BODIPY}$), 2.54 (s, 3H, $CH_{3BODIPY}$), 2.49 (s, 3H, $CH_{3BODIPY}$), 2.44 (s, 3H, $CH_{3BODIPY}$), 2.35 (s, 3H, $CH_{3BODIPY}$), 2.08 (s, 6H, CH_{3Ar}).
^{13}C-NMR (75 MHz, $CDCl_3$): δ 154.84, 151.32, 141.89, 137.02, 136.74, 135.69, 135.47, 134.49, 132.81, 132.28, 132.10, 131.78, 130.56, 128.51, 121.93, 120.37, 17.66, 17.61, 16.96, 15.53, 14.63, 13.33.
^{19}F-NMR (282 MHz, $CDCl_3$): δ -149.60 (1:1:1:1 pattern, $J(^{19}F\text{-}^{11}B)$ = 32.0 Hz).
HR-MS (EI), m/z: 432.23294 $[M]^{+\bullet}$, calcd. 432.2298 (Δ = 3.1 mmu).

Synthesis of imidazolium iodide 12·HI

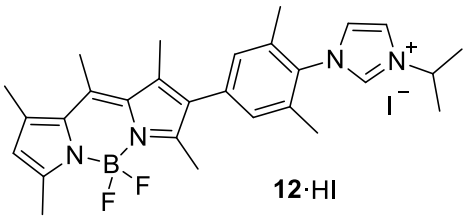

12·HI

To the imidazole **11** (500 mg, 1.15 mmol, 1 eq), 2-iodopropane (1.5 mL, 15 mmol, 13 eq) was added and the mixture was stirred in the sealed flask at 70°C overnight. The mixture was cooled to room temperature, 10 mL of diethyl ether were added and the precipitate was filtered off and washed with diethyl ether (3 x 10 mL) to afford the product, which was used in the next steps without further purification (0.65 g, 94% yield).
^{1}H-NMR (300 MHz, dmso-d_6): δ 9.59 (s, 1H, NCHN), 8.25 (s, 1H, NC*H*CHN), 8.08 (s, 1H, NCHC*H*N), 7.28 (s, 2H, H_{Ar}), 6.31 (s, 1H, H_{BODIPY}), 4.76 (sep, J = 6.6 Hz, 1H, $CH(CH_3)_2$), 2.70 (s, 3H, $CH_{3BODIPY}$), 2.46 (bs, 6H, $CH_{3BODIPY}$), 2.41 (s, 3H, $CH_{3BODIPY}$), 2.37 (s, 3H, $CH_{3BODIPY}$), 2.14 (s, 6H, CH_{3Ar}), 1.60 (d, J = 6.6 Hz, 6H, $CH(CH_3)_2$).
^{13}C-NMR (75 MHz, dmso-d6): δ 154.15, 149.61, 143.18, 142.65, 136.85, 136.04, 135.93, 135.62, 134.99, 132.62, 132.13, 130.86, 130.37, 123.97, 121.91, 121.55, 52.98, 22.30, 17.04, 17.00, 16.62, 14.95, 14.15, 12.96.

^{19}F-NMR (282 MHz, dmso-d6): δ -146.02 (1:1:1:1 pattern, $J(^{19}F\text{-}^{11}B)$ = 26 Hz).
HR-MS (EI), m/z: 432.22795 $[M - I - iPr]^{+\bullet}$, calcd. 432.2298 (Δ = -1.8 mmu).

Synthesis of imidazolium iodide 13·HI

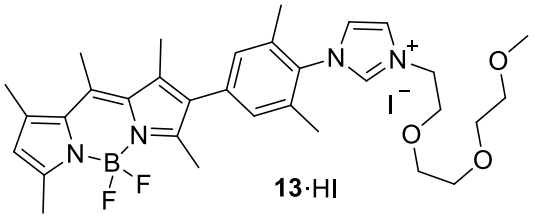

To the solution of imidazole **11** (500 mg, 1.15 mmol, 1 eq) in toluene (10 mL), 1-iodo-3,6,9-trioxadecane (473 mg, 1.75 mmol, 1.5 eq) was added and the mixture was stirred in the sealed flask at 100°C overnight. The mixture was cooled to room temperature, 30 mL of diethyl ether were added and the precipitate was filtered off and washed with diethyl ether (3 x 10 mL) to afford the product, which was used in the next steps without further purification (0.77 g, 95% yield).
^{1}H-NMR (500 MHz, $CDCl_3$): δ 9.79 (s, 1H, NCHN), 8.22 (t, J = 1.4 Hz, 1H, NC*H*CHN), 7.24 (t, J = 1.7 Hz, 1H, NCHC*H*N), 7.05 (s, 2H, CH_{3Ar}), 6.11 (s, 1H, H_{BODIPY}), 4.97 (t, J = 4.4 Hz, 2H, NC$H_2$$CH_2$O), 4.01 (t, J = 4.4 Hz, 2H, NCH_2CH_2O), 3.73 – 3.70 (m, 2H, OC$H_2$$CH_2$O), 3.64 – 3.61 (m, 2H, OCH_2CH_2O), 3.59 – 3.56 (m, 2H, OC$H_2$$CH_2$O), 3.46 – 3.43 (m, 2H, OCH_2CH_2O), 3.25 (s, 3H, OCH_3), 2.64 (s, 3H, $CH_{3BODIPY}$), 2.53 (s, 3H, $CH_{3BODIPY}$), 2.46 (s, 3H, $CH_{3BODIPY}$), 2.44 (s, 3H, $CH_{3BODIPY}$), 2.33 (s, 3H, $CH_{3BODIPY}$), 2.17 (s, 6H, CH_{3Ar}).
^{13}C-NMR (126 MHz, $CDCl_3$) δ 155.34, 150.48, 142.37, 142.17, 137.57, 136.63, 134.96, 132.96, 132.04, 131.64, 131.21, 128.62, 125.94, 124.99, 122.52, 122.16, 71.81, 70.32, 70.26, 69.04, 58.93, 50.52, 18.09, 17.64, 16.99, 15.52, 14.65, 13.24.
^{19}F-NMR (282 MHz, $CDCl_3$) δ -149.51 (1:1:1:1 pattern, $J(^{19}F\text{-}^{11}B)$ = 30.4 Hz).

Synthesis of complexes [(12)RhCl(cod)] and [(12)IrCl(cod)]
General procedure. To a Schlenk flask equipped with a stirring bar and containing imidazolium salt **4**·HI and Ag_2O, dichloromethane was added and the flask sealed. After 30 min of stirring in the dark at 40 °C, $[MCl(cod)]_2$ (M= Rh, Ir) was added and the mixture stirred for an additional 30 min at 40°C and then allowed to r.t. The resulting suspension was filtered through a short plug of celite. The filtrate was collected and evaporated under reduced pressure. The product was purified by column chromatography (cyclohexane / ethyl acetate, 2:1).

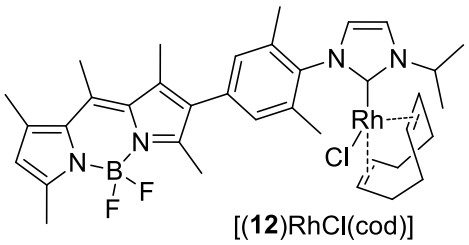

Complex [(**12**)RhCl(cod)] was obtained as an orange microcrystalline solid (120 mg, 69% yield) from **12**·HI (150 mg, 249 μmol, 1 eq), Ag_2O (28.9 mg, 125 μmol, 0.5 eq), $[RhCl(cod)]_2$ (61.4 mg, 125 μmol, 0.5 eq) and CH_2Cl_2 (4 mL).
^{1}H-NMR (300 MHz, $CDCl_3$): δ 7.13 (s, 1H, H_{Ar}), 7.10 (d, J = 1.9 Hz, 1H, NC*H*CHN), 6.95 (s, 1H, H_{Ar}), 6.88 (d, J = 1.9 Hz, 1H, NCHC*H*N), 6.18 (sep, J = 6.8 Hz, 1H, C*H*$(CH_3)_2$), 6.10 (s, 1H, H_{BODIPY}), 4.91 – 4.79 (m, 2H, H_{cod}), 3.51-3.56 (m, 1H, H_{cod}), 3.02 – 2.93 (m, 1H, H_{cod}), 2.67 (s, 3H, $CH_{3BODIPY}$), 2.55 (s, 3H, $CH_{3BODIPY}$), 2.53 (s, 6H, $CH_{3BODIPY}$), 2.46 (s, 3H, $CH_{3BODIPY}$), 2.39 (s, 3H, CH_{3Ar}), 2.22 – 1.93 (m, 4H, H_{cod}), 1.91 (s, 3H, CH_{3Ar}), 1.69 – 1.55 (m, 8H, H_{cod} + CH(CH_3)$_2$), 1.54 – 1.45 (m, 2H, H_{cod}).
^{13}C-NMR (75 MHz, $CDCl_3$): δ 181.32 (d, $J(^{13}C\text{-}^{103}Rh)$ = 51.4 Hz),, 154.56, 151.63, 141.86, 141.64, 137.90, 137.84, 136.88, 134.99, 134.83, 132.76, 131.91, 131.10, 129.51, 128.82, 123.40, 121.81, 116.97, 97.55 (d, $J(^{13}C\text{-}^{103}Rh)$ = 7.0 Hz), 96.85 (d, $J(^{13}C\text{-}^{103}Rh)$ = 7.4 Hz), 68.49 (d, $J(^{13}C\text{-}^{103}Rh)$ = 14.4 Hz), 66.78 (d, $J(^{13}C\text{-}^{103}Rh)$ = 14.5 Hz), 53.47, 34.81, 31.24, 29.90, 28.17, 27.63, 24.67, 23.17, 20.15, 18.14, 17.62, 16.97, 15.49, 14.66, 13.31.
^{19}F-NMR (282 MHz, $CDCl_3$): δ -149.63 (1:1:1:1 pattern, $J(^{19}F\text{-}^{11}B)$ = 31.4 Hz).
HR-MS (EI), m/z: 720.24481 $[M]^{+\bullet}$, calcd. 720.2445 (Δ = 0.3 mmu).

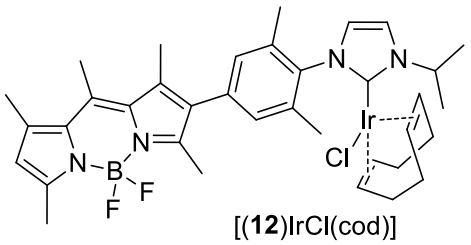

[(**12**)IrCl(cod)]

Complex [(**12**)IrCl(cod)] was obtained as an orange microcrystalline solid (153 mg, 75% yield) from **12**·HI (150 mg, 249 μmol, 1 eq), Ag_2O (28.9 mg, 125 μmol, 0.5 eq), $[IrCl(cod)]_2$ (83.6 mg, 125 μmol, 0.5 eq) and CH_2Cl_2 (4 mL).

^{1}H-NMR (500 MHz, $CDCl_3$): δ 7.12 (d, J = 2.0 Hz, 1H, NC*H*CHN), 7.06 (s, 1H, H_{Ar}), 6.94 (s, 1H, H_{Ar}), 6.87 (d, J = 1.8 Hz, 1H, NCHC*H*N), 6.10 (s, 1H, , H_{BODIPY}), 5.88 (sep, J = 6.7 Hz, 1H, C*H*(CH_3)$_2$), 4.52 (td, J = 7.5, 2.5 Hz, 1H, H_{cod}), 4.36 (q, J = 7.9 Hz, 1H, H_{cod}), 3.24 – 3.19 (m, 1H, H_{cod}), 2.67 (s, 3H, $CH_{3BODIPY}$), 2.55 (s, 3H, $CH_{3BODIPY}$), 2.51 (s, 3H, $CH_{3BODIPY}$), 2.45 (s, 3H, $CH_{3BODIPY}$), 2.42 (s, 3H, $CH_{3BODIPY}$), 2.37 (s, 3H CH_{3Ar}), 2.25 – 2.17 (m, 1H, H_{cod}), 2.02 – 1.95 (m, 4H, CH_{3Ar} + H_{cod}), 1.88 – 1.78 (m, 1H, H_{cod}), 1.73 – 1.64 (m, 2H, H_{cod}), 1.60 (d, J = 6.7 Hz, 3H, CH(C*H*$_3$)$_2$), 1.53 (d, J = 6.8 Hz, 3H, CH(C*H*$_3$)$_2$), 1.42 – 1.32 (m, 2H, H_{cod}), 1.16 – 1.09 (m, 1H, H_{cod}).

^{13}C-NMR (126 MHz, $CDCl_3$): δ 179.16, 154.49, 151.69, 141.83, 141.57, 137.69, 137.60, 136.91, 134.99, 134.79, 132.82, 132.73, 131.92, 130.95, 129.44, 123.19, 121.78, 116.78, 84.03, 82.38, 53.09, 52.26, 50.02, 35.64, 31.88, 30.68, 28.04, 24.54, 23.10, 19.99, 18.20, 17.61, 16.96, 15.48, 14.65, 13.31.

^{19}F-NMR (282 MHz, $CDCl_3$): δ -149.64 (1:1:1:1 pattern, J(^{19}F-^{11}B) = 31.0 Hz).

HR-MS (EI), m/z: 810.30616 $[M]^{+\bullet}$, calcd. 810.3019 (Δ = 4.3 mmu).

Synthesis of complexes [(12)RhI(cod)] and [(12)IrI(cod)]

General procedure

Method A. A flame-dried Schlenk flask equipped with stirring bar was loaded with $[MCl(cod)]_2$ and thf. Sodium *tert*.-pentylate (2.5M solution in thf) was added, the mixture stirred for 15 min at room temperature and then cooled to -10°C. After addition of imidazolium salt **4**·HI, the resulting mixture was stirred for another 15 min at -10°C and then for 1h at room temperature. After evaporation of the solvent under reduced pressure, the residue was purified by filtration through a silica pad (cyclohexane / ethyl acetate, 2:1). The filtrate was evaporated under reduced pressure and washed with pentane (10 mL) and methanol (5 mL).

Method B. A flame-dried Schlenk flask equipped with stirring bar was loaded with [(**12**)MCl(cod)] and KI. Thf was added and the mixture was stirred for 4 h at room temperature. The reaction mixture was filtered, the filtrate was evaporated under reduced pressure to afford the product.

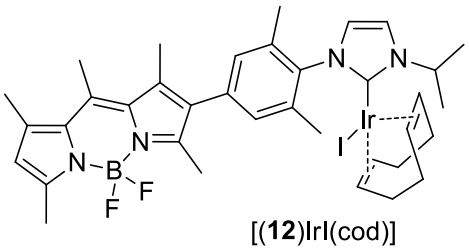

[(**12**)IrI(cod)]

Complex [(**12**)IrI(cod)] was obtained as orange microcrystalline solids. Method A: yield – 143 mg (46%) from $[IrCl(cod)]_2$ (114 mg, 0.17 mmol), sodium *tert*.-pentylate (172.9 μL, 0.43 mmol, 2.5 eq, 2.5 M solution in thf), **12**·HI (250 mg, 0.42 mmol, 2.4 eq) and thf (25 mL). Method B: yield – 60 mg (96%) from [(**12**)IrCl(cod)] (56 mg, 69 μmol, 1 eq), KI (12 mg, 0.69 mmol, 10 eq) and thf (4 mL).

^{1}H-NMR (300 MHz, $CDCl_3$): δ 7.13 (d, J = 1.8 Hz, 1H, NC*H*CHN), 7.03 (s, 1H, H_{Ar}), 6.93 (s, 1H, H_{Ar}), 6.89 (d, J = 1.6 Hz, 1H, NCHC*H*N), 6.10 (s, 1H, H_{BODIPY}), 5.85 (sep, J = 6.7 Hz, 1H, C*H*(CH_3)$_2$), 4.73 – 4.64 (m, 1H, H_{cod}), 4.61 – 4.52 (m, 1H, H_{cod}), 3.32 (d, J = 6.6 Hz, 1H, H_{cod}), 2.81 – 2.73 (m, 1H, H_{cod}), 2.67 (s, 3H, $CH_{3BODIPY}$), 2.55 (s, 3H, $CH_{3BODIPY}$), 2.52 – 2.48 (m, 6H, $CH_{3BODIPY}$), 2.46 (s, 3H, $CH_{3BODIPY}$), 2.36 (s, 3H, CH_{3Ar}), 2.26 – 2.05 (m, 2H, H_{cod}), 1.95 (s, 3H, CH_{3Ar}), 1.81 – 1.72 (m, 2H, H_{cod}), 1.59 (d, J = 6.7 Hz, 3H, CH(C*H*$_3$)$_2$), 1.51 (d, J = 6.7 Hz, 3H, CH(C*H*$_3$)$_2$), 1.37 – 1.14 (m, 2H, H_{cod}), 1.04 – 0.80 (m, 2H, H_{cod}).

^{13}C-NMR (75 MHz, $CDCl_3$): δ 178.47, 154.54, 151.63, 141.86, 141.61, 137.50, 137.40, 136.89, 135.32, 134.86, 132.75, 131.91, 131.11, 129.43, 123.99, 121.81, 116.99, 82.13,

80.71, 55.03, 53.53, 52.97, 35.45, 31.96, 30.75, 28.38, 24.69, 22.39, 21.94, 18.26, 17.65, 16.99, 15.50, 14.68, 13.32.
^{19}F-NMR (282 MHz, $CDCl_3$): δ -149.68 (1:1:1:1 pattern, $J(^{19}F\text{-}^{11}B)$ = 30.7 Hz).
MS (EI): m/z: 902 $[M]^{+\bullet}$ (HR-MS could not be obtained).

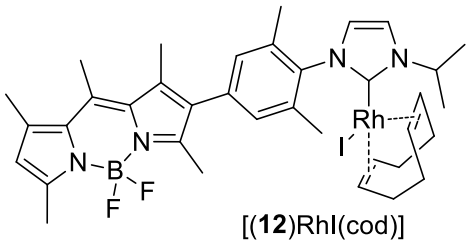
[(**12**)RhI(cod)]

Complex [(**12**)RhI(cod)] was obtained as an orange microcrystalline solid. Method A: yield – 107 mg (38%) from $[RhCl(cod)]_2$ (84 mg, 0.17 mmol), sodium *tert*.-pentylate (172.9 μL, 0.43 mmol, 2.5 eq, 2.5M solution in thf), **12**·HI (250 mg, 0.42 mmol, 2.4 eq) and thf (25 mL). Method B: yield – 55 mg (97%) from [(**12**)RhCl(cod)] (50 mg, 69 μmol, 1 eq), KI (12 mg, 0.69 mmol, 10 eq) and thf (4 mL).
^{1}H-NMR (500 MHz, $CDCl_3$): δ 7.11 (d, J = 2.0 Hz, 1H, NC*H*CHN), 7.10 (s, 1H, H_{Ar}), 6.94 (s, 1H, H_{Ar}), 6.91 (d, J = 1.8 Hz, 1H, NCHC*H*N), 6.14 (sep, J = 6.7 Hz, 1H, C*H*$(CH_3)_2$), 6.11 (s, 1H, H_{BODIPY}), 5.08 (bs, 2H, H_{cod}), 3.74 (t, J = 7.0 Hz, 1H, H_{cod}), 3.25 – 3.19 (m, 1H, H_{cod}), 2.67 (s, 3H, $CH_{3BODIPY}$), 2.58 (s, 3H, $CH_{3BODIPY}$), 2.56 (s, 3H, $CH_{3BODIPY}$), 2.52 (s, 3H, $CH_{3BODIPY}$), 2.46 (s, 3H, $CH_{3BODIPY}$), 2.38 (s, 3H, CH_{3Ar}), 2.13 – 1.94 (m, 3H, H_{cod}), 1.88 (s, 3H, CH_{3Ar}), 1.83 – 1.65 (m, 3H, H_{cod}), 1.63 (d, J = 6.7 Hz, 3H, CH(C*H*$_3)_2$), 1.56 (d, J = 6.8 Hz, 3H, CH(C*H*$_3)_2$), 1.42 – 1.37 (m, 2H, H_{cod}).
^{13}C-NMR (126 MHz, $CDCl_3$): δ 180.65 (d, $J(^{13}C\text{-}^{103}Rh)$ = 49.7 Hz), 154.62, 151.61, 141.87, 141.67, 137.75, 137.65, 136.86, 135.33, 134.94, 132.77, 131.93, 131.26, 129.52, 124.31, 121.84, 117.14, 95.32 (d, $J(^{13}C\text{-}^{103}Rh)$ = 6.7 Hz), 94.93 (d, $J(^{13}C\text{-}^{103}Rh)$ = 7.0 Hz), 71.39 (d, $J(^{13}C\text{-}^{103}Rh)$ = 13.7 Hz), 71.42 (d, $J(^{13}C\text{-}^{103}Rh)$ = 13.9 Hz), 53.62, 34.58, 30.97, 30.31, 27.99, 24.75, 22.47, 22.21, 18.20, 17.63, 16.99, 15.50, 14.67, 13.32.
^{19}F-NMR (282 MHz, $CDCl_3$): δ -149.66 (1:1:1:1 pattern, $J(^{19}F\text{-}^{11}B)$ = 31.0 Hz).
HR-MS (EI), m/z: 812.18824 $[M]^{+\bullet}$, calcd. 812.1871 (Δ = 1.1 mmu).

Synthesis of complexes [(13)RhI(cod)] and [(13)IrI(cod)]
General procedure. Synthesis of [(**13**)MI(cod)] was done similarly to the synthesis of [(**13**)MCl(cod)] from **13**·HI, Ag_2O, $[MCl(cod)]_2$ (M= Rh, Ir) in CH_2Cl_2 with a few changes. After filtration through the celite pad and evaporation, the residue was dissolved in small amount of thf, KI was added and the mixture was stirred for 4 h at room temperature. The reaction mixture was filtered, the volatiles were evaporated under reduced pressure and the residue was purified by column chromatography (cyclohexane / ethyl acetate, 1:1).

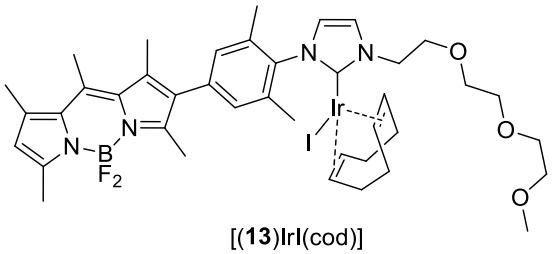
[(**13**)IrI(cod)]

Complex [(**13**)IrI(cod)] was obtained as an orange microcrystalline solid (97 mg, 75% yield) from **13**·HI (100 mg, 142 μmol, 1 eq), Ag_2O (16.4 mg, 72 μmol, 0.5 eq), $[IrCl(cod)]_2$ (47.5, 72 μmol, 0.5 eq), CH_2Cl_2 (4 mL) and KI (235 mg, 1.42 mmol, 10 eq).
^{1}H NMR (500 MHz, $CDCl_3$) δ 7.45 (d, J = 1.9 Hz, 1H), 7.02 (s, 1H), 6.93 (s, 1H), 6.83 (d, J = 1.9 Hz, 1H), 6.10 (s, 1H), 4.93 – 4.86 (m, 1H), 4.76 – 4.69 (m, 2H), 4.68 – 4.63 (m, 1H), 4.61 – 4.55 (m, 1H), 4.11 – 4.05 (m, 1H), 3.96 – 3.90 (m, 1H), 3.74 – 3.68 (m, 4H), 3.68 – 3.65 (m, 2H), 3.59 – 3.55 (m, 2H), 3.39 (s, 3H), 3.24 (t, J = 6.4 Hz, 1H), 2.80 – 2.74 (m, 1H), 2.66 (s, 3H), 2.55 (s, 3H), 2.50 (s, 3H), 2.48 (s, 3H), 2.45 (s, 3H), 2.36 (s, 3H), 2.13 – 2.06 (m, 1H), 1.95 (s, 3H), 1.94 – 1.88 (m, 1H), 1.80 – 1.67 (m, 2H), 1.41 – 1.32 (m, 2H), 1.25 – 1.21 (m, 1H), 0.99 – 0.91 (m, 1H).

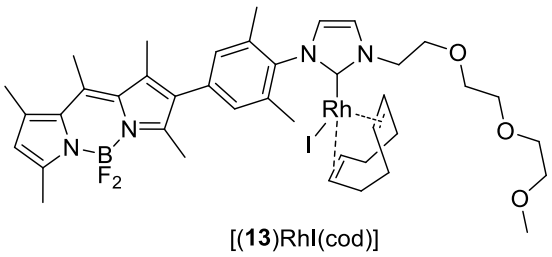

[(**13**)RhI(cod)]

Complex [(**13**)RhI(cod)] was obtained as an orange microcrystalline solid (96 mg, 82% yield) from **13**·HI (100 mg, 142 μmol, 1 eq), Ag_2O (16.4 mg, 72 μmol, 0.5 eq), $[RhCl(cod)]_2$ (35 mg, 72 μmol, 0.5 eq), CH_2Cl_2 (4 mL) and KI (235 mg, 1.42 mmol, 10 eq).

^{1}H-NMR (500 MHz, $CDCl_3$): δ 7.44 (d, J = 1.7 Hz, 1H), 7.09 (s, 1H), 6.94 (s, 1H), 6.85 (d, J = 1.7 Hz, 1H), 6.10 (s, 1H), 5.09 – 5.02 (m, 3H), 4.96 – 4.89 (m, 1H), 4.16 – 4.10 (m, 1H), 4.02 – 3.96 (m, 1H), 3.75 – 3.68 (m, 6H), 3.67 – 3.64 (m, 2H), 3.58 – 3.54 (m, 2H), 3.39 (s, 3H), 3.25 – 3.18 (m, 1H), 2.67 (s, 3H), 2.58 (s, 3H), 2.55 (s, 3H), 2.51 (s, 3H), 2.46 (s, 3H), 2.38 (s, 3H), 2.10 – 2.02 (m, 1H), 2.01 – 1.93 (m, 1H), 1.89 (s, 3H), 1.89 – 1.83 (m, 1H), 1.80 – 1.72 (m, 1H), 1.69 – 1.62 (m, 1H), 1.44 – 1.37 (m, 2H), 1.33 – 1.27 (m, 1H).

^{13}C-NMR (126 MHz, $CDCl_3$): δ 181.80 (d, J = 50.1 Hz), 154.60, 151.56, 141.86, 141.66, 137.68, 137.58, 136.83, 135.29, 134.92, 132.76, 132.68, 131.90, 131.20, 129.55, 123.61, 122.50, 121.83, 95.55 (d, J = 6.4 Hz), 95.23 (d, J = 6.9 Hz), 72.14, 71.82 (d, J = 13.9 Hz), 70.62 (d, J = 17.5 Hz), 70.44, 59.21, 52.46, 34.55, 34.26, 30.89, 30.32, 28.09, 22.46, 22.16, 18.20, 17.62, 16.97, 15.49, 14.66, 14.18, 13.31.

^{19}F NMR (282 MHz, $CDCl_3$) δ -149.63 (1:1:1:1 pattern, $J(^{19}F\text{-}^{11}B)$ = 30.1 Hz).

Synthesis of carbonyl complexes [(12)MX(CO)$_2$]

General procedure. To a Schlenk flask equipped with stirring bar and septa, the corresponding cod-complex and CH_2Cl_2 (2 mL) were added. A balloon with CO was connected via cannula and CO was bubbled through the stirred solution for 30 min at room temperature. The volatiles were evaporated under reduced pressure, pentane (5 mL) was added and the suspension sonicated for 5 min. The solid material was filtered off and washed with another batch of pentane (2 × 5 mL).

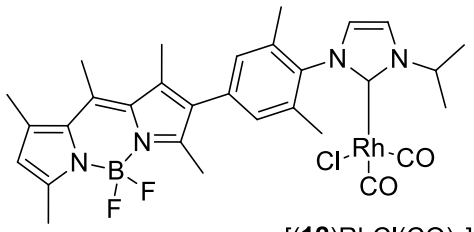

[(**12**)RhCl(CO)$_2$]

Complex [(**12**)RhCl(CO)$_2$] was obtained as an orange solid from [(**12**)RhCl(cod)] (30 mg, 42 μmol). Yield: 27 mg (96%).

^{1}H-NMR (300 MHz, $CDCl_3$): δ 7.25 (d, J = 1.9 Hz, 1H, NC*H*CHN), 7.05 (d, J = 1.8 Hz, 1H, NCHC*H*N), 7.02 (s, 2H, H_{Ar}), 6.10 (s, 1H, H_{BODIPY}), 5.50 (sep, J = 7.0 Hz, 1H, C*H*$(CH_3)_2$), 2.67 (s, 3H, $CH_{3BODIPY}$), 2.55 (s, 3H, $CH_{3BODIPY}$), 2.52 (s, 3H, $CH_{3BODIPY}$), 2.45 (s, 3H, $CH_{3BODIPY}$), 2.38 (s, 3H, $CH_{3BODIPY}$), 2.17 (s, 6H, CH_{3Ar}), 1.57 (d, J = 6.7 Hz, 6H, CH_{3Ar}).

^{13}C-NMR (75 MHz, $CDCl_3$): δ 185.37 (d, $J(^{13}C\text{-}^{103}Rh)$ = 53.9 Hz), 182.64 (d, $J(^{13}C\text{-}^{103}Rh)$ = 74.8 Hz), 175.09 (d, $J(^{13}C\text{-}^{103}Rh)$ = 44.1 Hz), 154.53, 151.69, 141.93, 141.64, 137.05, 136.96, 135.91, 135.50, 132.76, 132.48, 131.97, 130.59, 123.46, 121.81, 118.04, 53.51, 23.63, 18.61, 17.63, 17.01, 15.68, 14.66, 13.42.

^{19}F-NMR (282 MHz, $CDCl_3$): δ -149.64 (1:1:1:1 pattern, $J(^{19}F\text{-}^{11}B)$ = 31.7 Hz).

HR-MS (EI), m/z: 472.25989 $[M – Cl – Rh - 2CO – H]^{+\bullet}$, calcd. 472.2611 (Δ = -1.2 mmu).

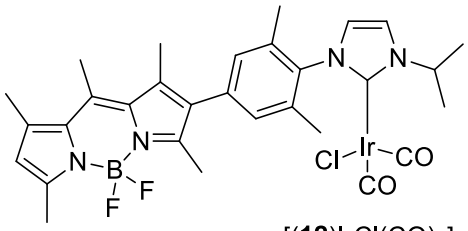

[(**12**)IrCl(CO)$_2$]

Complex [(**12**)IrCl(CO)$_2$] was obtained as an orange solid from [(**12**)IrCl(cod)] (30 mg, 37 μmol). Yield: 27 mg (97%).

^{1}H-NMR (500 MHz, $CDCl_3$): δ 7.27 (d, J = 1.9 Hz, 1H, NC*H*CHN), 7.03 (d, J = 1.6 Hz, 1H, NCHC*H*N), 7.01 (s, 2H, H_{Ar}), 6.10 (s, 1H, H_{BODIPY}), 5.50 (sep, J = 6.7 Hz, 1H, C*H*$(CH_3)_2$), 2.67 (s, 3H, $CH_{3BODIPY}$), 2.55 (s, 3H, $CH_{3BODIPY}$), 2.52 (s, 3H, $CH_{3BODIPY}$), 2.45 (s, 3H,

$CH_{3BODIPY}$), 2.37 (s, 3H, $CH_{3BODIPY}$), 2.16 (s, 6H, CH_{3Ar}), 1.57 (d, J = 6.8 Hz, 6H, CH(CH_3)$_2$).
^{13}C-NMR (126 MHz, $CDCl_3$): δ 180.87, 174.33, 168.03, 154.50, 151.72, 141.93, 141.61, 137.10, 136.70, 135.75, 135.61, 132.76, 132.50, 131.98, 130.57, 123.40, 121.80, 117.95, 53.36, 23.53, 18.60, 17.62, 17.01, 15.69, 14.66, 13.42.
^{19}F NMR (282 MHz, $CDCl_3$): δ -149.65 (1:1:1:1 pattern, J(^{19}F-^{11}B) = 31.8 Hz).
HR-MS (EI), m/z: 758.20088 $[M]^{+\bullet}$, calcd. 758.1978 (Δ = 3.1 mmu).

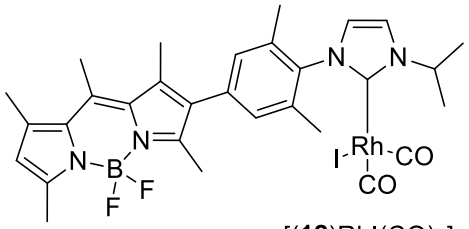

[(**12**)RhI(CO)$_2$]

Complex [(**12**)RhI(CO)$_2$] was obtained as an orange solid from [(**12**)RhI(cod)] (30 mg, 37 μmol). Yield: 27 mg (97%).
^{1}H-NMR (500 MHz, $CDCl_3$): δ 7.26 (s, 1H, NC*H*CHN), 7.07 (d, J = 1.8 Hz, 1H, NCHC*H*N), 6.99 (s, 2H, H_{Ar}), 6.10 (s, 1H, H_{BODIPY}), 5.43 (sep, J = 6.8 Hz, 1H, C*H*(CH_3)$_2$), 2.67 (s, 3H, $CH_{3BODIPY}$), 2.55 (s, 3H, $CH_{3BODIPY}$), 2.51 (s, 3H, $CH_{3BODIPY}$), 2.45 (s, 3H, $CH_{3BODIPY}$), 2.37 (s, 3H, $CH_{3BODIPY}$), 2.16 (bs, 6H, CH_{3Ar}), 1.55 (d, J = 6.5 Hz, 6H, CH(CH_3)$_2$).
^{13}C-NMR (126 MHz, $CDCl_3$): δ 186.96 (d, J(^{13}C-^{103}Rh) = 52.5 Hz), 181.92 (d, J(^{13}C-^{103}Rh) = 77.8 Hz), 173.23 (d, J(^{13}C-^{103}Rh) = 42.6 Hz), 154.53, 151.72, 141.93, 141.63, 137.08, 136.81, 135.52, 132.77, 132.48, 131.98, 130.67, 130.60, 124.25, 121.81, 118.11, 53.70, 28.19, 23.64, 17.62, 17.02, 15.70, 14.66, 13.43.
^{19}F-NMR (282 MHz, $CDCl_3$): δ -149.66 (1:1:1:1 pattern, J(^{19}F-^{11}B) = 31.0 Hz).
HR-MS (EI), m/z: 432.22593 $[M - Rh - 2CO - I - iPr]^{+\bullet}$, calcd. 432.2298 (Δ = -3.9 mmu).

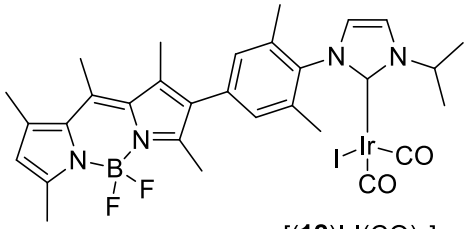

[(**12**)IrI(CO)$_2$]

Complex [(**12**)IrI(CO)$_2$] was obtained as an orange solid from [(**12**)IrI(cod)] (30 mg, 33 μmol). Yield: 28 mg (98%).
^{1}H-NMR (300 MHz, $CDCl_3$): δ 7.29 (s, 1H, NC*H*CHN), 7.06 (s, 1H, NCHC*H*N), 6.99 (s, 2H, H_{Ar}), 6.10 (s, 1H, H_{BODIPY}), 5.44 (sep, J = 7.0 Hz, 1H, C*H*(CH_3)$_2$), 2.67 (s, 3H, $CH_{3BODIPY}$), 2.55 (s, 3H, $CH_{3BODIPY}$), 2.51 (s, 3H, $CH_{3BODIPY}$), 2.45 (s, 3H, $CH_{3BODIPY}$), 2.37 (s, 3H, $CH_{3BODIPY}$), 2.16 (bs, 6H, CH_{3Ar}), 1.54 (d, J = 6.9 Hz, 6H, CH(CH_3)$_2$).
^{13}C-NMR (75 MHz, $CDCl_3$): δ 181.09, 171.51, 167.87, 154.48, 151.69, 141.93, 141.62, 137.11, 136.59, 135.58, 132.75, 132.45, 131.96, 130.83, 130.57, 124.12, 121.79, 118.10, 53.37, 24.10, 22.08, 20.51, 17.63, 17.02, 15.71, 14.66, 14.21, 13.43.
^{19}F-NMR (282 MHz, CDCl3): δ -149.66 (1:1:1:1 pattern, J(^{19}F-^{11}B) = 31.0 Hz).
HR-MS (EI), m/z: 850.13293 $[M + H]^{+\bullet}$, calcd. 850.1338 (Δ = -0.9 mmu).

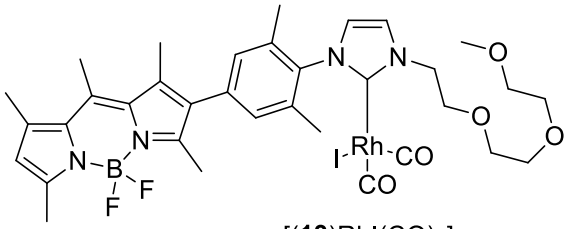

[(**13**)RhI(CO)$_2$]

Complex [(**13**)RhI(CO)$_2$] was obtained as an orange solid from [(**13**)RhI(cod)] (30 mg, 33 μmol). Yield: 26 mg (93%).
^{1}H-NMR (300 MHz, $CDCl_3$): δ 7.54 (d, J = 1.8 Hz, 1H, NC*H*CHN), 7.02 (d, J = 1.8 Hz, 1H, NCHC*H*N), 7.01 (s, 2H, H_{Ar}), 6.10 (s, 1H, H_{BODIPY}), 4.01-3.93 (m, 2H, CH_2), 3.71-3.65 (m, 8H, CH_2), 3.57-3.55 (m, 2H, CH_2), 3.39 (s, 3H, OCH_3), 2.67 (s, 3H, $CH_{3BODIPY}$), 2.55 (s, 3H, $CH_{3BODIPY}$), 2.51 (s, 3H, $CH_{3BODIPY}$), 2.45 (s, 3H, $CH_{3BODIPY}$), 2.37 (s, 3H, $CH_{3BODIPY}$), 2.19 (bs, 6H, CH_{3Ar}).
^{13}C NMR (126 MHz, $CDCl_3$) δ 187.80 (d, J(^{13}C-^{103}Rh) = 53.0 Hz), 181.62 (d, J(^{13}C-^{103}Rh) = 78.1 Hz), 174.59 (d, J(^{13}C-^{103}Rh) = 44.2 Hz), 154.54, 151.69, 141.93, 141.64, 137.05, 136.81, 135.54, 132.77, 132.46, 131.96, 130.69, 124.00, 123.40, 121.82, 72.14, 70.70, 70.65, 70.61, 70.16, 59.22, 52.20, 17.63, 17.02, 15.69, 14.66, 13.42.

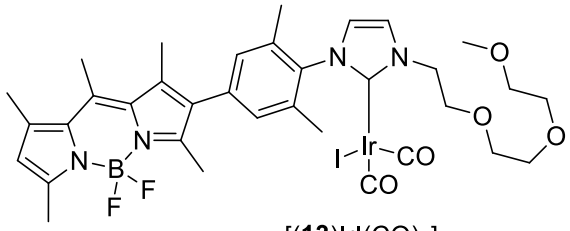

[(**13**)IrI(CO)$_2$]

Complex [(**13**)IrI(CO)$_2$] was obtained as an orange solid from [(**13**)IrI(cod)] (30 mg, 33 μmol). Yield: 27 mg (95%).
^{1}H-NMR (300 MHz, $CDCl_3$): δ 7.57 (d, J = 1.4 Hz, 1H, NC*H*CHN), 7.00 (d, J = 1.4 Hz, 1H, NCHC*H*N), 6.99 (s, 2H, H_{Ar}), 6.10 (s, 1H, H_{BODIPY}), 3.99 (bs, 2H, CH_2), 3.71-3.64 (m, 8H, CH_2), 3.58-3.56 (m, 2H, CH_2), 3.39 (s, 3H, OCH_3), 2.67 (s, 3H, $CH_{3BODIPY}$), 2.55 (s, 3H, $CH_{3BODIPY}$), 2.51 (s, 3H, $CH_{3BODIPY}$), 2.45 (s, 3H, $CH_{3BODIPY}$), 2.36 (s, 3H, $CH_{3BODIPY}$), 2.17 (bs, 6H, CH_{3Ar}).

Synthesis of complex [(12)AuI]

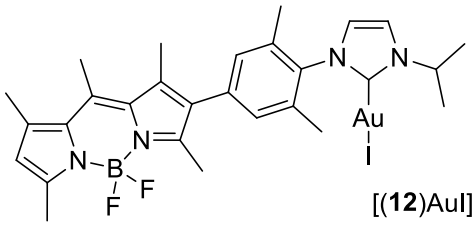

[(**12**)AuI]

A flame-dried Schlenk flask equipped with stirring bar was loaded with [AuCl(Me_2S)] (100 mg, 0.34 mmol, 1 eq), imidazolium salt **12**·HI (215 mg, 0.36 mmol, 1.05 eq), 10 mL of thf and cooled to -78°C on acetone – dry ice bath. Sodium *tert*.-pentylate (149.4 μL, 0.37 mmol, 1.1 eq, 2.5 M solution in thf) was added and the mixture stirred for 30 min at -78 °C in the dark. After removing the cold bath, the mixture was stirred for 1 h and then the volatiles removed in vacuo. The crude product was purified by filtration through the silica pad (cyclohexane / acetone, 2:1) to provide dark orange microcrystalline solid (142 mg, 59% yield).
^{1}H-NMR (300 MHz, $CDCl_3$): δ 7.24 (d, J = 1.9 Hz, 1H, NC*H*CHN), 7.00 (s, 2H, H_{Ar}), 6.97 (d, J = 1.9 Hz, 1H, NCHC*H*N), 6.10 (s, 1H, H_{BODIPY}), 5.26 (hept, J = 6.7 Hz, 1H, C*H*(CH_3)$_2$), 2.66 (s, 3H, $CH_{3BODIPY}$), 2.55 (s, 3H, $CH_{3BODIPY}$), 2.50 (s, 3H, $CH_{3BODIPY}$), 2.45 (s, 3H, $CH_{3BODIPY}$), 2.35 (s, 3H, $CH_{3BODIPY}$), 2.10 (s, 6H, CH_{3Ar}), 1.59 (d, J = 6.8 Hz, 6H, CH(C*H*$_3$)$_2$).
^{13}C-NMR (75 MHz, $CDCl_3$): δ 181.84, 154.48, 151.61, 142.03, 141.65, 137.36, 136.41, 135.83, 135.41, 132.76, 132.31, 131.93, 130.75, 122.06, 121.79, 116.74, 53.45, 23.65, 18.14, 17.63, 17.02, 15.78, 14.66, 13.45.
^{19}F-NMR (282 MHz, $CDCl_3$): δ -149.66 (1:1:1:1 pattern, J(^{19}F-^{11}B) = 31.3 Hz).
HR-MS (EI), m/z: 798.14807 $[M]^{+\bullet}$, calcd. 798.1477 (Δ = 0.4 mmu).

Synthesis of complex [(12)PdI$_2$(Clpy)]

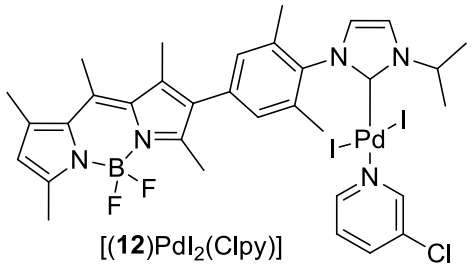

[(**12**)PdI$_2$(Clpy)]

A flame-dried Schlenk flask equipped with stirring bar was loaded with imidazolium salt **12**·HI (100 mg, 0.17 mmol, 1 eq), $Pd(OAc)_2$ (37.3 mg, 0.17 mmol, 1 eq), K_2CO_3 (115 mg, 0.83 mmol, 5 eq) and KI (55 mg, 0.34 mmol, 2 eq). 3-chloropyridine (1.0 mL) was added and the mixture stirred at 80°C in a sealed flask overnight. The reaction mixture was filtered through celite and the filtrate was evaporated under reduced pressure. The dark residue was dissolved it minimum amount of CH_2Cl_2 and precipitated by addition of pentane (ca. 10 mL). The precipitate was washed with additional pentane (5 mL) and methanol (2 mL). The product was obtained as dark magenta microcrystalline solid (140 mg, 89% yield).
^{1}H-NMR (500 MHz, $CDCl_3$): δ 8.73 (d, J = 2.2 Hz, 1H, 1-H_{Py}), 8.65 (dd, J = 5.4, 1.1 Hz, 1H, 3-H_{Py}), 7.66 – 7.59 (m, 1H, 5-H_{Py}), 7.18 (d, J = 2.0 Hz, 1H, NC*H*CHN), 7.16 (dd, J = 8.3, 5.5 Hz, 1H, 4-H_{Py}), 7.07 (d, J = 1.9 Hz, 1H, NCHC*H*N), 7.05 (s, 2H, CH_{3Ar}), 6.10 (s, 1H, H_{BODIPY}), 5.81 (hept, J = 6.7 Hz, 1H, C*H*(CH_3)$_2$), 2.67 (s, 3H, $CH_{3BODIPY}$), 2.56 (s, 3H, $CH_{3BODIPY}$), 2.54 (s, 3H, $CH_{3BODIPY}$), 2.45 (s, 3H, $CH_{3BODIPY}$), 2.40 (s, 9H, CH_{3Ar} + $CH_{3BODIPY}$), 1.65 (d, J = 6.8 Hz, 6H, CH(C*H*$_3$)$_2$).

^{13}C-NMR (126 MHz, $CDCl_3$): δ 154.37, 152.55, 151.84, 151.58, 145.67, 141.84, 141.49, 137.59, 137.02, 136.75, 136.42, 135.29, 134.21, 132.73, 132.11, 131.99, 130.77, 125.78, 124.56, 121.74, 117.55, 54.43, 22.80, 22.13, 17.61, 17.01, 15.71, 14.65, 13.46.
^{19}F-NMR (282 MHz, $CDCl_3$): δ -149.63 (1:1:1:1 pattern, $J(^{19}F\text{-}^{11}B)$ = 30.2 Hz).
The attempted determination of mass spectra with complex [(**12**)PdI_2(Clpy)] was unsuccessful, due to instability of this complex.

Synthesis of complex [(12)(SIMes)$RuCl_2$(ind)]

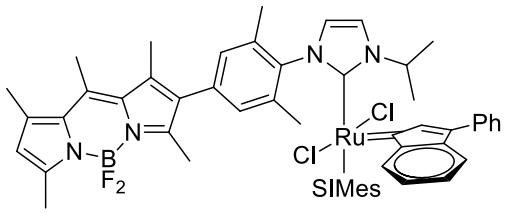

[(**12**)(SIMes)$RuCl_2$(ind)]

To a Schlenk flask equipped with a stirring bar containing imidazolium salt **12**·HI (100 mg, 166 μmol, 1 eq) and Ag_2O (19.2 mg, 83 μmol, 0.5 eq), dichloromethane (2 mL) was added and the flask sealed. After 30 min of stirring in the dark at 40 °C, volatiles were removed under reduced pressure, toluene (5 mL) and [(SIMes)$RuCl_2$(ind)py] (112 mg, 150 μmol, 0.9 eq) were added and the mixture was stirred at 60 °C for another 1 hour. The resulting suspension was cooled down to rt and filtered through a short plug of celite. The filtrate was collected and evaporated under reduced pressure. The product was purified by column chromatography (cyclohexane / ethyl acetate, 4:1) to afford a dark red microcrystalline solid (87 mg, 52% yield).
^{1}H-NMR (500 MHz, $CDCl_3$): δ 8.44 (d, J = 6.0 Hz, 1H), 7.61 (d, J = 7.4 Hz, 2H), 7.46 (t, J = 7.3 Hz, 1H), 7.32 (t, J = 7.6 Hz, 2H), 7.21 (s, 1H), 7.12 (d, J = 4.1 Hz, 2H), 7.05 – 6.94 (m, 3H), 6.65 (d, J = 7.0 Hz, 1H), 6.42 (s, 1H), 6.33 (s, 1H), 6.26 (s, 1H), 6.04 (s, 1H), 6.02 (s, 1H), 5.90 (s, 1H), 4.55 – 4.46 (m, 1H), 3.98 – 3.90 (m, 2H), 3.79 – 3.63 (m, 1H), 2.75 (s, 3H), 2.71 (s, 3H), 2.54 (s, 3H), 2.50 (s, 3H), 2.44 (s, 3H), 2.41 (s, 3H), 2.09 (s, 3H), 2.00 (s, 3H), 1.98 (s, 6H), 1.89 (d, J = 12.0 Hz, 6H), 1.64 (s, 3H), 1.30 – 1.23 (m, 6H).
^{13}C-NMR (126 MHz, $CDCl_3$): δ 153.22, 153.03, 141.27, 140.54, 139.73, 139.55, 139.36, 139.13, 138.31, 137.79, 137.32, 137.13, 137.06, 136.83, 136.74, 136.67, 136.63, 136.43, 136.37, 135.20, 133.32, 132.50, 132.28, 132.09, 130.14, 130.02, 128.94, 128.90, 128.82, 128.75, 128.46, 128.19, 127.19, 127.12, 126.31, 126.27, 124.77, 121.23, 117.29, 115.54, 52.98, 52.62, 52.35, 23.85, 23.53, 21.26, 21.13, 20.26, 20.18, 18.73, 18.70, 18.59, 18.35, 17.46, 16.94, 15.59, 14.47, 13.40.
^{19}F-NMR (282 MHz, $CDCl_3$): δ -149.81 (1:1:1:1 pattern, $J(^{19}F\text{-}^{11}B)$ = 27.7 Hz).
The attempted determination of mass spectra with complex [(**12**)(SIMes)$RuCl_2$(ind)] was unsuccessful, due to instability of this complex.

Synthesis of *N*-(2,6-dimethyl-4-((trimethylsilyl)ethynyl)phenyl)-N´-mesitylethane-1,2-diamine 14

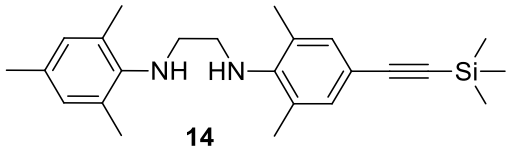

14

N-(4-bromo-2,6-dimethylphenyl)-*N*'-mesitylethane-1,2-diamine (2.64 g, 7.3 mmol, 1 eq) and TMS-acetylene (776 mg, 1125 μL, 9.5 mmol, 1.3 eq) were loaded into 250 mL flame-dried Schlenk flask equipped with a stirring bar. Diisopropylamine (100 mL) was added and the mixture degassed (1 cycle of freeze-pump-thaw). Na_2PdCl_4 (36 mg, 0.12 mmol, 2 mol %), CuI (23 mg, 0.12 mmol, 2 mol %) and $Cy_2tBuP{\cdot}HBF_4$ (83 mg, 0.24 mmol, 4 mol %) were added and the mixture heated up to 80°C in the sealed flask for 12 h. The formed white precipitate was filtered off and washed with diethyl ether (3 × 75 mL). Filtrate was evaporated under reduced pressure to provide product as brownish oil (2.4 g, 87 % yield). Diamine **14** was used in the next step without purification.
^{1}H NMR (300 MHz, $CDCl_3$) δ 7.13 (s, 2H, H_{Ar}), 6.84 (s, 2H, H_{Ar}), 3.29–3.02 (m, 6H, $NHCH_2CH_2NH$), 2.26 (s, 12H, CH_{3Ar}), 2.24 (s, 3H, CH_{3Ar}), 0.23 (s, 9H, CH_{3TMS}).

^{13}C NMR (126 MHz, $CDCl_3$) δ 146.94, 143.14, 132.76, 131.93, 130.19, 129.64, 128.32, 115.53, 106.04, 92.10, 49.09, 48.84, 20.66, 18.75, 18.40, 0.25.
HRMS (EI) m/z: 378.2460 $[M]^{+\cdot}$, calcd 378.2486 (Δ =-2.6 mmu).

Synthesis of *N*-(4-ethynyl-2,6-dimethylphenyl)-*N'*-mesitylethane-1,2-diamine 15

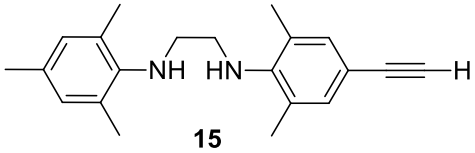

15

Diamine **15** (2.4 g, 6.4 mmol, 1 eq) and tetrabutylammonium fluoride hydrate (2.4 g, 7.6 mmol, 1.2 eq) were dissolved in THF (30 mL) and the mixture stirred for 60 min. Water (150 mL) was added and the product extracted with diethyl ether (3 × 30 mL). The combined organic layers were washed with brine, dried over $MgSO_4$, filtered and evaporated under reduced pressure to provide a brownish oil, which was used in the next step without purification (1.77 g, 91% yield).
^{1}H NMR (500 MHz, $CDCl_3$) δ 7.18 (s, 2H, H_{Ar}), 6.86 (s, 2H, H_{Ar}), 3.48 – 3.12 (m, 6H, $NHCH_2CH_2NH$), 2.99 (s, 1H, CCH), 2.32 – 2.28 (m, 12H, CH_3), 2.27 (s, 3H, CH_3).
^{13}C NMR (126 MHz, $CDCl_3$) δ 147.19, 143.13, 132.89, 131.98, 130.21, 129.66, 128.46, 114.44, 84.41, 75.50, 49.09, 48.82, 20.67, 18.80, 18.41.
HRMS (EI) m/z: 306.2079 $[M]^{+\cdot}$, calcd 306.2091 (Δ = -1.11 mmu).

Synthesis of diamine 16

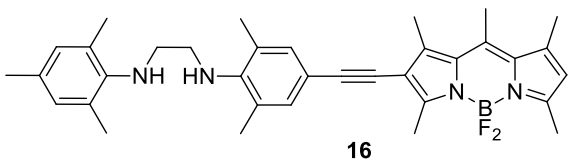

16

Iodo-pentamethyl-BODIPY (2.73 g, 7.0 mmol, 1.2 eq) and acetylene **15** (1.8 g, 5.9 mmol, 1 eq) were loaded into a 250 mL flame-dried Schlenk flask equipped with the stirring bar. Diisopropylamine (75 mL) and THF (75 mL) were added and the mixture degassed (1 cycle of freeze-pump-thaw). Na_2PdCl_4 (35 mg, 0.12 mmol, 2 mol %), CuI (23 mg, 0.12 mmol, 2 mol %) and $Cy_2tBuP{\cdot}HBF_4$ (80 mg, 0.24 mmol, 4 mol %) were added and the mixture heated to 70°C in the sealed flask and stirred at this temperature for 12 h. The formed white precipitate was filtered off and washed with THF (3 × 100 mL). The filtrate was evaporated under reduced pressure and the remaining dark viscous oil purified by column chromatography (cyclohexane / ethyl acetate: 4:1). The product was obtained (1.56 g, 47% yield) as a dark purple microcrystalline solid (1.56 g, 47% yield).
^{1}H NMR (300 MHz, $CDCl_3$) δ 7.18 (s, 2H, H_{Ar}), 6.85 (s, 2H, H_{Ar}), 6.09 (s, 1H, H_{bdp}), 3.54 – 3.07 (m, 6H, $NHCH_2CH_2NH$), 2.67 (s, 3H, $CH_{3\ bdp}$), 2.59 (s, 3H, $CH_{3\ bdp}$), 2.54 (s, 3H, $CH_{3\ bdp}$), 2.53 (s, 3H, $CH_{3\ bdp}$), 2.42 (s, 3H, $CH_{3\ bdp}$), 2.31 (s, 6H, $CH_{3\ Ar}$), 2.29 (s, 6H, $CH_{3\ Ar}$), 2.25 (s, 3H, $CH_{3\ Ar}$).
^{13}C NMR (75 MHz, $CDCl_3$) δ 155.26, 155.16, 146.64, 143.18, 142.30, 141.78, 140.32, 133.03, 132.09, 131.97, 131.21, 130.22, 129.66, 128.70, 122.03, 116.12, 115.83, 96.47, 80.44, 49.13, 48.94, 20.68, 18.83, 18.44, 17.54, 16.72, 15.99, 14.65, 13.58.
^{19}F NMR (282 MHz, $CDCl_3$) δ -149.74 (1:1:1:1 pattern, $J^1(^{19}F\text{-}^{11}B)$ = 31.0 Hz).
HRMS (EI) m/z: 566.3379 $[M]^{+\cdot}$, calcd 566.3387 (Δ =-0.8 mmu).

Synthesis of diamine 17

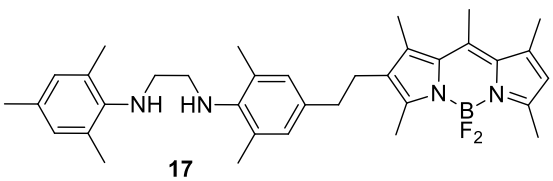

17

Diamine **16** (1.0 g, 1.8 mmol) and Pd/C (764 mg, 10 wt % Pd) were loaded into a pressure reactor and methanol (150 mL) added. The reaction mixture was stirred under pressure of hydrogen (5 atm) at rt for 4h, filtered and evaporated to give product as a bright orange microcrystalline solid (1.0 g, 98 % yield).

^{1}H NMR (300 MHz, $CDCl_3$) δ 6.84 (s, 2H, H_{Ar}), 6.80 (s, 2H, H_{Ar}), 6.03 (s, 1H, H_{Bdp}), 3.17 (s, 4H, NHCH_2CH_2NH), 2.68 – 2.56 (m, 9H, NH, ArCH_2CH_2bdp, $CH_{3\ Bdp}$), 2.52 (s, 3H, $CH_{3\ Bdp}$), 2.42 (s, 6H, $CH_{3\ Bdp}$), 2.32 – 2.28 (m, 15H, $CH_{3\ Bdp}$, $CH_{3\ Ar}$), 2.24 (s, 3H, $CH_{3\ Ar}$).
^{13}C NMR (75 MHz, $CDCl_3$) δ 153.91, 152.36, 144.19, 143.39, 140.66, 139.95, 137.89, 135.14, 132.15, 131.86, 131.70, 130.92, 129.98, 129.89, 129.64, 129.01, 120.83, 49.30, 36.09, 26.57, 20.68, 18.64, 18.53, 17.44, 16.78, 14.61, 14.47, 12.
^{19}F NMR (282 MHz, $CDCl_3$) δ -149.49 (1:1:1:1 pattern, $J(^{19}F\text{-}^{11}B)$ = 31.0 Hz).
HRMS (EI) m/z: 570.3705 $[M]^{+\cdot}$, calcd 570.3700 (Δ=0.5 mmu).

Synthesis of NHC-precursor 18

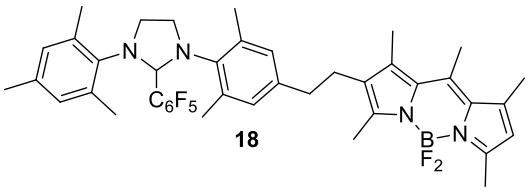

18

Diamine **16** (440 mg, 0.77 mmol, 1 eq) was dissolved in minimum amount of acetic acid and pentafluorobenzaldehyde was added (197 mg, 1 mmol, 1.3 eq). The mixture was stirred at room temperature for 12 h, the formed precipitate was filtered off, washed with methanol (3 × 10 mL) and dried under vacuum. The resulting bright orange microcrystalline solid (404 mg, 70% yield) was used in the next step without further purification.
^{1}H NMR (300 MHz, $CDCl_3$) δ 6.81 (s, 2H, H_{Ar}), 6.70 (bs, 2H, H_{Ar}), 6.39 (s, 1H, NCHN), 6.03 (s, 1H, H_{bdp}), 3.96 – 3.85 (m, 2H, NCH_2CH_2N), 3.62 – 3.48 (m, 2H, NCH_2CH_2N), 2.73 – 2.44 (m, 13H, ArCH_2CH_2bdp, $CH_{3\ bdp}$), 2.44 – 2.25 (m, 12H, CH_{3Ar}, $CH_{3\ bdp}$), 2.22 (s, 3H, $CH_{3\ Ar}$), 2.19 (s, 3H, $CH_{3\ Ar}$), 2.12 (s, 3H, $CH_{3\ Ar}$).
^{13}C NMR (126 MHz, $CDCl_3$) δ 153.91, 152.55, 140.62, 140.01, 139.72, 139.21, 139.00, 137.78, 135.67, 132.08, 131.88, 130.39, 130.10 (br), 129.64, 129.03, 120.87, 117.80, 117.69, 117.60, 71.62, 51.15, 51.03, 36.11, 26.12, 20.79, 19.25 (br), 17.42, 16.66, 14.41, 14.29, 12.17. $^{13}C\text{-}^{19}F$ coupling constants could not be resolved.
^{19}F NMR (282 MHz, $CDCl_3$) δ -139.44 (dd, J = 22.0, 7.9 Hz, 1F), -149.61 (1:1:1:1 pattern, J ($^{19}F\text{-}^{11}B$) = 31.0 Hz), -152.27 (dd, J = 22.8, 7.8 Hz, 1F), -158.65 (t, J = 20.9 Hz, 1F), -166.15 (td, J = 21.5, 7.4 Hz, 1F), -166.41 (td, J = 21.7, 8.0 Hz, 1F).
HRMS (EI) m/z: 580.3528 $[M - C_6F_5H]^{+\cdot}$, calcd 580.3542 (Δ =-1.5 mmu)

Synthesis of Iridium complex 19

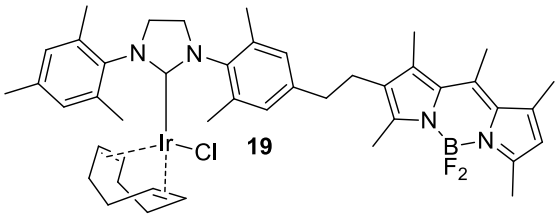

19

Imidazolidine **18** (150 mg, 0.2 mmol, 1 eq), $[IrCl(cod)]_2$ (68 mg, 0.1 mmol, 0.5 eq) and toluene (6 mL) were loaded into 25 mL flame-dried Schlenk flask equipped with a stirring bar. The flask was, heated to 70 °C and stirred at this temperature for 2 h. The resulting orange solution was cooled to room temperature and the solvent evaporated under reduced pressure. The product was purified by column chromatography (cyclohexane / ethyl acetate, 4 : 1) to provide the product as an orange microcrystalline solid (166 mg, 89 % yield).
^{1}H NMR (500 MHz, $CDCl_3$) δ 6.98 (s, 1H, H_{Ar}), 6.96 – 6.90 (m, 3H, H_{Ar}), 6.03 (s, 1H, H_{bdp}), 4.15 – 4.05 (m, 2H, H_{cod}), 3.94 – 3.86 (m, 4H, NCH_2CH_2N), 3.13 – 3.03 (m, 2H, H_{cod}), 2.75 – 2.63 (m, 4H, $ArCH_2CH_2bdp$), 2.61 (s, 3H, CH_3), 2.56 (s, 6H, CH_3), 2.51 (s, 3H, CH_3), 2.46 (s, 3H, CH_3), 2.41 (s, 3H, CH_3), 2.37 (s, 3H, CH_3), 2.35 (s, 3H, CH_3), 2.32 (s, 3H, CH_3), 2.31 (s, 3H, CH_3), 1.66 – 1.55 (m, 4H, H_{cod}), 1.34 – 1.29 (m, 4H, H_{cod}).
^{13}C NMR (126 MHz, $CDCl_3$) δ 207.46, 153.51, 152.50, 141.39, 141.07, 140.20, 138.54, 138.14, 137.92, 137.03, 136.39, 135.71, 135.29, 132.18, 132.00, 130.42, 129.96, 129.31, 128.51, 127.96, 120.90, 83.92, 83.79, 51.94, 51.91, 51.77, 51.50, 36.42, 33.55, 28.83, 28.71, 26.31, 21.18, 20.08, 19.99, 18.67, 18.57, 17.47, 16.96, 14.78, 14.50, 12.66.
^{19}F NMR (282 MHz, $CDCl_3$) δ -146.39 (1:1:1:1 pattern, $J(^{19}F\text{-}^{11}B)$ = 30.5 Hz).
HRMS (EI) m/z: 916.3821 $[M]^{+\cdot}$, calcd 916.3800 (Δ = -2.1 mmu).

Synthesis of Iridium complex 20b

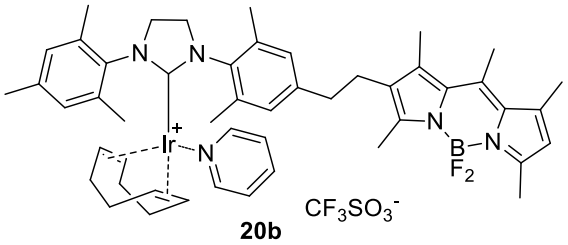

20b

To the flame-dried Schlenk flask containing complex **19** (150 mg, 0.16 mmol, 1 eq), CH_2Cl_2 (3 mL), was added, followed by pyridine (20 μL, 0.25 mmol, 1.5 eq) and [$Ag(CF_3SO_3)$] (42 mg, 0.16 mmol, 1 eq). The reaction mixture was stirred for one hour then filtered through a plug of celite. The filtrate evaporated under reduced pressure. The solid residue was dissolved in a minimum amount of dichloromethane and precipitated from diethyl ether. The precipitate was collected by filtration and dried under vacuum. Complex **20b** was obtained as an orange microcrystalline solid (171 mg, 94 % yield).

^{1}H NMR (500 MHz, $CDCl_3$) δ 7.78 (tt, J = 7.6, 1.6 Hz, 1H, H_{py}), 7.70 (dt, J = 5.0, 1.5 Hz, 2H, H_{py}), 7.30 – 7.23 (m, 2H, H_{py}), 7.08 (s, 1H, H_{Ar}), 7.02 (s, 1H, H_{Ar}), 6.90 (s, 1H, H_{Ar}), 6.86 (s, 1H, H_{Ar}), 6.04 (s, 1H, H_{bdp}), 3.97 (bs, 2H, H_{cod}), 3.84-3.75 (m, 4H, H_{cod}, CH_2), 3.19 – 3.13 (m, 2H, CH_2), 2.73 (s, 4H, NCH_2CH_2N), 2.63 (s, 3H, CH_3), 2.49 (s, 3H, CH_3), 2.47 (s, 3H, CH_3), 2.44 (s, 3H, CH_3), 2.42 (s, 3H, CH_3), 2.41-2.38 (m, 6H, CH_3), 2.34 (s, 3H, CH_3), 2.02 – 1.79 (m, 10H, CH_3, H_{cod}), 1.65 – 1.51 (m, 4H, H_{cod}).

^{13}C NMR (75 MHz, $CDCl_3$) δ 201.06, 152.98, 151.04, 142.60, 141.19, 140.77, 139.23, 138.26, 137.83, 136.54, 136.31, 135.79, 132.15, 132.08, 130.18, 130.06, 129.92, 129.87, 129.37, 126.18, 121.18, 84.02, 83.71, 65.36, 64.84, 52.91, 52.80, 36.27, 32.60, 32.41, 29.24, 29.08, 26.18, 21.20, 18.48, 18.29, 17.53, 16.94, 14.78, 14.53, 12.60.

^{19}F NMR (282 MHz, $CDCl_3$) δ -81.16 (s, 3F), -149.40 (1:1:1:1 pattern, $J(^{19}F\text{-}^{11}B)$ = 29.5 Hz, 2F).

The attempted determination of mass spectrum of complex **20b** was unsuccessful due to its instability.

Synthesis of Iridium complex 20c

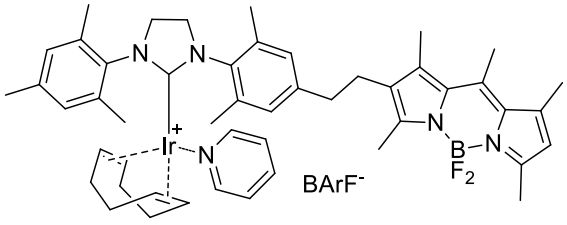

20c

To the flame-dried Schlenk flask containing complex **19** (30 mg, 0.033 mmol, 1 eq) dichloromethane (2 mL) was added, followed by pyridine (27 μL, 0.33 mmol, 10 eq) and sodium tetrakis[3,5-bis(trifluoromethyl)phenyl]borate (29 mg, 0.033 mmol, 1 eq). The reaction mixture was stirred in a sealed flask for 1 h and filtered through a plug of celite. The filtrate was evaporated under reduced pressure. Pentane (10 mL) was added to the resulting highly viscous residue, the mixture sonicated for 10 min and the solvent removed by decantation. This procedure was repeated three times and residue was dried under vacuum. The formed amorphous material was triturated to give product as an orange microcrystalline solid (55 mg, 92 % yield).

^{1}H NMR (500 MHz, $CDCl_3$) δ 7.71 (s, 8H, H_{BARF}), 7.66 (d, J = 5.1 Hz, 2H, H_{py}), 7.54 – 7.49 (m, 5H, H_{py}, H_{BARF}), 7.10 (s, 1H, H_{Ar}), 7.07 – 7.01 (m, 3H, H_{Ar}, H_{py}), 6.84 (s, 1H, H_{Ar}), 6.77 (s, 1H, H_{Ar}), 6.06 (s, 1H, H_{bdp}), 3.95 – 3.88 (m, 2H, H_{cod}), 3.83 – 3.77 (m, 2H, H_{cod}), 3.76 – 3.69 (m, 2H, $ArCH_2CH_2bdp$), 3.15 – 3.08 (m, 2H, $ArCH_2CH_2bdp$), 2.73 (s, 4H, NCH_2CH_2N), 2.63 (s, 3H, CH_3), 2.49 (s, 3H, CH_3), 2.45 (s, 3H, CH_3), 2.43 – 2.39 (m, 9H, CH_3), 2.36 (s, 3H, CH_3), 2.25 (s, 3H, CH_3), 1.95 – 1.84 (m, 7H, CH_3, H_{cod}), 1.79 (s, 3H, CH_3), 1.65 – 1.59 (m, 2H, H_{cod}), 1.58 – 1.51 (m, 2H, H_{cod}).

^{13}C NMR (126 MHz, $CDCl_3$) δ 201.40, 161.86 (1:1:1:1 pattern, $J(^{13}C\text{-}^{11}B)$ = 49.8 Hz), 153.37, 152.74, 151.07, 142.87, 141.16, 141.08, 139.63, 137.59, 137.43, 136.57, 136.42, 135.92, 135.51, 134.95, 132.26, 132.02, 130.22, 130.10, 129.72, 129.57, 129.06 (qq, $J(^{13}C\text{-}^{19}F)$ = 32.3 Hz, 4.8 Hz), 125.68, 124.71 (q, $J(^{13}C\text{-}^{19}F)$ = 272.5 Hz), 121.45, 117.59, 84.58, 84.06,

77.16, 65.99, 65.31, 52.73, 52.57, 36.21, 32.56, 32.28, 29.17, 28.97, 26.03, 21.03, 18.30, 17.95, 17.46, 16.84, 14.59, 14.53, 12.50.
^{19}F NMR (282 MHz, $CDCl_3$) δ -62.42 (s, 24F, CF_3), -146.29 (1:1:1:1 pattern, $J(^{19}F\text{-}^{11}B)$ = 31.0 Hz).
The attempted determination of mass spectrum of complex **20c** was unsuccessful due to its instability.

Synthesis of hydride complex 21b

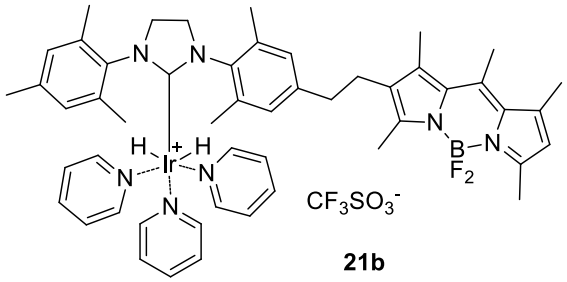

21b

To a flame-dried Schlenk flask equipped with stirring bar and septum, complex **21b** (33 mg, 0.03 mmol, 1 eq), methanol (4 mL) and pyridine (240 μL, 3 mmol, 100 eq) were added. A balloon with hydrogen was connected through a cannula, and H_2 was bubbled through the stirred solution for 1 h at room temperature. The volatiles were evaporated under reduced pressure, diethyl ether (5 mL) was added, and the suspension was sonicated for 5 min. The solid material was filtered off and washed with another batch of diethyl ether. Complex **21b** was obtained as an orange solid (19 mg, 51% yield).
^{1}H NMR (500 MHz, C_5D_5N) δ 8.14 – 8.12 (m, 1.5H, H_{py}), 7.56 – 7.52 (m, 0.7H, H_{py}), 6.91 – 6.87 (m, 1.5H, H_{py}), 6.80 (s, 2H, H_{Ar}), 6.57 (s, 2H, H_{Ar}), 6.10 (s, 1H, H_{bdp}), 3.89 – 3.83 (m, 4H, NCH_2CH_2N), 2.71 (s, 3H, $CH_{3\ bdp}$), 2.68 – 2.65 (m, 2H, $ArCH_2CH_2bdp$), 2.60 – 2.58 (m, 2H, $ArCH_2CH_2bdp$), 2.53 (s, 3H, $CH_{3\ bdp}$), 2.41 (s, 3H, $CH_{3\ bdp}$), 2.34 – 2.32 (m, 12H, $CH_{3\ Ar}$), 2.31 (s, 3H, $CH_{3\ bdp}$), 2.30 (s, 3H, $CH_{3\ bdp}$), 2.12 (s, 3H, $CH_{3\ Ar}$), -22.43 (s, 2H, H_{Ir}).
^{13}C NMR (75 MHz, C_5D_5N) δ 195.19, 155.79, 154.03, 152.92, 142.28, 141.62, 141.31, 140.24, 139.04, 138.80, 138.00, 137.09, 136.75, 136.55, 132.86, 131.21, 126.20, 124.56, 121.73, 51.78, 51.59, 36.82, 26.48, 21.19, 19.22, 19.09, 17.58, 17.15, 15.01, 14.86, 13.15.
^{19}F NMR (282 MHz, C_5D_5N) δ -79.06 (s, 2F, CF_3), -146.84 (1:1:1:1 pattern, $J(^{19}F\text{-}^{11}B)$ = 31.0 Hz, BF_2).
The attempted determination of mass spectrum of complex **21b** was unsuccessful due to its instability.

Synthesis of compounds 23 and 28
General procedure. To a flame-dried Schlenk flask equipped with stirring bar and containing corresponding benzaldehyde, THF and 2,4-dimethylpyrrole were added. One drop of trifluoroacetic acid was introduced into the flask and the solution was stirred for 4 h at room temperature. Then chloranil was added and the reaction mixture was additionally stirred for 30 min. The dark solution was then treated 100lefins100lamine and the flask was placed into an ice bath. The reaction mixture was stirred for 5 min and boron trifluoride diethyletherate was slowly added dropwise during 15 min. Resulted mixture was stirred for additional 1 h at room temperature. The dark solution was washed was concentrated under reduced pressure and dissolved in dichloromethane (200 mL), washed with saturated sodium hydrogen carbonate solution (200 mL), water (3 × 100 mL) and brine (200 mL). The organic phase was dried over anhydrous magnesium sulfate, filtered and the filtrate was evaporated under reduced pressure. The dark viscous oily material was purified by column chromatography.

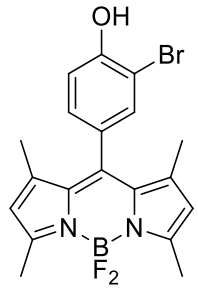

23

BODIPY **23** was obtained as orange microcrystalline solid (1.34 g, 32 % yield) from 3-bromo-4-hydroxybenzaldehyde (2.0 g, 10 mmol, 1 eq), 2,4-dimethylpyrrole (2.1 g, 22 mmol, 2.2 eq), thf (250 ml), chloranil (2.6 g, 10.5 mmol, 1.05 eq), 101lefins101lamine (15 mL, 107 mmol, 10 eq), boron trifluoride diethyletherate (16 mL, 130 mmol, 13 eq). Eluent – cyclohexane / ethyl acetate, 4:1.

^{1}H NMR (300 MHz, $CDCl_3$) δ 7.43 – 7.40 (m, 1H, H_{Ar}), 7.17 – 7.13 (m, 2H, H_{Ar}), 5.99 (s, 2H, H_{BODIPY}), 5.78 (bs, 1H, OH), 2.55 (s, 6H, CH_3), 1.48 (s, 6H, CH_3).

^{13}C NMR (75 MHz, $CDCl_3$) δ 156.01, 153.14, 143.09, 139.60, 131.79, 129.30, 128.66, 121.55, 116.98, 110.82, 14.97, 14.76.

HR-MS (EI), m/z: 418.06618 $[M]^{+\bullet}$, calcd. 418.0664 (Δ = -0.2 mmu).

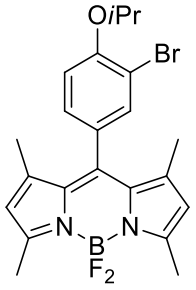

28

BODIPY **28** was obtained as orange microcrystalline solid (2.05 g, 34 % yield) from 3-bromo-4-isopropoxybenzaldehyde (3.0 g, 12.3 mmol, 1 eq), 2,4-dimethylpyrrole (2.6 g, 27 mmol, 2.2 eq), thf (300 ml), chloranil (3.2 g, 13.0 mmol, 1.05 eq), 101lefins101lamine (17 mL, 123 mmol, 10 eq), boron trifluoride diethyletherate (19.7 mL, 160 mmol, 13 eq). Eluent – cyclohexane / ethyl acetate, 8:1.

^{1}H NMR (300 MHz, $CDCl_3$) δ 7.48 (d, J = 2.1 Hz, 1H, H_{Ar}), 7.14 (dd, J = 8.4, 2.1 Hz, 1H, H_{Ar}), 7.02 (d, J = 8.5 Hz, 1H, H_{Ar}), 5.99 (s, 2H, H_{BODIPY}), 4.64 (hept, J = 6.2 Hz, 1H, CH(CH_3)$_2$), 2.55 (s, 6H, $CH_{3\ BODIPY}$), 1.48 (s, 6H, $CH_{3\ BODIPY}$), 1.43 (d, J = 6.1 Hz, 6H, CH(CH_3)$_2$).

^{13}C NMR (75 MHz, $CDCl_3$) δ 155.84, 155.26, 143.10, 139.97, 133.21, 131.75, 128.42, 128.26, 121.47, 115.83, 114.33, 72.51, 22.06, 14.90, 14.73.

Synthesis of styrenes 24 and 29

General procedure. To a flame-dried Schlenk flask equipped with stirring bar and containing corresponding aryl bromide **23** or **28** and tetrakis(triphenylphosphine)palladium(0), toluene and tributyl(vinyl)tin were added and the reaction mixture was additionally degassed (1 cycle of freeze-pump-thaw). Flask was sealed; the initial solution was heated up to 110 °C and remained stirred at this temperature overnight. The dark red suspension was allowed to cool to room temperature and concentrated under reduced pressure. Dark oily residue were purified by column chromatography.

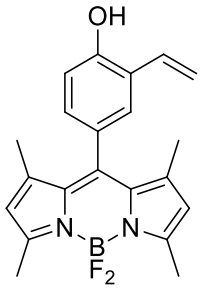

24

24 was obtained as an orange microcrystalline solid (0.74 g, 84 % yield) from **23** (1.0 g, 2.4 mmol, 1 eq), $Pd(PPh_3)_4$ (138 mg, 0.12 mmol, 5 mol %), toluene (25 mL) and tributyl(vinyl)tin (802 μL, 2.74 mmol, 1.15 eq). Eluent: cyclohexane/ethyl acetate, 4 : 1.

^{1}H NMR (300 MHz, $CDCl_3$) δ 7.31 (d, J = 2.2 Hz, 1H, H_{Ar}), 7.02 (dd, J = 8.2, 2.1 Hz, 1H, H_{Ar}), 6.95 (dd, J = 17.7, 11.1 Hz, 1H, H_{vinyl}), 6.90 (d, J = 8.1 Hz, 1H, H_{Ar}), 5.98 (s, 2H, H_{BODIPY}), 5.74 (dd, J = 17.7, 1.2 Hz, 1H, H_{vinyl}), 5.39 (dd, J = 11.2, 1.1 Hz, 2H, H_{vinyl}, OH), 2.55 (s, 6H, $CH_{3\ BODIPY}$), 1.48 (s, 6H, $CH_{3\ BODIPY}$).

^{13}C NMR (75 MHz, $CDCl_3$) δ 155.53, 153.56, 143.27, 141.66, 131.91, 130.76, 128.50, 127.53, 127.11, 125.92, 121.32, 116.81, 116.80, 14.91, 14.73.

HR-MS (EI), m/z: 366.17081 $[M]^{+\bullet}$, calcd. 366.1715 (Δ = -0.7 mmu).

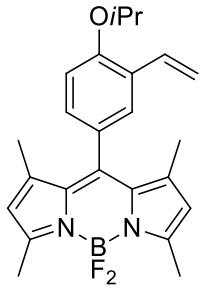

29

29 was obtained as an orange microcrystalline solid (153 mg, 86 % yield) from **28** (200 mg, 0.434 mmol, 1 eq), tetrakis(triphenylphosphine)palladium(0) (25 mg, 0.022 mmol, 5 mol %), toluene (5 mL) and tributyl(vinyl)tin (145.8 μL, 0.500 mmol, 1.15 eq). Eluent: cyclohexane/ethyl acetate, 10 : 1.

^{1}H NMR (300 MHz, $CDCl_3$) δ 7.39 (d, J = 2.2 Hz, 1H, H_{Ar}), 7.13 – 6.97 (m, 3H, H_{Ar}, H_{vinyl}), 5.98 (s, 2H, H_{BODIPY}), 5.72 (dd, J = 17.8, 1.3 Hz, 1H, H_{vinyl}), 5.26 (dd, J = 11.2, 1.3 Hz, 1H, H_{vinyl}), 4.63 (hept, J = 6.1 Hz, 1H, $CH(CH_3)_2$), 2.56 (s, 6H, $CH_{3\ BODIPY}$), 1.48 (s, 6H, $CH_{3\ BODIPY}$), 1.40 (d, J = 6.0 Hz, 6H, $CH(CH_3)_2$).

^{13}C NMR (75 MHz, $CDCl_3$) δ 155.69, 155.40, 143.27, 142.02, 131.93, 131.31, 128.87, 128.25, 127.02, 126.41, 121.24, 115.06, 114.74, 71.23, 22.18, 14.85, 14.71.

Synthesis of (11-bromoundecyl)triisopropoxysilane

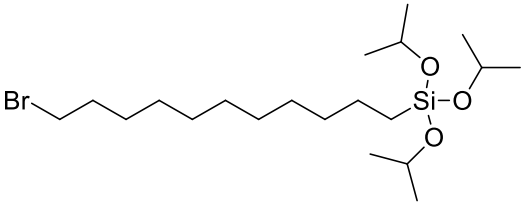

To a flame-dried Schlenk flask equipped with a stirring bar, dry 2-propanol (15 mL) and 102lefins102lamine (15 mL) were added. The reaction mixture was cooled to -10 °C and (11-bromoundecyl)trichlorosilane (2 g, 5.4 mmol) was added dropwise. Resulted white suspension was allowed to warm up to r.t., filtered under reduced pressure and the colorless filtrate was evaporated to provide the product as a colorless liquid (2.34 g, 98% yield).

^{1}H NMR (300 MHz, $CDCl_3$) δ 4.20 (p, J = 6.1 Hz, 3H), 3.40 (t, J = 6.9 Hz, 2H), 1.92 – 1.79 (m, 2H), 1.47 – 1.24 (m, 18H), 1.19 (d, J = 6.1 Hz, 16H), 0.62 – 0.52 (m, 2H).

Synthesis of styrene 25

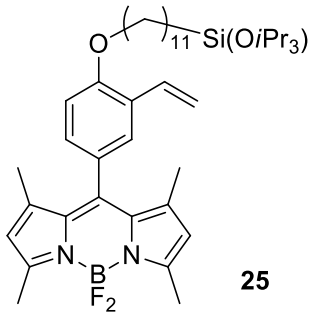

25

To a flame-dried Schlenk tube equipped with a stirring bar containing **24** (50 mg, 0.147 mmol, 1 eq), dry acetonitrile (4 mL), (11-bromoundecyl)triisopropoxysilane (63 mg, 0.143 mmol, 1.05 eq), Cs_2CO_3 (89 mg, 0.294 mmol, 2 eq) and KI (23 mg, 0.147 mmol, 1 eq) were added. Flask was sealed; the initial solution was heated up to 60 °C and remained stirred at this temperature overnight. The solution was allowed to cool to room temperature, concentrated under reduced pressure, dissolved in pentane (10 mL) and filtered through the celite pad. Evaporation of formed solution provided the product (97 mg, 98% yield) as dark oily residual which was used without further purification.

^{1}H NMR (300 MHz, $CDCl_3$) δ 7.37 (d, J = 2.2 Hz, 1H, H_{Ar}), 7.15 – 6.91 (m, 3H, H_{Ar} + $H_{styrene}$), 6.0 (s, 2H, H_{BODIPY}), 5.74 (dd, J = 17.8, 1.4 Hz, 1H, $H_{styrene}$), 5.28 (dd, J = 11.2, 1.4 Hz, 1H, $H_{styrene}$), 4.04 (t, J = 6.5 Hz, 2H, OCH_2), 3.82 (q, J = 7.0 Hz, 3H, $OCH(CH_3)_2$) 2.55 (s, 6H, CH_3 BODIPY), 1.92 – 1.81 (m, 2H, CH_2), 1.46 (s, 6H, $CH_{3\ BODIPY}$), 1.43 – 1.27 (m, 16H, CH_2), 1.23 (t, J = 7.0 Hz, 18H, $OCH(CH_3)_2$), 0.68 – 0.59 (m, 2H, CH_2Si).

^{13}C NMR (126 MHz, $CDCl_3$) δ 156.93, 155.43, 143.32, 142.06, 131.99, 131.17, 128.40, 127.75, 126.90, 126.38, 121.25, 115.32, 112.44, 68.76, 64.93, 33.45, 32.08, 29.77, 29.73, 29.61, 29.44, 26.32, 25.73, 23.16, 22.84, 14.92, 14.72, 12.21.

Synthesis of 26

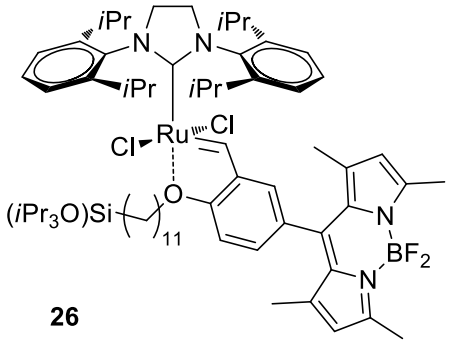

26

A flame-dried Schlenk tube containing corresponding [$RuCl_2$(SIPr)(3-phenylindeneylidene)(py)] (120 mg, 0.14 mmol, 1 eq) was evacuated and back-filled with argon three times. Toluene (4 mL) and styrene **28** (108 mg, 0.14 mmol, 1 eq) were added, the flask was sealed and the mixture was stirred at 65 °C for 4 h and then cooled to rt and evaporated under reduced pressure. Solid dark brownish residue were treated with a small amount of pentane (5 mL) and the suspension was kept in an ultrasonic bath for 1 min. The solid residue was filtered, washed with small amount of methanol (2 mL) and pentane (5 mL) and dried under vacuum to provide the product as a light brownish microcrystalline solid (138 mg, 77 % yield).

^{1}H NMR (500 MHz, $CDCl_3$) δ 16.34 (s, 1H, RuCHAr), 7.53 (t, J = 7.7 Hz, 2H, H_{Ar}), 7.35 (m, 5H, H_{Ar}), 6.97 (d, J = 8.4 Hz, 1H, H_{Ar}), 6.72 (d, J = 2.2 Hz, 1H, H_{Ar}), 5.96 (s, 2H, H_{BODIPY}), 4.18 (s, 4H, NCH_2CH_2N), 3.83 (q, J = 6.7 Hz, 4H, $OCH(CH_3)_2$), 3.62 – 3.54 (m, 6H, OCH_2 + $CH(CH_3)_2$), 2.56 (s, 6H, $CH_{3\ BODIPY}$), 1.83 (t, J = 7.9 Hz, 2H, CH_2), 1.48 – 1.13 (m, 70H, $CH_{3\ BODIPY}$ + $CH_{3\ iPr}$ + CH_2), 0.75-0.55 (m, 2H, CH_2Si).

Synthesis of 30-SIMes and 30-SIPr

General procedure. A flame-dried Schlenk tube containing corresponding [$RuCl_2$(NHC)(3-phenylindeneylidene)(py)] (1 eq) was evacuated and back-filled with argon three times. Methylene chloride, styrene **29** (1 eq) and Amberlyst resin (dry form, 4.70 mmol H^+/g) were added, the flask was sealed and the mixture was stirred at 40 °C for 30 min and then filtered, to separate the resin. The filtrate was evaporated under vacuum. The remaining solid was treated with pentane and the suspension was kept in an ultrasonic bath for 1 min. The solid residue was filtered, washed with small amount of methanol and pentane and dried under vacuum to provide the product.

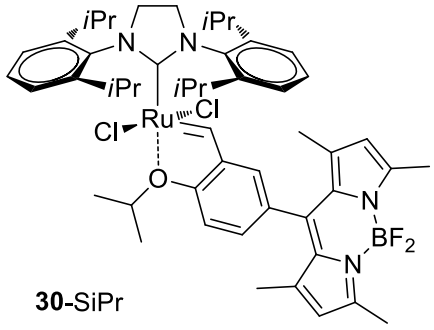

30-SiPr

30-SIPr was obtained as a light brownish microcrystalline solid (91 mg, 79 % yield) from [$RuCl_2$(SIPr)(3-phenylindeneylidene)(py)] (100 mg, 0.12 mmol), methylene chloride (2 mL), **29** (49.1 mg, 0.12 mmol) and Amberlyst resin (125 mg).

^{1}H NMR (300 MHz, $CDCl_3$) δ 16.38 (s, 1H, RuCH), 7.53 (t, J = 7.5 Hz, 2H, H_{Ar}), 7.39 – 7.32 (m, 5H, H_{Ar}), 6.93 (d, J = 8.3 Hz, 1H, H_{Ar}), 6.72 (s, 1H, H_{Ar}), 5.96 (s, 2H, H_{BODIPY}), 4.99 (hept, J = 5.6 Hz, 1H, $CH(CH_3)_2$), 4.17 (s, 4H, NCH_2CH_2N), 3.66 – 3.53 (m, 4H, $CH(CH_3)_2$), 2.56 (s, 6H, $CH_{3\ BODIPY}$), 1.40 (d, J = 6.0 Hz, 6H, $CH(CH_3)_2$), 1.31 – 1.16 (m, 30H, $CH(CH_3)_2$, $CH_{3\ BODIPY}$).

^{13}C NMR (75 MHz, $CDCl_3$) δ 155.72, 154.00, 152.89, 149.21, 144.85, 143.48, 132.12, 130.20, 128.86, 128.44, 124.54, 121.44, 121.26, 113.69, 75.92, 54.73, 28.98, 26.67, 23.52, 21.76, 14.91, 14.76.

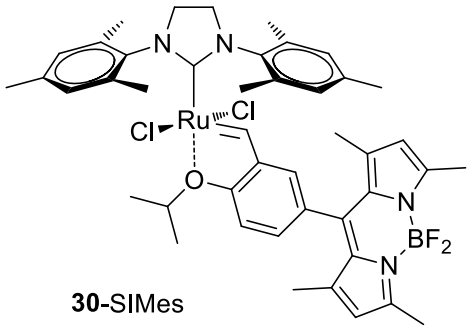

30-SIMes

30-SIMes was obtained as a light brownish microcrystalline solid (83 mg, 71 % yield) from [$RuCl_2$(SIMes)(3-phenylindeneylidene)(py)] (100 mg, 0.13 mmol), methylene chloride (2 mL), **29** (54.6 mg, 0.12 mmol) and Amberlyst resin (140 mg).

^{1}H NMR (300 MHz, $CDCl_3$) δ 16.71 (s, 1H, RuCH), 7.33 (d, J = 8.3 Hz, 1H, H_{Ar}), 6.95 (d, J = 8.3 Hz, 1H, H_{Ar}), 7.03 (s, 4H), 6.74 (s, 1H, H_{Ar}), 5.98 (s, 2H, H_{BODIPY}), 4.99 (hept, J = 5.6 Hz, 1H, C*H*$(CH_3)_2$), 4.17 (s, 4H, NCH_2CH_2N), 3.66 – 3.53 (m, 4H, C*H*$(CH_3)_2$), 2.56 (s, 6H, $CH_{3\ BODIPY}$), 1.40 (d, J = 6.0 Hz, 6H, CH(C*H*$_3)_2$), 1.31 – 1.16 (m, 30H, CH(C*H*$_3)_2$, $CH_{3\ BODIPY}$).

^{13}C NMR (75 MHz, $CDCl_3$) δ 156.71, 154.22, 152.43, 149.01, 142.81, 141.42, 130.10, 129.40, 126.95, 126.24, 124.51, 121.41, 121.26, 112.70, 75.94, 29.73, 27.91, 25.66, 22.41, 21.89, 14.76, 14.51.

HR-MS (EI), m/z: 872.25097 $[M]^{+\bullet}$, calcd. 872.2536 (Δ = -2.6 mmu).

Synthesis of complex 31

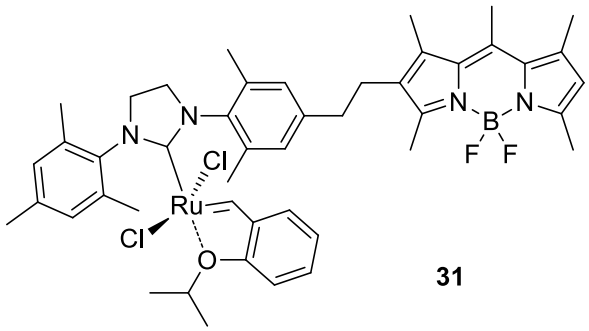

31

A flame-dried Schlenk tube containing Grubbs-Hoveyda I gen. complex (90 mg, 0.15 mmol, 1 eq) and **18** (112 mg, 0.15 mmol, 1 eq) was evacuated and back-filled with argon three times. Toluene (4 mL) was added, the flask was sealed and the mixture was stirred at 100 ^{0}C for 3 h. After that, the mixture was allowed to cool to r.t., CuCl (15 mg, 0.15 mmol, 1 eq) was added and resulted suspension was stirred for additional 30 min at r.t. Next, all volatiles were evaporated under reduced pressure and remaining dark solid was purified by column chromatography (cyclohexane – ethyl acetate, 4:1, v/v) to provide the product as a light brownish microcrystalline solid (15 mg, 11 % yield).

^{1}H NMR (500 MHz, $CDCl_3$) δ 16.57 (s, 1H, RuCHAr), 7.47 (ddd, J = 8.6, 7.3, 1.6 Hz, 1H, H_{Ar}), 7.09 (s, 2H, H_{Ar}), 7.07 (s, 2H, H_{Ar}), 6.93 (dd, J = 7.6, 1.6 Hz, 1H, H_{Ar}), 6.84 (t, J = 7.4 Hz, 1H, H_{Ar}), 6.78 (d, J = 8.3 Hz, 1H, H_{Ar}), 6.05 (s, 1H, H_{BODIPY}), 4.87 (p, J = 6.2 Hz, 1H, OC*H*$(CH_3)_2$), 4.19 (s, 4H, NCH_2CH_2N), 2.73 (bs, 4H, CH_2), 2.63 (s, 3H, $CH_{3\ BODIPY}$), 2.56 – 2.45 (m, 15H, $CH_{3\ Ar}$ + $CH_{3\ BODIPY}$), 2.42 (d, J = 8.2 Hz, 9H, $CH_{3\ Ar}$ + $CH_{3\ BODIPY}$), 1.54 (s, 3H, $CH_{3\ Ar}$), 1.27 (d, J = 6.3 Hz, 6H, OCH(C*H*$_3)_3$).

^{13}C NMR (126 MHz, $CDCl_3$) δ 211.74, 153.31, 152.91, 152.43, 145.49, 142.58, 140.95, 140.38, 138.98, 137.63, 132.08, 130.49, 129.68, 129.55, 128.77, 122.81, 122.41, 121.07, 113.07, 75.13, 51.70, 36.65, 29.86, 27.09, 26.70, 21.30, 21.26, 17.52, 16.90, 14.80, 14.55, 12.70.

Synthesis of complex 32

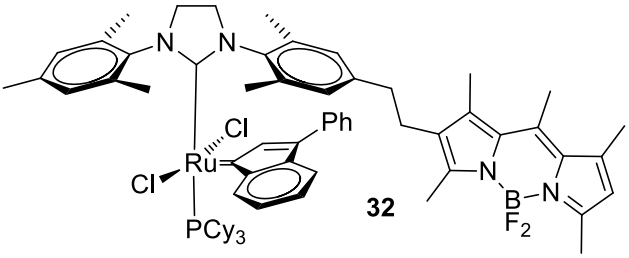

32

A flame dried Schlenk flask containing **18** (130 mg, 0.174 mmol, 1 eq) and [$(Pcy_3)_2RuCl_2$(ind)] (160 mg, 0.174 mmol, 1 eq) was evacuated and back-filled with argon three times. Toluene (7 mL) was added, the flask was sealed and the mixture was stirred at 100 ^{0}C for 4 h. Next, all volatiles were evaporated under

reduced pressure and remaining dark brownish solid was purified by column chromatography (cyclohexane – ethyl acetate, 1:1, v/v). **32** was obtained as a red-brownish microcrystalline solid (140 mg, 66% yield).
In NHR spectra two rotamers can be observed and precise integration and assignment of peaks is not possible.
^{1}H NMR (500 MHz, Chloroform-*d*) δ 8.61 – 8.53 (m, 1H), 7.65 – 7.60 (m, 2H), 7.44 – 7.38 (m, 1H), 7.34 – 7.27 (m, 2H), 7.26 – 7.23 (m, 1H), 7.16 – 7.06 (m, 2H), 6.99 – 6.90 (m, 3H), 6.45, 6.36 (two singulets, 1H), 6.36 (t, J = 1.4 Hz, 0H), 5.99 – 5.92 (m, 2H), 3.98 – 3.91 (m, 2H), 3.85 – 3.68 (m, 2H), {2.71 – 2.67 (m), 2.65 (s), 2.64 (s), 2.62, 2.61-2.58 (m), 2.56 (s), 2.52 (s), 2.45 (s), 2.44 (s), 2.36 (s), 2.34 (s), 2.33 (s), 2.27 (s), 2.26 (s), 2.21 (s), 2.17 (s), 2.15 (s), 2.12-2.04 (m), 2.02 (s), 2.01 (s)} (37H), 1.55 – 1.33 (m, 15H), 1.05 – 0.87 (m, 15H).
^{13}C NMR (126 MHz, $CDCl_3$) δ 292.64, 217.65, 217.14, 153.82, 152.90, 145.38, 145.25, 142.09, 141.26, 141.08, 140.92, 140.66, 140.39, 140.02, 139.73, 139.52, 138.81, 138.46, 138.38, 137.98, 137.79, 137.52, 137.38, 137.19, 137.11, 136.75, 136.50, 135.82, 132.34, 131.10, 130.33, 129.74, 129.65, 129.45, 129.40, 129.31, 129.24, 129.03, 128.51, 128.41, 128.07, 127.92, 127.82, 127.27, 126.75, 126.72, 121.22, 116.47, 116.29, 53.02, 52.46, 36.66, 36.47, 33.45, 33.32, 29.79, 29.70, 28.24, 28.16, 28.12, 28.04, 26.72, 26.66, 26.07, 25.34, 22.75, 21.59, 21.41, 20.80, 20.70, 20.65, 19.31, 19.27, 19.23, 19.09, 17.77, 17.74, 17.14, 17.10, 14.94, 14.75, 14.45, 12.72.
^{31}P NMR (121 MHz, $CDCl_3$) δ 25.94, 25.75.
^{19}F NMR (282 MHz, $CDCl_3$) δ -148.92 – -150.20 (m).

5.2. Quantum yields determination

Quantum yields were determined according to the literature procedure[291] using rhodamine 6G (from Sigma-Aldrich, BioReagent, suitable for fluorescence) as the standard. Absorption and emission spectra for imidazole **11**, imidazolium salt **12**·HI, complexes based on carbene **12** were obtained in ethyl acetate (excitation wavelength: 512 nm), for compounds **17-19**, **20c** in 1,2-dichloroethane (excitation at 510 nm), for complexes **20b** and **21b** in pyridine (excitation at 510 nm) and for **27** and **30**-SIMes in toluene (excitation at 504 nm) over a range of concentrations (250 nM to 1.0 μM) where a linear correlation between concentration and absorption was observed and the absorbance was within 0.01 to 0.1. The quantum yield was calculated according to the equation $\Phi_x = \Phi_{st}\left(\frac{Grad_x}{Grad_{st}}\right)\left(\frac{\eta_x}{\eta_{st}}\right)^2$ where the subscripts *st* and *x* denote standard and test respectively, Φ is the fluorescence quantum yield, *Grad* the gradient from the plot of integrated fluorescence intensity *vs* absorbance, and η the refractive index of the solvent. Φ_{st} = 0.95 in EtOH.

5.3. Monitoring of the reaction of cod-complexes with CO

General conditions. All experiments were carried out in quartz cuvettes with a path length of 10.00 mm equipped with septa and stirring bar. The temperature (25 °C) was adjusted using a thermostat and controlled with a thermometer. The following general procedure was applied in all experiments with CO: $1.8\cdot10^{-6}$ mol of cod-complex was dissolved in ethyl acetate (10 mL) to give $1.8\cdot10^{-4}$ mol·L^{-1} solution. 4450 μL of ethyl acetate were filled in a cuvette. This amount was calculated such that, after addition of a stock solution of cod-complex, the complex concentration is $2.0\cdot10^{-6}$ M and cuvette is filled to the very top. The cuvette was then placed in the spectrometer, CO was added using the gas-tight syringe (2.2 μL, 90 nmol, 10 eq) through the septa and was allowed to adjust to the respective temperature. The measurement was started at the moment of the addition of the corresponding amount of preheated stock solution of cod-complex (50 μL, $1.8\cdot10^{-4}$ mol·L^{-1}, 9.0 nmol, 1 eq).

5.4. Detection of CO in ambient atmosphere

100 mL round-bottom flask (total volume 120 mL) equipped with stirring bar was filled with a solution of [(**12**)IrCl(cod)] in ethyl acetate (20 mL, $1 \cdot 10^{-5}$ mol·L^{-1}) and sealed with septa. All experiments were done at room temperature under air atmosphere. Calculated amount of CO (5 or 10 μL) was added using gas-tight syringe into the gas phase. For the monitoring of the reaction progress, samples (250 μL) were taken at the specified times and added to the quartz cuvette filled with 1 mL of ethyl acetate. Emission spectra of formed solution ($2.0 \cdot 10^{-6}$ mol·L^{-1}) were recorded.

5.5. Fluorometric [(12)AuI] determination

All measurements were carried out in the same quartz cuvette with a path length of 10 mm. Four stock solution of [(**12**)AuI] were prepared in ethyl acetate using dilution method. The concentrations of these stock solutions were calculated such that, after the addition of 0.5 mL of stock solution to 2 mL of ethyl acetate, the complex concentrations are 1.0, 5.0, 10.0 and $50.0 \cdot 10^{-9}$ mol·L^{-1}. The cuvette was filled with 2 mL of ethyl acetate and reference spectrum was recorded, excitation wavelength – 506 nm. Then, 0.5 mL of a corresponding stock solution of the complex was added to the cuvette and emission spectra were recorded. The spectra of the complex were calculated by subtraction of reference spectra from the crude spectra of the complex.

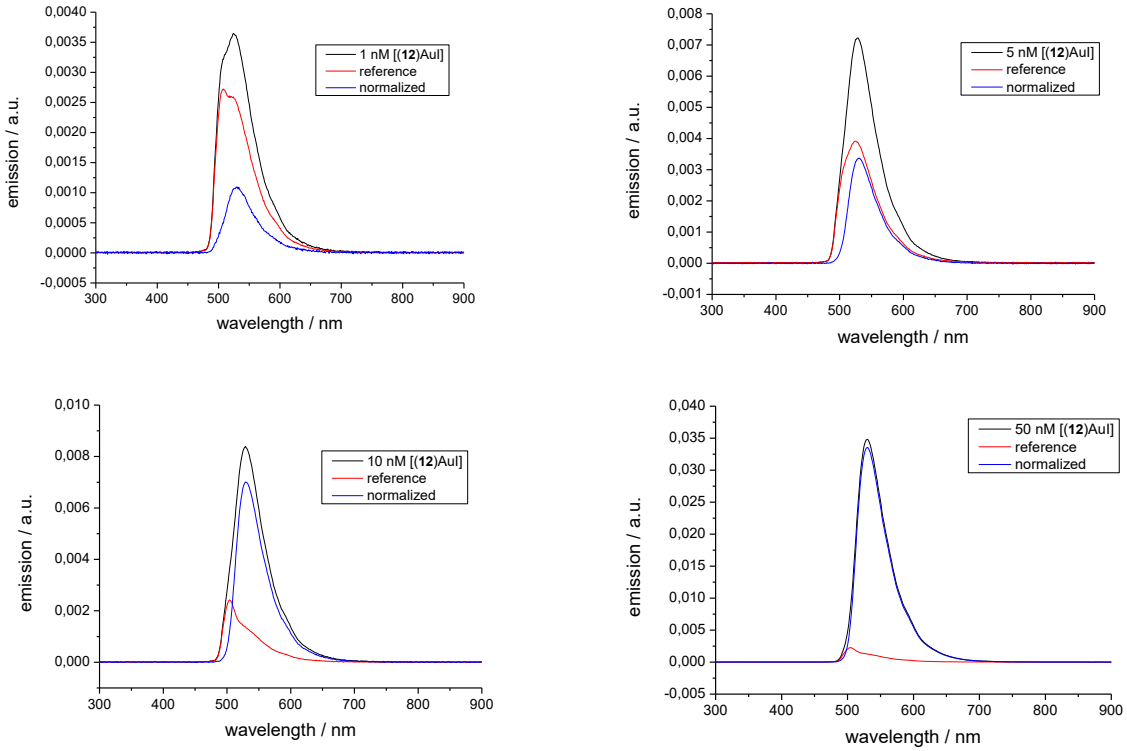

Figure 5.1. Crude (black), reference (red) and normalized (blue) fluorescence spectra of 1.0, 5.0, 10.0 and $50.0 \cdot 10^{-9}$ mol·L^{-1} solutions of [(**12**)AuI] in EtOAc.

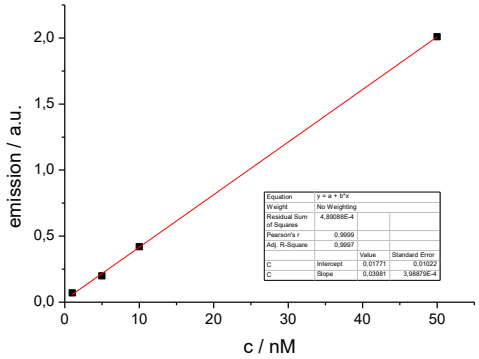

Figure 5.2. Emission vs. concentration plot for [(**12**)AuI] solutions in ethyl acetate.

5.6. Monitoring of the reaction of complexes 20 with hydrogen

General conditions. All experiments were carried out in quartz cuvettes with a path length of 10.00 mm equipped with septa and stirring bar. The temperature (298K) was adjusted using a thermostat and controlled with a thermometer. The following general procedure was applied in all experiments with H_2: $1.0 \cdot 10^{-6}$ mol of the complex was dissolved in 1,2-dichloroethane or methanol (10 mL) to give $1.0 \cdot 10^{-4}$ mol·L^{-1}solution. 1,2-dichloroethane or methanol 2970 μL and 30 μL of a stock solution of the complex were filled in a cuvette. For measurements in the presence of substrate, cuvette was filled with catalyst stock solution (30 μL), substrate and 1,2-dichloroethane. The substrate concentration was defined as c(S) = n(S)/[V(S) + V(solvent) + V(stock solution)]. The cuvette was then placed in the spectrometer and was allowed to adjust to the respective temperature. The measurement was started and after few minutes hydrogen flow was applied to the cuvette through the cannula. Hydrogen was slowly bubbled during the measurement.

5.7. Catalyst Screening

Preparation of catalyst and substrate stock solution for the reaction with 0.5 mol % (c = $1 \cdot 10^{-5}$ mol·L^{-1}) of catalyst and allylbenzene (c = 0.002 mol·L^{-1}) with tetradecane as internal standard. Screenings with another catalyst loadings and substrate concentrations were done in a similar way. Iridium complex **20c** (1.2 mg, $6.6 \cdot 10^{-7}$ mol) was weighed into 10 mL Schlenk tube. The tube was evacuated, backfilled with argon and 1,2-dichloroethane (658 μL) was added to give a $1.0 \cdot 10^{-3}$ molL^{-1} solution of catalyst. Into another 25 mL Schlenk tube, allylbenzene (266 μL, 0.002 mol) and tetradecane (260 μL, 0.001 mol) were added and diluted to 10 mL with 1,2-dichloroethane to give 0.2 M solution of the substrate. The reaction was carried out at r.t. in a sealed 10-mL Schlenk tube equipped with septa, stirring bar and connected to a balloon filled with hydrogen. The tube was evacuated and backfilled with hydrogen three times. 1,2-dichloroethane (4.9 mL) and substrate stock solution (50 μL) were added via syringe and mixture was vigorously stirred for 30 min and catalyst stock solution (50 μL) was added. For the determination of substrate conversion, samples (100 μL) were taken after the specified times via syringe and injected into GC vials. The conversions were determined by GC. Monitoring of fluorescence intensity for this reaction was done in fluorescence quartz cuvette with a path length of 10.00 mm equipped with septa and stirring bar. A cuvette was filled with 1,2-dichloroethane (2960 μL) and substrate stock solution (30 μL). Hydrogen was bubbled through the cuvette for 30 min. Catalyst stock solution (30 μL) was injected with a syringe and at this moment measurement was started.

5.8. Hydrogen detection

Complex **20b** (2.22 mg, $2.0 \cdot 10^{-6}$ mol) was dissolved in propylene carbonate (2 mL) to give 1 mM solution. A small strip of filter paper was moistened with this solution and placed into a flask. The flask was sealed with septa and calculated amount of hydrogen was added using a gas-tight syringe. For the experiment with pure hydrogen, the flask was evacuated and backfilled with hydrogen. After 10 min paper was removed from the flask and a photo was taken under UV-lamp in the dark.

5.9. Fluorescence and UV/Vis experiments

All experiments were carried out in 1 cm×1 cm quartz cuvette (Hellma Analytics, Lot.: 111-10-40). The temperature (30 °C) was adjusted using a thermostat and controlled with a thermometer. BuVE, DEDAM, or 1-hexene were used as substrates for measurements. The following general procedure was applied in all experiments with 108lefins: $1.00 \cdot 10^{-6}$ mol of pre-catalyst was dissolved in abs. toluene (10 mL) to give a $1.00 \cdot 10^{-4}$ mol·L^{-1} solution. Calculated amount of stock solution of pre-catalyst was filled in a cuvette and an additional amount of toluene was added. These amounts were calculated such that, after the addition of substrate, the pre-catalyst concentration is $1.00 \cdot 10^{-6}$ – $3.00 \cdot 10^{-5}$ mol·L^{-1}, depending on the conducted experiment. The cuvette was then placed in the spectrometer and was allowed to adjust to the respective temperature. The measurement was started in the moment of the addition of the corresponding amount of preheated (same temperature as inside the cuvette) substrate. During the measurement the cuvette was closed with a PTFE stopper (not gas tight).

List of abbreviations

Ac	acetyl
Alk	alkyl
Ar	aryl
BAPTA	1,2-bis(o-aminophenoxy)ethane-n,n,n',n'-tetraacetic acid
BArF	tetrakis[3,5-bis(trifluoromethyl)phenyl)borate
BODIPY	4,4-difluoro-4-bora-3*a*,4*a*-diaza-*s*-indacen
Bu	butyl
BuVE	butylvinyl ether
cod	*cis*,*cis*-1,5-cyclooctadiene
cy	cyclohexyl
DBU	1,8-diazabicycloundec-7-ene
DCM	dichloromethane
DDQ	2,3-dichloro-5,6-dicyano-1,4-benzoquinone
DEDAM	diethyl diallylmalonate
DFT	density functional theory
DMF	dimethylformamide
DMSO	dimethyl sulfoxide
DOX	doxorubicin, an anticancer chemotherapy agent
DSSC	dye-sensitized solar cells
EDG	electron donating group
Et	ethyl
EWG	electron withdrawing group
FRET	fluorescence or förster energy transfer
GC	gas chromatography
HOMO	highest occupied molecular orbital
ICT	intramolecular (internal) charge transfer
*i*Pr	isopropyl
L	ligand
LE	local excited
LMCT	ligand-to-metal charge transfer
LUMO	lowest unoccupied molecular orbital
*m*CPBA	meta-chloroperoxybenzoic acid
Me	methyl
Mes	mesityl
MS	mass spectrometry
NHC	*n*-heterocyclic carbene
NIPAM	*n*-isopropylacrylamide
NMR	nuclear magnetic resonance
OPV	organic dyes photovoltaic
PCE	power conversion efficiency
PDT	photodynamic therapy
PEG	polyethylene glycol
PET	photoinduced electron transfer
Ph	phenyl
py	pyridine

r.t., rt	room temperature
RET	resonance energy transfer
SIMes	1,3-bis(2,4,6-trimethylphenyl)imidazolin-2-ylidene
SIPr	1,3-bis(2,6-diisopropylphenyl)imidazolin-2-ylidene
SMFM	single molecule fluorescent microscopy
TBAF	tetra-*n*-butylammonium fluoride
Tf	triflyl, trifluoromethanesulfonyl
TFA	trifluoroacetic acid
THF	tetrahydrofuran
*t*Pent	1,1-dimethylpropyl
UV-Vis	ultraviolet-visible spectroscopy

References

[1] Y. Mely, G. Duportail, *Fluorescent Methods to Study Biological Membranes*, Springer, **2012**.

[2] S. H. Cody, D. A. Williams, *Fluorescent and Luminescent Probes for Biological Activity*, Academic Press, **1999**.

[3] W. Rettig, B. Strehmel, S. Schrader, H. Seifert, *Applied Fluorescence in Chemistry, Biology and Medicine*, Springer, **2012**.

[4] C. Gell, D. Brockwell, A. Smith, *Handbook of Single Molecule Fluorescence Spectroscopy*, Oxford University Press, **2006**.

[5] A. Cornea, P. M. Conn, *Fluorescence Microscopy, Super-Resolution and Other Novel Techniques*, Academic Press, **2014**.

[6] M. Hof, R. Hutterer, R. Fidler, *Fluorescence Spectroscopy in Biology*, Springer, **2005**.

[7] F. Photophysical, *Fluorescence Imaging for Surgeons*, Springer, **2015**.

[8] L. Marcu, P. M. W. French, D. S. Elson, *Fluorescence Lifetime Spectroscopy and Imaging: Principles and Applications in Biomedical Diagnostics*, CRC Press, **2014**.

[9] A. Kamkaew, S. H. Lim, H. B. Lee, L. V. Kiew, L. Y. Chung, K. Burgess, *Chem. Soc. Rev.* **2013**, *42*, 77–88.

[10] N. Boens, V. Leen, W. Dehaen, *Chem. Soc. Rev.* **2012**, *41*, 1130–1172.

[11] K. P. Carter, A. M. Young, A. E. Palmer, *Chem. Rev.* **2014**, *114*, 4564–4601.

[12] M. J. Culzoni, A. Munoz de la Pena, A. Machuca, H. C. Goicoechea, R. Babiano, *Anal. Methods* **2013**, *5*, 30–49.

[13] J. Han, K. Burgess, *Chem. Rev.* **2010**, *110*, 2709–2728.

[14] R. W. Sinkeldam, N. J. Greco, Y. Tor, *Chem. Rev.* **2010**, *110*, 2579–2619.

[15] A. Bessette, G. S. Hanan, *Chem. Soc. Rev.* **2014**, *43*, 3342–405.

[16] S. P. Singh, T. Gayathri, *Eur. J. Org. Chem.* **2014**, *2014*, 4689–4707.

[17] J. R. Lakowicz, *Principles of Fluorescence Spectroscopy*, Springer, **2006**.

[18] D. M. Jameson, *Introduction to Fluorescence*, Springer, **2014**.

[19] A. P. Demchenko, *Introduction to Fluorescence Sensing*, Springer, **2008**.

[20] B. Valeur, *Molecular Fluorescence: Principles and Applications*, Wiley, **2012**.

[21] G. G. Stokes, *Philos. Trans. R. Soc. London* **1853**, *143*, 385–396.

[22] L. Yuan, W. Lin, K. Zheng, L. He, W. Huang, *Chem. Soc. Rev.* **2013**, *42*, 622–661.

[23] Y. Ni, J. Wu, *Org. Biomol. Chem.* **2014**, *12*, 3774–91.

[24] K. Umezawa, D. Citterio, K. Suzuki, *Anal. Sci.* **2014**, *30*, 327–349.

[25] M. S. T. Goncalves, *Chem. Rev.* **2009**, *109*, 190–212.

[26] A. Treibs, F.-H. Kreuzer, *Justus Liebigs Ann. Chem.* **1968**, *718*, 208–223.

[27] G. Ulrich, R. Ziessel, A. Harriman, *Angew. Chem., Int. Ed.* **2008**, *47*, 1184–1201.

[28] T. E. Wood, A. Thompson, *Chem. Rev.* **2007**, *107*, 1831–1861.

[29] A. Loudet, K. Burgess, *Chem. Rev.* **2007**, *107*, 4891–4932.

[30] N. Boens, B. Verbelen, W. Dehaen, *Eur. J. Org. Chem.* **2015**, *2015*, 6577–6595.

[31] G. Fan, L. Yang, Z. Chen, *Front. Chem. Sci. Eng.* **2014**, *8*, 405–417.

[32] A. Atilgan, E. Tanriverdi, R. Guliyev, T. B. Uyar, S. Erbas-Cakmak, E. U. Akkaya, *Angew. Chem., Int. Ed.* **2014**, *53*, 10678–10681.

[33] Z. Yang, Y. He, J. H. Lee, N. Park, M. Suh, W. S. Chae, X. Peng, H. Jung, C. Kang, J. S. Kim, *J. Am. Chem. Soc.* **2013**, *135*, 9181–9185.

[34] T. V. Goud, A. Tutar, J. F. Biellmann, *Tetrahedron* **2006**, *62*, 5084–5091.

[35] L. Yu, K. Muthukumaran, I. V. Sazanovich, C. Kirmaier, E. Hindin, J. R. Diers, P. D. Boyle, D. F. Bocian, D. Holten, J. S. Lindsey, *Inorg. Chem.* **2003**, *42*, 6629–6647.

[36] D. Wang, J. Fan, X. Gao, B. Wang, S. Sun, X. Peng, *J. Org. Chem.* **2009**, *74*, 7675–7683.

[37] X. Zhou, C. Yu, Z. Feng, Y. Yu, J. Wang, E. Hao, Y. Wei, X. Mu, L. Jiao, *Org. Lett.* **2015**, *17*, 4632–4635.

[38] A. Poirel, A. De Nicola, R. Ziessel, *J. Org. Chem.* **2014**, *79*, 11463–11472.

[39] W. Wu, Y. Geng, M. Wu, J. Zheng, R. Wang, L. Zhan, J. Zhang, *Faming Zhuanli Shenqing*, **2014**, CN 103804402 A.

[40] T. Bruhn, G. Pescitelli, S. Jurinovich, A. Schaumlöffel, F. Witterauf, J. Ahrens, M. Bröring, G. Bringmann, *Angew. Chem., Int. Ed.* **2014**, *53*, 14592–14595.

[41] C. W. Wan, A. Burghart, J. Chen, F. Bergstroem, L. B.-A. Johansson, M. F. Wolford, T. G. Kim, M. R. Topp, R. M. Hochstrasser, K. Burgess, *Chem. - Eur. J.* **2003**, *9*, 4430–4441.

[42] L. Jiao, C. Yu, M. Liu, Y. Wu, K. Cong, T. Meng, Y. Wang, E. Hao, *J. Org. Chem.* **2010**, *75*, 6035–6038.

[43] L. Wu, K. Burgess, *Chem. Commun.* **2008**, 4933–4935.

[44] V. Leen, Synthesis and Application of Reactive BODIPY Dyes, Katholieke Universiteit Leuven, **2010**.

[45] J. Bañuelos, V. Martín, C. F. A. Gómez-Durán, I. J. A. Córdoba, E. Peña-Cabrera, I. García-Moreno, Á. Costela, M. E. Pérez-Ojeda, T. Arbeloa, Í. L. Arbeloa, *Chem. - Eur. J.* **2011**, *17*, 7261–7270.

[46] E. Peña-Cabrera, A. Aguilar-Aguilar, M. González-Domínguez, E. Lager, R. Zamudio-Vázquez, J. Godoy-Vargas, F. Villanueva-García, *Org. Lett.* **2007**, *9*, 3985–3988.

[47] V. Leen, P. Yuan, L. Wang, N. Boens, W. Dehaen, *Org. Lett.* **2012**, *14*, 6150–6153.

[48] K. Tram, H. Yan, H. A. Jenkins, S. Vassiliev, D. Bruce, *Dye. Pigment.* **2009**, *82*, 392–395.

[49] A. Schmitt, B. Hinkeldey, M. Wild, G. Jung, *J. Fluoresc.* **2009**, *19*, 755–758.

[50] I. J. Arroyo, R. Hu, G. Merino, B. Z. Tang, E. Peña-Cabrera, *J. Org. Chem.* **2009**, *74*, 5719–5722.

[51] L. P. Jameson, S. V. Dzyuba, *Beilstein J. Org. Chem.* **2013**, *9*, 786–790.

[52] E. Deniz, G. C. Isbasar, Ö. A. Bozdemir, L. T. Yildirim, A. Siemiarczuk, E. U. Akkaya, *Org. Lett.* **2008**, *10*, 3401–3403.

[53] N. Boens, W. Qin, M. Baruah, W. M. De Borggraeve, A. Filarowski, N. Smisdom, M. Ameloot, L. Crovetto, E. M. Talavera, J. M. Alvarez-Pez, *Chem. - Eur. J.* **2011**, *17*, 10924–10934.

[54] G. Sevinç, B. Küçüköz, H. Yilmaz, G. Şirikçi, H. G. Yaglioglu, M. Hayvali, A. Elmali, *Sens. Actuators, B* **2014**, *193*, 737–744.

[55] M. Tian, X. Peng, F. Feng, S. Meng, J. Fan, S. Sun, *Dye. Pigment.* **2009**, *81*, 58–62.

[56] M. Gupta, S. Mula, M. Tyagi, T. K. Ghanty, S. Murudkar, A. K. Ray, S. Chattopadhyay, *Chem. - Eur. J.* **2013**, *19*, 17766–17772.

[57] C. N. Baki, E. U. Akkaya, *J. Org.Chem* **2001**, *66*, 1512–1513.

[58] M. Baruah, W. Qin, N. Basaric, W. M. De Borggraeve, N. Boens, *J. Org. Chem.* **2005**, *70*, 4152–4157.

[59] T. Gareis, C. Huber, O. S. Wolfbeis, J. Daub, *Chem. Commun.* **1997**, *1*, 1717–1718.

[60] L. Gai, J. Mack, H. Lu, H. Yamada, D. Kuzuhara, G. Lai, Z. Li, Z. Shen, *Chem. - Eur. J.* **2014**, *20*, 1091–1102.

[61] T. Werner, C. Huber, S. Heinl, M. Kollmannsberger, J. Daub, O. S. Wolfbeis, *Fresenius' J. Anal. Chem.* **1997**, *359*, 150–154.

[62] M. Baruah, W. Qin, C. Flors, J. Hofkens, R. A. L. Vallée, D. Beljonne, M. Van Der Auweraer, W. M. De Borggraeve, N. Boens, *J. Phys. Chem. A* **2006**, *110*, 5998–6009.

[63] M. Kollmannsberger, K. Rurack, U. Resch-Genger, J. Daub, *J. Phys. Chem. A* **1998**, *102*, 10211–10220.

[64] Y. Urano, D. Asanuma, Y. Hama, Y. Koyama, T. Barrett, M. Kamiya, T. Nagano, T. Watanabe, P. L. Choyke, H. Kobayashi, *Nat. Med.* **2009**, *15*, 104–109.

[65] S. Madhu, M. R. Rao, M. S. Shaikh, M. Ravikanth, *Inorg. Chem.* **2011**, *50*, 4392–4400.

[66] J. Zhang, M. Yang, C. Li, N. Dorh, F. Xie, F.-T. Luo, A. Tiwari, H. Liu, *J. Mater. Chem. B* **2015**, *3*, 2173–2184.

[67] F. Han, Y. Xu, D. Jiang, Y. Qin, H. Chen, *Anal. Biochem.* **2013**, *435*, 106–113.

[68] E. Teknikel, C. Unaleroglu, *Dye. Pigment.* **2015**, *120*, 239–244.

[69] B. D. Gutierrez-Ramos, J. Banuelos, T. Arbeloa, I. L. Arbeloa, P. E. Gonzalez-Navarro, K. Wrobel, L. Cerdan, I. Garcia-Moreno, A. Costela, E. Pena-Cabrera, *Chem. - Eur. J.* **2015**, *21*, 1755–1764.

[70] C. Thivierge, J. Han, R. M. Jenkins, K. Burgess, *J. Org. Chem.* **2011**, *76*, 5219–5228.

[71] S. Bakthavatsalam, A. Sarkar, A. Rakshit, S. Jain, A. Kumar, A. Datta, *Chem. Commun.* **2015**, *51*, 2605–2608.

[72] B. Sui, X. Yue, M. G. Tichy, T. Liu, K. D. Belfield, *Eur. J. Org. Chem.* **2015**, *2015*, 1189–1192.

[73] B. Sui, S. Tang, T. Liu, B. Kim, K. D. Belfield, *ACS Appl. Mater. Interfaces* **2014**, *6*, 18408–18412.

[74] W. Duan, H. Wei, T. Cui, B. Gao, *J. Mater. Chem. B* **2015**, *3*, 894–898.

[75] H. Xiao, J. Li, K. Wu, G. Yin, Y. Quan, R. Wang, *Sens. Actuators, B* **2015**, *213*, 343–350.

[76] R. S. Singh, R. K. Gupta, R. P. Paitandi, A. Misra, D. S. Pandey, *New J. Chem.* **2015**, *39*,

2233–2239.

[77] K. R. Gee, A. Rukavishnikov, A. Rothe, *Comb. Chem. High Throughput Screening* **2003**, *6*, 363–366.

[78] S. Zhu, J. Zhang, J. Janjanam, G. Vegesna, F.-T. Luo, A. Tiwari, H. Liu, *J. Mater. Chem. B* **2013**, *1*, 1722–1728.

[79] B. Wu, L. Xu, S. Wang, Y. Wang, W. Zhang, *Polym. Chem.* **2015**, *6*, 4279–4289.

[80] B. Sui, X. Yue, B. Kim, K. D. Belfield, *ACS Appl. Mater. Interfaces* **2015**, *7*, 17565–17568.

[81] X. Zhang, Y. Xiao, X. Qian, *Angew. Chem., Int. Ed.* **2008**, *47*, 8025–8029.

[82] E. Karakus, M. Üçüncü, M. Emrullahoglu, *Chem. Commun.* **2014**, *50*, 1119–1121.

[83] D. P. Kennedy, C. M. Kormos, S. C. Burdette, *J. Am. Chem. Soc.* **2009**, *131*, 8578–8586.

[84] J. Wang, Y. Hou, C. Li, B. Zhang, X. Wang, *Sens. Actuators, B* **2011**, *157*, 586–593.

[85] L. Wang, G. Fang, D. Cao, *J. Fluoresc.* **2014**, *24*, 1757–1766.

[86] A. K. Mahapatra, R. Maji, K. Maiti, S. S. Adhikari, C. Mukhopadhyay, D. Mandal, *Analyst* **2014**, *139*, 309–317.

[87] S. Madhu, M. Ravikanth, *Inorg. Chem.* **2014**, *53*, 1646–1653.

[88] B. Umasekhar, E. Ganapathi, T. Chatterjee, M. Ravikanth, *Dalton Trans.* **2015**, *44*, 16516–16527.

[89] B. Taner, A. N. Kursunlu, E. Güler, *Spectrochim. Acta, Part A* **2014**, *118*, 903–907.

[90] P. Ashokkumar, H. Weißhoff, W. Kraus, K. Rurack, *Angew. Chem., Int. Ed.* **2014**, *53*, 2225–2229.

[91] J. Cao, C. Zhao, P. Feng, Y. Zhang, W. Zhu, *RSC Adv.* **2012**, *2*, 418–420.

[92] J. Xu, S. Sun, Q. Li, Y. Yue, Y. Li, S. Shao, *Anal. Chim. Acta* **2014**, *849*, 36–42.

[93] L. Fu, F. F. Wang, T. Gao, R. Huang, H. He, F. L. Jiang, Y. Liu, *Sens. Actuators, B* **2015**, *216*, 558–562.

[94] H. Sun, X. Dong, S. Liu, Q. Zhao, X. Mou, H. Y. Yang, W. Huang, *J. Phys. Chem. C* **2011**, *115*, 19947–19954.

[95] S. K. Sarkar, P. Thilagar, *Chem. Commun.* **2013**, *49*, 8558–8560.

[96] C. A. Swamy P, S. Mukherjee, P. Thilagar, *Inorg. Chem.* **2014**, *53*, 4813–4823.

[97] R. Misra, T. Jadhav, B. Dhokale, S. M. Mobin, *Dalton Trans.* **2015**, *44*, 16052–16060.

[98] C. A. P. Swamy, S. Mukherjee, P. Thilagar, *Chem. Commun.* **2013**, *49*, 993–995.

[99] Z. Ekmekci, M. D. Yilmaz, E. U. Akkaya, *Org. Lett.* **2008**, *10*, 461–464.

[100] A. Dvivedi, P. Rajakannu, M. Ravikanth, *Dalton Trans.* **2015**, *44*, 4054–4062.

[101] R. Guliyev, O. Buyukcakir, F. Sozmen, O. A. Bozdemir, *Tetrahedron Lett.* **2009**, *50*, 5139–5141.

[102] A. Coskun, E. Deniz, E. U. Akkaya, *Tetrahedron Lett.* **2007**, *48*, 5359–5361.

[103] A. Coskun, B. T. Baytekin, E. U. Akkaya, *Tetrahedron Lett.* **2003**, *44*, 5649–5651.

[104] B. Turfan, E. U. Akkaya, *Org. Lett.* **2002**, *4*, 2857–2859.

[105] X. Chen, X. Tian, I. Shin, J. Yoon, *Chem. Soc. Rev.* **2011**, *40*, 4783–4804.

[106] J. Fan, H. Mu, H. Zhu, J. Du, N. Jiang, J. Wang, X. Peng, *Ind. Eng. Chem. Res.* **2015**, *54*, 8842–8846.

[107] E. Wang, H. Qiao, Y. Zhou, L. Pang, F. Yu, J. Zhang, T. Ma, *RSC Adv.* **2015**, *5*, 73040–73045.

[108] J. J. Hu, N.-K. Wong, Q. Gu, X. Bai, S. Ye, D. Yang, *Org. Lett.* **2014**, *16*, 3544–3547.

[109] P. Venkatesan, S.-P. Wu, *Analyst* **2015**, *140*, 1349–1355.

[110] B. Wang, P. Li, F. Yu, J. Chen, Z. Qu, K. Han, *Chem. Commun.* **2013**, *49*, 5790–5792.

[111] S. R. Liu, M. Vedamalai, S. P. Wu, *Anal. Chim. Acta* **2013**, *800*, 71–76.

[112] R. Saito, A. Ohno, E. Ito, *Tetrahedron* **2010**, *66*, 583–590.

[113] A. Khatchadourian, K. Krumova, S. Boridy, T. N. An, D. Maysinger, G. Cosa, *Biochemistry* **2009**, *48*, 5658–5668.

[114] P. Oleynik, Y. Ishihara, G. Cosa, *J. Am. Chem. Soc.* **2007**, *129*, 1842–1843.

[115] J. Xu, Q. Li, Y. Yue, Y. Guo, S. Shao, *Biosens. Bioelectron.* **2014**, *56*, 58–63.

[116] H. X. Zhang, J. B. Chen, X. F. Guo, H. Wang, H. S. Zhang, *Talanta* **2013**, *116*, 335–342.

[117] G. K. Vegesna, S. R. Sripathi, J. Zhang, S. Zhu, W. He, F. T. Luo, W. J. Jahng, M. Frost, H. Liu, *ACS Appl. Mater. Interfaces* **2013**, *5*, 4107–4112.

[118] X. Zhang, B. Wang, C. Wang, L. Chen, Y. Xiao, *Anal. Chem.* **2015**, *87*, 8292–8300.

[119] C. L. Teoh, D. Su, S. Sahu, S. W. Yun, E. Drummond, F. Prelli, S. Lim, S. Ham, T. Wisniewski, Y. T. Chang, *J. Am. Chem. Soc.* **2015**, *137*, 13503–13509.

[120] J. C. T. Carlson, L. G. Meimetis, S. A. Hilderbrand, R. Weissleder, *Angew. Chem., Int. Ed.* **2013**, *52*, 6917–6920.

[121] X. Shao, R. Kang, Y. Zhang, Z. Huang, F. Peng, J. Zhang, Y. Wang, F. Pan, W. Zhang, W. Zhao, *Anal. Chem.* **2015**, *87*, 399–405.

[122] D. Kand, T. Saha, M. Lahiri, P. Talukdar, *Org. Biomol. Chem.* **2015**, *13*, 8163–8168.

[123] J. Shao, H. Sun, H. Guo, S. Ji, J. Zhao, W. Wu, X. Yuan, C. Zhang, T. D. James, *Chem. Sci.* **2012**, *3*, 1049–1061.

[124] L. Zhang, H. Zhu, M. Li, X. Gu, *Chem. Commun.* **2015**, *51*, 13135–13137.

[125] H. L. Kee, C. Kirmaier, L. Yu, P. Thamyongkit, W. J. Youngblood, M. E. Calder, L. Ramos, R. R. Birge, J. S. Lindsey, D. Holten, *J. Phys. Chem. B* **2005**, *109*, 20433–20443.

[126] Y. Wu, M. Štefl, A. Olzyńska, M. Hof, G. Yahioglu, P. Yip, D. R. Casey, O. Ces, J. Humpolíčková, M. K. Kuimova, *Phys. Chem. Chem. Phys.* **2013**, *15*, 14986–14993.

[127] I. López-Duarte, T. T. Vu, M. A. Izquierdo, J. A. Bull, M. K. Kuimova, *Chem. Commun.* **2014**, *50*, 5282–5284.

[128] M. R. Dent, I. López-Duarte, C. J. Dickson, N. D. Geoghegan, J. M. Cooper, I. R. Gould, R. Krams, J. A. Bull, N. J. Brooks, M. K. Kuimova, *Phys. Chem. Chem. Phys.* **2015**, *17*, 18393–18402.

[129] S. Raut, J. Kimball, R. Fudala, H. Doan, B. Maliwal, N. Sabnis, A. Lacko, I. Gryczynski, S. V Dzyuba, Z. Gryczynski, *Phys. Chem. Chem. Phys.* **2014**, *16*, 27037–27042.

[130] J. D. Kimball, S. Raut, L. P. Jameson, N. W. Smith, Z. Gryczynski, S. V. Dzyuba, *RSC Adv.* **2015**, *5*, 19508–19511.

[131] D. Wang, R. Miyamoto, Y. Shiraishi, T. Hirai, *Langmuir* **2009**, *25*, 13176–13182.

[132] R. Paris, I. Quijada-Garrido, O. Garcia, M. Liras, *Macromolecules* **2011**, *44*, 80–86.

[133] H. Wang, Y. Wu, P. Tao, X. Fan, G. C. Kuang, *Chem. - Eur. J.* **2014**, *20*, 16634–16643.

[134] H. Wang, Y. Wu, Y. Shi, P. Tao, X. Fan, X. Su, G. C. Kuang, *Chem. - Eur. J.* **2015**, *21*, 3219–3223.

[135] L. Yao, S. Xiao, F. Dan, *J. Chem.* **2013**, *Vol. 2013*, 10 pages, doi: dx.doi.org/10.1155/2013/697850.

[136] S. G. Awuah, Y. You, *RSC Adv.* **2012**, *2*, 11169–11183.

[137] J. Zhao, K. Xu, W. Yang, Z. Wang, F. Zhong, *Chem. Soc. Rev.* **2015**, *44*, 8904–8939.

[138] T. Yogo, Y. Urano, Y. Ishitsuka, F. Maniwa, T. Nagano, *J. Am. Chem. Soc.* **2005**, *127*, 12162–12163.

[139] A. Kamkaew, K. Burgess, *J. Med. Chem.* **2013**, *56*, 7608–7614.

[140] Q. X. Zhou, W. H. Lei, Y. J. Hou, Y. J. Chen, C. Li, B. W. Zhang, X. S. Wang, *Dalton Trans.* **2013**, *42*, 2786–2791.

[141] T.-J. Wang, Y.-J. Hou, Y.-J. Chen, K. Li, X.-X. Cheng, Q.-X. Zhou, X. Wang, *Dalton Trans.* **2015**, 12726–12734.

[142] I. S. Turan, F. P. Cakmak, D. C. Yildirim, R. Cetin-Atalay, E. U. Akkaya, *Chem. - Eur. J.* **2014**, *20*, 16088–16092.

[143] L. Meng, W. Zhang, D. Li, Y. Li, X. Hu, L. Wang, G. Li, *Chem. Commun.* **2015**, *51*, 14381–14384.

[144] M. Mao, X. Zhang, L. Cao, Y. Tong, G. Wu, *Dye. Pigment.* **2015**, *117*, 28–36.

[145] Z. E. Galateia, N. Agapi, N. Vasilis, G. D. Sharma, C. G. Athanassios, *J. Mater. Chem. C* **2015**, *3*, 5652–5664.

[146] G. D. Sharma, S. A. Siddiqui, A. Nikiforou, G. E. Zervaki, I. Georgakaki, K. Ladomenou, A. G. Coutsolelos, *J. Mater. Chem. C* **2015**, *3*, 6209–6217.

[147] M. Fava, *J. Clin. Psychiatry* **1998**, *59*, 18–22.

[148] T. K. Khan, M. Bröring, S. Mathur, M. Ravikanth, *Coord. Chem. Rev.* **2013**, *257*, 2348–2387.

[149] X. Zhang, Y. Zhang, L. Chen, Y. Xiao, *RSC Adv.* **2015**, *5*, 32283–32289.

[150] W. Liu, J. Yao, C. Zhan, *RSC Adv.* **2015**, *5*, 74238–74241.

[151] M. Shah, K. Thangaraj, M. Soong, L. T. Wolford, J. H. Boyer, *Heteroat. Chem.* **1990**, *1*, 389–399.

[152] J. H. Boyer, A. M. Haag, G. Sathyamoorthi, T. G. Pavlopoulos, *Heteroat. Chem.* **1993**, *4*, 39–49.

[153] G. Sathyamoorthi, J. H. Boyer, T. H. Allik, S. Chandra, *Heteroat. Chem.* **1994**, *5*, 403–407.

[154] M. Benstead, Dipyrrin Complexes and Their Uses As Self Assembling Materials, The University of Hull, **2010**.

[155] A. Costela, I. García-Moreno, M. Pintado-Sierra, F. Amat-Guerri, M. Liras, R. Sastre, F. L. Arbeloa, J. B. Prieto, I. L. Arbeloa, *J. Photochem. Photobiol., A* **2008**, *198*, 192–199.

[156] M. J. Ortiz, I. Garcia-Moreno, A. R. Agarrabeitia, G. Duran-Sampedro, A. Costela, R. Sastre, F. Lopez Arbeloa, J. Banuelos Prieto, I. Lopez Arbeloa, *Phys. Chem. Chem. Phys.* **2010**, *12*, 7804–7811.

[157] D. Zhang, V. Martín, I. García-Moreno, A. Costela, M. E. Pérez-Ojeda, Y. Xiao, *Phys. Chem. Chem. Phys.* **2011**, *13*, 13026–13033.

[158] I. Esnal, G. Duran-Sampedro, A. R. Agarrabeitia, J. Banuelos, I. Garcia-Moreno, M. A. Macias, E. Pena-Cabrera, I. Lopez-Arbeloa, S. de la Moya, M. J. Ortiz, *Phys. Chem. Chem. Phys.* **2015**, *17*, 8239–8247.

[159] G. Duran-Sampedro, A. R. Agarrabeitia, I. Garcia-Moreno, L. Gartzia-Rivero, S. de la Moya, J. Bañuelos, Í. López-Arbeloa, M. J. Ortiz, *Chem. Commun.* **2015**, *51*, 11382–11385.

[160] in *MAK- und BAT-Werte-Liste 2015, Dtsch. Forschungsgemeinschaft Stoffliste*, Wiley, Weinheim, Germany, **2015**, pp. 18–153.

[161] S. H. Heinemann, T. Hoshi, M. Westerhausen, A. Schiller, *Chem. Commun.* **2014**, *50*, 3644–3660.

[162] S. W. Ryter, J. Alam, A. M. K. Choi, *Physiol. Rev.* **2006**, *86*, 583–650.

[163] L. Wu, R. Wang, *Pharmacol. Rev.* **2005**, *57*, 585–630.

[164] X. Zhang, J. Yin, J. Yoon, *Chem. Rev.* **2014**, *114*, 4918–4959.

[165] L. Yuan, W. Lin, L. Tan, K. Zheng, W. Huang, *Angew. Chem., Int. Ed.* **2013**, *52*, 1628–1630.

[166] G. S. Marks, H. J. Vreman, B. E. McLaughlin, J. F. Brien, K. Nakatsu, *Antioxid. Redox Signal.* **2002**, *4*, 271–277.

[167] K. L. Karau, R. H. Johnson, R. C. Molthen, A. H. Dhyani, S. T. Haworth, C. C. Hanger, D. L. Roerig, C. Hanger, D. L. Roerig, A. Christopher, *Am. J. Physiol. Hear. Circ. Physiol.* **2001**, *280*, 483 – 488.

[168] S. S. Park, J. Kim, Y. Lee, *Anal. Chem.* **2012**, *84*, 1792–1796.

[169] U. Hasegawa, A. J. Van Der Vlies, E. Simeoni, C. Wandrey, J. A. Hubbell, *J. Am. Chem. Soc.* **2010**, *132*, 18273–18280.

[170] S. McLean, B. E. Mann, R. K. Poole, *Anal. Biochem.* **2012**, *427*, 36–40.

[171] J. M. Barbe, G. Canard, S. Brandes, R. Guilard, *Chem. - Eur. J.* **2007**, *13*, 2118–2129.

[172] B. W. Michel, A. R. Lippert, C. J. Chang, *J. Am. Chem. Soc.* **2012**, *134*, 15668–15671.

[173] T. Yan, J. Chen, S. Wu, Z. Mao, Z. Liu, *Org. Lett.* **2014**, *16*, 3296–3299.

[174] K. S. Davidge, G. Sanguinetti, C. H. Yee, A. G. Cox, C. W. McLeod, C. E. Monk, B. E. Mann, R. Motterlini, R. K. Poole, *J. Biol. Chem.* **2009**, *284*, 4516–4524.

[175] J.-M. Barbe, G. Canard, S. Brandès, F. Jérôme, G. Dubois, R. Guilard, *Dalton Trans.* **2004**, 1208–1214.

[176] J. Esteban, J. V. Ros-Lis, R. Martinez-Manez, M. D. Marcos, M. Moragues, J. Soto, F. Sancenon, *Angew. Chem., Int. Ed.* **2010**, *49*, 4934–4937.

[177] M. E. Moragues, J. Esteban, J. V. Ros-Lis, R. Martinez-Monez, M. D. Marcos, M.

Martinez, J. Soto, F. Sancenon, *J. Am. Chem. Soc.* **2011**, *133*, 15762–15772.

[178] J. Wang, J. Karpus, B. S. Zhao, Z. Luo, P. R. Chen, C. He, *Angew. Chem., Int. Ed.* **2012**, *51*, 9652–9656.

[179] S. Leuthäußer, D. Schwarz, H. Plenio, *Chem. - Eur. J.* **2007**, *13*, 7195–7203.

[180] W. A. Herrmann, *Angew. Chem., Int. Ed.* **2002**, *41*, 1290–1309.

[181] L. Benhamou, E. Chardon, G. Lavigne, S. Bellemin-Laponnaz, V. César, *Chem. Rev.* **2011**, *111*, 2705–2733.

[182] T. Droege, F. Glorius, *Angew. Chem., Int. Ed.* **2010**, *49*, 6940–6952.

[183] L. A. Schaper, S. J. Hock, W. A. Herrmann, F. E. Kühn, *Angew. Chem., Int. Ed.* **2013**, *52*, 270–289.

[184] J. D. Egbert, C. S. J. Cazin, S. P. Nolan, *Catal. Sci. Technol.* **2013**, *3*, 912–926.

[185] D. Bézier, J. B. Sortais, C. Darcel, *Adv. Synth. Catal.* **2013**, *355*, 19–33.

[186] S. J. Hock, L.-A. Schaper, W. A. Herrmann, F. E. Kühn, *Chem. Soc. Rev.* **2013**, *42*, 5073–5089.

[187] S. P. Nolan, *Acc. Chem. Res.* **2011**, *44*, 91–100.

[188] G. C. Vougioukalakis, R. H. Grubbs, *Chem. Rev.* **2010**, *110*, 1746–1787.

[189] C. Valente, S. Calimsiz, K. H. Hoi, D. Mallik, M. Sayah, M. G. Organ, *Angew. Chem., Int. Ed.* **2012**, *51*, 3314–3332.

[190] D. Enders, O. Niemeier, A. Henseler, *Chem. Rev.* **2007**, *107*, 5606–5655.

[191] M. P. Conley, C. Coperet, C. Thieuleux, *ACS Catal.* **2014**, *4*, 1458–1469.

[192] A. Kiel, J. Kovacs, A. Mokhir, R. Krämer, D. P. Herten, *Angew. Chem., Int. Ed.* **2007**, *46*, 3363–3366.

[193] A. Rybina, C. Lang, M. Wirtz, K. Grußmayer, A. Kurz, F. Maier, A. Schmitt, O. Trapp, G. Jung, D. P. Herten, *Angew. Chem., Int. Ed.* **2013**, *52*, 6322–6325.

[194] E. van der Spoel, M. P. Rozing, J. J. Houwing-Duistermaat, P. Eline Slagboom, M. Beekman, A. J. M. de Craen, R. G. J. Westendorp, D. van Heemst, *Aging* **2015**, *7*, 956–963.

[195] V. Sashuk, L. H. Peeck, H. Plenio, *Chem. - Eur. J.* **2010**, *16*, 3983–3993.

[196] V. Sashuk, D. Schoeps, H. Plenio, *Chem. Commun.* **2009**, 770–772.

[197] J. C. Garrison, W. J. Youngs, *Chem. Rev.* **2005**, *105*, 3978–4008.

[198] U. Hintermair, U. Englert, W. Leitner, *Organometallics* **2011**, *30*, 3726–3731.

[199] T. Strassner, S. Ahrens, Alexander Zeller, *Process for Preparation of Novel Aryl-substituted N-heterocyclic Carbene Bis-2-imidazolylidene Platinum and Palladium Chelate Complexes as Stable Catalysts for Partial Oxidation of Methane to Methanol*, **2006**, WO 2006058535 A2.

[200] V. Lakshmi, M. Rajeswara Rao, M. Ravikanth, *Org. Biomol. Chem.* **2015**, *13*, 2501–2517.

[201] R. D. Savka, H. Plenio, *J. Organomet. Chem.* **2012**, *710*, 68–74.

[202] L. H. Peeck, H. Plenio, *Organometallics* **2010**, *29*, 2761–2766.

[203] J. Nasielski, N. Hadei, G. Achonduh, E. A. B. Kantchev, C. J. O'Brien, A. Lough, M. G. Organ, *Chem. - Eur. J.* **2010**, *16*, 10844–10853.

[204] G. Ulrich, R. Ziessel, A. Haefele, *J. Org. Chem.* **2012**, *77*, 4298–4311.

[205] S. M. Canham, J. Y. Bass, O. Navarro, S. G. Lim, N. Das, S. A. Blum, *Organometallics* **2008**, *27*, 2172–2175.

[206] H. Weissman, E. Shirman, T. Ben-Moshe, R. Cohen, G. Leitus, L. J. W. Shimon, B. Rybtchinski, *Inorg. Chem.* **2007**, *46*, 4790–4792.

[207] Y. Gabe, Y. Urano, K. Kikuchi, H. Kojima, T. Nagano, *J. Am. Chem. Soc.* **2004**, *126*, 3357–3367.

[208] R. Visbal, M. C. Gimeno, *Chem. Soc. Rev.* **2014**, *43*, 3551–3574.

[209] H. J. Park, Y. K. Chung, *Inorg. Chim. Acta* **2012**, *391*, 105–113.

[210] S. Tasan, O. Zava, B. Bertrand, C. Bernhard, C. Goze, M. Picquet, P. Harvey, F. Denat, A. Casini, E. Bodio, *Dalton Trans.* **2013**, *42*, 6102–6109.

[211] G. M. Chu, A. Guerrero-Martínez, I. Fernández, M. Á. Sierra, *Chem. - Eur. J.* **2014**, *20*, 1367–1375.

[212] A. Citta, E. Schuh, F. Mohr, A. Folda, M. L. Massimino, A. Bindoli, A. Casini, M. P. Rigobello, *Metallomics* **2013**, *5*, 1006–1015.

[213] J. Du, M. Hu, J. Fan, X. Peng, *Chem. Soc. Rev.* **2012**, *41*, 4511–4535.

[214] S. Wolf, H. Plenio, *J. Organomet. Chem.* **2009**, *694*, 1487–1492.

[215] T. Ueno, Y. Urano, K. I. Setsukinai, H. Takakusa, H. Kojima, K. Kikuchi, K. Ohkubo, S. Fukuzumi, T. Nagano, *J. Am. Chem. Soc.* **2004**, *126*, 14079–14085.

[216] EMEA European Medicines Agency, *Regul. Doc.* **2008**, 1–34.

[217] C. H. S. Hitchcock, *J. Sci. Food Agric.* **2000**, *80*, 131–136.

[218] J. R. Wilkins, G. E. Stoner, E. H. Boykin, *Appl. Microbiol.* **1974**, *27*, 949–952.

[219] W. Shin, *Anal. Bioanal. Chem.* **2014**, *406*, 3931–3939.

[220] C. Schwarz, Z. Poss, D. Hoffmann, J. Appel, *Recent Advances in Phototrophic Prokaryotes*, Springer, **2010**.

[221] R. B. Gupta, in *Hydrog. Fuel Prod. Transp. Storage*, Taylor & Fransis, **2009**, pp. 495–534.

[222] J. Jiang, G. M. Ma, H. T. Song, H. Y. Zhou, C. R. Li, Y. T. Luo, H. Bin Wang, *Rev. Sci. Instrum.* **2015**, *86*, 106103–106106.

[223] H. Yan, X. Zhao, C. Zhang, Q. Z. Li, J. Cao, D. F. Han, H. Hao, M. Wang, *Opt. Commun.* **2016**, *359*, 157–161.

[224] P. C. Chou, H. I. Chen, I. P. Liu, W. C. Chen, C. C. Chen, J. K. Liou, C. J. Lai, W. C. Liu, *Int. J. Hydrogen Energy* **2015**, *40*, 9006–9012.

[225] D. T. Phan, A. S. M. I. Uddin, G. S. Chung, *Sens. Actuators, B* **2015**, *220*, 962–967.

[226] D. Dutta, S. K. Hazra, J. Das, C. K. Sarkar, S. Basu, *Sens. Actuators, B* **2015**, *212*, 84–92.

[227] V. S. Nguyen, V. Jubera, A. Garcia, H. Debéda, *Appl. Surf. Sci.* **2015**, *357*, 14–21.

[228] “Element One, inc.,” can be found under http://www.elem1.com/, **2016**.

[229] D. K. Benson, R. D. Smith, W. Hoagland, “Novel Wide-Area Hydrogen Sensing Technology,” can be found under http://www.elem1.com/, **2010**.

[230] R. Crabtree, *Acc. Chem. Res.* **1979**, *12*, 331–337.

[231] J. J. Verendel, O. Pamies, M. Dieguez, P. G. Andersson, *Chem. Rev.* **2014**, *114*, 2130–2169.

[232] X. Cui, K. Burgess, *Chem. Rev.* **2005**, *105*, 3272–3296.

[233] S. J. Roseblade, A. Pfaltz, *Acc. Chem. Res.* **2007**, *40*, 1402–1411.

[234] G. Xu, S. R. Gilbertson, *Org. Lett.* **2005**, *7*, 4605–4608.

[235] M. Schilz, H. Plenio, *J. Org. Chem.* **2012**, *77*, 2798–2807.

[236] G. W. Nyce, S. Csihony, R. M. Waymouth, J. L. Hedrick, *Chem. - Eur. J.* **2004**, *10*, 4073–4079.

[237] M. Fekete, O. Bay, S. B. Duckett, S. Hart, R. E. Mewis, N. Pridmore, P. J. Rayner, A. Whitwood, *Inorg. Chem.* **2013**, *52*, 13453–13461.

[238] S. P. Smidt, N. Zimmermann, M. Studer, A. Pfaltz, *Chem. - Eur. J.* **2004**, *10*, 4685–4693.

[239] S. P. Smidt, A. Pfaltz, E. Martinez-Viviente, P. S. Pregosin, A. Albinati, *Organometallics* **2003**, *22*, 1000–1009.

[240] D. F. Chodosh, R. H. Crabtree, H. Felkin, S. Morehouse, G. E. Morris, *Inorg. Chem.* **1982**, *21*, 1307–1311.

[241] Y. Xu, M. A. Celik, A. L. Thompson, H. Cai, M. Yurtsever, B. Odell, J. C. Green, D. M. P. Mingos, J. M. Brown, *Angew. Chem., Int. Ed.* **2009**, *48*, 582–585.

[242] R. H. Crabtree, P. C. Demou, D. Eden, J. M. Mihelcic, C. A. Parnell, J. M. Quirk, G. E. Morris, *J. Am. Chem. Soc.* **1982**, *104*, 6994–7001.

[243] L. D. Vazquez-Serrano, B. T. Owens, J. M. Buriak, *Inorg. Chim. Acta* **2006**, *359*, 2786–2797.

[244] V. Farina, C. Shu, X. Zeng, X. Wei, Z. Han, N. K. Yee, C. H. Senanayake, *Org. Process Res. Dev.* **2009**, *13*, 250–254.

[245] J. W. Morzycki, *Steroids* **2011**, *76*, 949–966.

[246] A. Leitgeb, J. Wappel, C. Slugovc, *Polym. Chem.* **2010**, *51*, 2927–2946.

[247] A. H. Hoveyda, S. J. Malcolmson, S. J. Meek, A. R. Zhugralin, *Angew. Chem., Int. Ed.* **2010**, *49*, 34–44.

[248] R. R. Schrock, *Acc. Chem. Res.* **1986**, *19*, 342–348.

[249] P. Schwab, M. B. France, J. W. Ziller, R. H. Grubbs, *Angew. Chem., Int. Ed.* **1995**, *34*, 2039–2041.

[250] J. S. Kingsbury, J. P. A. Harrity, P. J. Bonitatebus, A. H. Hoveyda, *J. Am. Chem. Soc.* **1999**, *121*, 791–799.

[251] J.-L. Hérisson, Y. Chauvin, *Makromol. Chemie* **1970**, *141*, 161–176.

[252] T. Cordes, S. A. Blum, *Nat. Chem.* **2013**, *5*, 993–999.

[253] N. M. Esfandiari, Y. Wang, J. Y. Bass, T. P. Cornell, D. A. L. Otte, M. H. Cheng, J. C. Hemminger, T. M. McIntire, V. A. Mandelshtam, S. A. Blum, *J. Am. Chem. Soc.* **2010**, *132*, 15167–15169.

[254] N. M. Esfandiari, Y. Wang, T. M. McIntire, S. A. Blum, *Organometallics* **2011**, *30*, 2901–2907.

[255] N. M. Esfandiari, Y. Wang, J. Y. Bass, S. A. Blum, *Inorg. Chem.* **2011**, *50*, 9201–9203.

[256] G. De Cremer, M. B. J. Roeffaers, E. Bartholomeeusen, K. Lin, P. Dedecker, P. P. Pescarmona, P. A. Jacobs, D. E. De Vos, J. Hofkens, B. F. Sels, *Angew. Chem., Int. Ed.* **2010**, *49*, 908–911.

[257] M. Wirtz, A. Grüter, P. Rebmann, T. Dier, D. A. Volmer, V. Huch, G. Jung, *Chem. Commun.* **2014**, *50*, 12694–12697.

[258] G. De Cremer, B. F. Sels, D. E. De Vos, J. Hofkens, M. B. J. Roeffaers, *Chem. Soc. Rev.* **2010**, *39*, 4703–4717.

[259] D. P. Herten, A. Rybina, J. Balbo, G. Jung, in *Methods Phys. Chem.*, Wiley, **2012**, pp. 711–735.

[260] J. R. Lakowicz, in *Princ. Fluoresc. Spectrosc.*, Springer, **2006**, pp. 759–797.

[261] N. M. Esfandiari, S. A. Blum, *J. Am. Chem. Soc.* **2011**, *133*, 18145–18147.

[262] B. Scheinhardt, J. Trzaskowski, M. C. Baier, B. Stempfle, A. Oppermann, D. Wöll, S. Mecking, *Macromolecules* **2013**, *46*, 7902–7910.

[263] M. Wirtz, A. Grüter, F. Heib, V. Huch, J. Zapp, D.-P. Herten, M. Schmitt, G. Jung, *Methods Appl. Fluoresc.* **2015**, *3*, 44001–44007.

[264] T. Vorfalt, K. J. Wannowius, V. Thiel, H. Plenio, *Chem. - Eur. J.* **2010**, *16*, 12312–12315.

[265] T. Vorfalt, K. J. Wannowius, H. Plenio, *Angew. Chem., Int. Ed.* **2010**, *49*, 5533–5536.

[266] V. Thiel, M. Hendann, K. J. Wannowius, H. Plenio, *J. Am. Chem. Soc.* **2012**, *134*, 1104–1114.

[267] D. J. Nelson, S. Manzini, C. A. Urbina-Blanco, S. P. Nolan, *Chem. Commun.* **2014**, *50*, 10355–10375.

[268] G. C. Vougioukalakis, R. H. Grubbs, *Chem. - Eur. J.* **2008**, *14*, 7545–7556.

[269] I. W. Ashworth, I. H. Hillier, D. J. Nelson, J. M. Percy, M. A. Vincent, *Chem. Commun.* **2011**, *47*, 5428–5430.

[270] V. Thiel, K. J. Wannowius, C. Wolff, C. M. Thiele, H. Plenio, *Chem. - Eur. J.* **2013**, *19*, 16403–16414.

[271] F. Nuñez-Zarur, X. Solans-Monfort, L. Rodríguez-Santiago, M. Sodupe, *Organometallics* **2012**, *31*, 4203–4215.

[272] F. Nuñez-Zarur, X. Solans-Monfort, L. Rodríguez-Santiago, R. Pleixats, M. Sodupe, *Chem. - Eur. J.* **2011**, *17*, 7506–7520.

[273] P. Kos, R. Savka, H. Plenio, *Adv. Synth. Catal.* **2013**, *355*, 439–447.

[274] L. H. Peeck, R. D. Savka, H. Plenio, *Chem. - Eur. J.* **2012**, *18*, 12845–12853.

[275] P. E. Romero, W. E. Piers, *J. Am. Chem. Soc.* **2007**, *129*, 1698–1704.

[276] E. M. Leitao, E. F. Van Der Eide, P. E. Romero, W. E. Piers, R. McDonald, *J. Am. Chem. Soc.* **2010**, *132*, 2784–2794.

[277] C. Hinderling, C. Adlhart, P. Chen, *Angew. Chem., Int. Ed.* **1998**, *37*, 2685–2689.

[278] C. E. Webster, *J. Am. Chem. Soc.* **2007**, *129*, 7490–7491.

[279] A. P. Blum, T. Ritter, R. H. Grubbs, *Organometallics* **2007**, *26*, 2122–2124.

[280] C. A. Urbina-Blanco, A. Poater, T. Lebl, S. Manzini, A. M. Z. Slawin, L. Cavallo, S. P. Nolan, *J. Am. Chem. Soc.* **2013**, *135*, 7073–7078.

[281] F. Bergstroem, I. Mikhalyov, P. Haeggloef, R. Wortmann, T. Ny, L. B.-A. Johansson, *J. Am. Chem. Soc.* **2002**, *124*, 196–204.

[282] I. Mikhalyov, N. Gretskaya, F. Bergström, L. B.-A. Johansson, *Phys. Chem. Chem. Phys.* **2002**, *4*, 5663–5670.

[283] D. Tleugabulova, Z. Zhang, J. D. Brennan, *J. Phys. Chem. B* **2002**, *106*, 13133–13138.

[284] J. Karolin, M. Fa, M. Wilczynska, T. Ny, L. B. Johansson, *Biophys. J.* **1998**, *74*, 11–21.

[285] M. Fa, F. Bergström, P. Hägglöf, M. Wilczynska, L. B. Å. Johansson, T. Ny, *Structure* **2000**, *8*, 397–405.

[286] H. H. Soon, A. G. Wenzel, T. T. Salguero, M. W. Day, R. H. Grubbs, *J. Am. Chem. Soc.* **2007**, *129*, 7961–7968.

[287] T. Vorfalt, S. Leuthäußer, H. Plenio, *Angew. Chem., Int. Ed.* **2009**, *48*, 5191–5194.

[288] S. Wolf, H. Plenio, *J. Organomet. Chem.* **2010**, *695*, 2418–2422.

[289] C. Bonnier, D. D. Machin, O. Abdi, B. D. Koivisto, *Org. Biomol. Chem.* **2013**, *11*, 3756–3760.

[290] M. Döbbelin, I. Azcune, M. Bedu, A. Ruiz De Luzuriaga, A. Genua, V. Jovanovski, G. Cabañero, I. Odriozola, *Chem. Mater.* **2012**, *24*, 1583–1590.

[291] U. Resch-Genger, K. Rurack, *Pure Appl. Chem.* **2013**, *85*, 2005–2013.

Lebenslauf

Persönliche Daten

Name, Vorname:	Kos, Pavlo
Adresse:	Klausenburger Str. 128 64295 Darmstadt
Geburtsdatum, -ort:	05.08.1988, Novyi Rozdil, Ukraine
Familienstand:	ledig

Promotion

04/2016	**voraussichtlicher Abschluss der Promotion (Dr. rer. nat.)**
02/2016	**Abgabe der Dissertation**
10/2011 – 07/2016	**Praktischer Teil der Dissertation** unter der Leitung von Prof. Dr. H. Plenio, Technische Universität Darmstadt im Fachbereich Anorganische Chemie. Titel der Doktorarbeit: Synthesis and application of new BODIPY-tagged NHC-metal-complexes

Studium

09/2009 - 06/2011	**Magisterdiplom**, Nationale Taras-Schewtschenko-Universität Kyiv, Fachbereich Chemie, Schwerpunkt organische Chemie. Titel der Magisterdiplomarbeit: Synthese von Derivativen, teilweise hydrierter Asolo(s)pyrimidine
09/2005 - 06/2009	**Diplom der Bachelors**, Nationale Taras Schewtschenko-Universität Kyiv, Fachbereich Chemie, Schwerpunkt organische Chemie.

Schulausbildung

09/2002 – 05/2005	**Physisch-mathematisches Lyzeum** der Nationalen Ivan-Franko-Universität Lviv
09/1995 – 05/2002	**Grundschule**, Novyi Rozdil, Ukraine

Darmstadt, 25.04.2016

Pavlo Kos

Klausenburger Str. 128

64295 Darmstadt

25.02.2016

Erklärung

Ich erkläre hiermit, daß ich meine Dissertation selbstständig und nur mit den angegebenen Hilfsmitteln angefertigt habe.

Pavlo Kos

Pavlo Kos
Klausenburger Str. 128
64295 Darmstadt

25.02.2016

Erklärung

Ich erkläre hiermit, noch keinen Promotionsversuch unternommen zu haben.

Pavlo Kos

Zusammenfassung der Ergebnisse

Das primäre Ziel dieser Arbeit war die Entwicklung einer Synthese zur Herstellung BODIPY-markierte NHC-Metallkomplexe, sowie die Untersuchung der Eignung dieser Substanzen als Fluoreszenzsensoren. Dabei hat sich gezeigt, dass die Modifikation der Elektronendichte am Metallzentrum erheblichen Einfluss auf die Effizienz der Fluoreszenzlöschung ausübt. Auf Basis dieser Erkenntnisse, wurde ein Fluoreszenz-Chemodosimeter für die Detektion von CO Gas und der erste Fluoreszenz Wasserstoffsensor entwickelt.

In den folgenden Abschnitten werden die wichtigsten Aspekte meiner Arbeit als kurze Zusammenfassung dargestellt.

1. Ein neuartigers BODIPY-markiertes NHC **12** und BODIPY–markierte NHC Komplexe mit Ir, Rh, Au, Ru und Pd wurden hergestellt (Abbildung 1).

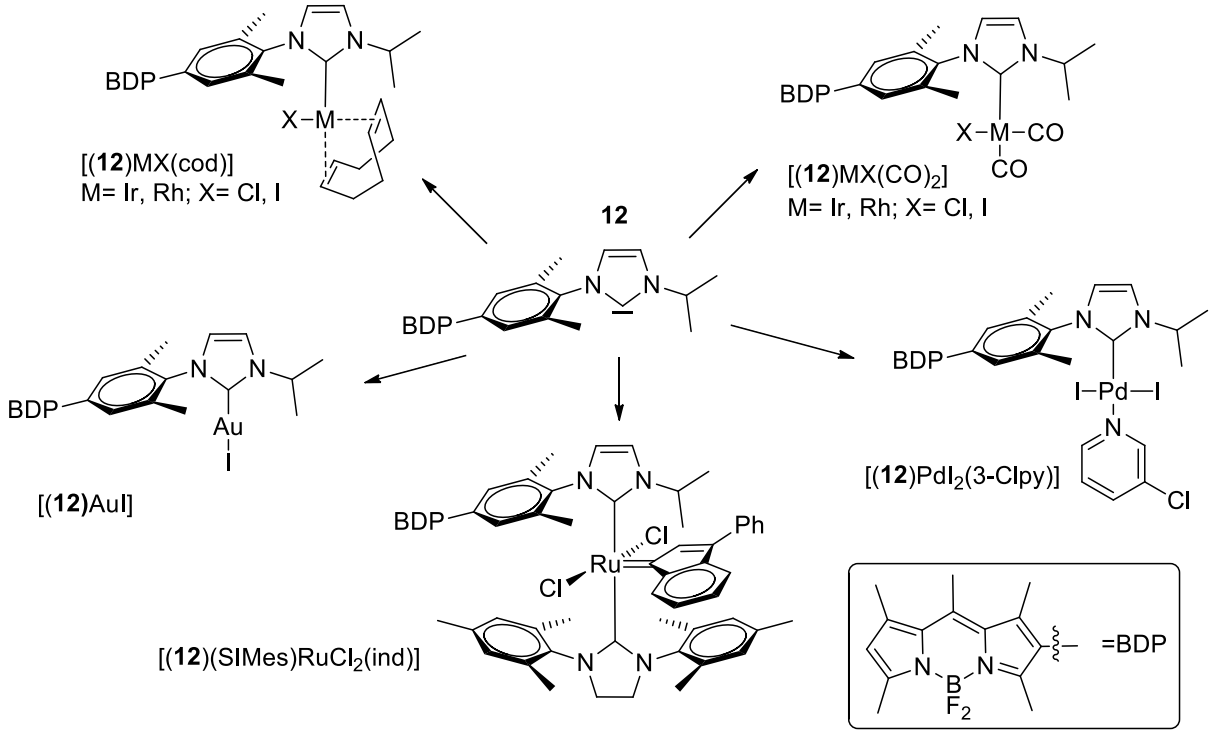

Abbildung 1: BODIPY-markierte NHC-Metallkomplexe.

2. Die spektroskopischen Eigenschaften der neuen Komplexe wurden bestimmt. Die synthetisierten Verbindungen zeichnen sich durch sehr unterschiedliche Fluoreszenzeigenschaften aus: stark gequenchte Komplexe ($\Phi<0.01$) mit Ru oder elektronenreichem Ir und Rh, ein teilweise gequenchter Pd-Komplex ($\Phi=0.033$) und ein stark fluoreszierender Au–Komplex ($\Phi=0.70$). Ligandenaustauschreaktionen führen zu ausgeprägten Änderungen in der Helligkeit der BODIPY Einheit in den metallorganischen Komplex von Rh, Ir, und Au. Die Manipulation der Elektronendichte an den Übergangsmetallen reguliert die Effizienz des PET Quenchens, da elektronenreiche Übergangsmetalle zu verringerter Fluoreszenz führen, wohingegen elektronenarme Metallzentren zu einer erhöhten Fluoreszenzemission führen.

3. Bei der Reaktion mit Kohlenmonoxid wurden die Komplexe [(**12**)MX(cod)] (M=Rh, Ir; X=Cl, I; $\Phi=0.008$ bis 0.016) in stark fluoreszierende Komplexe überführt [(**12**)MX$(CO)_2$] ($\Phi=0.53$-0.70). Der Fluoreszenzanstieg der Rh und Ir–Komplexe, kann auf die verringerte Elektronendichte in den Rh oder Ir Carbonylkomplexen zurückgeführt werden (Abbildung 2).

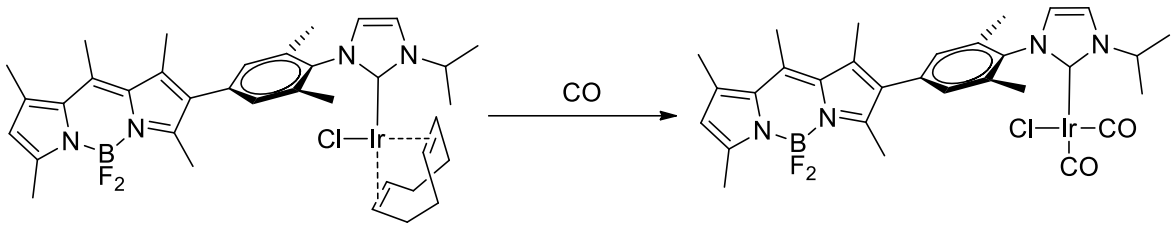

[(**12**)IrCl(cod)], Φ=0.008 [(**12**)IrCl(CO)$_2$], Φ=0.63

Abbildung 2: Reaktion von [(**12**)IrCl(cod)] mit CO.

Die neu entwickelten cod-Komplexe können als effiziente Chemodosimeter für CO, mit ausgezeichneten „turn-on" Verhältnissen und schnellen Ausprechzeiten, verwendet werden. Das Signal wird durch die cod→CO Ligandenaustauschreaktion erzeugt, welche in weniger als 4 s für den Ir-Komplex und in 20 s für den Rh-Komplex abgeschlossen ist, was zu einem mehr als 50-fachen Anstieg in der Emissionsintensität führt. Darüber hinaus besitzen diese Komplexe eine hervorragende Empfindlichkeit gegenüber CO. In diesen Sinne führt die Zugabe von weniger als einem Nanomol CO-Gas zu der Lösung von [(**12**)IrCl(cod)], zu einer nachweisbaren Änderung der Fluoreszenzintensität (Abbildung 3).

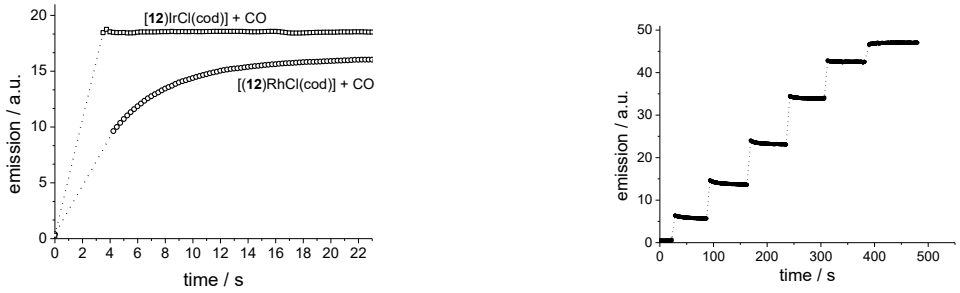

Abbildung 3: Links: Emission-Zeit Kurve der Reaktion von [(**12**)MCl(cod)] (M=Rh, Ir) (c = 2.0·10^{-6} mol·L^{-1} in Ethylacetat, 25°C) mit CO (10 equiv; c = 2.0·10^{-5} mol·L^{-1}, 9.0·10^{-9} mol). Rechts: Emission-Zeit Kurve der Reaktion von [(**12**)IrCl(cod)] (c = 1.0·10^{-5} mol·L^{-1} in Ethylacetat, 25°C) mit CO (6×0.6(±0.2) μL); Die letzte Zugabe führt zu voller Emissionsintensität.

Die neu entwickelten Komplexe sind feuchtigkeits- und luftstabil und eignen sich für die Ermittlung des CO-Gehalts in der atmosphärischen Luft. *In-vivo*-Studien von eng verwandten triethylenglykolsubstituierten Komplexen [(**13**)MI(cod)] (M=Rh, Ir), durchgeführt in Kooperation mit Prof. Dr. Stefan H. Heinemann (Friedrich-Schiller-Universität Jena) zeigten, dass diese Komplexe für die CO-Detektion in lebenden Zellen aufgrund der geringen Fluoreszenzresonanz in wäßrigen Medium aufgrund einer relativ hohen Zytotoxizität nicht geeignet sind.

4. Ein BODIPY markierter Crabtree Ir Komplex wurden synthetisiert. Die oxidative Addition von H_2 überführt den schwach fluoreszierenden Ir^I Komplex (Φ= 0.038) in die stark fluoreszierende Ir^{III} Spezies (Φ = 0.51, Abbildung 4).

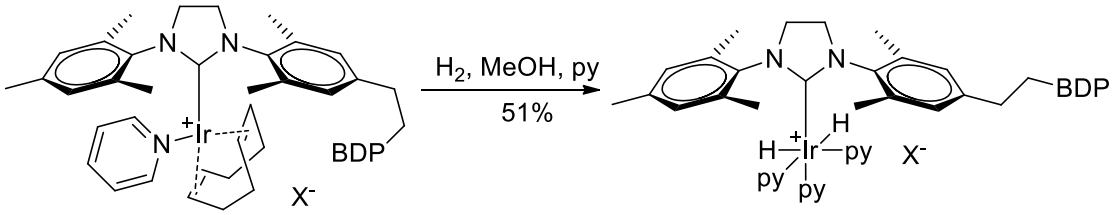

20b (X = CF_3SO_3), Φ= 0.038
20c (X = BArF)

21b (X = CF_3SO_3), Φ=0.51
21c (X = BArF)

Abbildung 4: Reaktion der BODIPY-markierten Crabtree Komplexe **20** mit H_2.

5. Die katalytischen Eigenschaften der neuen Iridium-Komplexe wurden untersucht. Die Reaktion mit dem Testsubstrat Allylbenzol und Wasserstoff bei Raumtemperatur in Gegenwart von **20c**, liefert das vollständig hydrierte Produkt innerhalb von 10 min in nahezu quantitativer Ausbeute bei 0.5 mol% Katalysatorbeladung in 1,2-Dichlorethan. Die zeitabhängige Fluoreszenzintensität der Komplexe **20** ($1.0 \cdot 10^{-6}$ mol·L^{-1} in 1,2-Dichlorethan, 0.1 mol % Katalysator) wurde während der katalytischen Reaktionen mit verschiedenen Olefin Substraten beobachtet. Die Zunahme der Fluoreszenzintensität ist praktisch die gleiche wie die, welche für das Experiment unter den gleichen Reaktionsbedingungen in Abwesenheit von Substrat beobachtet wird (Abbildung 5). Auf dieser Grundlage ist es wahrscheinlich, dass eine Iridium Dihydrid Spezies als Ruhezustand der katalytischen Reaktion vorliegt.

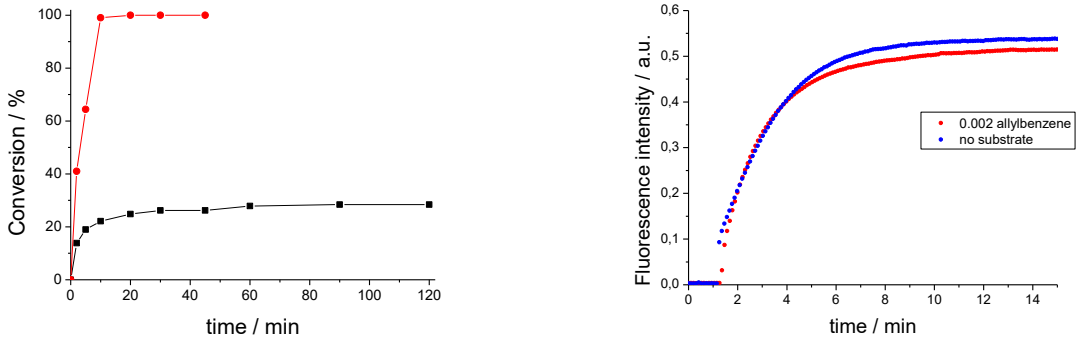

Abbildung 5: Links: Umsatz-Zeit Kurve für die katalytische Hydrierung von 0.1 mol·L^{-1} Allylbenzol mit **20c** ($1.0 \cdot 10^{-3}$ mol·L^{-1}, 1 mol %) (rot) und 0.002 mol·L^{-}1 Allylbenzol mit **20c** ($1.0 \cdot 10^{-5}$ mol·L^{-1}, 0.5 mol %) (schwarz) in 1,2-Dichlorethan mit Wasserstoff. Rechts: Fluoreszenz–Zeit Kurve für die katalytische Hydrierung von 0.002 mol·L^{-1} Allylbenzol mit **20c** ($1.0 \cdot 10^{-3}$ mol·L^{-1}, 0.5 mol %) (rot); die selben Reaktionsbedingungen ohne Olefin (blau).

6. Ein Verfahren zur H_2-Detektion auf einem Papierstreifen wurde entwickelt. Durch Imprägnierung des Filterpapiers mit einer Lösung von **20b** in Propylencarbonat in einer H_2-haltigen Atmosphäre ist es möglich, Wasserstoff in einer Konzentration entsprechend der unteren Explosionsgrenze (4% Vol) nachzuweisen. Eine optische Unterscheidung von 4% Vol und 1 % Vol ist möglich (Abbildung 6).

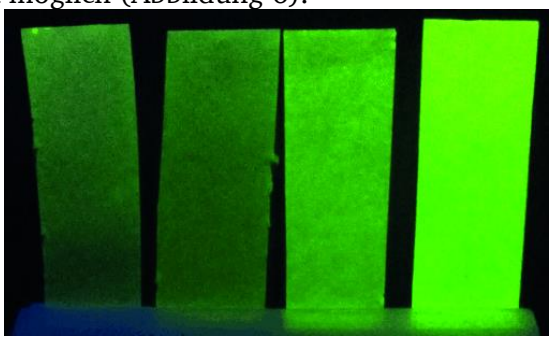

Abbildung 6: Vier Filterpapierstreifen (von links nach rechts: a–d) befeuchtet mit eine Lösung von **20b** in Propylencarbonat und bestrahlt mit UV-Licht. Streifen (a) der Umgebungsluft ausgesetzt; Streifen (b) dem 1 % (vol) H_2 ausgesetzt; Streifen (c) dem 4 % (vol) H_2 ausgesetzt (untere Explosionsgrenze), und Streifen (d) reinem H_2 ausgesetzt.

In Abwesenheit von H_2, ist die Lösung von **20b** in diesem Lösungsmittel sehr stabil und die Fluoreszenzeigenschaften ändern sich über längere Zeit in Gegenwart von Umgebungsluft nicht. Dieses Papierstreifen–Assay ist relativ günstig, einfach zu bedienen und empfindlich genug um Wasserstoff an seiner unteren Explosionsgrenze nachzuweisen. Dieser Papierstreifen Test könnte zur gängigen Methode zur Erkennung von industriellen H_2 Lecks weiterentwickelt werden. Die Komplexe **20** sind die ersten publizierten fluoreszierenden molekularen Sonden für H_2.

7. Fünf BODIPY-markierte Metathese-Komplexe wurden synthetisiert, wobei das Fluorophor entweder am NHC oder an der Benzylidengruppe gebunden ist (Abbildung 7). Die Fluoreszenz von BODIPY in allen Komplexen ist durch Ruthenium stark verringert.

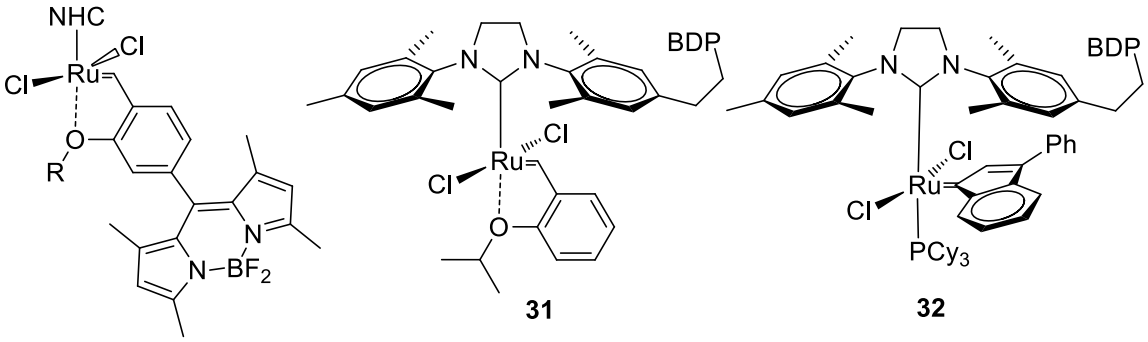

26: NHC= SIPr, R= $(CH_2)_{11}Si(OiPr)_3$
30-NHC: NHC= SIMes, SIPr; R= *i*Pr

Abbildung 7: Neulich entwickelte BODIPY-markierte Metathese-Komplexe.

8. Komplex **26** wurde für die Beobachtung der ROMP eines Norbornens auf der Einzelmolekülebene verwendet. Dazu wurde **26** auf der Glasoberfläche immobilisiert und die modifizierten Deckgläser mit einem TIRF-Mikroskop untersucht. Es wurden die Fluoreszenzeigenschaften der kovalent an die Oberfläche gebundenen einzelnen Moleküle untersucht. Die Bestrahlung der Probe mit Laserlicht führt zum hochfrequenten Blinken des Farbstoffs. Dieses kann auf die kontinuierlichen „on-off" Zustände in Folge des Photobleaching von BODIPY bezogen werden. Der aktive Zustand besitzt jedoch unter den verwendeten Messparametern eine zu kurze Lebenszeit, um eine weitere Beobachtung der ROMP auf der Ebene einzelner Moleküle zu ermöglichen. Eine weitere Verbesserung der Katalysatorstruktur und der Erfassungsparameter ist erforderlich.

9. Die synthetisierten Verbindungen **30** bis **32** wurden mit verschiedenen Olefinen zur Reaktion gebracht und Änderungen in den Emissions- und Absorptionsspektren mittels Fluoreszenz und UV/Vis-Spektroskopie überwacht. Bei der Initiierung des Komplexes **30**–SIMES, wird eine ausgeprägte Erhöhung (bis zu 30-fach) der Fluoreszenzintensität der BODIPY Einheit beobachtet. Eine detaillierte kinetische Analyse der Emission-Zeit Kurven bei 512 nm zeigt identische Werte der Geschwindigkeitskonstanten im Vergleich zu denen, des Abfalls der Absorptionsintensität des LMCT Bandes. Dies legt nahe, dass die Dissoziation der Ru–O-Bindung ein limitierender Schritt der Startreaktion ist.

In dieser Arbeit wurde gezeigt, dass die Fluoreszenzspektroskopie ein sehr nützliches Werkzeug in der metallorganischen Chemie sein kann. Veränderungen in der Elektronendichte am Metallzentrum des fluorophor-markierten Komplexes haben Veränderungen in der Emissionsintensität von fluoreszierenden Markierungen zur Folge. Dieses Phänomen kann für die Entwicklung molekulare Sensoren verwendet werden. Darüber hinaus könnten solche Komplexe für die detaillierte Untersuchung katalytischer Umwandlungen an Metallzentren wertvoll sein. Erkennbare Änderungen in der Fluoreszenz, können als Nachweis und für die Quantifizierung der einzelnen Spezies in komplexen Reaktionsgemischen verendet werden. Dies ist bereits in geringsten Konzentrationen möglich, die unterhalb der Nachweisgrenze der meisten andern spektroskopischen Methoden liegen.